Design and Manufacturing of a Cryostat for a Compact Cryogenic Neutron Moderator for Operation at Temperatures below 10 K

Entwicklung und Bau eines Kryostaten für einen kompakten kryogenen Neutronenmoderator zum Betrieb bei Temperaturen unterhalb von 10 K

Von der Fakultät für Maschinenwesen der Rheinisch-Westfälischen Technischen Hochschule Aachen zur Erlangung des akademischen Grades eines Doktors der Ingenieurwissenschaften genehmigte Dissertation

vorgelegt von

Alexander Schwab

Berichter/in: Univ.-Prof. Dr. rer. nat. Ghaleb Natour

Univ.-Prof. Dr. rer. nat. habil. Thomas Brückel

Univ.-Prof. Dr.-Ing. Lorenz Singheiser

Tag der mündlichen Prüfung: 16.04.2024

Diese Dissertation ist auf den Internetseiten der Universitätsbibliothek online verfügbar.

Abstract

The High Brilliance Neutron Source (HBS), a future high-current accelerator-driven neutron source (Hi-CANS), is producing a neutron peak brightness comparable to or higher than that of currently operating medium-flux research reactors. A key feature of the HBS is its use of multiple target-moderator-reflector (TMR) units, in which neutrons are released by low-energy proton reactions in a tantalum target and subsequently slowed down by interactions with compact thermal and cold moderators. Additionally, by using only one cold moderator for each attached neutron scattering instrument, the neutron spectrum can be optimized with regards to the instrument's requirements.
For the generation of low-energy neutrons ($E < 25$ meV), a multitude of materials can be used as cold neutron moderators at cryogenic temperatures. The cold neutron brightness scales with the total neutron yield but additionally depends on the moderator material and its geometry and operating conditions as well as the surrounding structures like thermal moderators, reflectors and the neutron transport system. In the case of some potential cold moderator materials, a reduction of the operating temperature below the commonly used 20 K can be of benefit. From previously used cold moderators, solid methane was chosen as a candidate for a compact cold moderator operated at temperatures of $T \leq 10$ K. Its geometry and dimensions were chosen from the results of nuclear simulations using MCNP6.1. Following, a system for the use of solid cryogenic moderator materials for temperatures of $T \leq 10$ K was designed, manufactured and tested. The thermal and structural boundary conditions and operating parameters of the cryogenic system were defined and critical areas were subjected to a more detailed analytical examination. The problem of heat transfer in a molecular solid and the effect of high radiation levels on the moderator material for a proton beam power of approximately 100 kW at the target were paramount. To ensure the system's safety and stability during operation and to minimize possible malfunctions, the nuclear code RCC-MRx was applied, which takes into consideration not only the stability of the components but also their behavior under nuclear irradiation.
After manufacturing, assembly and commissioning of the system, it was tested experimentally with and without neutrons at the Big Karl experimental hall of the COSY (COoler SYnchrotron) facility at Forschungszentrum Jülich, using solid methane as a moderator material at different temperatures between $T \leq 10$ K and 100 K. The recorded neutron time of flight (ToF) spectra were analyzed and compared to the results of previous measurements performed with liquid parahydrogen. The calculation of the neutron brightness from the experimental data using the software VITESS3.4 allows an assessment of the moderator's performance at the full-power HBS facility. The results show that the energy spectrum of solid methane can be shifted to low energies by decreasing its temperature, even below 20 K. A solid cylinder of methane at 7.5 K with a diameter of 2 cm generates a higher peak and time-averaged brightness at thermal energies than a liquid parahydrogen moderator, but shows a lower brightness at low energies up to a factor of 20.

Kurzfassung

Die High Brilliance Neutron Source (HBS), eine zukünftige Hochstrom-Beschleuniger-getriebene Neutronenquelle (Hi-CANS), erzeugt eine Peak-Brightness, die mit der von derzeit im Betrieb befindlichen Mittelfluss-Forschungsreaktoren vergleichbar ist oder diese sogar übertrifft. Ein Hauptmerkmal der HBS ist die Nutzung mehrerer Target-Moderator-Reflektor-Einheiten (TMR), in denen Neutronen durch niederenergetische Protonenreaktionen in einem Tantalum-Target freigesetzt und anschließend durch Wechselwirkungen mit kompakten thermischen und kalten Moderatoren abgebremst werden. Weiterhin kann durch die Nutzung individueller kalter Moderatoren für jedes angeschlossene Instrument das Spektrum hinsichtlich dessen Anforderungen optimiert werden.
Zur Erzeugung von niederenergetischen Neutronen ($E < 25$ meV) kann eine Vielzahl unterschiedlicher Materialien bei kryogenen Temperaturen als kalte Moderatoren verwendet werden. Neben der Neutronenausbeute am Target hängt die Brightness auch von Moderatormaterial und -geometrie sowie Betriebsbedingungen und umgebender Struktur aus thermischem Moderator, Reflektor und Neutronentransportsystemen ab. Im Falle einiger kalter Moderatoren kann eine Reduzierung der Betriebstemperatur unter die üblicherweise genutzten 20 K vorteilhaft sein. Von diesen wurde festes Methan als Kandidat für einen kompakten kalten Moderator, betrieben bei $T \leq 10$ K, ausgewählt. Die Geometrie und Abmessungen wurden dabei nach Ergebnissen nuklearer Simulationen mit MCNP6.1 festgelegt. Anschließend wurde ein System zur Nutzung fester kryogener Moderatormaterialien bis zu Temperaturen von $T \leq 10$ K ausgelegt, gefertigt und getestet. Die thermischen und strukturellen Rand- und Betriebsbedingungen des kryogenen Systems wurden definiert und kritische Bereiche einer ausführlicheren Prüfung unterzogen. Hierbei musste die Herausforderung der äußerst geringen Wärmeleitung in einem molekularen Festkörper bei derart tiefen Temperaturen und die Auswirkungen hoher Strahlungslevel auf das Moderatormaterial bei einer Protonenstrahlleistung von 100 kW am Target bewältigt werden. Um die Sicherheit und Stabilität des Systems während des Betriebs zu gewährleisten und mögliche Fehlfunktionen zu minimieren, wurde es anhand des Regelwerks RCC-MRx ausgelegt, das nicht nur die Stabilität der Komponenten sondern auch ihr Verhalten unter nuklearer Bestrahlung berücksichtigt.
Nach Fertigung, Montage und Inbetriebnahme wurde das System experimentell mit und ohne freie Neutronen in der Big Karl-Experimentierhalle des COSY (COoler SYnchrotron) am Forschungszentrum Jülich mit festem Methan bei Temperaturen zwischen $T \leq 10$ K und 100 K getestet. Die aufgenommenen Flugzeitspektren (ToF) wurden analysiert und mit den Ergebnissen vorheriger Messungen mit flüssigem Parawasserstoff verglichen. Die Berechnung der Neutronen-Brightness aus den experimentellen Daten mittels der Software VITESS3.4 erlaubt eine Einschätzung der Moderatorperformance an der Volllast-HBS. Die Ergebnisse zeigen, dass sich das Energiespektrum festen Methans durch eine Absenkung der Temperatur zu geringeren Energien verschieben lässt, auch unterhalb von 20 K. Ein Methan-Zylinder bei 7.5 K mit einem Durchmesser von 2 cm erzeugt eine höhere Peak- und zeitlich gemittelte Brightness bei thermischen Energien als ein flüssiger Parawasserstoffmoderator, allerdings eine bis zum Faktor 20 geringere Brightness bei geringen Energien.

Contents

List of Figures

List of Tables

List of Symbols, Indices and Abbreviations

Roman symbols

A	Surface	mm^2
C	Torque	$\mathrm{N} \cdot \mathrm{m}$
c_p	Specific isobaric heat capacity	$\mathrm{J} \cdot \mathrm{kg}^{-1} \cdot \mathrm{K}^{-1}$
d	Diameter	mm
DC	Duty cycle	-
E	Energy	J
E_{eff}	Effective emissivity	-
f	Frequency	$\mathrm{Hz} = 1\mathrm{s}^{-1}$
f_A	Correlation factor	-
f_{fr}	Coefficient of friction	-
G	Gasket mean diameter	mm
H	Height	mm
h	Planck's constant	$\mathrm{J} \cdot \mathrm{s}$
$h_{lat,vap}$	Latent heat of evaporation	$\mathrm{J} \cdot \mathrm{kg}^{-1}$
h_T	Heat transfer coefficient	$\mathrm{W} \cdot \mathrm{m}^{-2} \cdot \mathrm{K}^{-1}$
I_{CO}	Uncertainty of tightening means	-
K	Specific force per length	$\mathrm{N} \cdot \mathrm{m}^{-1}$
k	Wavenumber	cm^{-1}
k_B	Boltzmann constant	$\mathrm{J} \cdot \mathrm{K}^{-1}$
L	Length	mm
$l_{fitting}$	Length of fitting	mm
m	Mass	g
m_n	Neutron refractive index	-
$\dot{m}$	Mass flow	g/s

n	Number of layers	-
Nu	Nusselt number	-
P	Primary stress	MPa
P_e	Perimeter	mm
p	Pressure	$1\,\mathrm{bar}{=}10^5\,\mathrm{Pa}$
p_{thread}	Thread pitch	mm
$\dot{Q}$	Heat flux	W
Q	Secondary stress	Pa
Q_L	Leakage rate	$\mathrm{Pa{\cdot}m^3{\cdot}s^{-1}}$
$\dot{q}$	Specific heat flux	$\mathrm{W{\cdot}m^{-2}}$
R	Moderating ratio	-
R_m	Ultimate tensile strength	MPa
r_N	Bending radius	mm
R_p	Yield Strength	MPa
s	Lateral deformation	mm
S_m	Allowable stress	MPa
T	Temperature	K
t	time	s
t_w	Wall thickness	mm
U	Voltage	V
V	Volume	$\mathrm{cm^3}$
V_A	Fatigue usage fraction	-
v	Velocity	$\mathrm{m \cdot s^{-1}}$
W	Width	mm
x	Distance	mm
x_{col}	Number of collisions	-

Greek symbols

α	Auxiliary number	-
α_{abs}	Absorption	-
ϵ	Strain	$\mathrm{mm \cdot mm^{-1}}$
θ	Angle	$^\circ$

Λ	Mean free path	cm
λ_n	Wavelength	$\text{Å} = 10^{-10}\,\text{m}$
λ_{th}	Thermal conductivity	$\text{W} \cdot \text{m}^{-1} \cdot \text{K}^{-1}$
μ	Attenuation factor	cm^{-1}
ξ	Logarithmic energy decrement	-
ρ	Density	$\text{g} \cdot \text{cm}^{-3}$
Σ	Macroscopic cross section	cm^{-1}
σ	Cross section	barn $= 10^{-28}\,\text{m}^2$
σ_b	Bending stress	MPa
σ_{eq}	Equivalent stress	MPa
σ_m	Mean stress	MPa
τ	Thread root shear stress	MPa
ϕ	Porosity	-
ω	Angular frequency	s^{-1}

Indices

∞	Infinity
0	initial
12	Between surfaces 1 (= cold) and 2 (= warm)
a	Absorption
abs	Absorption
avg	Average
B	Bolt
b	Bending
bar(g)	Gauge pressure
c	Cross sectional
coh	Coherent
com	Compression
cond	Conduction
cool	Coolant
crit	Critical
D	Design

det	Detector
eff	Effective
el	Elastic
evac	Evacuated
ext	external
f	final, pitch
fr	Free
gen	Generation
hyd	Hydraulic
i	Inner, internal, index
inc	Incoherent
inel	Inelastic
kin	Kinetic
l	Local
m	membrane
max	Maximum
mod	Moderator
n	Neutron
o	Outer
op	Operation
p	Proton, pulse
rad	Radiation
s	Scattering
sh	Shield
th	Thermal
ToF	Time of flight
tot	Total
vac	Vacuum
w	Wall

Abbreviations

AM	Additive Manufacturing

ANSYS	Analysis Systems
B-PE	Borated polyethylene
CAB	Centro Atómico Bariloche
CAD	Computer-aided design
CANS	Compact Accelerator-driven Neutron Source
CM	Cold moderator
CME	Crucible melt extraction
DGUV	Deutsche Gesetzliche Unfallversicherung e. V.
EB	Electron beam
ENDF	Evaluated Nuclear Data File
FEA	Finite element analysis
FLUKA	Fluktuierende Kaskade (engl.: fluctuating cascade)
FPGA	Field-Programmable Gate Array
GM	Gifford-McMahon
GMP	Gas-management panel
HBS	High Brilliance Neutron Source
HD-PE	High-density polyethylene
Hi-CANS	High-Current Accelerator-driven Neutron Source
IFAM	Institut für Fertigungstechnik und angewandte Materialforschung
ILL	Institut Laue-Langevin
IWU	Institut für Werkzeugmaschinen und Umformtechnik
JCNS	Jülich Centre for Neutron Science
JULIC	Juelich Light Ion Cyclotron
LANL	Los Alamos National Laboratory
LH_2	Liquid hydrogen
LHe	Liquid helium
Linac	Linear Accelerator
LPBF	Laser powder bed fusion
MCNP	Monte Carlo N-Particle
McStas	Monte carlo Simulation of triple axis spectrometer
MFC	Mass flow controller
MLI	Multi-layer insulation

n	Neutron
p	Proton, primary particle
p-H_2	Parahydrogen
PC	Pressure controller
PHITS	Particle and Heavy Ion Transport Code System
PLC	Programmable logic control
PnV	Pneumatic valve
ppi	Pores per inch
PT	Pressure transducer, Pulse tube
RAL	Rutherford Appleton Laboratory
RCC-MRx	Règles de Conception et de Construction des Matériels Mécaniques des ilots nucleaires RNR
RFQ	Radio Frequency Quadrupole
TIG	Tungsten inert gas
TL	Transfer line
TMP	Turbomolecular pump
TMR	Target-Moderator-Reflector
ToF	Time of flight
TS-II	Target Station II
UCN	Ultracold neutron
VCN	Very cold neutron
VI	Virtual Instrument
VITESS	Virtual Instrumentation Tool for the ESS
ZEA-1	Central Institute of Engineering, Electronics and Analytics (ZEA) - Engineering and Technology

Chapter 1

Introduction

Neutrons are an important tool for the investigation of the structure and dynamics of matter on an atomic scale. Due to their neutral charge, neutrons penetrate matter more deeply than X-rays or electrons and interact directly with the nuclei of atoms via nuclear forces. As a result, the interaction probability of nuclides with neutrons does not increase with atomic number, and neutrons can also be used as a probe for light elements, e. g. light hydrogen or oxygen. Furthermore, the neutron's magnetic moment enables the investigation of the magnetic properties of matter via scattering on unpaired electrons of magnetic atoms.
Especially cold neutrons ($E_n \leq 10$ meV) are indispensable when it comes to the investigation of matter from the nano- to a molecular scale. Examples of their application are the analysis of polymer composition and dynamics, of biomolecules and of inhomogeneities of crystalline and amorphous structures. Typically used techniques include small-angle neutron scattering (SANS, see Figure 1.1) and reflectometry. In engineering applications, the former can be used to investigate effects of heat treatment in metals, for example in weld connections, or the size of metallic precipitates [1].

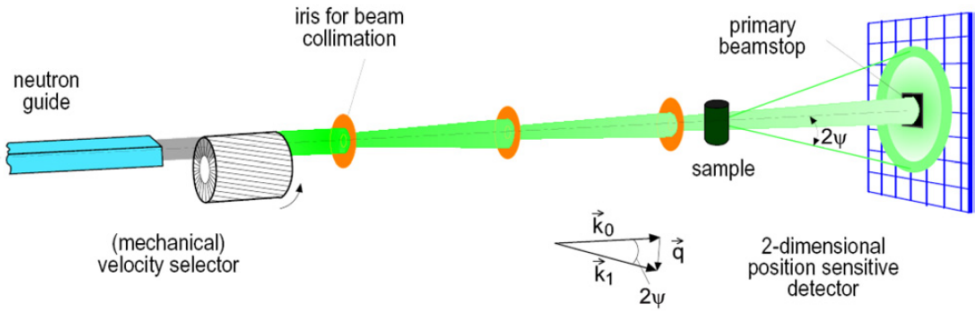

Figure 1.1: Schematic view of a small-angle neutron-scattering instrument (image taken from [2]).

Due to the neutron's low interaction probability, large intensities are required to obtain meaningful results from neutron scattering experiments. For this, a number of facilities like fission research reactors (e. g. *ILL* in Grenoble, France) or spallation sources (like *ISIS* near Didcot, United Kingdom) are available. These facilities collectively offer a total of several thousand hours of beam time per year, which covers a large part of the present demand. However, in recent years, several European research reactors have been shut down [3]. This is partly owed to their condition, having been built between the 1960s and 1980s, calling for expensive modernizations that are often times not feasible. In addition, new political regulations regarding the handling and operation of radioactive material in some

European countries make the operation of such sources more difficult.
Although a new high-flux facility like ESS will allow a lot of new and important experiments to happen, it cannot cover the total demand for beam time present in the neutron user community. Therefore, a network of medium-sized accelerator-driven neutron sources (CANS) could in principal complement the existing and planned large-scale facilities. Especially the proposed High-Current Accelerator-driven Neutron Sources (Hi-CANS) offer the opportunity to create a neutron peak brightness of the cold moderators that is comparable or even exceeding that of reactor-based sources. In addition, the reduced beam power and pulsed operation as well as the optimized setup result in lower levels of radioactivity induced by neutron and gamma radiation and therefore in less activated material. Furthermore, no fissionable materials are necessary. For the case of multiple target-moderator-reflector units, the modular design allows a further operation of parts of the facility during repair or modifications to the source.
The planned High Brilliance Neutron Source (HBS) is an example of such a Hi-CANS, using a pulsed proton beam with a maximum energy of 70 MeV and a peak proton current of 89.3 mA to produce neutrons via low-energy (p,n) reactions [4].
Due to the low levels of radiation produced - compared to spallation and fission processes - neutron moderators and transport devices can be positioned much closer to the target or core than is the case for the other two types of facilities. This way, the overall lower neutron yield can be used much more efficiently. Additionally, the use of multiple compact thermal and cold moderators per target station provides an opportunity to increase the number of usable neutrons at the sample position by optimizing the individual moderators with regards to their attached instrument's requirements.

1.1 Motivation

The number of usable cold neutrons available at the sample position in a scattering experiment is largely dependent on the efficiency of the cold moderator to slow down high-energy neutrons. Another factor is the ability to extract a large part of the neutrons from the moderator before they are being absorbed.
The novel concept for the HBS to use compact cryogenic moderators adjusted to the specific needs of individual instruments calls for a thorough investigation of potential materials. Apart from liquid parahydrogen, which is the most commonly used cold moderator at spallation sources and whose properties as a low-dimensional moderator have been investigated extensively in recent years, other options, e. g. hydrocarbons, deuterium or clathrate hydrates, are potential candidates. However, most of these materials have previously been used as bulk moderators, feeding a large number of instruments at the same time. Monte Carlo simulations help in assessing the optimum compact dimensions for such moderators to obtain the highest brightness. Yet, the available data is often scarce and only available for certain temperatures. Furthermore, inconsistencies between existing scattering cross sections increase the uncertainty of the theoretically calculated results.
With an average beam power of 100 kW per target, the HBS represents a link between the low-energy compact neutron sources and the high-energy spallation sources. This offers the opportunity to use materials as cold moderators that are not feasible for the latter due to constraints imposed from nuclear heating and potential radiation damages. However, this feasibility has to be proven for a facility like HBS by performing thermodynamical and structural simulations as well as experimental validations. Even though the dimensions of the moderators are only in the range of up to a few cm, the pulsed beam operation can introduce large temperature rises in the material if the moderator cooling is not carefully considered. Such temperature rises would diminish the efficiency of the cold moderator and might even cause parts of the moderator to melt or evaporate. Especially for solid cryogenic moderators, the specific characteristics of the moderator material have to be

known and adopted to properly assess the moderator's behavior during beam operation. Again, this data is often times not available or exclusively in certain temperature regions for most materials below their freezing point.

1.2 Goal of the thesis

In the context of the HBS project at Forschungszentrum Jülich, two commonly used cold moderators have previously been investigated both by simulations as well as experimentally by using time of flight (ToF) measurements. In a next step, the possibility to shift the resulting neutron spectrum to lower energies is investigated by decreasing the operating temperature of the moderator material.
An experimental cold moderator cryostat usable for different potential materials can help in obtaining experimental results with free neutrons, which in turn can be compared to existing data. For the design of such a cryostat, a high degree of interchangeability is important, so that the cold moderator vessel can be easily exchanged. Also, the cooling capacity should cover a large range to allow the cryostat to be used at different beam powers.
For this, a system containing a cryostat for the production of the cold moderator at the desired temperature as well as a control panel for operating the cryostat is designed, manufactured and tested. This system is planned to be used at a prototype facility to investigate the neutronic performance of different materials. The emphasis during the design phase is on the investigation of the boundary conditions imposed by the demand for lower temperatures and the resulting design choices. The choice of material and geometry for the first candidate of a cold moderator used with this cryostat is made based on nuclear simulations using the Monte Carlo code MCNP6.1. Due to uncertainties in the scattering kernels used for these simulations, an experimental investigation is necessary to correctly estimate the moderator's performance. The obtained results from time of flight measurements can subsequently be used to review nuclear simulation results, making the design of future cold moderators more reliable.

1.3 Structure of the thesis

The outline of the thesis is as follows:

Basics of neutron production and moderation
The concept of high-current accelerator-driven neutron sources (Hi-CANS) is presented and compared to different types of neutron facilities. An emphasis lies on the role of the cold moderator inside this type of facility. A classification of neutrons according to their energy is given and the neutron moderation process is described.

Choice of cold moderators for temperatures below 10 K
Previously used cold moderator materials are listed and their advantages and disadvantages are compared. Important factor in the choice of a moderator material is its efficiency to increase the number of neutrons with energies below 10 meV for a compact geometry and by operating it at temperatures of 10 K and below. On the basis of a literature survey and nuclear simulations performed at JCNS, a moderator material and geometry is chosen.

Cryostat and process design
According to the requirements of neutron moderation and the boundary conditions from its intended operational site, basic engineering design choices are presented and compared to alternative options. The basis for these choices is created by analytical calculations as well as numerical simulations, where needed. The design of the control system necessary to

operate the cryostat system is presented and the requirements from common engineering codes that ensure a reliable and safe operation are satisfied.

Prototype manufacturing and inspection
Manufacturing choices for the different sections of the cryostat system are discussed and presented. The manufacturing process is followed and documented and several non-destructive and destructive test methods are used to ensure a reliable state of the system.

Commissioning and experimental validation
The commissioning of the cryostat and the system's operation with and without the use of neutrons is presented. The experimental setup is demonstrated and the results of neutron time of flight measurements are analyzed and compared to those of previously used moderator materials.

Discussion and Outlook
The consequences of the experimental results with regards to possible optimizations of the system are discussed and further options for using different geometries and materials are reviewed.

Chapter 2

Neutron production and moderation

2.1 Neutron production

There are several ways to provide free neutrons for science, with large differences in the energy required for their generation, the number of neutrons released per single reaction and the levels of radioactivity generated. For high-intensity experiments, the most commonly used neutron production processes are either based on fission reactions, e. g. in research reactors like the high-flux reactor at the Institute Laue-Langevin (ILL) in Grenoble, France, or spallation, as used in sources like the ISIS neutron and muon source at the Rutherford Appleton Laboratory, England. But also low-energy proton reactions in the sub-100 MeV region can be utilized to generate neutrons. Their neutron yield is typically lower compared to the other two options, but the development of novel concepts using high-current proton accelerators and high-brightness moderators could potentially outperform research reactors with regards to the obtainable peak brightness. The following paragraphs give a short overview of the aforementioned processes and their advantages and disadvantages.

Nuclear fission: In research reactors, free neutrons are produced by the absorption of a thermal neutron inside fissionable material, e. g. enriched uranium (U-235). The fission reaction generates two to three high-energy neutrons, which in turn are slowed down to thermal energies and once more induce fission processes (see Figure 2.1, top left). To avoid a critical chain reaction inside the reactor core, control rods of a neutron-poisonous material are used to absorb neutrons. In research reactors, less fuel is needed compared to power reactors, since the main focus is not the generation of energy but of free neutrons. Since the process of fission is a continuous one, the neutrons are produced with a constant intensity over time. Therefore, additional tools like neutron choppers, monochromators or velocity selectors are necessary to divide the neutron beam into different energies or wavelengths, which is a prerequisite for performing time of flight measurements.
Fission reactors are limited in the effective thermal neutron flux to around 10^{15} n/(cm$^2 \cdot$ s) [5] due to a limit in cooling capability. Since many of the existing facilities were built in the 1950s to 1970s, they are partially outdated and often in need of retrofitting.

Spallation: In a spallation process, a heavy metal target with a high atomic number Z is bombarded with very high-energy particles (e. g. protons with several hundred MeV to several GeV). Typical target materials include tungsten and tantalum due to their large number of neutrons per atom (> 100). During the spallation reaction, almost two thirds of the energy is transformed into heat and several fragments are emitted. Apart from the neutrons that are directly knocked out of the target during the proton collisions, neutrons are evaporated in a secondary reaction by the excited nuclei of the target material. In this reaction, up to thirty neutrons can be produced per proton and target nucleus (see Figure 2.1, center). The applied high-energy proton beam can either be produced by a

linear accelerator (linac), a cyclotron, or a combination of these two. This enables a pulsed production of protons (and therefore neutrons), which allows the performance of time of flight measurements. By performing such measurements, information on the structure and dynamics of matter can be obtained from analyzing the energy or wavelength of the neutrons scattered by the sample.

Low-energy proton reactions: Another - less frequently used - way to produce neutrons is through low-energy proton capture reactions, e. g. (p,n) (see Figure 2.1, bottom right) or (p,2n) reactions. Although basically similar in principle to the spallation process, the neutron output and energy is drastically lower due to the lower energy of the primary particles. On the other hand, less unwanted particles are released that would require additional shielding. For a lot of the existing facilities, the energy of the protons is only at several MeV. Typical target materials for proton energies of up to 30 MeV include beryllium (Be) and lithium (Li), since their atomic number Z is low and incident protons can overcome their Coulomb barrier and induce a reaction. At higher energies, materials like tungsten (W) or tantalum (Ta) are preferred due to their high atomic number Z and consequently higher neutron content.
Although less effective in neutron yield compared to spallation or fission sources, unwanted radiation levels are also lower, allowing the positioning of components closer to the source as it is realizable for spallation sources. Therefore, the ratio of neutrons that can be used for experiments to that of neutrons released in general can be higher if the necessary methods are applied.

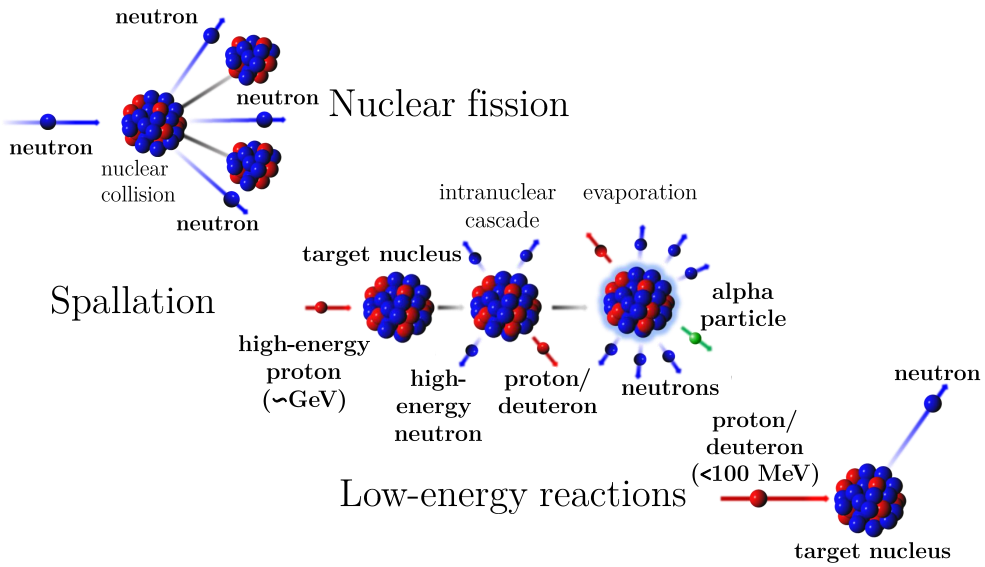

Figure 2.1: Different forms of neutron production. Fission (left), spallation (center) and low-energy proton reactions (right) (images taken from [6], text adapted for visibility)

The largest part of the free neutrons that are generated in the aforementioned neutron sources usually has energies in the order of a few tenth to several MeV. To be usable for scattering experiments, their wavelength has to be in the order of the atomic or molecular structure inside the investigated sample. Therefore, the neutrons have to be slowed down by repeated collision with atomic nuclei (so-called *moderation*).

2.2 Moderation process

The neutrons released from metal targets by accelerated protons usually show an energy distribution with a peak at some tenth of MeV to several MeV, depending on the proton energy of the primary particles, the target material and its dimensions. An exemplary energy spectrum calculated by a nuclear simulation (MCNP6.1) for an HBS target station with a 70 MeV proton beam is depicted in Figure 2.2.

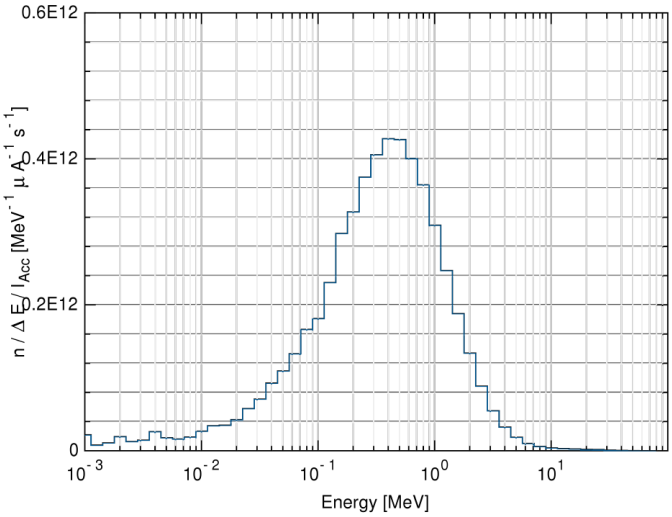

Figure 2.2: Energy spectrum of free neutrons produced in a tantalum target with a proton energy of 70 MeV via Ta(p, xn) reactions, integrated over 4π (taken from [4]).

A large fraction of the produced neutrons have energies above 0.1 MeV, which corresponds to wavelengths of $\lambda_n \leq 9 \times 10^{-4}$ Å. To obtain a good resolution in scattering experiments, the wavelength of the neutrons should match the relevant length scales of the sample under investigation. This value usually ranges from 1 Å (10^{-10} m) to 1 µm [7]. Therefore, the free neutrons produced in an accelerator-driven source have to be slowed down to those energies to be usable as probes for the structure or dynamics of matter.
Neutrons can be classified according to several quantities like energy, wavelength, temperature and velocity, which are transformable by applying the Boltzmann or Planck's constant, k_B and h, respectively. A possible classification, partly assembled from [8] and [9], which includes the energy ranges crucial in neutron moderation, is given in Table 2.1. Depending on the field of research or application, the boundary values and number of energy ranges may change.

Table 2.1: Classification of neutrons by their energy, temperature and wavelength as well as corresponding moderator temperature (categories and values assembled from [8], [9]).

	Neutron energy [meV]	**Neutron temp. [K]**	**Neutron wavelength [Å]**	**Moderator option (& T_{mod})**
Hot	100–500	1000–6000	1–0.4	Graphite ($T_{mod} = 2000$ K)
Thermal	15–100	60–1000	4–1	Light water ($T_{mod} = 300$ K)
Cold	0.1–15	1–120	30–3	LH_2 ($T_{mod} = 20$ K)
Very cold	3×10^{-4}–0.1	0.004–1	500–30	Solid D_2 ($T_{mod} = 5$ K)
Ultra cold	$< 3 \times 10^{-4}$	< 0.004	> 500	He II (($T_{mod} = 2$ K)

In general, *neutron moderation* describes the process of energy transfer from free neutrons with higher energies to the atoms or nuclei of a moderating material (the so-called *moderator*). This energy transfer can happen by various mechanisms, depending on the energy of the neutron and the nature and state of the moderator atoms or molecules.
The process can be roughly divided into two parts. One is the process of *slowing down* or *down-scattering* the neutrons, the other one is called *thermal scattering*. The first process is mainly taking place for neutron energies in the region of some MeV down to some eV, while the latter one occurs below the binding energy of atoms (sub-eV).
Depending on the purpose of the moderator, each of these two processes can be more important and pose different requirements. In the case of a thermal moderator, the slowing down is usually more important than for a cold moderator (as long as the latter is "coupled", which means fed with thermal neutrons from a pre-moderator). On the other hand, the number of available very low-energy levels, which allow an energy transfer of their respective energy, is not as crucial as it is for a cold moderator, since the neutrons only have to be thermalized at room temperature ($E = 25$ meV).

Slowing down:
Down to energies of some electronvolts (eV) - which corresponds to the binding energy of atoms - the energy transfer happens mainly by elastic collisions. This means that the kinetic energy E_{kin} of the system **moderator atom** $\leftrightarrow$ **neutron** stays constant. In this case, the moderator atoms can be regarded as initially at rest (no thermal motion) and without any connection to neighbouring atoms (no chemical bindings), since the neutrons are able to kick the moderator atoms out of their position. There is no significant atomic level-order [10] and due to this lack of intermolecular or -atomic interaction, the characteristics of compound materials (e. g. molecules) can be regarded by simply summing up the contribution of the different atoms in the compound.
It is known from classical mechanics that the highest energy transfer occurs if the impacting bodies have the same mass. This is also applicable to the interaction between neutrons and matter, meaning that the highest energy transfer occurs for an ideal collision between a neutron and a proton ($m_n = 1.675 \times 10^{-27}$ kg, $m_p = 1.673 \times 10^{-27}$ kg). For a head-on collision, the neutron is able to transfer all of its energy to the nucleus of the moderator. However, in reality, all kinds of collisions between incident angles of 0° to 180° and energy transfers of 0% to 100% occur.
The probability of an individual interaction (e. g. scattering or absorption) between a neutron and a nucleus in a material is described by the respective microscopic neutron cross section σ. It is usually expressed in the unit barn, which corresponds to 10^{-28} m^2, and can be understood as the effective area that a nucleus presents to an incident neutron [11].
The microscopic cross section can be classified according to the type of reaction of interest: absorption cross section σ_a and scattering cross section σ_s, which can be classified into an elastic and inelastic part ($\sigma_{s,el}$ and $\sigma_{s,inel}$, respectively), which in turn can be divided into incoherent and coherent parts ($\sigma_{s,el,inc}$, $\sigma_{s,el,coh}$, $\sigma_{s,inel,inc}$ and $\sigma_{s,inel,coh}$). In slow neutron scattering, unlike in the nuclear physics sense, "elastic" denotes a change in the neutron's direction, while its energy stays constant. This is caused, for example, by an interaction of the neutron's magnetic moment with the unpaired electrons in a magnetic atom or a scattering event without energy transfer due to the neutron's low energy. Inelastic scattering, on the other hand, includes a change in energy of the neutron by exciting inelastic excitations in an atom or molecule (e. g. vibrations or rotations). Coherent and incoherent interactions describe the way a neutron wave interacts with a compound of nuclei. If the nuclei are ordered (e. g. in a crystalline material), the resulting scattering is mainly coherent. Hydrogenous materials, on the other hand, are mainly incoherent scatterers and the scattered neutron waves have random relative phases.

For hydrogen, the total neutron cross section $\sigma_{tot} = \sigma_s + \sigma_a$ stays constant over a large region of incident neutron energies (see Figure 2.3, left). The absorption cross section can be divided into two parts, depending on the energy of the neutrons. In the thermal energy region, σ_a decreases with increasing energy, following the 1/v law, where $\sigma_a \propto \frac{1}{v} \propto \frac{1}{\sqrt{E}}$. Due to the decreasing velocity of the neutron, the time spent close to the moderator atoms increases, resulting in a higher absorption probability. For higher energies, some materials show a resonance region, in which σ_a has sharp peaks, which occur when the neutron energy matches the discrete quantum states of the material's nuclei.

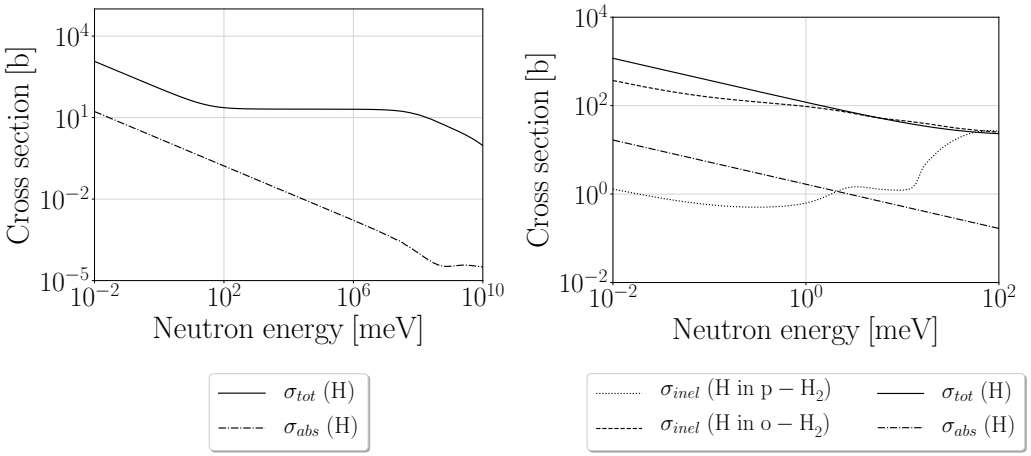

Figure 2.3: Total and absorption cross section of hydrogen (^{1}H) (left) as well as inelastic scattering cross sections of hydrogen in para- and ortho-H_2 (right) vs. incident neutron energy. (values taken from [12]).

The effectiveness of a moderator for slowing down fast neutrons in the slowing-down region is frequently described by the mean logarithmic energy decrement per collision ξ [13], which takes the probability of all possible scattering angles into account:

$$\xi = \ln\left(\frac{E_1}{E_2}\right) = 1 + \frac{\alpha}{1-\alpha} \cdot \ln \alpha \tag{2.1}$$

where E_1 and E_2 are the energies of the neutron before and after the collision, respectively, and $\alpha = (\frac{A-1}{A+1})^2$ with the atomic mass A of the atom. For atoms with $A > 10$, the energy decrement can be calculated approximately as

$$\xi \approx \frac{2}{A + 2/3} \tag{2.2}$$

with a relative error of less than 0.1% compared to Equation 2.1. For mixtures of isotopes, e. g. H_2O or CH_4, the mean logarithmic energy decrement per collision can be calculated as follows:

$$\xi = \frac{\sum(\xi_i \cdot \Sigma_{fr,i})}{\sum \sigma_{fr}} \tag{2.3}$$

with the free macroscopic scattering cross section Σ_{fr} of the respective isotopes, which is the product of the number density N of atoms in the moderator and the scattering probability in form of the microscopic free scattering cross section σ_{fr} (which corresponds to the elastic scattering cross section $\sigma_{s,el}$ above $E = 1$ eV).
Using ξ, one can calculate the number of collisions x_{col} necessary to slow down neutrons from a starting energy E_0 to a desired final energy E_f by using the following formula [14]:

$$x_{col} = \frac{1}{\xi} \cdot \ln\left(\frac{E_0}{E_f}\right) \tag{2.4}$$

To obtain the distance travelled by a neutron of a certain energy between two subsequent collisions, it is possible to calculate the mean free path Λ from the macroscopic cross section Σ_{fr} [14]:

$$\Lambda = \frac{1}{\Sigma_{fr}} = \frac{1}{N \cdot \sigma_{fr}} \tag{2.5}$$

In addition to its scattering characteristics, a good moderator should have a low absorption probability. The effect of neutron absorption can be rated by its macroscopic absorption cross section $\Sigma_a = N \cdot \sigma_a$. A good figure of merit for the comparison of the slowing-down efficiency of different moderators is thus the "moderating ratio" [15]:

$$R_{mod} = \xi \cdot \Sigma_s / \Sigma_a. \tag{2.6}$$

Thermal scattering:
For neutron energies below the binding energy of atoms ($E_n < 1$ eV), the energy has to be transferred via elemental excitations like molecular vibrations and rotations. Depending on the specific neutron energy, various mechanisms contribute to the interaction. This is also the energy region where differences in the materials used for cold and thermal moderators become important.
The cross section of most moderator materials ceases to be constant below an energy of approximately 0.1 eV and starts to rise continuously with decreasing neutron energy (see Figure 2.3, right, for hydrogen). The free neutron scattering cross section changes to a bound state and a distinction between coherent and incoherent scattering is necessary, since a collision does not only affect single atoms, but also whole molecular structures. For molecular crystals this is true due to the long-range order of the molecules in the lattice of the solid. Although the number of scattering events increases, this does not necessarily mean that the neutron energy changes, since a lot of these interactions are elastic from a neutron scattering point-of-view, as described above.
For moderation in an infinite medium in thermal equilibrium with an environment at temperature T, the resulting thermal-neutron spectrum can be approximated by a Maxwell-Boltzmann distribution [13]

$$N(E) = 2\pi N \frac{\sqrt{E}}{(\pi E_T)^{3/2}} \exp\left(-\frac{E}{E_T}\right), \tag{2.7}$$

where $N(E)$ is the neutron number density per unit energy and E_T is the energy at temperature T.
When taking the effects of neutron absorption and under-moderation into account, the Maxwell-Boltzmann distribution has to be adjusted to still describe the resulting spectrum by replacing the energy E_T by an energy $E_{T_{eff}}$ at an effective temperature T_{eff}, higher than the actual temperature of the moderator:

$$E_{T_{eff}} = k_B \cdot T_{eff} \tag{2.8}$$

For energies of several hundred down to some tens of meV, energy transfer largely happens via the excitation of intramolecular vibrations (e. g. stretching or compression of a molecular bond, like the OH-bond in water). At even lower energies, energy transfer happens mainly via collective excitations in a periodic, elastic arrangement of atoms or molecules in condensed matter, so-called *phonons*. These excitations can be divided into *acoustic* and *optical* phonons, depending on their dispersion relation $\omega(k)$, which connects the frequency of the excitation with the wavelength λ or wavenumber $k = \frac{2\pi}{\lambda}$. The ability to take up energy depends on the number of available possible phonon excitations or modes. While acoustic phonons exhibit modes of excitation at low frequencies or energies due to their $\omega \propto k$ relation, optical phonons approach a non-zero constant value with increasing wavelength (or decreasing wavenumber). The total of the different modes is called the *phonon*

density of states and is generally a good indicator for the effectiveness of the material to take up energy in a specific energy region.
Below the typical phonon energies, rotational motions can provide the means for further slowing down the neutrons (e. g. rotations of the hydrogen atoms in a methane molecule). However, these modes of excitation are not pronounced in all materials, which is why some materials are more effective than others at slowing down neutrons to energies of only a few meV. At even lower energies, magnetic excitations (so-called *magnons*) offer a possibility for energy transfer, although those kinds of mechanisms are usually used for the production of ultracold neutrons. With decreasing moderator temperature in the cryogenic regime, some of the degrees of freedom of the molecules are frozen and can therefore not be excited, which causes some materials to not be as effective as cold moderators at low temperatures (< 20 K).

Absorption: As mentioned earlier, the neutron absorption probability in hydrogenous materials increases inversely proportional to the neutron's velocity, since the neutrons spend more time in the vicinity of individual moderator atoms. At neutron energies of $E < 10$ meV, the absorption in hydrogen represents a significant problem for large moderator volumes. Although the extent of thermalization increases, more neutrons are absorbed with decreasing energy due to the decreasing mean free path between absorption interactions. At the same time, the probability of scattering to induce an energy transfer declines. Therefore, the choice of the optimum dimensions of a cold moderator is a trade-off between the allowable absorption and the achievable thermalization. Low-dimensional moderators offer the opportunity to increase the brightness in exchange for a thermalization to lower neutron energies.

2.3 Cold moderator types

There is a large number of possible materials that are usable as cold neutron moderators due to their high hydrogen density and their multitude of molecular degrees of freedom. A selection of the most commonly used or investigated materials is given in Table 2.2.

Table 2.2: List of commonly used materials for cold neutron moderation.

Material	Symbol	Facility
Hydrogen	H_2	in operation at: ESS, J-PARC, SNS, ISIS
Deuterium	D_2	in operation at: FRM-II, ILL
Methane	CH_4	in operation at: ISIS, LENS
Mesitylene	C_9H_{12}	in operation at: IBR-2, KUANS
Ethane	C_2H_6	-
Triphenylmethane	$C_{19}H_{16}$	tested at ISIS
(Water-)Ice	H_2O	tested at Forschungszentrum Jülich
Hydrate clathrates	e. g. CH_4/H_2O	-
Ammonia	NH_3	tested at IPNS

One of the most commonly used materials since several decades and especially as a low-dimensional moderator in recent years [16] is molecular hydrogen in its liquid form (LH_2). Its condensation leads to several benefits: on the one hand, the moderator temperature and therefore its equilibrium energy are decreased, while simultaneously increasing its density and therefore hydrogen content per volume. On the other hand, the spin configuration of the diatomic hydrogen molecule changes with decreasing temperature from its normal form at room temperature (75% orthohydrogen, 25% parahydrogen) to almost 100% parahydrogen at the normal boiling point.
This conversion is also a reason why LH_2 is widely used, since the neutron inelastic scattering cross section $\sigma_{s,inel}$ starts to differ for the two spin states below a neutron energy of approximately 70 meV (see Figure 2.3, left). At 10 meV, the inelastic scattering cross section of liquid parahydrogen is approximately 20 times lower than that of orthohydrogen. Although this characteristic leads to less scattering events in the same moderator volume due to a larger mean free path Λ_s for interactions, it allows a more efficient extraction of partially moderated neutrons from the edges of the moderator and reduces the amount of neutrons that are absorbed inside the moderator volume. This leads to a large overall gain in intensity, since the moderator can be extended in axial direction, resulting in a so-called *cold finger* moderator due to its quasi one-dimensional shape.
Another group of materials commonly used or investigated as cold neutron moderators are hydrocarbons (CH_4, C_2H_6, C_9H_{12}, etc.). They are most frequently used in solid form, due to their comparably high freezing temperature (90.7 K, 90.4 K, 228.4 K, respectively) and their number of modes for energy transfer in crystalline state. Due to the multiple hydrogen atoms, they usually exhibit a large number of molecular translational, vibrational and rotational degrees of freedom that offer modes for energy transfer even at low energies in the meV-region.
The methane (CH_4) molecule has a tetrahedral shape with a carbon atom in the center-of-mass, surrounded by four hydrogen atoms at the corners of the tetrahedron [17]. At room temperature, it forms a colour- and odorless gas, which is highly flammable. Its liquefaction and freezing temperatures at normal pressure are 111.7 K and 90.7 K, respectively. At normal pressure, methane exhibits two solid phases, depending on its temperature. Above approximately 20.4 K, the lattice is in phase I and forms a face-centered cubic (fcc), in which all of the hydrogen atoms of the CH_4 tetrahedrons are free to rotate. Below 20.4 K, there is a change to phase II, in which only 1/4th of the rotors are still free and the rest performs librational and rotational tunneling motions [18]. The former describes a recip-

rocating motion, while the latter is a quantum effect, in which the rotating atoms in a librational motion are indistinguishable [19].
Mesitylene (C_9H_{12}) is an aromatic hydrocarbon, with a benzene ring (C_6H_6) in its center and with three methyl groups (CH_3) symmetrically ordered around the benzene. It is a liquid at room temperature, which makes it safer to use in cryogenic applications than gaseous hydrocarbons since there is no pressurization of equipment during warm-up. However, it is also highly flammable.
There are certain drawbacks to using cold moderators in solid state, especially for high-power sources. One of the reasons is the usually poor thermal conductivity λ_{th} of molecular solids, which for temperatures between 4 K and 20 K has a maximum of 0.1 to 2 $\frac{\mathrm{W}}{\mathrm{m \cdot K}}$. Therefore, it is necessary to make sure that the energy deposition into the cold moderator does not exceed the cooling rate to avoid a stepwise increase of temperature during beam operation.
Another drawback is the conversion of the moderator molecules into hydrogen and other hydrocarbons by radiolysis. The hydrogen freezes inside the solid matrix of the moderator and can lead to high pressures on the walls of the moderator vessel for increasing temperatures. These temperature increases may occur as spikes due to a sudden release of energy that is stored in the moderator during the radiolysis process and is commonly referred to as "burps". This problem has been reported especially for methane and has led to the destruction of moderator vessels in the past [20]. It is therefore necessary to repeatedly warm-up the moderator and vessel to release the energy stored in it. The problem of radiolytic hydrogen formation is not that strong in mesitylene, which is why it has been used as a substitute for methane in some instances [21]. However, its efficiency as a cold moderator is significantly lower compared to methane.
Another previously investigated cold moderator material is light water (H_2O). Compared to its application as a thermal moderator in liquid form, it can also be frozen and cooled down to cryogenic temperatures to be used as a cold moderator [22]. It has a high proton density and, although having only few reported low-frequency modes [20], shows a similar moderating efficiency at 20 K as molecular liquid hydrogen for larger volume moderators [23], [24]. Nevertheless, water ice shows a similar behaviour as methane for longer periods of irradiation, with temperature spikes due to the release of stored energy.
As a mixture of water ice with other materials, clathrate hydrates also show a good cold moderation efficiency, but are hard to handle, since they either have to be prefabricated and transported under cryogenic conditions to the operation site or fabricated in-situ. Like methane and water ice, they show a problematic behaviour with regards to radiation of high power and for longer intervals.
Apart from using single materials for the production of cold or very cold neutrons, the concept of composite cold moderators has been investigated in the past for mixtures of liquid hydrogen and solid methane [25]. It was shown that for large moderators (12×12 cm^2), the intensity of an LH_2 source could be enhanced by using a disc of solid methane behind it (in the direction of the flight path). For the production of very cold (VCN) to ultra cold neutrons (UCN), this concept is known as a VCN or UCN "converter". Especially solid methane and liquid orthohydrogen show a good efficiency for the production of neutrons in such low-energy regions as compact moderators (3 cm diameter, 1 cm thickness) [26].

2.4 CANS & Hi-CANS

Neutron sources based on the principle of neutron generation by low-energy nuclear reactions were first built in the 1970s and usually apply proton beam powers of up to some kW. Due to their small size and number of instruments - compared to spallation sources or research reactors -, they were termed "Compact Accelerator-driven Neutron Sources" (CANS). Some examples of existing facilities are given in Table 2.3. The present work focuses on the production of neutrons by using protons.

Table 2.3: List of existing compact accelerator-driven neutron sources (CANS) (values taken from [27], [28]).

Facility	Location	Particle type	Beam power	Target	Cold moderator
LENS (Low Energy Neutron Source)	Indiana, USA	p	6 kW	Be	solid CH_4
HUNS (Hokkaido University Neutron Source)	Hokkaido, JP	e	3.2 kW	Pb	solid C_9H_{12}
KUANS (Kyoto University Accelerator-driven Neutron Source)	Kyoto, JP	p	0.35 kW	Be	solid C_9H_{12}
RANS (Riken Accelerator-driven Neutron Source)	Tokyo, JP	p	0.7 kW	Be	solid C_9H_{12}

The sources based on (p,n) reactions typically use linacs to accelerate pulses of protons to the desired high speeds and the corresponding energies. The linac consists of a proton source, a low energy beam transport (LEBT) section, an RFQ (radio frequency quadrupole) , a medium energy beam transport (MEBT) section, and a possible high energy beam transport (HEBT) section. The time structure of the pulsing sequence can either be generated in the ion source or by using an ExB chopper.
The neutrons are released by impinging the accelerated proton pulses onto a light metal target (e. g. beryllium). The protons are captured by the atoms of the target material, which thereupon emits one to several particles (neutrons, protons, deuterons), of which the neutron emitting reaction channels are of importance. The freed neutrons are subsequently slowed down by interactions with a moderator material to change their wavelength to distances of one to several Å used in scattering experiments. To increase the number of fast neutrons colliding with the moderators – and therefore the neutrons reaching the sample –, the moderators are surrounded by a reflector material, from which the neutrons can be scattered back into the moderator. All of the components described above are contained in a so-called Target-Moderator-Reflector (TMR) assembly (or unit). From these TMR assemblies, the neutrons are led by neutron transport systems (e. g. neutron guides) to the scattering instruments, where they interact with a sample under investigation.
A more recent concept for an accelerator-driven neutron source uses a similar setup as a CANS, but produces neutrons with proton beam powers in the order of 50 - 100 kW, mainly by increasing the beam current while keeping the proton energy low enough to avoid a spallation reaction ($E_p < 100$ MeV). This is achieved by using a high power linac with peak energies of several MW [4]. Additionally, the overall number of instruments can be increased by the construction of multiple TMR units. Facilities of this sort have been proposed by several European countries (HBS in Germany [29], ICONE in France [30], ARGITU in Spain [31]) and are currently in the design and prototyping phase. Due to their high proton current and to differentiate them from the multitude of small sources, they are called "High Current Accelerator-driven Neutron Sources" (Hi-CANS).

The planned Jülich High Brilliance Neutron Source (J-HBS) is such a facility with three TMR units and a maximum proton beam power of 100 kW per target. It will use proton pulses with an energy of up to 70 MeV, a peak current of up to 89.3 mA and a duty cycle of 1.6%. A schematic model of the facility in its current planning state is shown in Figure 2.4.

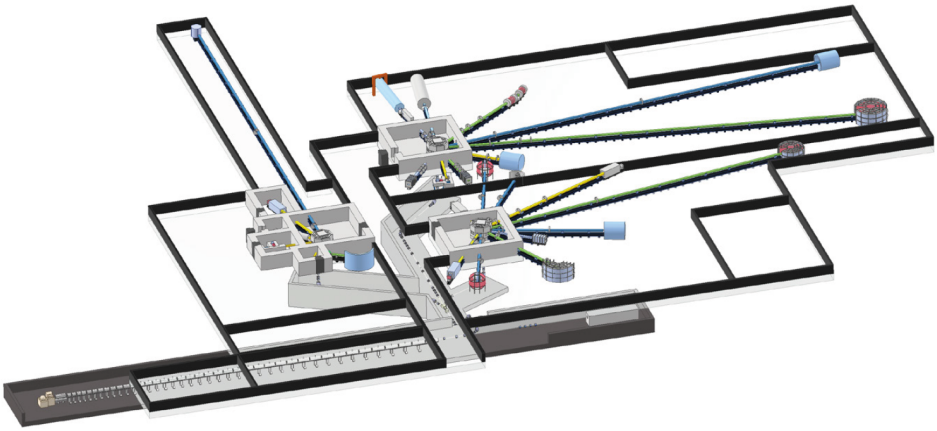

Figure 2.4: Model of the planned Jülich High Brilliance Neutron Source (J-HBS) (Figure taken from [32]).

The three TMR units are operated in parallel, each of them providing various instruments with neutrons of different wavelengths and with different pulse frequencies (one TMR unit with 24 Hz and two TMR units with 96 Hz). With a duty cycle of 1.6%, the corresponding proton pulse widths are 666.67 µs and 166.67 µs, respectively.
A multiplexer system, consisting of a kicker and a three-field septum magnet is used to spatially separate the proton pulse sequences created in the ExB chopper to allow them to be transported to the different TMR units [33]. The proton pulses are entering the TMR units from the bottom and hit a horizontally arranged target. Figure 2.5, top, shows different cut views of a TMR unit in more detail, with the shielding layers of lead and borated polyethylene surrounding the inner part, which is composed of the neutron target, thermal moderator and reflector. The target is made of tantalum (Ta), since its neutron yield exceeds that of other metals like beryllium (Be) or Vanadium (V) above a proton energy of approximately 42 MeV [34]. Inside the TMR units, several compact cold or thermal moderators are used to slow down the neutrons to wavelengths in the order of atomic to molecular distances (several Å). Feeding only one to two instruments with cold neutrons from a single moderator allows the optimization of each of those moderators to the requirements of the individual instruments. This optimization process is described in more detail in chapter 3. The cold moderators are inserted into the TMR units by using so-called *moderator plugs* (see Figure 2.5, bottom). They keep the moderator vessel in its intended position and connect it to the necessary infrastructure to condense and cool it, while shielding the outside of the TMR unit from radiation generated inside it with blocks of borated polyethylene and lead.

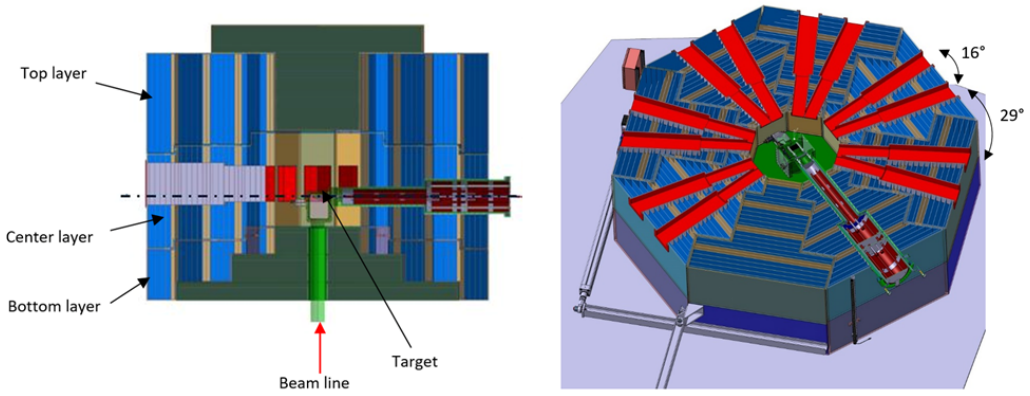

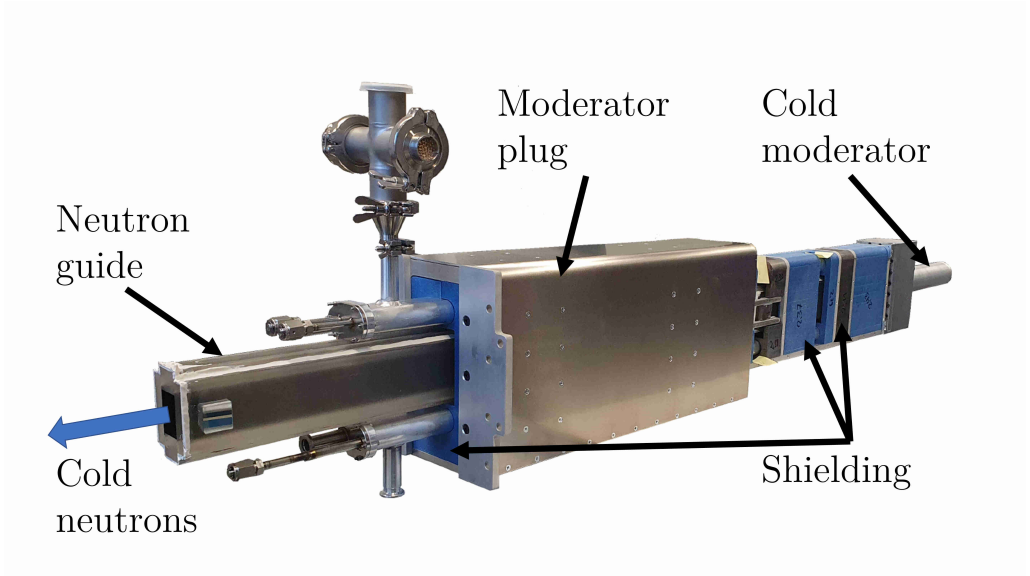

Figure 2.5: Top: Cut through a model of a TMR unit for the J-HBS, side view (left) and isotropic view (right) (partly taken from [32]). Bottom: Moderator plug for a prototype TMR unit of the HBS (photograph taken from [32], captions added for explanation).

Chapter 3

Cold moderator optimization

Due to their modular design, accelerator-driven neutron sources offer the possibility to optimize individual parts of the facility (e. g. accelerator, TMR unit, neutron guide, etc.). This way, the number of usable neutrons (within a defined angle and wavelength range) at the sample position can be enhanced. Since the flux at the sample position is the last value to be known in an optimization problem and is difficult to determine, the neutron brightness with the unit

$$[B] = \frac{\mathrm{n}}{\mathrm{cm}^2 \cdot \mathrm{s} \cdot \mathrm{sr}} \tag{3.1}$$

is introduced. It describes the number of neutrons emitted from a source per unit time (s^{-1}), within a specific divergence range (sr^{-1}) from a specific moderator surface (cm^{-2}). It is therefore a characteristic of the neutron moderator (or *source*). By applying Liouville's theorem, which states that the brightness transfer is always BT ≤ 1 [13], the upper limit of the flux at the sample position can be estimated if the instrument's spatial, angular and wavelength acceptance are known. When normalizing the brightness to energy or wavelength, one obtains the *spectral brightness* B_{spec} with units

$$[B_{spec}] = \frac{\mathrm{n}}{\mathrm{cm}^2 \cdot \mathrm{s} \cdot \mathrm{sr} \cdot \text{Å}} \text{ and } [B_{spec}] = \frac{\mathrm{n}}{\mathrm{cm}^2 \cdot \mathrm{s} \cdot \mathrm{sr} \cdot \mathrm{meV}}, \tag{3.2}$$

respectively. The term *brilliance* is often used analogous to brightness, although the normalization factors might differ slightly from the ones stated above. However, in this thesis, the two terms are used interchangeably. The definition of spectral brightness is used for the comparison of different moderator options with regards to wavelength (Å^{-1}) or energy (meV^{-1}).

The brightness at pulsed neutron sources is usually presented in the form of *peak brightness*, the "maximum instantaneous brightness during a pulse" [35], and the *time-averaged brightness*, which is the brightness averaged over a whole repetition period (i. e. one pulse period = pulse width t_p plus time until next pulse Δt). Whether or not the peak or time-averaged brightness are favorable depends on the requirements of the specific instrument.

There are different ways of optimizing the efficiency of a cold moderator with regards to neutron brightness, either by changing the cold moderator itself or by adjusting its surrounding infrastructure (thermal moderator, reflector, beam tube). Methods of the latter are often applied when tailoring the time structure of the TMR unit towards a better resolution. Measures include so-called *decouplers* and *heterogenous poisons*, both of which consist of slow-neutron absorbing material. The decoupler prohibits slow neutrons from the reflector to enter the moderator and beam path section to prevent a broadening of the pulse. Poisoning, on the other hand, is placed inside the moderator itself or in beam direction and is used to limit the diffusion time of slow neutrons leaking from the moderator [14]. Both of these measures narrow the pulse length, but simultaneously reduce their time-integrated intensity.

Furthermore, it is possible to increase the brightness by preventing cold neutrons from

escaping from the beam path. This can be done by coating the beam path with a material that reflects neutrons of low energy. Options include nanodiamonds and MgH_2 [36].
When optimizing the cold moderator itself, factors like the choice of material, the geometry (shape and size) and the operating temperature provide ways of increasing the brightness. However, when changing those factors, it is paramount to consider the effect of nuclear heating in the cold moderator and surrounding materials and the heat transfer from the cold moderator to a cooling source (refrigerant, heat sink). Also, technical feasibility and engineering constraints (e. g. required wall thicknesses) have to be taken into account.
Following, potential ways of increasing the emission of cold neutrons from a cold moderator and hence brightness are presented in more detail, with the resulting choice presented. Subsequently, the optimization of a simplified TMR assembly with the chosen cold moderator material is performed for the proton beam properties of a potential Hi-CANS using a Monte Carlo particle transport code and its feasibility and limits are demonstrated.

3.1 Reduction of operating temperature

One potential way of optimizing the cold neutron brightness is by reducing the temperature of the moderating material. This can shift the energy-dependent spectrum of the moderator towards lower values and therefore increase the cold neutron intensity [23]. In theory, the *most probable* energy of a neutron thermalized within a material of a specific temperature T can be described by the Boltzmann constant $k_B = 8.617 \times 10^{-5}$ eV $\cdot$ K^{-1} [37]. The average kinetic energy of a neutron thermalized at a specific temperature T is

$$E_{n,kin} = \frac{3}{2} \cdot k_B \cdot T \tag{3.3}$$

due to the neutron's three degrees of freedom (x, y, z). For example, the average kinetic energy of a neutron thermalized in a medium held at a temperature of $T = 293$ K, e.g. water at room temperature, is approximately 38 meV. The most probable energy of a neutron at this temperature, on the other hand, is $E_n = k_B \cdot T = 25$ meV. The formula is taken from the kinetic theory of gases and is valid as long as the neutron energy is high enough and the interaction between the neutrons and the atoms of the moderator can be described by a free gas model.
To find cold neutron moderator materials that show a gain in efficiency down to temperatures of $T = 10$ K and below for a compact geometry, a literature research was conducted. Most materials tend to reach a certain limit, below which a further reduction in temperature has no significant effect on neutron moderation. Even though the probability for scattering rises with decreasing neutron energy for cold moderator materials, only a fraction of the collisions between the neutrons and the moderator atoms leads to an energy transfer due to a decrease in the inelastic scattering [38], which is responsible for energy transfer at low neutron energies. At the same time, the probability for the absorption of neutrons inside the moderator material rises linearly with the inverse neutron velocity $(1/v)$. This is why the thermalization process saturates at a certain neutron temperature T_n depending on the volume of the moderator and its operating temperature T_{mod}.
For a compact cold moderator, the effect of the operating temperature and related thermalization is often affected by the dimensions of the moderator, since the neutrons leave the moderator before reaching thermal equilibrium. This is called *under-moderation* and – depending on the application – might be desired to reduce the effect of absorption or diffusion. However, this process results in a higher effective neutron temperature compared to that obtained by using large volume cold moderators. Some reported effective neutron temperatures are given in Table 3.1 with the respective moderator volume and temperature.

Table 3.1: Effective neutron temperatures $T_{n,eff}$ for specific moderator temperatures T_{mod} and volumes V_{mod} reported for previously used cold neutron moderators (values extracted from [39], [40] and [41]).

Moderator	T_{mod} in [K]	$T_{n,eff}$ in [K]	V_{mod} in [cm^3]
s-CH_4 [39]	22	38	720
s-CH_4 [40]	20	25	~6200
s-C_9H_{12} (phase II) [39]	20	48	720
s-C_9H_{12} [41]	24	46	~6200

Solid methane in phase II (below 20.4 K) and solid ortho-deuterium show the lowest reachable neutron temperatures. However, since deuterium needs a relatively large volume to sufficiently thermalize neutrons due to its low scattering cross section (σ_s = 7.6 barns/molecule) [42], it is not a suitable choice for a TMR unit demanding low-dimensional moderators. Methane in phase II, on the other hand, needs less volume to

moderate and is therefore the **material of choice** for testing a compact cold moderator at temperatures of $T \leq 10$ K.

3.2 Geometry optimization

Another way of increasing the number of usable neutrons is by adapting the moderator geometry and dimensions to its specific scattering and absorption cross sections, σ_s and σ_a, respectively, and their development with changes in neutron energy for a specific region of interest. Each moderator material has its optimum dimensions for a specific geometry depending on the desired neutron output and moderating characteristics as well as the surrounding setup (e. g. material and geometry of the thermal moderator and reflector). If the dimensions are too small, the moderator cannot efficiently slow down enough neutrons, resulting in an under-moderated energy or wavelength spectrum (the peak and average neutron temperature are too high). If the dimensions are too large, neutrons are absorbed inside the moderator volume before leaving it, resulting in a higher degree of thermalization but also in an overall reduction of brightness.
Table A.1 in Appendix A1 gives values for the density and mean free paths of different commonly used cold moderator materials. The melting temperatures and densities are taken from [43] if not stated otherwise. The mean free paths for scattering and absorption are calculated from cross sections given by [14]. One example for the optimization of the cold moderator dimensions is the reduction in diameter and simultaneous elongation of a cylindrical moderator. For the right material, e. g. liquid parahydrogen, this adaptation can largely increase the cold neutron flux normalized to the emitting surface. Due to a drop in the scattering cross section for neutrons with energies below 40 meV, the mean free path Λ of a neutron inside the moderator material between two interactions increases from approximately $\Lambda_{th} \approx 1$ cm to $\Lambda_c \geq 10$ cm. Therefore, a so-called *one-dimensional* geometry – i. e. a cylinder with a small radius in the order of the mean free path at thermal energies and a large length in the order of the mean free path for energies $E_n < 10$ meV – increases the cold neutron brightness due to a larger illuminated volume while simultaneously reducing the rate of absorption of neutrons in the moderator material.
A large fraction of the scattered and moderated neutrons leaves the moderator after one collision. Since the lowest rotational energy level spacing for hydrogen is the transition from para- to orthohydrogen with $\Delta E = 15$ meV [20], neutrons with lower energies can't transfer any more energy to the hydrogen molecules, due to their inability to induce such a transition. This is why, for one-dimensional LH_2 moderators, the resulting energy spectrum shows a peak at around 15 meV (or 2.3 Å). For larger LH_2 moderators, this effect is cancelled out due to the occurrence of multiple collisions for most neutrons and the resulting spectrum approaches that of neutrons fully thermalized at the liquid hydrogen temperature.
When using materials with a high scattering cross section at low energies, like solid CH_4 or liquid o-H_2 with a similar geometry, the outcome is different due to the short mean free path at neutron energies below 10 meV ($\Lambda_c \leq 1$ cm). Therefore, neutrons are mainly emitted from only the first centimeter of length (when viewed from the neutron instrument side) after one collision. The additional volume behind that first centimeter leads to a moderation of the neutrons, but due to multiple scattering events the amount of absorption is higher and the scattered neutrons form a more or less isotropic cloud. Therefore, using a larger volume of cold moderator by increasing its length does not necessarily cause a higher brightness and a shorter solid cylinder is advisable when using such materials. To investigate this effect for solid CH_4, length values ranging from $L_{mod} = 1$ cm to $L_{mod} = 9$ cm are used for the simulations presented in the following subsection.

Commonly used *one-dimensional* and *two-dimensional* moderator geometries include the aforementioned solid cylinder or a slab with low thickness. However, there are other ways to shape the moderator to make use of its specific neutron moderation characteristics. One option, which is frequently used in thermal moderator design, is the so-called *re-entrant hole* configuration (see Figure 3.1). This shape can increase the brightness due to the con-

tribution of neutrons thermalized in the ring around the center hole (in case of a circular cross section). The principle is similar to that of the long cylinder when using p-H_2, since the illuminated length of the moderator is increased while keeping the absorption at an acceptable level. This geometric configuration has been investigated for methane [44], with promising results, which is why it was chosen as one option for the optimization study of a solid methane moderator in section 3.3.

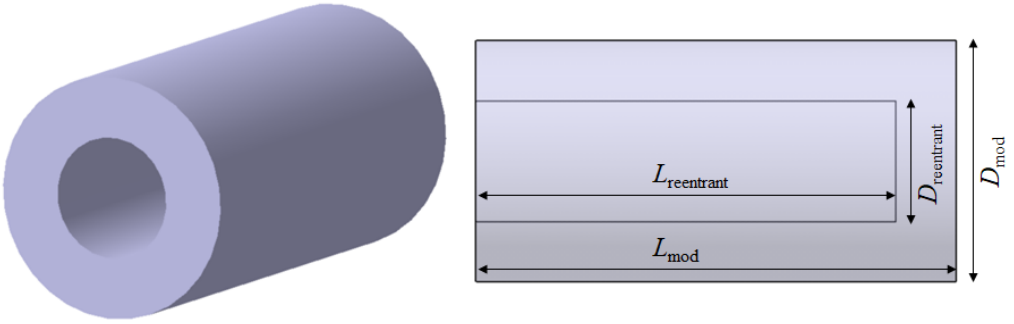

Figure 3.1: Exemplary geometry of a cylindrical re-entrant hole configuration.

Further geometries, like an inclined long moderator or a stepwise moderator, could in principal increase the moderator's efficiency but have not yet been investigated experimentally. Such geometries need to be adapted to a specific case (desired neutron spectrum, e. g. high brightness or high overall intensity) first.
Yet another option proposed for the design of cold moderators is the concept of a convoluted moderator. Such a moderator consists of "alternating layers of moderating material and largely transparent non-moderating material (possibly void)" [45] or "perfect crystals to provide an exit path for neutrons moderated to energies below the crystal's Bragg cut-off [...]" [46]. The layers are supposed to create a higher neutron intensity at the guide by allowing an extraction of the neutrons above and below the layers of moderator without multiple scattering events "from locations deep within the moderator" [46]. A problem with this concept when applied to CANS or Hi-CANS requiring low-dimensional moderators is its space requirement to make sure that there are enough layers of moderator and void and they are large enough.
Although it is usually helpful to roughly calculate the mean free path for a cold moderator by using the cross sections at a desired energy range as a first estimation, it is not a reliable method for finding the optimum dimensions. The moderation process, especially if a thermal moderator and reflector are included, is usually too complex to be calculated analytically. Statistical simulations offer a possibility to determine the optimum dimensions for a given geometry more precisely. This procedure is presented in the following section.

3.3 Optimization by neutron transport simulations

In the context of this thesis, several nuclear simulations were performed. While the creation of the necessary input files and the actual performance of the simulations were carried out by Dr. J. Li of the institute JCNS-2 at Forschungszentrum Jülich, the conceptual ideas and analysis of the simulation data were a part of this thesis.

Due to the large number and variety of particles and their multiple forms of interaction (scattering, absorption, emission and multiplicative effects like an (n,2n) reaction) involved in the processes of neutron production and moderation, an analytical mathematical description is generally not feasible. An alternative is offered by numerical methods, by which one can find an approximate solution to a problem that may be too complex for analytical methods.
There are two approaches for solving the underlying transport equations. One is based on a deterministic method, for which the geometry under investigation is divided into smaller parts (discretization). The neutron transport equation is solved as a differential equation with its boundary conditions initially taken from the overall problem and subsequently generated for the nodes of the single elements. Although such methods yield information on the neutron flux throughout the whole model, they require large sets of algebraic equations and therefore computing power.
Another approach is to use stochastic methods. One of the most common one for solving radiation transport problems is the Monte Carlo method. It randomly samples the trajectories (also called "histories") for each of a large number of particles by using probabilistic descriptions of the possible interactions in its flight path [47]. Those probabilities were either calculated or obtained by experimental investigations. Since the Monte Carlo method does not solve an explicit equation, the average behaviour of the particles (or trajectories) has to be recorded at a specific location [48]. To obtain precise results from the sample set when using the Monte Carlo method, a large number of histories is usually necessary.
For a calculation of large numbers of trajectories for different particle types and energy regions, several computer codes were developed in the second half of the 20th century (e. g. MCNP or FLUKA) or the beginning of the 21st century (e. g. PHITS). For the present problems, MCNP in version 6.1 is used. The creation of the input file and the performance of the simulations were performed by experts at JCNS-2. Therefore, only a rudimentary description of the basic functionality of the code and the simulation preparation are given and the main focus will be on the analysis of the simulation results.

3.3.1 Monte Carlo N-Particle Code

The Monte Carlo code MCNP was first created at the Los Alamos National Laboratory (LANL) in 1977 by merging multiple individual codes for different particle types (MCN for neutrons, MCG and MCP for photons) [49]. At that point, it allowed the calculation of the transport of neutrons, photons and electrons. In 1999, MCNPX was released, which additionally included 34 sub-nuclear particles and light ions and was expanded later to include all 2205 heavy ions [50]. It was merged with MCNP5 in 2013 to MCNP6, of which the recent version is MCNP6.2.
MCNP6 models the interaction of (particle) radiation with matter over broad continuous energy ranges and in dependence of time. The geometry of the investigated setup is three-dimensional and is defined by first-order (plane) and second-order (e. g. ellipsoid or parabolloid) surfaces as well as fourth-order elliptical tori. If available, the interaction probabilities of the different particles with specific materials are taken from extensive nuclear data libraries (ENDF: Evaluated Nuclear Data File, ENDL: Evaluated Nuclear Data Library, ACTL: Activation Library). Otherwise, the data is calculated from physics model algorithms available in MCNP [50]. Of special importance for the problems posed in this

thesis are the thermal scattering data tables $S(\alpha, \beta)$, which have to be taken from external data libraries like ENDF. They include molecular bindings and crystalline effects in condensed matter, which are important for neutron energies in the sub-eV region.
To execute a simulation, the user has to create an input file first, which can be read by MCNP6. It includes information on the geometry and materials used in the problem, a source definition and the size and location of tallies (surface or volume detectors). Furthermore, it is possible to incorporate several variance reduction techniques, which allow a more efficient convergence of the model and therefore an increase in statistics, which in turn reduces the uncertainty of the obtained results [48].

3.3.2 Simulation input

To calculate the effectiveness of a target-moderator-reflector assembly, specific data is necessary as input to determine specific values like neutron intensity or energy deposition through or in certain surfaces or volumes. One part of this input is the geometry of the investigated setup. It is created by defining different cells through their geometrical boundaries. A material is assigned to each of these cells, which is directly connected to the data tables of interactions between the types of particles and the materials, as mentioned above. Additionally, the materials have to be given a mass or atomic density and a temperature, since these properties also affect the material's interaction probability. For high neutron energies, the neutron scattering probability can be calculated from a free gas model, since the interaction is mainly incoherent and the spectrum produced is a Maxwellian one. In reality, absorption processes occur that lead to deviations from the ideal shape and to a decrease in intensity [47].
For slow neutrons, the behaviour changes and scattering often becomes coherent. Therefore, the scattering cross section has to be adjusted. For some materials at cryogenic temperatures and for low neutron energies, so-called *thermal scattering tables* are available. These are more accurate than the free gas model, since they take coherent effects due to chemical bonds or other interactions between atoms of a material into account.
To record the neutron flux or energy deposition at a specific position, so-called *tallies* have to be defined. The tally type defines the quantity that is being recorded during the simulation (e. g. surface current, surface flux, energy deposition, etc.). For those different tally types, surfaces or volumes can be chosen. The desired results can either be saved as a time-averaged value or time-dependent as dump files. Furthermore, the tally geometries can be refined by meshing to obtain information on the spatial resolution of a quantity of interest.

Source: The source is defined by its dimensions and shape as well as the type and energy of the incident particles. A simulation of the comprehensive reactions inside the target material requires a high computing power. It is therefore performed once in a first simulation, while for later simulations, a "virtual source" is used, which takes the results from the first simulation stored in a so-called *source file*. This procedure significantly reduces the duration of subsequent simulations and allows a choice of the required particle types (e. g. n: neutrons, p: photons, e: electrons, h: protons).

Geometry: The geometry used for the simulations performed in the context of this thesis is depicted in Figure 3.2. It is a simplified version of the problem and omits characteristics of the real setup like structural materials (vessels, supports, bolts, etc.) and air or vacuum gaps, in which neutrons are absorbed or by which their pulses are elongated. Therefore, the performance of the simulated setup is overestimated by approximately 20% compared to the real setup [32]. Figure 3.2 shows a cylindrical cold moderator (green, various diameters) embedded in a spherical thermal moderator (yellow, diameter 20 cm) embedded in a spherical reflector (purple, diameter 80 cm). From the left, a part of the evacuated

beamline with a target (blue, diameter 11.28 cm, thickness 0.5 cm) is inserted into the reflector and thermal moderator. The target geometry is a simplified version of the current target design for the full-power HBS, which has additional cooling channels and a water beam stop as well as a larger amount of tantalum for incorporating the coolant tubes. The beam stop's impact is reproduced by not taking into account the protons from the target reactions in the subsequent moderators and reflector.
The cold moderator is positioned inside an evacuated channel, through which the neutrons are extracted. Its diameter is 2.4 cm larger than that of the cold moderator to allow a gap of 1.2 cm of vacuum on all sides. The thickness of the thermal moderator between target and cold moderator is kept at 1.3 cm for all simulations to ensure that the cold moderator is fed with a sufficient amount of thermal neutrons. This thickness was determined in previous simulations at JCNS-2 as an optimum value for the generation of a sufficiently dense thermal neutron cloud in the region of the cold moderator vessel. For parameter studies, the cold moderator is varied in shape (solid cylinder, re-entrant hole) and dimensions (diameter, length).

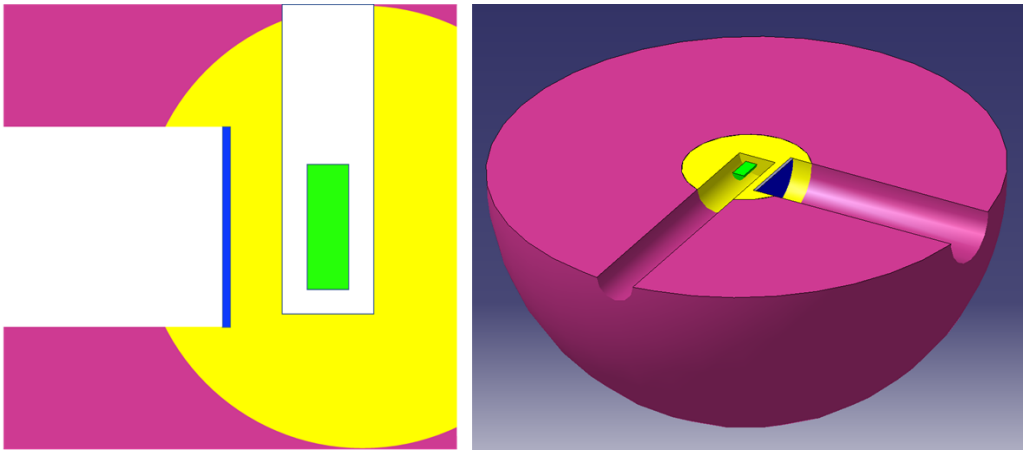

Figure 3.2: Outline of the simulation setup used for MCNP6.1 simulations with a solid methane cold moderator (green), a polytheylene thermal moderator (yellow), a lead reflector (purple) and a tantalum target (blue). MCNP view (left), CAD view (right).

Materials: The material of the target is tantalum with a density of 16.69 g/cm^3, the thermal moderator is polyethylene with a density of 0.95 g/cm^3 and the reflector is made of lead with a density of 11.34 g/cm^3. All three components are assumed to be at room temperature (293 K) and the corresponding continuous-energy neutron data is taken from ENDF/B-VII.1. For polyethylene, the thermal cross section library provided by the ENDF database is chosen for low-energy neutrons.
The material used for the cold moderator is methane at temperatures of 22 K, 10 K and 5 K. For the latter two temperatures, scattering kernels calculated by R. Granada and his team at the Centro Atómico Bariloche (CAB) are used (according to [51]). The 22 K scattering kernel is part of the ENDF library since version ENDF/B-VI [52].

Tallies: Surface tallies are positioned at the front surface of the cold moderator directed towards the extraction channel (surface 302.2 = A_{CM}) and inside the extraction channel at the exit of the reflector (surface 301.2 = $A_{Ex,ref}$) (see Figure 3.3). Their respective diameters correspond to the outer diameter of the solid cylinder cold moderator (302 = V_{CM}) and the diameter of the extraction channel (301). Volume tallies were used for calculating the energy deposition in cell 302.

Two tally types were applied:

1. F1 in mode:n (neutrons) for calculating the surface current, i. e. the number of particles crossing a specified surface area. The value is neither normalized to the area nor distinguishes by direction [53]. The unit is therefore simply the number of particles of the pre-defined particle type crossing a specified surface.

2. F6 in mode:n,p,e (neutrons, photons, electrons) for the simulation with only methane and mode:n,p,e,h,a (additionally protons and alpha particles, see subsection 4.3.2) for calculating the energy deposition.

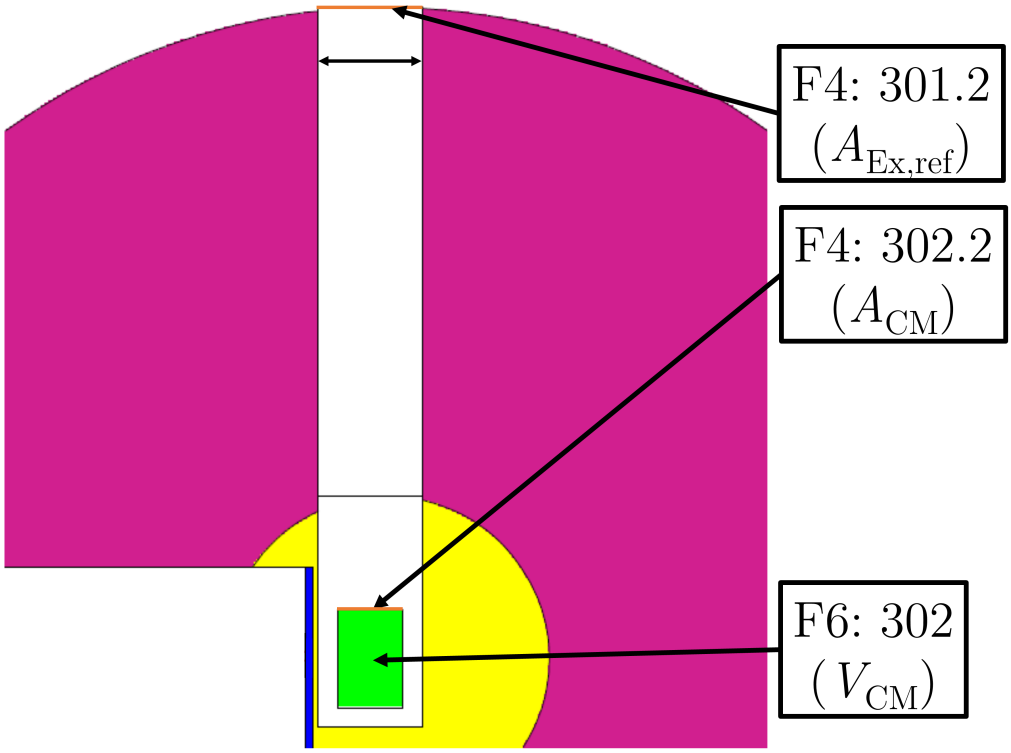

Figure 3.3: Position of the surface tallies used for recording the neutron surface current (tally F1: 301.2 = $A_{Ex,ref}$ and 302.2 = A_{CM}) and the volume tally used for recording the energy deposition (tally F6: 302 = V_{CM}).

The number of simulated histories before terminating the simulation run was 3.5×10^8 for most runs, apart from one run with more particles (3.5×10^9) for comparison and the simulations of energy deposition into the moderator vessel including aluminum and helium (1.5×10^8), which are presented in section 4.3.

3.3.3 Analysis & results

After the simulation is performed, the input information, a summary of the execution of the simulation and the results for the predefined tallies are saved to an output file. To allow further processing, also by auxiliary code, the results for the previously defined tallies are additionally saved in a file called "MCTAL", which is in ASCII format and omits any further information (input, warnings, etc.).
For the analysis of the obtained data for the previously described geometry and parameters, a python code called "McTal.py" is used that was developed at JCNS-2 by Dr. P. Zakalek. It allows the read-out of the "MCTAL" file as well as a manipulation of the data in terms of normalization, time structure modification and the plotting of 2D and 3D data. In the default settings, the data is normalized to the integrated values of time, energy and angle.

The presented results in the following paragraphs are normalized to an angle range from 0° to 5° (corresponds to a cone with an opening angle of 10°), to the surface area of the tally and to the integrated proton current and the time/energy/angle binning. Both the peak and integrated time-averaged brightness are determined, with the following procedure:

- **Peak brightness:** The peak brightness is determined by locating the maximum intensity in the time spectra for each energy bin for a single pulse.
- **Time-averaged brightness:** The time-averaged brightness is determined by integrating the intensities of each time spectrum per energy bin for a single pulse and dividing them by the pulse period of a 24 Hz target station ($T_{pulse} = 41.67$ ms).

Since the instruments of the HBS are designed for a high peak brightness, the results in the following sections are presented only for that value. The time-averaged brightness results are additionally presented in subsection A.2.1.

Length variation: Energy-dependent results of the different simulation runs are depicted in Figure 3.4. The graphs show the peak neutron brightness, normalized to the area of the tally. For the left graph, the detector tally is situated at surface A_{CM} (front surface of the cold moderator facing the exit of the extraction channel). Its diameter is 2 cm ($A_{CM} = 3.14$ cm^2), corresponding to that of the cold moderator. For the right graph, the tally is positioned at surface $A_{Ex,ref}$ (exit of the extraction channel), with a diameter of 4.2 cm ($A_{Ex,ref} = 15.21$ cm^2). The data is compared for solid methane at $T = 5$ K.

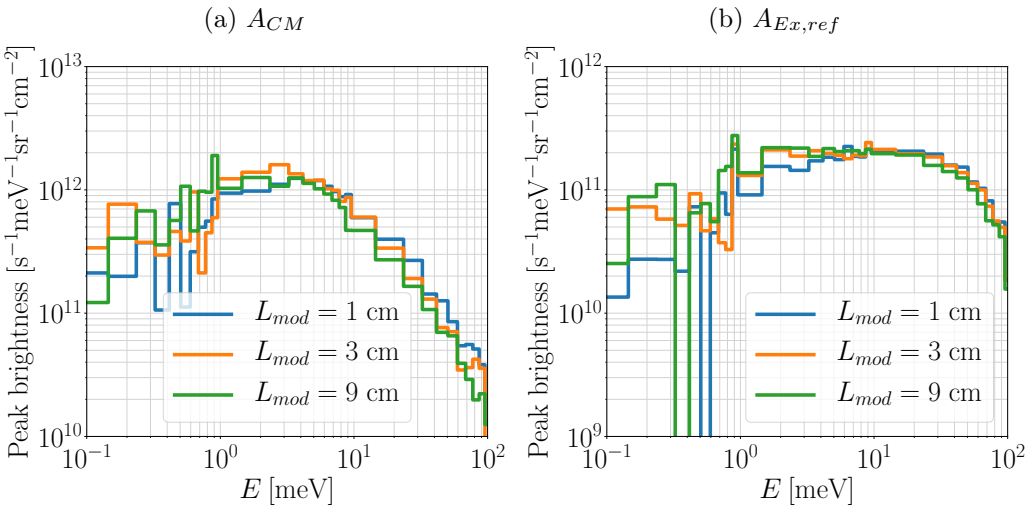

Figure 3.4: Peak brightness for a solid cylinder of solid methane at $T = 5$ K with a diameter of $d_{mod} = 2$ cm and different lengths L_{mod}.

At the emitting surface of the cold moderator (A_{CM}), it is apparent from the results that the peak brightness is lower in the region from 1 meV to 10 meV for $L_{mod} = 1$ cm compared to the other two cases. This can be attributed to an under-moderation for 1 cm thickness as well as to a lower number of neutrons emitted in that angle range from the shell surface of the solid cylinder. There is a higher peak brightness in the thermal energy range, which is caused by the fact that less neutrons are moderated in the smaller volume. The length of $L_{mod} = 3$ cm emits more neutrons in the region of 1 meV to 5 meV than the other two options and the length of $L_{mod} = 9$ cm shows a lower peak brightness for the whole energy range above $E_n = 1$ meV. Below that value, no clear distinction is possible due to the low statistics, but the differences appear to be small.
At the surface of the exit from the reflector ($A_{Ex,ref}$), the differences are small for all lengths between $E_n \approx 4...20$ meV. The better performance of the $L_{mod} = 9$ cm cylinder

for this tally surface is probably caused by a larger amount of neutrons being emitted from the larger shell surface of the cold moderator into the direction of the tally. However, the differences are again small and do not indicate the necessity of a length as large as $L_{mod} = 9$ cm.

Diameter variation: The energy-dependent peak brightnesses at A_{CM} and $A_{Ex,ref}$ of the different simulation runs are depicted in Figure 3.5. Diameters of $d_{mod} = 2$ cm and $d_{mod} = 4$ cm were investigated as lower and upper limits of the diameter, respectively. The data is again compared for solid methane at $T = 5$ K.
The results at A_{CM} (left graph) show a higher peak brightness of the cylinder with $d_{mod} = 2$ cm for neutron energies of $E_n \geq 3$ meV and a slightly lower performance below that energy. At $A_{Ex,ref}$, the larger diameter shows a significantly higher peak brightness for neutron energies of $E_n \leq 9$ meV. This is partly caused by a larger absolute amount of moderating material in radial direction, but the differences are enlarged by the larger ratio of $A_{CM}/A_{Ex,ref}$ for the larger diameter. However, from a perspective of moderating performance, the larger diameter cold moderator is preferable. To obtain more reliable results, simulations with additional tallies of various diameters were performed at a later stage during the present work. Their results confirmed the better performance of the larger diameter. To obtain the optimum diameter, further simulations with smaller intervals between $d_{mod} = 2$ cm and $d_{mod} = 4$ cm are necessary.

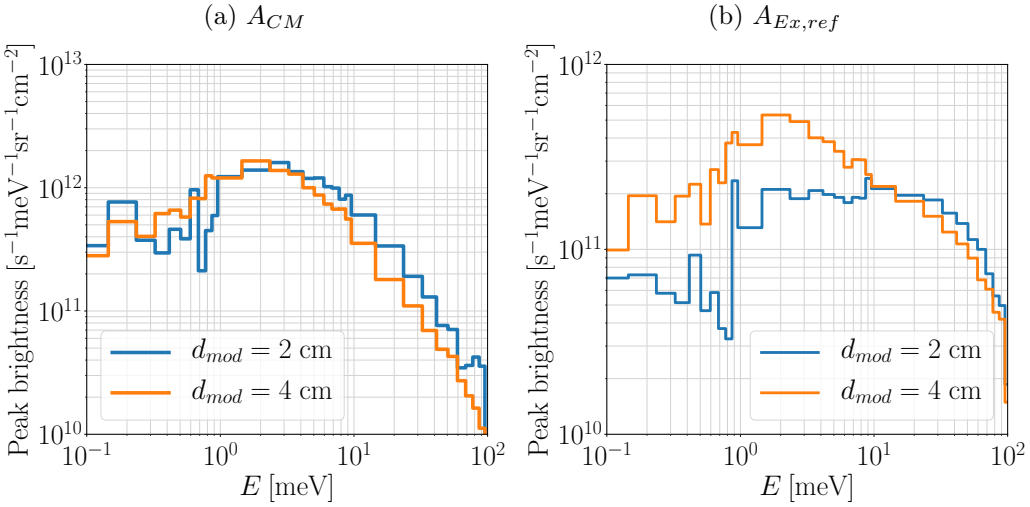

Figure 3.5: Peak brightness for a solid cylinder of solid methane at $T = 5$ K with a length of $L_{mod} = 3$ cm and different diameters d_{mod} at surface A_{CM} (left graph) and at surface $A_{Ex,ref}$ (right graph).

Temperature variation: Figure 3.6 shows the energy-dependent results compared for the simulation runs with different scattering kernels for solid methane at various temperatures. The moderator is a solid cylinder with dimensions of $d_{mod} = 2$ cm and $L_{mod} = 3$ cm. It is apparent that the difference in moderator temperature is not observable in the spectra. The deviations below 1 meV can be attributed to the low statistics in this energy region. Between 1 meV and 10 meV, there are only slight deviations, which can also be attributed to statistical variances. In these deviations, there is no trend observable towards higher intensities with lower temperatures, but rather a random distribution. These results are unexpected when compared to those found in the literature.
According to [54], a decrease in temperature from 22 K to 4 K should increase the peak neutron flux by a factor of around 1.125 and shift the peak position from 3...4 meV to 2 meV. This observation is in accordance with the simulations performed at the Low En-

ergy Neutron Source (LENS) at Indiana State University [55], using their own scattering kernel. Gallmeier et al. [56], however, report a reduction in very cold neutron output by a factor of 2 if one compares the scattering kernel for solid methane at 4 K from the Centro Atómico Bariloche to that of the LENS facility.
One possible explanation is that the cold moderator volume is not sufficiently large to introduce the effects of a temperature decrease onto the obtained neutron spectra. Simulation results for a diameter of $d_{mod} = 4$ cm with decreasing temperature show a possible dependence on cold moderator volume, but are inconclusive. Although the thickness of the solid methane moderator used in experiments at the LENS facility is only 1 cm, the width is much larger (square cross section with 12 cm edge lengths) than the outer diameter of the solid cylinder used in the present simulations.

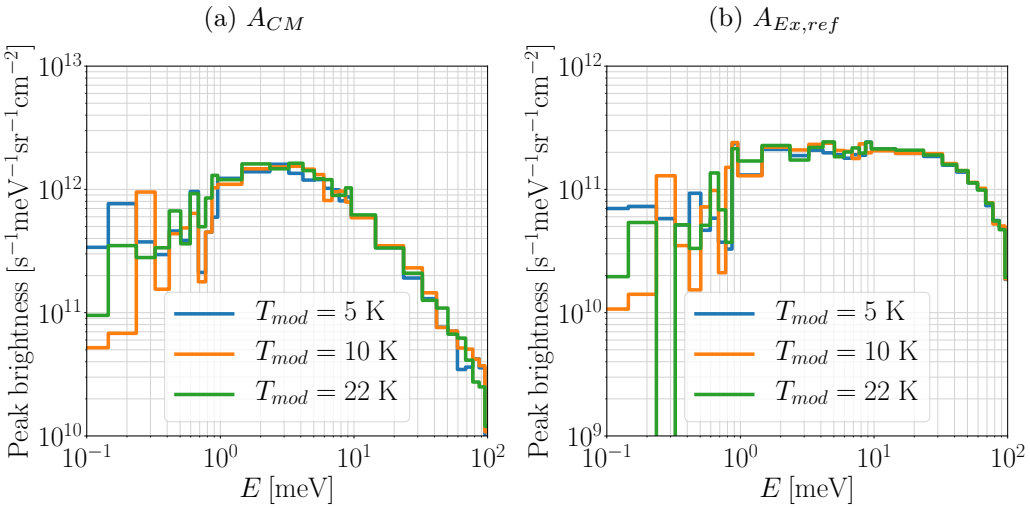

Figure 3.6: Peak brightness for a solid cylinder ($d = 2$ cm, $L = 3$ cm) of solid methane at different temperatures T_{mod}.

Geometry variation: Apart from the solid cylinder geometry, a re-entrant hole geometry is investigated for different thicknesses of the base and ring around the re-entrant hole, ranging from 0.4 cm to 1.2 cm. Figure 3.7 shows a model of the cold moderator in the TMR assembly. The diameter of the extraction channel is kept at a constant value of 6 cm, as well as the length and diameter of the re-entrant hole ($d_{hole} = 2$ cm, $L_{hole} = 10$ cm).
The investigated tallies included the ring surface at the cold moderator surface facing the exit of the extraction channel (surface 302.2 = $A_{CM,outer}$), the base and top surface of the re-entrant hole (surface 303.2 = $A_{CM,bottom}$ and 304.2 = $A_{CM,inner}$, respectively) and again the cross section of the extraction channel at the reflector exit (surface 301.2 = $A_{Ex,ref}$).
Figure 3.8, left, shows a comparison in energy-dependent peak brightness for $A_{CM,inner}$ for different ring thicknesses surrounding the re-entrant hole. It is apparent from the spectra that there is an under-moderation for the thicknesses of 0.4 cm and 0.6 cm. However, the increase in peak brightness gets smaller with increasing thickness, indicating that a value between 1.0 cm and 1.2 cm should be an optimum value. Results for the other tally surfaces are included in subsection A.2.2. They show that an integration of the ring surface of the cold moderator ($A_{tot} = A_{CM,inner} + A_{CM,outer}$) further increases the brightness for the larger ring thicknesses.
Figure 3.8, right, shows the peak brightness of the solid cylinder geometries with different diameter and the re-entrant hole with a thickness of 1.2 cm. Additionally, the results for a simulation using a solid cylinder parahydrogen cold moderator with a diameter of 2 cm and a length of 10 cm are included. The applied tally surfaces are A_{CM} for solid cylinders

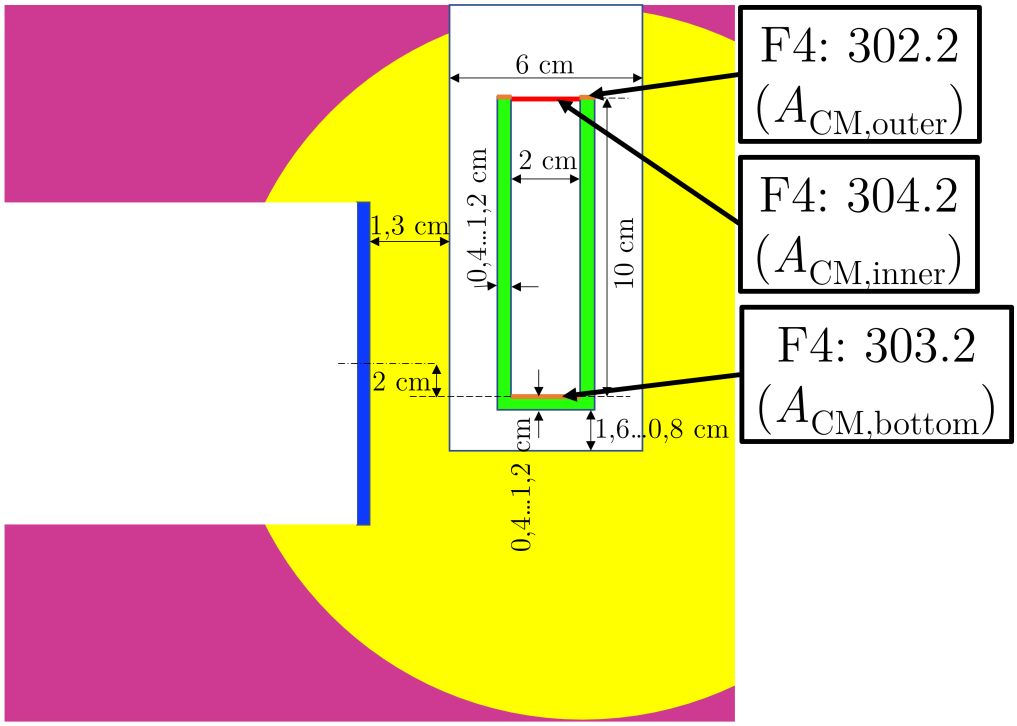

Figure 3.7: Top view of the MCNP geometry containing the spherical TMR assembly using a cold moderator in re-entrant geometry with dimensions.

and $A_{CM,inner}$ for the re-entrant hole. All results are normalized to the respective tally surface areas ($A_{CM} = A_{CM,inner} = 3.14$ cm^2 for the $d_{mod} = 2$ cm solid cylinders and the re-entrant hole and $A_{CM} = 12.57$ cm^2 for the $d_{mod} = 4$ cm solid cylinder).

The spectra show that the re-entrant hole geometry with a methane thickness of 1.2 cm and a total length of 11.2 cm outperforms all solid cylinders for energies between 1 meV and 4 meV in peak brightness. Its CH_4 volume, however, is larger by a factor of 3.7 and 14.7 compared to the $d_{mod} = 4$ cm and $d_{mod} = 2$ cm solid cylinder, respectively. Due to the associated large energy deposition and the complexity in manufacturing, the re-entrant hole geometry is not used as an option for the prototype manufactured in the context of this thesis. However, a more detailed investigation of this geometry is advised for future cold moderator designs, since it is a potential candidate to produce a higher peak brightness than liquid p-H_2 for low energies.

Energy deposition: For the simulation of the energy deposition, MCNP6.1 outputs the results in unit MeV $\cdot$ g^{-1} $\cdot$ p^{-1}, where p stands for the number of primary particles (e. g. protons or neutrons) used in the source definition of the simulation problem. These primary particles produce secondary particles (e. g. neutrons, photons, electrons), which can in turn produce further particles. Since the real target has a water beam stop, the protons from the target reaction do not interact with the cold moderator. To reproduce this effect, the source is defined by only passing the neutrons from the target reaction and omitting all other contributions. The heat load into the cold moderator is determined by the number of particles interacting inside the specified meshtally.
In the case of protons as primary particles, the energy deposition has to be multiplied with the integrated flux of protons hitting the target and the mass of the material inside the tally to obtain the time-averaged total heat generated inside the moderator vessel in unit [W]. This integrated number of protons depends on the proton beam characteristics (frequency f, duty cycle DC).

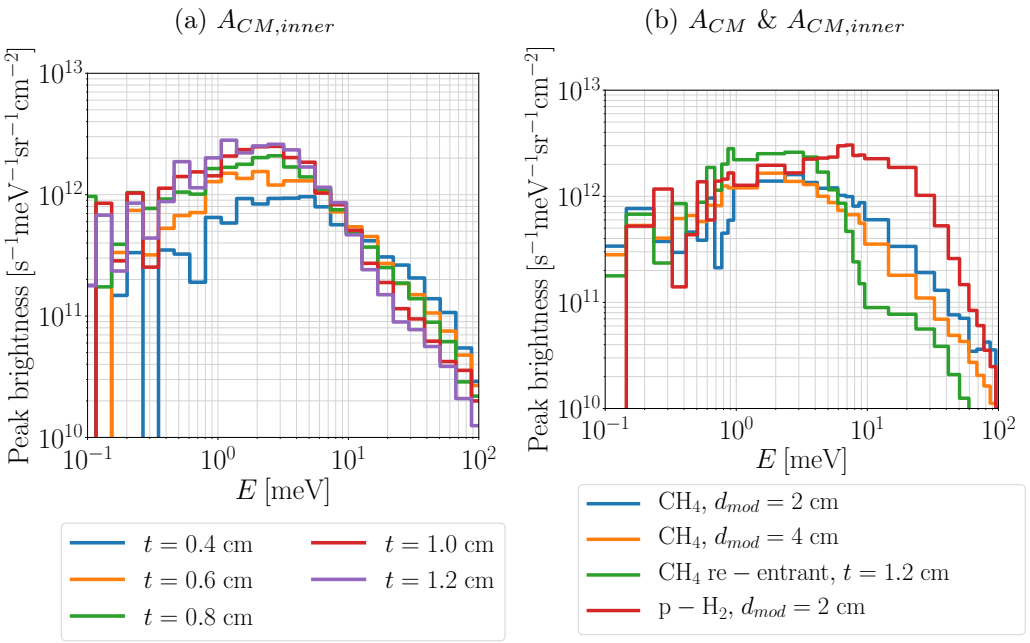

Figure 3.8: (a) Peak brightness at $A_{CM,inner}$ for re-entrant moderators with different ring and bottom thicknesses t; (b) Comparison of solid cylinders (L_{mod} = 3 cm) with different diameters d_{mod} and re-entrant hole CH_4 cold moderators compared to a solid cylinder liquid parahydrogen (p-H_2) moderator with a length of L_{mod} = 10 cm at T = 20 K (right graph).

In the aforementioned simulations for the solid cylinders, the energy deposition into the cold moderator (cell 302 = V_{CM}) was recorded in addition to the surface currents. The particle types considered include neutrons, photons and electrons. The results for the solid cylinder cold moderator are shown graphically in Figure 3.9 in dependence of cold moderator volume. It is noticeable that the amount of energy deposited in the cold moderator scales almost linearly with the volume of the moderator. Deviations from the linear behaviour are due to the material's distance from the source, which increases with growing volume.
In MCNP, the contribution by photons includes the energy deposition by electrons generated due to the photon collisions. However, this mode is only valid for larger cells, where all energy by electrons is deposited within the cell. For smaller cells, MCNP overestimates the energy deposition and the electron contribution should be regarded individually.
The results in Figure 3.9 for photons and electrons only show the contribution due to secondary particles. In a real setup, the photon contributions from gamma rays emitted from the target have to be included as well. This increases the photon/electron contribution by an order of magnitude, as is shown in the results of subsection 4.3.2, where the primary photons from the target reaction are taken into account.

3.3.4 Conclusions and remark on uncertainty

The design of the cold moderator vessel for an experimental setup is affected by the presented simulation results in the following way:

1. The length comparison presented above as well as a previously performed qualitative comparison between lengths of L_{mod} = 3 cm, L_{mod} = 6 cm and L_{mod} = 9 cm indicate that the optimum length lies between L_{mod} = 1 cm and L_{mod} = 6 cm. An increase in moderator volume and the related higher energy deposition is not desirable

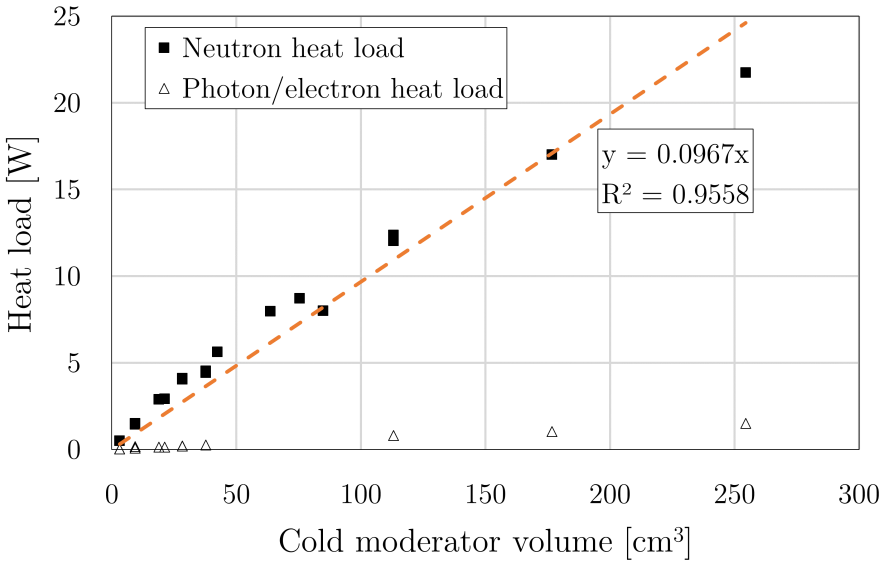

Figure 3.9: Heat load by neutrons $\dot{Q}_n$ and secondary photons/electrons $\dot{Q}_\gamma$ in [W] vs. cold moderator volume in [cm^3]. The averaged proton current and energy are $I_p = 89.3$ mA and $E_p = 70$ MeV, respectively. With a duty cycle of 1.6%, these values yield an assumed proton beam power of $P_p = 100$ kW. Linear fit and coefficient of determination (R^2) included.

without a benefit in cold neutron brightness. Therefore, a length of approximately $L_{mod} = 3...4$ cm is chosen for the present application.

2. A diameter of less than $d_{mod} = 2$ cm is problematic due to a larger under-moderation of the neutrons inside the cold moderator. On the other hand, even though an increase in diameter to $d_{mod} = 4$ cm could potentially enhance the cold neutron brightness, it involves several disadvantages:
   1) The heat load by energy deposition increases by a factor of 4, which complicates maintaining the cold moderator at a stable temperature (see subsection 4.3.2).
   2) At the full power HBS, a total amount of 8...12 instruments per TMR unit requires a sufficient amount of extraction channels in the vicinity of the target. A larger cold moderator diameter yields a larger extraction channel diameter, which increases the distance between some of the cold moderators and the target.
   Therefore, for first experiments, a cold moderator diameter of $d_{mod} = 2$ cm is chosen.

3. According to the simulation results with scattering kernels for different temperatures, a reduction to 5 K does not observably increase the cold neutron brightness. Since this result is unexpected, an experimental investigation is beneficial in assessing the effectiveness of a temperature reduction.

4. The investigated re-entrant hole geometry enhances the cold neutron brightness compared to the solid cylinder. At the same time, it increases the volume by a factor of almost 15 compared to the solid cylinder with a 2 cm diameter and 3 cm length. The geometry is therefore not chosen for a first experimental setup due to a more complex manufacturing procedure. However, a more detailed investigation of the re-entrant hole geometry with shorter cylindrical ring volumes is advised. Further investigations, for which there was not enough time in the context of this work, could potentially be beneficial for future designs of cold moderators.

5. The heat load onto the cold moderator vessel and adjacent materials is largely dependent on volume. Therefore, unnecessary material should be avoided to reduce the

required cooling power and keep the moderator temperature at a more stable value throughout its volume.

To assess the impact of the number of simulated primary particles on the curve progression of the spectra, an additional simulation with an order of magnitude higher primary particles was performed. Figure 3.10 shows the energy spectra of the peak brightness for the same moderator material (CH_4) and geometry ($d_{mod} = 1$ cm, $L_{mod} = 1$ cm) for a number of $3.5 \cdot 10^8$ and $3.5 \cdot 10^9$ of primary particles.
The results show that the curve progression below 1 meV for the simulation with $3.5 \cdot 10^9$ primary particles is much smoother than the one with less particles. However, at the same time, the runtime of a single simulation run increases drastically. When comparing the results of the F6 tally for both cases, the relative error of the total energy deposition by neutrons and photons/electrons is around 0.06%.

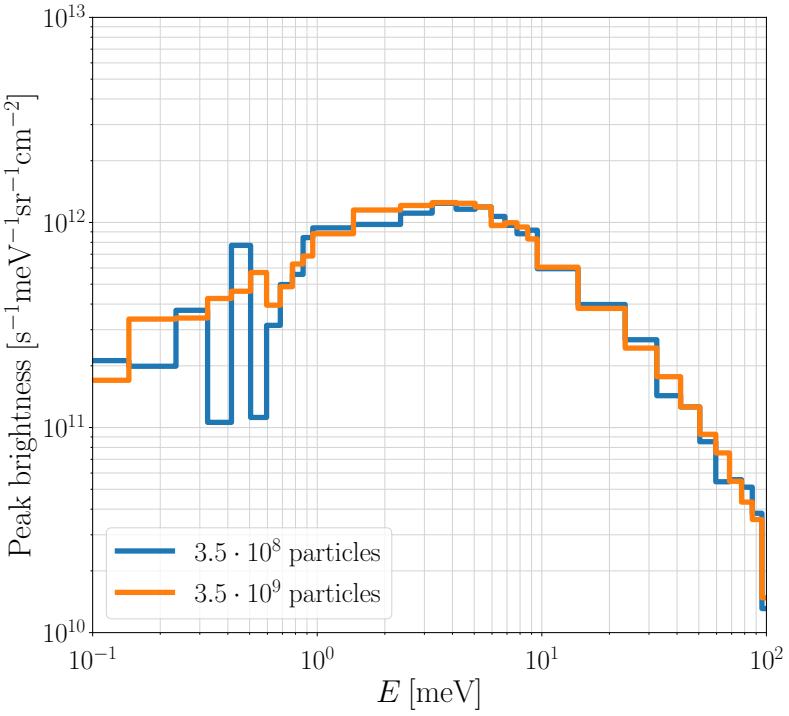

Figure 3.10: Peak brightness vs. energy for a solid cylinder methane moderator with dimensions $d_{mod} = 1$ cm and $L_{mod} = 1$ cm and a temperature of $T_{mod} = 5$ K for different numbers of primary particles.

Chapter 4

Cryostat design

To produce a batch of solid methane and to cool it to temperatures of approximately 10 K and below, a cryogenic system, consisting of a cryostat and control system, is designed. Apart from geometrical constraints due to its planned operation at a prototype target-moderator-reflector (TMR) unit, questions regarding the thermal and structural design are discussed and choices are presented in the following subchapters.

4.1 General requirements & boundary conditions

There are several basic requirements that have to be met by the design of the cryogenic system:

1. **Operating temperature:**
   The moderator material should be cooled down to and maintained at a temperature of approximately 10 K and below during operation.

2. **Moderator position:**
   The moderator vessel should stay in its intended position with its center axis congruent to the center axis of the attached neutron guide and a maximum allowable angular deviation of 1°. A translational motion of $\Delta z = \pm 2$ mm is allowed in z-direction, whereas the deviation in direction of x and y shall be limited to $\Delta x = \Delta y = \pm 0.5$ mm (see coordinate system in Figure 4.2).

3. **Area of application:**
   The cryostat is used inside a prototype TMR unit of the HBS facility (see Figure 4.1), so its dimensions should be chosen in a way that it fits the intended ducts of the TMR unit and can incorporate a neutron guide element.

4. **Flexibility:**
   Since the cryostat is an experimental setup and planned to be used for the testing of various moderator geometries and materials, a high degree of interchangeability is desired to avoid the manufacturing of a completely new cryostat for each moderator option.

5. **Isolation vacuum:**
   A vacuum pressure of $p_{vac} \leq 5 \cdot 10^{-4}$ mbar for insulation purposes shall be achieved before the start of a cooldown.

6. **Leak tightness:**
   The leak tightness of the connections (e. g. welds, screw connections) shall ensure a leakage rate of $Q_L \leq 1 \cdot 10^{-8}$ mbar $\cdot$ l $\cdot$ s^{-1}.

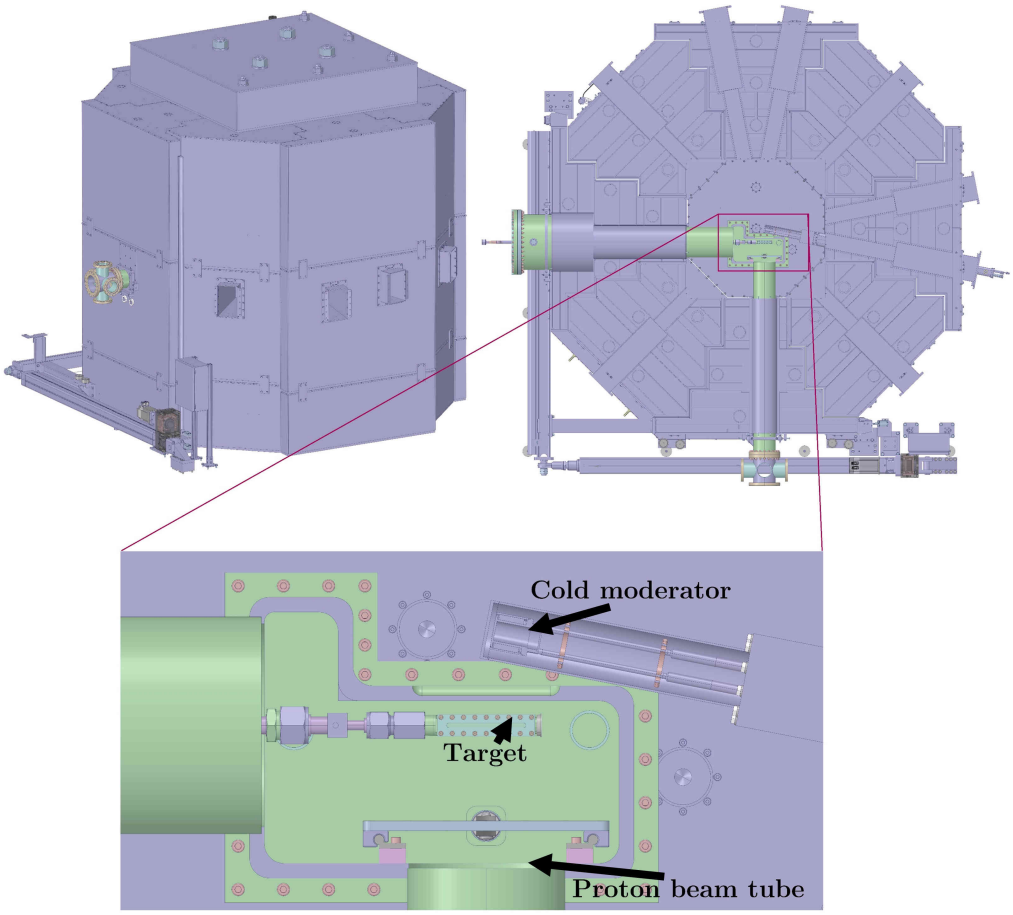

Figure 4.1: Isometric view (top left), cut top view (top right) and detailed view of the moderator location (bottom) of the planned prototype TMR of the HBS facility (design by ZEA-1, FZJ).

Point 1) requires a comprehensive calculation of the heat fluxes into the cold parts of the cryogenic system to allow for an estimate of the required cooling power. The sources of heat input can be categorized into two types, a **static** and a **dynamic** one. The former includes heat fluxes that mainly stay constant during operation whereas the latter is dependent on the time characteristics of the pulsed proton beam operation. These topics are covered in section 4.3.

Point 2) depends on the mechanical fixation of the moderator vessel inside the vacuum recipient, on the compensation of its potential movements during cool down and ultimately on its final position in the state of operation. A deviation in angle of the moderator's center axis is not as problematic as a translational motion relative to the neutron guide's center axis. The latter would result in a larger loss of cold neutrons due to higher incident angles between the cold moderator and the neutron guide entrance. Since the largest amount of neutrons is emitted into the direction of the center axis of the solid cylinder, less neutrons would be transmitted by the guide (see Figure 4.2). A calculation of the expected movement of the moderator vessel during cool down is performed in subsection 4.5.3.

Point 3) is largely governed by the dimensions of the smaller section of the moderator duct of the TMR unit and of the included neutron guide. Both are shown schematically in a cut view in Figure 4.3. The duct dimensions are fixed values due to the design of the prototype TMR unit, whereas the neutron guide dimensions are based on neutron guides available at Forschungszentrum Jülich and are considered upper limits due to their

relatively large dimensions, with an entrance and exit window of 45×30 mm^2 ($H \times W$). State-of-the-art guides are typically smaller in size and therefore a better fit for the intended application using low-dimensional moderators. However, the larger guide can be replaced at a later stage by a smaller version and the residual clearance can be filled with additional shielding elements.

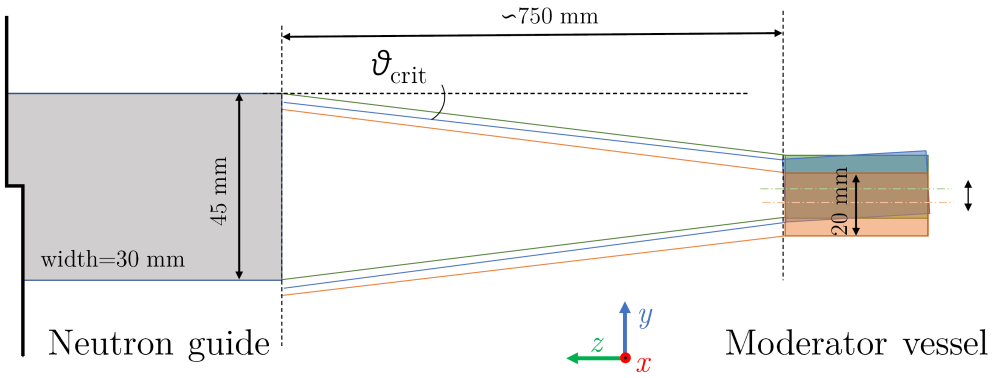

Figure 4.2: Schematic view of the critical angle and its dependence on a shift in position of the cold moderator.

Although specific geometrical constraints and boundary conditions of the prototype TMR vary from those at a TMR unit planned for a full power HBS facility, a lot of the design choices are applicable. The heat load introduced by the considerably higher proton beam power and the applicable range of materials are differing factors. The design choices discussed in this thesis are based on the conditions introduced by the full power case. Any deviations in the prototype design, which is the basis for manufacturing the apparatus in the context of this work, are highlighted.

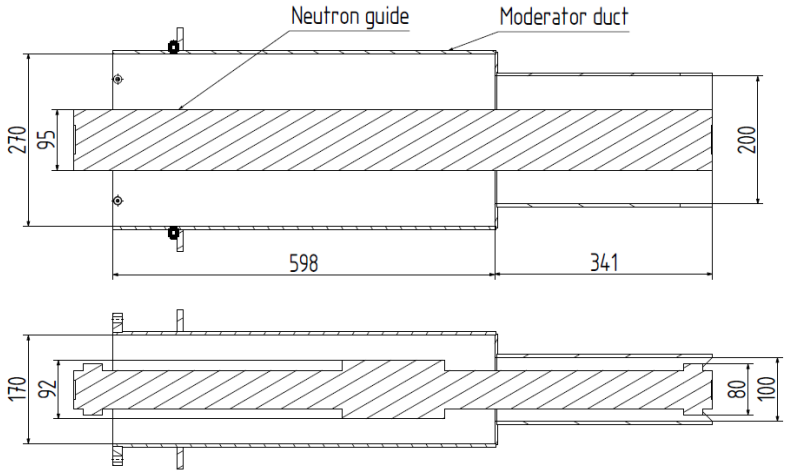

Figure 4.3: Cut side (a) and top (b) view of the moderator duct of the prototype TMR including existing neutron guide. The guide's maximum outer dimensions of $H = 95$ mm and $W = 92$ mm are significantly larger than the inner dimensions to ensure a sufficient stability for an internal vacuum.

4.2 Finite element method

4.2.1 Basics of the finite element method

In many fields of engineering – e. g. structural mechanics, heat transfer or fluid mechanics – problems can be mathematically described by differential equations. Since it is often times not feasible or even possible to find exact solutions for these equations, they are approximated by numerical methods. Different methods commonly used to obtain discrete solutions for continuous differential equations include the finite difference method, the method of weighted residuals and the Rayleigh-Ritz method [57]. The latter two are variational methods, in which the differential equation is transformed into an equivalent weighted-integral form. The solution over a given domain is then assumed to be a linear combination

$$\overline{u}(x) = \sum_{i=1}^{n} c_i \phi_i \tag{4.1}$$

of approximation functions ϕ_i (also called trial or test functions), which have to be continuous over the domain and satisfy the specified boundary conditions exactly, and undetermined coefficients c_i [58]. The latter are determined in a way that the equivalent form of the differential equation is satisfied. The variational methods differ in the choice of the integral form, the weight functions and the approximation functions. For example, when using the method of weighted residuals, an approximate solution is calculated, based on unknown, constant parameters and trial functions, which differs by a residual error from the exact solution. The constant parameters are therefore evaluated as to reduce the residual error [58].
The Rayleigh-Ritz method, on the other hand, determines the maximum or minimum of a functional, which is used to depict the differential equation. The method for determining said maximum or minimum is called the variational method. Principles like that of minimum potential energy guarantee that a function exists which makes the functional minimum or maximum [57]. A problem with using these methods is the construction of a suitable approximation or trial function for more complex domains.
In the finite element analysis (FEA), which is based on the concept of the aforementioned methods, the approximation functions are calculated not for the total domain, but for a set of smaller subdomains, so-called *finite elements*. These elements constitute a mesh of (usually) simple geometries with defined boundaries and connection points (nodes). The latter are either located only at the corners of the elements or additionally in between, depending on the order of the element (linear or quadratic). A quadratic element allows a more precise reproduction of the original shape at the expense of computing time. Figure 4.4 shows various element options for the 1-, 2- and 3-dimensional case.
The values at the nodes are calculated explicitly, while the values inside an element are interpolated from the nodal values by using so-called interpolation functions (also called shape functions). The nodal values correspond to the unknown constants in the variational methods, while the interpolation functions are equivalent to the approximation functions and – like them – often have a polynomial form of the independent variables. They are chosen to satisfy required conditions dictated by the values at the nodes [58]. The nodal values furthermore serve as boundary conditions for the adjoining elements, so that every element connected at a single node shares the same value, which ensures continuity over the complete domain. This is why, for complex problems, the discrete equations can only be solved for the whole set of elements, which "is subjected to certain continuity, boundary, and/or initial conditions" [59].
In FEA, the accuracy of the obtained solution is dependent on the refinement of the mesh. When refining the mesh, it is important that the solution is sequential (compatibility) and converges asymptotically to the exact solution (completeness) [58].

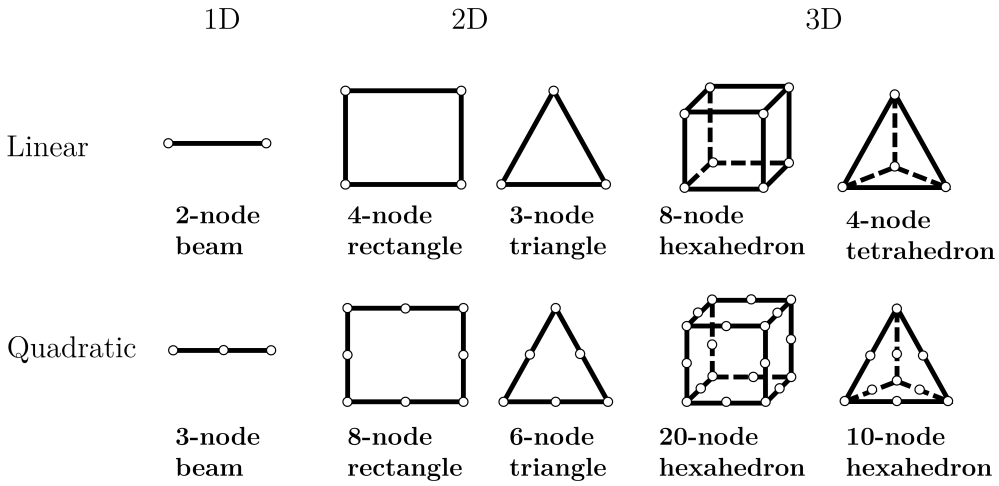

Figure 4.4: Commonly used element types in finite element analysis for different dimensions and order.

4.2.2 ANSYS® Workbench 19

To estimate the influence of a more complex geometry and temperature-dependent material properties on the temperature and heat transfer as well as on the stresses and deformations in structural materials, numerical simulations using the finite element method are performed. For this, the software ANSYS (ANalysis SYStems) Workbench 2019 R3 is used. It offers the possibility to define the physics of the problem and all necessary boundary conditions and requirements in a graphical user interface similar to a CAD environment. The accuracy of the simulation results depends largely on the definition of the utilized materials and the correctness and completeness of their thermodynamical properties in dependence of temperature. Especially at cryogenic temperatures towards the normal boiling temperature of liquid helium, the properties may vary largely and irregularly. The ANSYS engineering data base usually encompasses a multitude of different materials, but often lacks information on these properties at temperatures below 0 °C down to cryogenic temperatures. Therefore, material properties for such temperatures have to be provided from external sources. The precision of the simulation results can be improved by increasing the amount of applied data points. ANSYS Workbench interpolates the values in between the available data, which can often times be accurate enough but is especially problematic at cryogenic temperatures due to irregular behaviour.
Furthermore, structural material properties like yield strength or elasticity can vary largely when using different alloys of a material, so it is necessary to check whether one of the available materials or alloys represents the real material in use. New material options can be created and existing material properties can be modified by editing the section "Engineering Data". For the present simulations, material properties from room temperature down to approximately 4 K are defined for the aluminum alloy Al-5083 (AlMg4.5Mn0.7), stainless steel 304, Invar36 (Fe-Ni alloy) (all taken from [60]) and the polyimid-based plastic Vespel SP-1 [61].
In a next step, either a new geometry can be created by using one of the built-in CAD tools (DesignModeler or SpaceClaim) or by uploading pre-designed geometries. However, the imported models have to be opened in one of the aforementioned CAD tools before they can be processed further. Some functions in DesignModeler or SpaceClaim can facilitate the later stages, for example by merging or dividing faces or bodies, simplifying less important regions of the model and generating a shared topology, which is important for a consistent mesh and therefore for a continuous solution at transition points between parts. The created or uploaded geometry is applied in one of several modules, e. g. "Static

Structural" or "Steady-State Thermal", depending on the underlying physics of the problem. Here, the predefined materials can be allocated to different parts of the geometry and contact conditions between different parts can be defined, if necessary (e. g. "bonded" for welded connections or "frictional" for bolted connections). Although a more realistic contact condition may give a more precise result, it may at the same time drastically increase the computing power necessary to find a solution. Therefore, it is important to estimate in advance in how far simplifications can be accepted and what impact on the obtained results are to be expected.
Another important part of the pre-processing is the division of the bodies or surfaces into smaller elements by a function called "Meshing". Apart from the possibility to create an automatic mesh, global and local mesh controls are available to refine it. An automatic mesh can be used as a starting point, but usually requires modifications to obtain more reliable results. This can be performed by adjusting the element type, size and order.
When meshing a body or surface, it is important to use a rather uniform assembly of similar elements to avoid unfavorable shapes of elements at regions of interest. A deviation of the ideal shape of the element introduces errors to the applied shape function and can cause incorrect results. Furthermore, e. g. in three-dimensional cases, the use of hexahedral elements can decrease the necessary computing power. However, its generation might be more difficult and time-consuming, depending on the complexity of the body to be meshed. For some problems, tetrahedral meshes are preferable, although linear order tetrahedral elements are known to be inaccurate compared to quadratic tetrahedral or hexahedral meshes and should therefore not be used [62] for the simulation of structural components. Still, they can be used for accurately solving non-structural analyses. Additionally, the accuracy of the solution can be improved by using a finer mesh in critical regions (local mesh control). Here, with increasing number of elements, the result should converge asymptotically to a specific value and the required refinement of the mesh depends on the pre-determined allowable deviation of the result from this value. At locations of discontinuities (e. g. edges), elements of large size can lead to inaccurate results due to their low resolution. If the mesh is refined in those regions, the discontinuities cause the stresses to rise indefinitely. In such cases, there are different opportunities to assess the problem to yield usable results, which are presented in section 4.5.
Since a finer mesh over a whole domain usually increases the computing time immensely, there are several options to deal with this. One option is to use local mesh controls to refine the mesh only in regions of interest. The other option is to reduce the overall size of the model to be meshed, which can either be done by making use of symmetries or by using "sub-models". For the latter, a region of the overall domain is cut free and can be meshed individually. The deformations in the cut surfaces resulting from a coarser model are then used as boundary constraints for the sub-model. Since the deformations are not as dependent on the mesh size as are the stresses, this method can yield accurate results.
The boundary conditions used for the present steady-state thermal simulations are temperatures and heat fluxes. By giving the temperatures at certain surfaces at a starting time t_0, the algorithm can calculate the temperature distribution in a body and the corresponding heat fluxes using the thermodynamic properties of the body's material mentioned above.
Boundary conditions for the structural simulations include supports (e. g. fixed or in the form of remote displacements to allow for a deformation of the assigned surface or edge), pressures (internal and external) and thermal conditions to include stresses due to deformations caused by thermal contraction. Another way to include thermal conditions is to calculate a temperature profile in steady-state thermal and use it as an input for the structural simulation. This way, the accuracy of the problem's depiction can be increased compared to the assumption of homogeneous temperature values in specific components, since the temperatures have a continuous progression in reality.

4.3 Thermal design

4.3.1 Basic layout & boundary conditions

The choice of methane requires a transportation of the cold moderator material into and out of the cold moderator section in gaseous or liquid state. While there are concepts of transporting a cryogenic moderator into the moderator vessel in solid state [63], this process requires a complex setup and operating procedure with movable components at cryogenic temperatures. Furthermore, operating such a moderator at temperatures of $T \leq 10$ K is only feasible by using large amounts of cryogenic helium as a coolant medium.
Due to the small required moderator volume ($V_{mod} = 10...15$ cm^3, see dimensions and volumes in Table 4.1), the condensation of the methane is performed inside the cold moderator vessel. To accomplish this, the vessel is designed in a way that the heat can easily be exchanged with a cooling source (liquid cryogen or heat sink of a mechanical refrigerator). Figure 4.5 shows the basic operating principle of the stationary moderator system. Although an open cooling system with a warm-up and external re-liquefaction of the coolant is depicted, also a closed-cycle cooling is possible. This is the preferable option for a regular operation, especially when using liquid helium, due to its high cost. Furthermore, interruptions for replacing the coolant supply are not necessary. However, for an experimental system and infrequent operation, an open cooling system can be less expensive (see subsection 4.3.3) and more flexible for modifications.

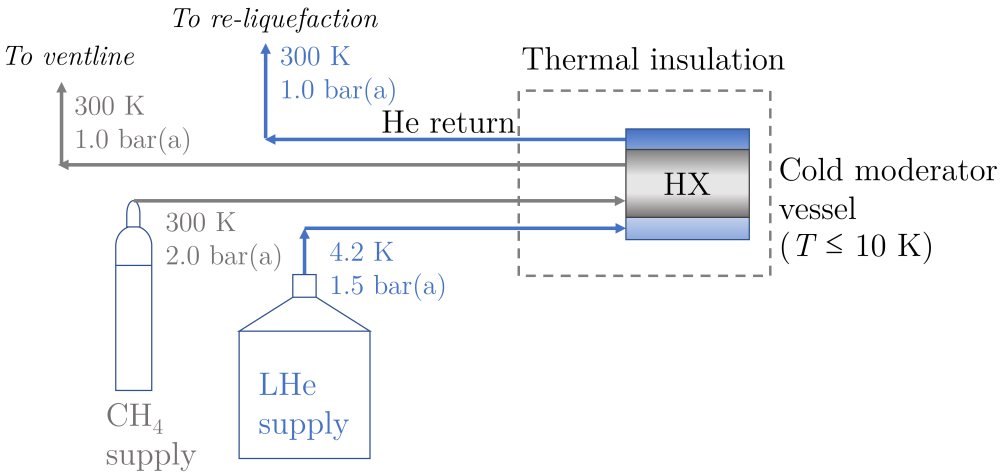

Figure 4.5: Schematic layout of the basic operating principle of the moderator system and its key components.

Table 4.1: Dimensions of the cold moderator and volume depending on the medium manufacturing tolerances.

Diameter [mm]	20 ± 0.2
Length [mm]	40 ± 0.3
Min. volume [ml]	12.2
Max. volume [ml]	12.9

From the requirements stated in section 4.1, the general setup is as follows:
The system is divided into two sections, one part containing the cold moderator (CM) and another the transfer lines (TL) (and/or thermal bridge to cooling source). The latter is split into a moderator and a cooling section to avoid thermal contact due to limited space. The basic geometry is depicted in Figure 4.6.
In a first step, the necessary cooling power of the cooling source has to be determined by

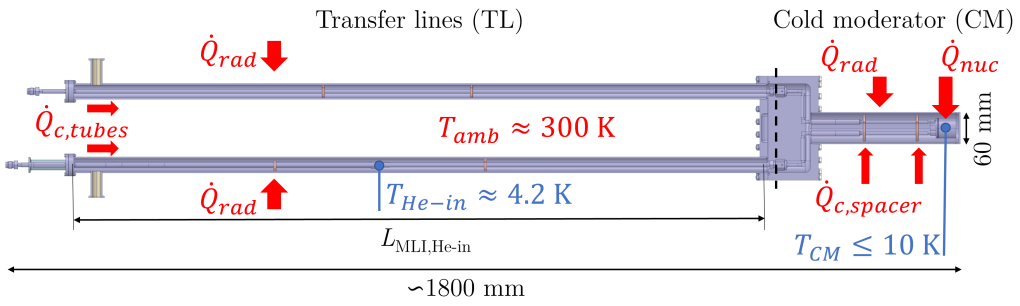

Figure 4.6: Cut CAD view of the geometry of the cryostat with the different sections.

estimating the heat load onto the supply line of the coolant and the cold moderator vessel. From these calculations, the suitability of available cooling techniques is assessed for the present case and maximum moderator temperatures during operation are estimated.

4.3.2 Heat load

The lowest achievable temperature depends on the supply temperature of the coolant and the heat load introduced into the cryogenic parts of the moderator system, which build the basis for the required cooling power. It can be classified into two types, a static part and a dynamic part. The former does not change with time after achieving thermal equilibrium at the desired temperature, while the latter depends on the time structure of the pulsed beam operation. Following, the two parts are characterized and preliminary values are calculated analytically as well as by performing numerical simulations. The heat loads are calculated for the case of a fluid coolant, since cooling by solid conduction is not an option for the present case. This is explained in more detail in subsection 4.3.3.

Static heat load:
The static heat fluxes comprise thermal radiation and heat conduction through solids and fluids. Free convection is neglected due to the demand of an insulation vacuum pressure of $p_{vac} \leq 10^{-4}$ mbar, at which the number of remaining particles between the warm and cold parts of the system is insignificant for thermal transport [64]. The heating of materials due to particle interactions is treated in the section "Dynamic heat load".

Thermal radiation: The power $\dot{Q}_{rad}$ emitted from a grey body with an emissivity $\epsilon < 1$, with a radiating surface area A at a Temperature T can be calculated by applying the Stefan-Boltzmann law

$$\dot{Q}_{rad} = A \cdot \epsilon \cdot k_B \cdot T^4 \tag{4.2}$$

with the Boltzmann constant $k_B = 5.670 \times 10^{-8} \frac{\mathrm{W}}{\mathrm{m^2 \cdot K^4}}$. Using this formula, the heat transfer $\dot{Q}_{rad,12}$ between two surfaces can be described as [65]

$$\dot{Q}_{rad,12} = k_B \cdot \ E_{eff} \cdot A \cdot (T_2^4 - T_1^4) \tag{4.3}$$

where subscripts 1 and 2 denote the cold and warm surfaces, respectively. For coaxial cylinders or concentric spheres, the area A in Equation 4.3 is the enclosed one. In cryogenic applications, this is usually the cold surface, therefore A_1. For the case of parallel plates, the smaller plate defines area A [65].
The effective emissivity E_{eff} for the radiation heat transfer between two surfaces can be calculated from the emissivities ϵ_1 and ϵ_2 and the areas A_1 and A_2. It changes depending on the arrangement of the surfaces (parallel plates or coaxial cylinders/concentric spheres) and the type of reflection (specular for $\epsilon \ll 1$ or diffusive for $\epsilon \approx 1$). In the present work,

the emissivities are expected to be low ($\epsilon \leq 0.2$) and the cold surfaces are mostly enclosed by the warm surfaces (see Figure 4.6). Therefore, the effective emissivity can be calculated by following formula [65]

$$E_{eff} = \frac{\epsilon_1 \cdot \epsilon_2}{\epsilon_2 + \epsilon_1 - \epsilon_1 \cdot \epsilon_2} \tag{4.4}$$

Since the emissivities of the relevant bodies are not precisely known, values from literature have to be applied. Their magnitude mainly depends on the surface conditions, with values of $\epsilon < 0.1$ for polished and Al- and Ag-coated surfaces and $\epsilon > 0.1$ for as-received and oxidized metals [66]. It is common practice to assume somewhat higher values to obtain a conservative estimate of the radiation heat load.
Table 4.2 shows the heat load by radiation onto the different sections of the cryostat. The cold temperatures used for the calculations are the mean temperatures between the inlet and outlet of the tubes and a temperature of $T_{mod} = 7$ K for the cold moderator vessel. The warm temperatures are set to $T = 295.2$ K and the emissivities are set to $\epsilon = 0.2$. The heat load onto the cooling supply amounts to the largest fraction due to its length of more than 1.5 m and its low temperature of $T \approx 5$ K.

Table 4.2: Calculated values for the radiative heat flows for the different parts of the cryostat with and without the use of MLI in the transfer line sections.

Section	$\dot{Q}_{rad}$ in [W]	$\dot{Q}_{rad,MLI}$ in [W]
Cooling supply	3.9	0.9
Cold moderator vessel	0.6	0.6
Cooling exhaust (if needed)	3.1	0.8
Moderator tubes	2×2.5	2×0.8
Total	10.1	3.1

A reduction of the thermal radiation heat load, especially for the helium supply tubes, is possible by applying layers of so-called multi-layer insulation (MLI) onto the radiating surfaces to reduce the emissivity. MLI consists of sheets of aluminized mylar separated by spacers and is commercially available with different numbers of layers. The effectiveness of the MLI insulation increases with an increasing number of layers, with an optimum density of about 30 layers/cm [65]. Above that number, heat transfer by thermal conduction rises due to an increasing thermal conductivity between the different radiating layers. In the present application, a sheet with a total number of 10 layers is used to reduce the heat flow by thermal radiation onto the helium supply tube. Since the helium return gas has to be fully warmed up to room temperature, no MLI is attached to it. However, such an additional isolation is preferable for a closed cycle to reduce the required power for re-liquefaction.
The effect of MLI on the radiative heat transfer can be calculated by following formula [67]

$$\dot{q}_{rad,MLI} = \frac{\epsilon_i \cdot \epsilon_k}{(n+1) \cdot \epsilon_i + 2\epsilon_k} \cdot k_B \cdot (T_2^4 - T_1^4) \tag{4.5}$$

with the number n for the adjacent (uncooled) layers and the emissivities $\epsilon_i = \frac{\epsilon_0 \cdot \epsilon_s h}{\epsilon_s h + \epsilon_0 - \epsilon_0 \cdot \epsilon_s h}$ and $\epsilon_k = \frac{\epsilon_s h}{2 - \epsilon_s h}$, where ϵ_0 is the emissivity of the surfaces and $\epsilon_s h$ of the shields.
Due to its rather poor resistance to gamma radiation and its potentially negative effect on neutron transport, it should not be used to shield the moderator vessel and directly attached tubes. Therefore, its effect on heat load is only considered for the cooling part of the transfer line sections. According to the above equation, the heat load in the transfer line section through the oval tubes can be reduced to 0.2 W, which reduces the overall heat load by radiation onto the helium supply to 0.9 W.

Solid conduction: The thermal conduction heat flux can be calculated by applying

Fourier's law [68]

$$\dot{Q}_{cond} = \lambda(T) \cdot A \cdot \frac{\mathrm{d}T}{\mathrm{d}x} \tag{4.6}$$

with the temperature-dependent thermal conductivity $\lambda(T)$, the cross section for heat transfer by conduction A and the temperature gradient over a differential length element $\frac{\mathrm{d}T}{\mathrm{d}x}$. There are several ways to reduce the heat transfer due to thermal conduction, as is apparent from Equation 4.6:

- Choosing a material with a low thermal conductivity λ
- Reducing the cross section area A of the conductance path
- Increasing the length x of the conductance path
- Intercepting heat flows by thermal bridges to heat sinks (e. g. coolant return lines) to reduce the effective temperature difference dT

Heat transfer due to thermal conduction happens through several paths inside the cryostat. A large part is caused by the use of spacers to keep the inner tubes in position and avoid thermal contact between them and the outer walls of the vacuum recipient. Typically used materials for spacers in cryogenic applications have a low thermal conductivity. Examples are plastics, like polyethylene or polyimide, but also stainless steel, in case the environmental conditions require a more robust material. In the present design, spacers are made of Vespel SP-1, a bulk polyimide with a low thermal conductivity, high strength and a good machinability. Since the distance between the inner walls of the vacuum recipient and the tubes is small due to geometrical constraints imposed by the dimensions of the prototype TMR, labyrinthic grooves around the tube's feed-through and small contact areas are incorporated to reduce the heat load.
Figure 4.7 shows a comparison between the spacers as solid discs and in a cryogenically optimized design for the transfer line and the cold moderator sections.

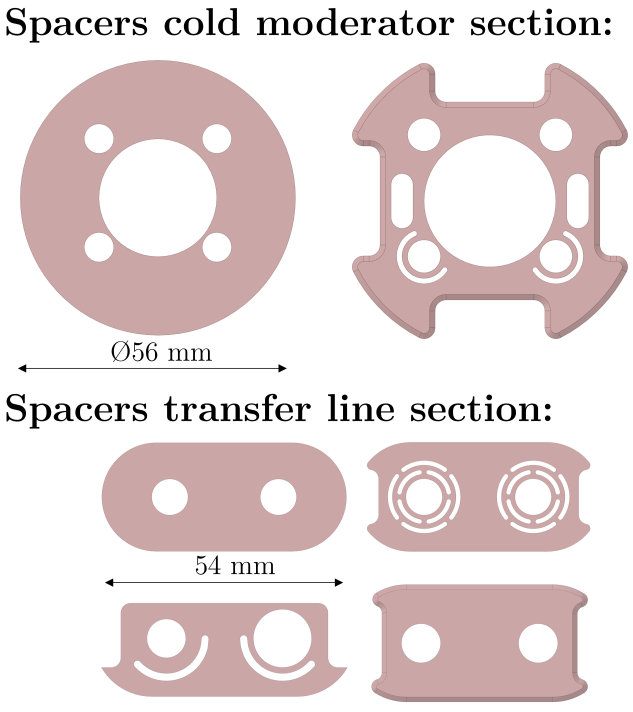

Figure 4.7: Front view of the spacer designs as solid discs and thermally optimized.

To assess the heat load by solid conduction through the spacers, the module "Steady-state

Thermal" in ANSYS Workbench is applied. The temperature of the outer surfaces facing the vacuum recipient is set to 295.15 K, while the surface facing the coolant inlet tube is set to 4.2 K. Both assumptions are conservative, since the lower thermal contact conductance in vacuum is neglected. The thermal conductivity data for the Vespel SP-1 is taken from [69].
Table 4.3 lists the heat load by solid conduction onto the different tubes for the different spacers and designs. It is apparent that the heat load can be reduced by a factor of approximately 6...7 for the helium tubes and of 1.2 for the moderator tubes.

Table 4.3: Heat load by solid conduction through the spacers onto the different lines (He supply, He return and moderator) for the different spacers in solid disc and optimized design.

Spacer	$\dot{Q}_{Solid}$ in [W]	$\dot{Q}_{Optimized}$ in [W]
CM section, He supply	1.2	0.2
CM section, He return	1.1	0.2
TL section, He supply	2.1	0.3
TL section, He return	2.1	0.4
TL section, He intake	2.0	0.2
TL section, moderator	1.4	1.1

Apart from the spacers, the tubes for fluid transfer themselves conduct heat from their fixed connection points to the moderator vessel. In the present prototype cryostat, the only fixed positions are the welding joints at the feed-throughs to the ambient surrounding (left side in Figure 4.6). This ensures enough flexibility of the tubing and moderator vessel to move during cool down.
During operation, mainly the moderator tubes conduct heat to the cold moderator. However, due to the large length between the fixed connection and the moderator vessel, the heat flux by thermal conduction only amounts to approximately 42 mW per moderator tube. For the coolant return line, the heat flux by solid conduction is mostly compensated by the cooling capacity of the coolant flow. The heat flux onto the coolant supply line is reduced by using a coaxial thin-walled stainless-steel tube with a sufficient length as an intake for the insulated coolant transfer line. This connection also acts as a thermal decoupling from the flange plate to avoid cryogenic temperatures at the sealed connection. Figure 4.8 shows the operating principle of the insulated coolant transfer line intake for liquid helium. This way, the heat load onto the liquid helium is reduced to 91 mW.
Another cause for heat load by solid conduction is the use of wires to connect tempera-

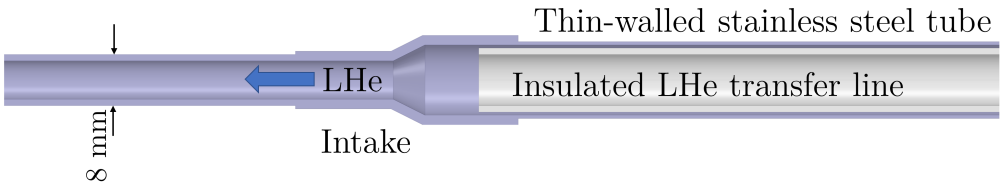

Figure 4.8: Operating principle of the intake of the insulated coolant transfer line.

ture sensors and heaters at the moderator vessel to the vacuum-compatible feed-through at the other end of the cryostat (top ISO flange on the oval tube at the left side of Figure 4.6). The wires' cross sections should be chosen as small as feasible (without limiting the required current) for the required task and an extra length should be incorporated to allow the attachment of the wire to a cold surface as a heat sink. Furthermore, the extra length gives the wire a flexibility, so that it can stretch in case of thermal contraction

without breaking, as long as the wires are not mounted too tightly and are under tension. Typically used sizes for wires in cryogenic application are 32 AWG ($A_{wire} = 0.0324$ mm^2) or 36 AWG ($A_{wire} = 0.0127$ mm^2). To reduce the solid conduction through the wire, the materials of choice are phosphor bronze or manganin due to their low thermal conductivity. To obtain accurate readings, the sensor and directly attached wire have to be at the same temperature as the sample. Therefore, the wires have to be thermally anchored.
In the present setup, quad-twist phosphor bronze wire with 36 AWG is chosen. By thermally anchoring the wire to a location at a temperature close to the measured value (e. g. $T \approx 10$ K), the heat load by conduction is reduced by a factor of around 29 from 1.1 mW to 0.04 mW for four sensors (16 wires in total). If copper was used instead, the heat load would be around 16.2 mW. However, with regards to the moderator heating by nuclear energy deposition, these values are negligible. The thermal conductivity of the Nichrome (nickel-chromium) heater wire is even lower than that of phosphor bronze and is therefore not considered here.
To estimate the temperature profiles in the different tubes of the cryostat more accurately, a simulation using the ANSYS Workbench module "Steady-state thermal" is performed. The model contains the tubes, spacers and cold moderator vessel as well as the oval flange connections, where the tubes are connected to the vacuum recipient. The rest of the vacuum recipient is omitted to reduce the run time of the simulation.
As boundary conditions, the surfaces of the spacers close to the vacuum recipient are set to $T_w = 295.2$ K and a convection condition is attached to the outside surfaces of the oval flanges ($h_{air} = 25.3$ W/(m$^2 \cdot$ K)). Furthermore, the helium supply and return lines are equipped with a fluid flow of helium. Its mass flow is $\dot{m}_{He} = 0.2$ g/s and the initial temperatures are set to $T_{He,supply} = 4.2$ K and $T_{He,return} = 10$ K. The temperature of the cold moderator vessel is set to a mean intermediate temperature of $T_{m,mod} = 7$ K. Thermal radiation is modeled by assuming a radiative heat exchange to the ambient at 295.2 K (view factor 1.0). This method yields slightly higher values than the "surface-to-surface" option, since no view factors are calculated, but has a drastically lower run time.
Figure 4.9 shows the temperature distribution along the tubes. It is apparent that the temperature along the helium supply and return tubes only increases slightly due to the high cooling capacity of the helium mass flow, while the moderator tubes are above 200 K for most of their length. This is caused by the heat load through the spacers and the low cooling effect along the relatively long moderator tubes. Therefore, the radiation heat load differs significantly from the one presented in Table 4.2. The heat fluxes from the simulation of the whole tubing and cold moderator assembly are listed in Table 4.4. Figure 4.9 shows the temperature profile at the thermal decoupling of the helium exhaust tube. Although the helium mass flow has a temperature of approximately $T_{He,return} \approx 15$ K at the outlet of the vacuum recipient, the thin stainless steel tube between the helium return tube and the oval flange cause the temperature of the oval flange to stay at room temperature.

Table 4.4: Heat load by solid conduction, thermal radiation and total heat flux onto the tubing and cold moderator vessel.

Section	$\dot{Q}_{rad}$ in [W]	$\dot{Q}_{cond}$ in [W]	$\dot{Q}_{tot}$ in [W]
CM	0.7	3.4	4.2
He supply	2.1	2.1	4.2
He return	3.5	3.4	7.0
Moderator tubes	1.0	2.1	3.1

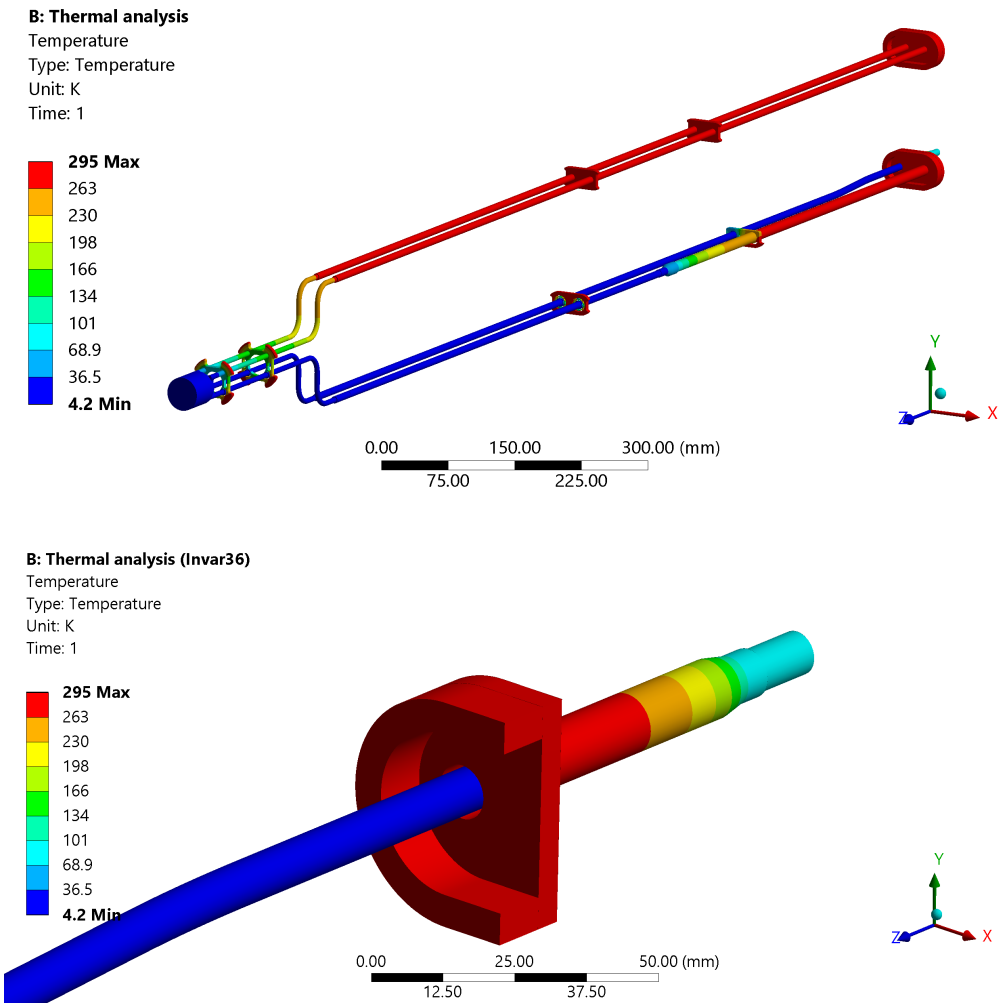

Figure 4.9: Top: Temperature distribution in the tubes, spacers and cold moderator vessel of the cryostat. Bottom: Temperature distribution at the stainless steel thermal decoupling tube between the oval flange and the helium return line.

Dynamic heat load:
The dynamic component of the heat load consists of the energy deposited by nuclear particles mentioned in chapter 3. Unlike the static part, it changes with time. Its specific time structure depends on the pulsing of the proton beam used for neutron production. The dynamic heat load consists of the interactions of nuclear radiation with the nuclei and electrons of the moderator atoms. Heat is transferred mainly by scattering and absorption processes, with probabilities depending on the incident particles' energies and the chosen moderator and structural materials. Apart from the interactions of primary particles created in the target (mainly neutrons and gamma photons, since the protons are intercepted by a water beam stop), secondary particles (neutrons, gamma photons, protons, electrons) can further contribute to the dynamic heat load.
Since a correct analytical calculation of the underlying processes and contributions is not feasible, they are determined by performing simulations using the aforementioned Monte Carlo N-Particle code (MCNP6.1). Such simulations allow the calculation of the energy deposition caused by the different particles inside the moderator volume and its surrounding vessel and coolant. The precision of such simulations depends largely on the number of the simulated primary particles, while the accuracy depends on the underlying physical model and the nuclear data applied.
For the case of a 24 Hz target station and a duty cycle of 1.6%, the pulse period is $T_{pulse} = 41.667$ ms and the pulse width is $\Delta t_{pulse} = 0.667$ ms. Therefore, the time without pulse between the end of the previous and the beginning of the next pulse is $t_{no\ pulse} = 41$ ms. Since a proton has an elementary charge of 1 e, the number of protons hitting the target per second can be calculated from the maximum current of $I_p \approx 89.3$ mA and the factor $6.24 \cdot 10^{18}$ e/C for the conversion of Coulomb to elementary charges. It is approximately $8.9 \cdot 10^{15}$ p/s. Using the mass of the individual cells and the proton current and converting the energy from eV to J (1 eV = 1.602×10^{-19} J), one obtains the value of heat deposited in W.
In a more detailed simulation using the final design of the moderator vessel, the cold moderator part includes solid methane as a moderator, aluminium (Al-27) as a structural material and liquid helium as coolant. Although the helium is in gaseous state when entering the cold moderator vessel, the assumption of a higher density serves as a conservative estimation. The cold moderator is incorporated into the input geometry in a simplified way, transforming the aluminium from the cooling channels to cylindrical layers (see Figure 4.10), so that the overall volume is analogous.
The whole moderator vessel consists of 4 cells: one for the solid methane, one for the long aluminium section, one for the short aluminium section and one for the helium layer. The separation of the aluminum allows an easier transformation of the body into MCNP geometry. The tracked particle types include neutrons, photons, electrons, protons and alpha particles. Table 4.5 shows the amount of heat introduced into the cold moderator vessel and the corresponding ratios of the total heat load per material.
Following, an assessment of the effect of the pulsed beam operation on energy deposition due to radiation is made for the 24 Hz target station. Since the values obtained by MCNP6.1 are time-averaged, the actual heat load during each pulse is higher, followed by periods of no heat load. By dividing the time-integrated heat load by the pulse frequency and duration of the pulses, one obtains the maximum heat load during one single pulse:

$$\dot{Q}_{pulse} = \frac{\dot{Q}_{avg}}{f_{pulse} \cdot t_{pulse}} = 62.5 \cdot \dot{Q}_{avg} \tag{4.7}$$

The total heat load onto the cold moderator vessel and its contents during one single pulse is therefore approximately 162.5 W.
Another factor that has to be considered is the heating of the cylindrical vacuum shell around the cold moderator vessel to determine if an active cooling of the vacuum shell is

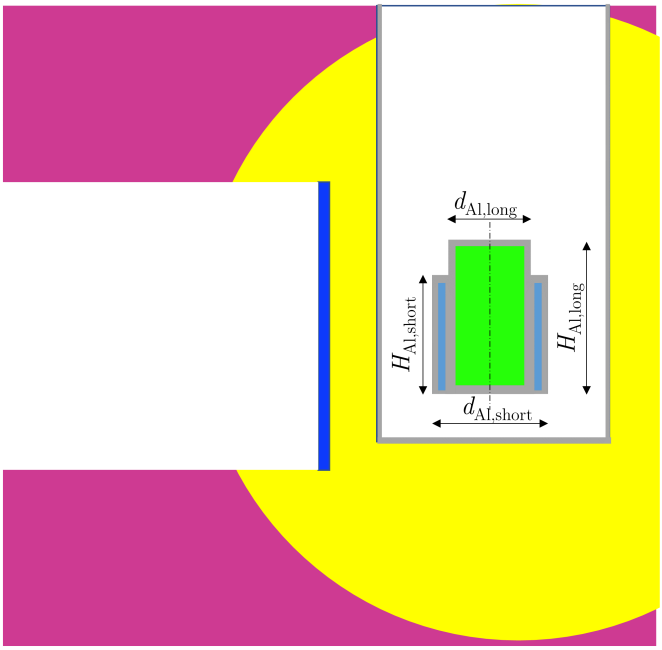

Figure 4.10: MCNP6.1 input geometry consisting of a solid methane cold moderator (bright green), an aluminum vessel and surrounding vacuum tube (dark grey), liquid helium (blue), a thermal moderator (yellow), a lead reflector (purple) and a tantalum target (dark blue).

necessary. According to the simulation above the total heat load by neutrons and photons/electrons is 3.6 W, of which about 60% are deposited in the first 6 cm of length in the direction originating from the target location. Assuming a natural convection coefficient of air of $h_{air} = 25.3\ \mathrm{W/(m^2 \cdot K)}$ at the outer surface of the cylindrical vacuum jacket, the resulting maximum temperature is $T_{max} = 320$ K (see Figure 4.11).
For a transient thermal analysis using 62.5 times the deposited energy during a pulse, the temperature during one pulse period (41.667 ms) only rises by $\Delta T = 0.01$ K. However, for 24 pulses per second, a temperature increase of 50 K would only take approximately 209 s, assuming a steady increase. Since a maximum temperature of the vacuum jacket of 75 °C should not be exceeded during operation (see subsection 4.5.1), active cooling might be required to avoid a thermal expansion of the vacuum jacket. This could either be realized by attaching the vacuum jacket to a colder component (e. g. a light water thermal moderator) or by generating an air flow and increasing the convection heat transfer to the surrounding air. In a real target station, there is a small gap filled with air between the vacuum recipient surrounding the cold moderator vessel and the thermal moderator. Therefore, either a thermal coupling between the vacuum recipient and the thermal moderator or a ventilation of the air gap would be required.

Since the nuclear heat fluxes by energy deposition are mainly dependent on the amount and kind of material in the radiation field and the energy and flux of the primary particles, the possibilities to reduce them are limited. One option is the optimization of the moderator vessel with regards to stability and cooling efficiency to avoid excess material. Other options include a reduction of proton beam energy or current or a positioning of the cold moderator further away from the target, but these choices would simultaneously reduce the cold neutron flux or brightness produced by the cold moderator.

Table 4.5: Heat load into the different sections of the cold moderator vessel by energy deposition in [W] and ratio of total in [%].

Material	**Particle**	Neutron	Photon + Electron	Total
Methane	$\dot{Q}$ in [W]	1.415	0.161	1.576
($m = 6.409$ g)	Ratio [%]	89.8	10.2	100.0
Aluminum	$\dot{Q}$ in [W]	0.2	0.8	1.0
($m = 41.520$ g)	Ratio [%]	19.9	80.1	100.0
Helium	$\dot{Q}$ in [W]	2.4×10^{-3}	4.6×10^{-4}	2.8×10^{-3}
($m = 0.018$ g)	Ratio [%]	83.8	16.2	100.0
=				
Cold moderator	$\dot{Q}$ in [W]	1.6	1.0	2.6
($m = 47.947$ g)	Ratio [%]	62.6	37.4	100.0
Vacuum sleeve	$\dot{Q}$ in [W]	0.7	2.9	3.6
($m = 448.069$ g)	Ratio [%]	19.4	80.6	100.0

4.3.3 Moderator cooling

Using the results from the previous subsection, an assessment of the feasibility of different cooling techniques is possible. There are two ways of indirectly cooling the moderator vessel in a setup like the one presented in Figure 4.5, namely:

1. by using cryogenic liquids (LHe, LN_2, LH_2) and
2. by using a mechanical refrigerator (so-called *cryocooler*)

The advantage of the first option lies mainly in its easy availability and large range of cooling capacity: theoretically, the available cooling power can easily be increased by increasing the flow of coolant along the object to be cooled (as long as the surface and heat transfer properties are large enough). One major disadvantage is the need of a constant supply of cryogenic liquid in case there is no continuous re-liquefaction incorporated into the system, and the cost involved. As is apparent from Point 1) of the requirements in section 4.1, only liquid helium is a possible cryogenic fluid to cool the moderator down to $T \leq 10$ K, since all other materials are solid at this temperature. Helium has a latent heat of evaporation of $h_{lat,vap} = 20.64$ J/g at normal pressure [43], which yields a cooling power of approximately 10.3 W for a continuous mass flow of 0.5 g/s. Including the specific enthalpy between evaporation and the upper limit of 10 K, the same mass flow yields a cooling power of around 27 W.
Mechanical cryogenic refrigerators, e. g. Pulse Tube (PT) or Gifford-McMahon (GM) cryo-coolers, offer a continuous closed cycle operation. This exempts the user of the necessity to refill or exchange any coolant supply, which is especially suited for areas where access is limited, e. g. in a radiation control area. Depending on the service life time, the higher initial investment pays off due to its comparatively low operation cost (mostly cooling water and electricity).
The major disadvantage of using cryocoolers is their maximum cooling capacities at low temperature: commercial cryocoolers typically don't exceed values of 2 W at 4.2 K base temperature (see Table 4.6). Furthermore, they are dependent on a heat carrier if it is not

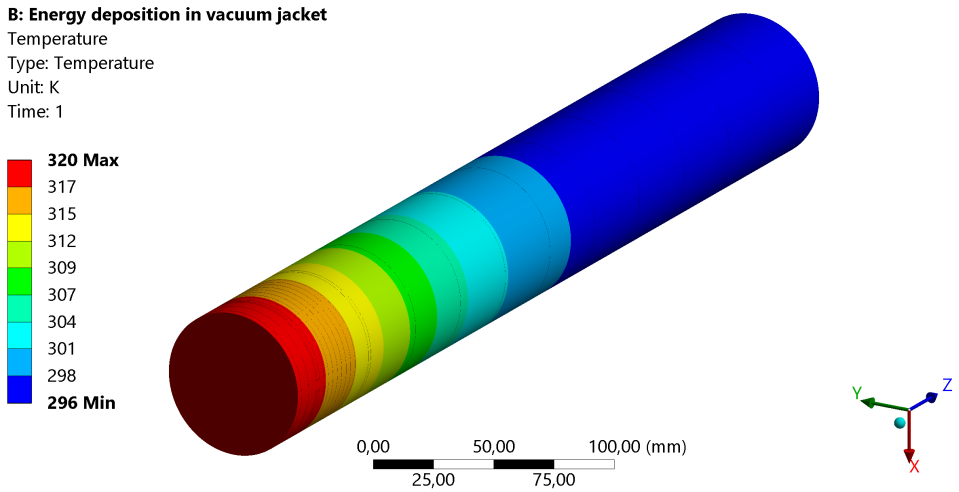

Figure 4.11: Temperature distribution inside the cylindrical vacuum jacket around the cold moderator cooled by natural convection of air. The energy deposition was taken from simulations performed with MCNP6.1.

possible to directly connect the cryocooler's cold head to the body that needs to be cooled. This can either be a material with a large thermal conductivity, like high purity copper or aluminum, or a coolant cycle attached to the cold head via a heat exchanger. There are efforts to build such fluid flow closed cycle systems [70], [71], but they usually work at $T \geq 40$ K and are not commercially available yet. The option of a solid thermal bridge is problematic for the present setup, due to the low available space. A total heat load of 4 W would require a diameter of copper and aluminum bars of $d = 100$ mm to obtain a maximum temperature of $T = 7$ K. For a copper bar of such diameter, its weight poses another problem, especially if additional spacers are undesired.

Table 4.6: Exemplary characteristics of a cryocooler and liquid helium.

Cooling technique	Cryocooler	LHe
Base temperature [K]	2.8	4.2
Cooling capacity at 4.2 K [W]	2	variable
Acquisition cost [Euro]	$\approx$ 60000	$\approx$ 5000 (transfer line)
Cost per 24 h of operation (date: Oct. 2023) [Euro]	71	350

Another disadvantage is their lack of flexibility and their rather slow response time compared to cryogenic liquids due to thermal conduction being the main type of heat transfer. If one compares the cost of the two different options (see Table 4.6), it is apparent that the cryocooler is less expensive for longer periods of operation life time. However, before the initial cost is paid off, approximately 100 LHe dewars with a capacity of 250 l of liquid helium can be purchased.

The large distance between the cold moderator vessel - where the cooling power is needed - and the outside of the TMR unit - where the radiation level is low - makes cooling with liquid helium a suitable choice for the present cryogenic system. In addition, the system is an experimental one and the calculations of heat fluxes include some uncertainties, making cryogenic liquids the more reliable choice.

Cooling with liquid helium is possible in two ways: bath (or *natural convection*) cooling as well as flow (or *forced convection*) cooling. The former is usually applied if the heat load is in the order of some mW and the cooling capacity of the helium bath is large in comparison to the heat load, e. g. when cooling relatively small samples.

Helium cooling by forced convection allows the removal of larger amounts of energy from

the system to be cooled and is especially suited if space is limited, which is the case for the present problem. By adapting the characteristics of the flow and the channel, the heat transfer coefficient h_T can be increased. Furthermore, a closed cycle cooling system offers the possibility to increase the pressure in the system. By increasing the pressure to the critical point for helium at $p_{cr} = 2.26$ bar(a), the heat transfer coefficient h_T can theoretically be increased to $h_T = 3956\ \mathrm{W \cdot m^{-2} \cdot K^{-1}}$ (see Figure 4.12). This is another reason for realizing a closed cycle cooling system for a frequently operated cryostat at a full-power Hi-CANS. For the present case, where heat load due to nuclear heating is negligible, the heat transfer at atmospheric pressure is sufficient.

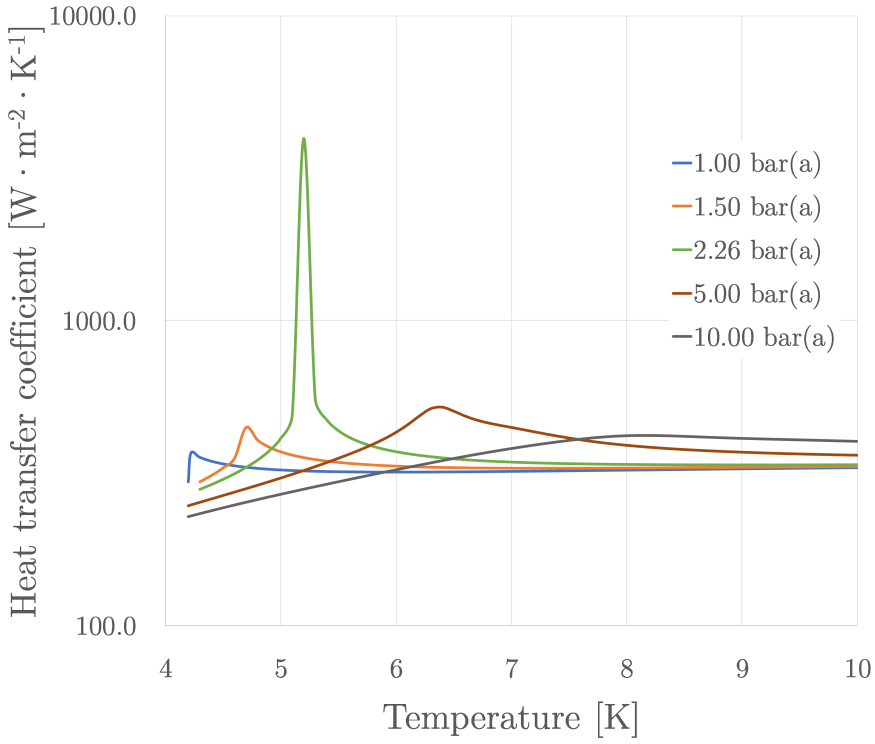

Figure 4.12: Heat transfer coefficient h_T in dependence of temperature T and pressure p of the helium.

To avoid excess material in the neutron flight path towards the neutron guide, the cylindrical moderator volume should be cooled from its shell surface. Therefore, a design similar to one realized in a previously manufactured cryostat for the provision of liquid hydrogen as a cold moderator is applied [72]. In this design, the content of an inner cylindrical volume is cooled from its shell surface by conducting a fluid flow of coolant through a channel running back and forth along the length of the inner vessel (see Figure 4.13).
The cooling labyrinth enables a temperature profile in which the lowest temperature is located at the bottom of the cylindrical cavity that incorporates the cold moderator material. This is desired to avoid a premature freezing of the moderator material at the inlet or outlet of the vessel, in case there is no temperature control. In addition, a section not actively cooled by the cryogenic helium is included at the front of the moderator to ensure an initial melting of the frozen moderator at the inlet and outlet.
Apart from the heat load and the cooling power the cold moderator temperature is governed mainly by the thermodynamic properties of the moderator material. When applying a hydrogenous solid like frozen methane as a cold moderator, it is especially important to take these properties into account to ensure a sufficient and uniform cooling. Especially its specific isobaric heat capacity c_p and its thermal conductivity λ_{th} are of high significance: the former allows an estimation of the energy the moderator can absorb before warming

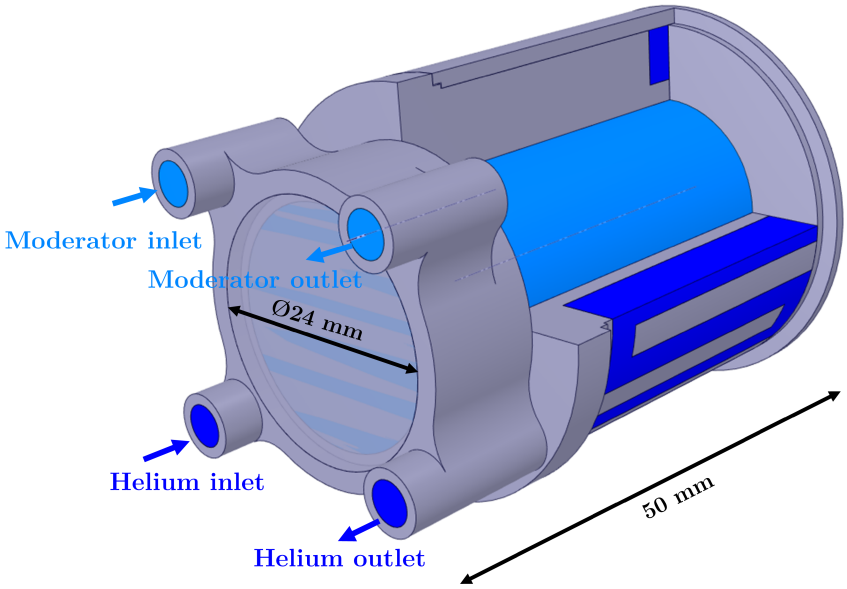

Figure 4.13: Cut view of a CAD model of the cold moderator vessel with a helium cooling channel.

up to a specific temperature or even change its physical state of matter, the latter is important in the overall assessment of the cooling efficiency. Since the use of liquid helium enables a flexible and fast cooling and the structural material has a relatively high thermal conductivity, the cooling is mainly governed by the rate of heat transfer through the solid methane.

This poses a problem, as thermodynamic properties are only partially reported and hard to find for most cryogenic solids, mostly due to their infrequent application compared to cryogenic liquids like LH_2 or LHe. Values given in literature for the thermal conductivity of solid methane are restricted to specific temperature regions (e. g. 2 K to 32 K [73]) or single temperatures around transition points (freezing temperature [74] or phase transition temperature [75]). Since the intended application described in this thesis is limited to temperatures ranging from approximately 5 K to 20 K, the values reported in [73] are used for calculations. In the mentioned publication, values from approximately 2 K to 31 K are shown graphically. Since the exact values are not reported, they have to be extracted optically from the graph. The left hand side graph in Figure 4.14 shows all available values from the mentioned source. To more precisely assess the effect of nuclear heating on a solid methane moderator for the full power HBS, values for the specific (isobaric) heat capacity c_p have to be known. They are tabulated in [76] and given in graphical form in Figure 4.14, right, for the available values. The peak at approximately 20 K is caused by a transition of the methane from phase I to phase II and a corresponding change in behaviour of the molecules.

From these values as well as the dynamic heat load from subsection 4.3.2, it is possible to assess a preliminary temperature profile inside the moderator vessel. The simplified problem is shown schematically in Figure 4.15. In a first approach, the temperature at the center axis of the solid methane cylinder is estimated analytically under the assumption of a constant coolant temperature and thermal conductivity of the materials as well as an ideal thermal contact between the methane and the aluminum wall. A uniform heat generation is obtained from the simulations regarding energy deposition due to nuclear radiation.

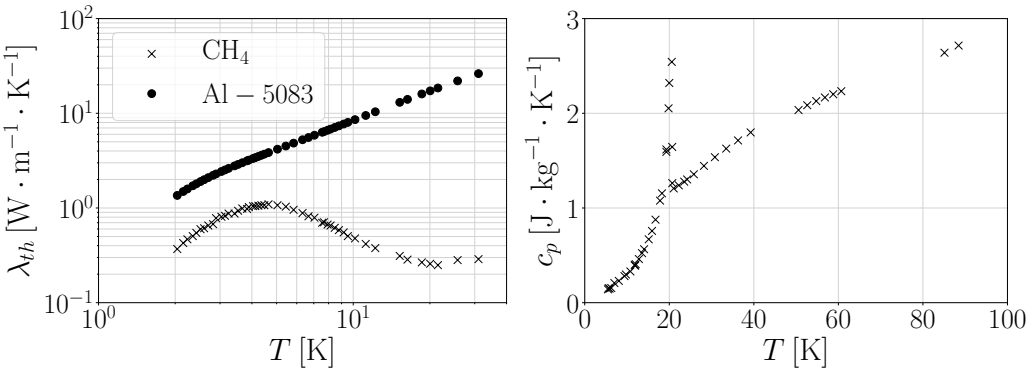

Figure 4.14: Diagram for the thermal conductivity and specific isobaric heat capacity of solid methane vs. temperature (values taken from [73] and [76], respectively). Thermal conductivity of aluminum alloy 5083 [60] (used for cold moderator vessel) added for comparison.

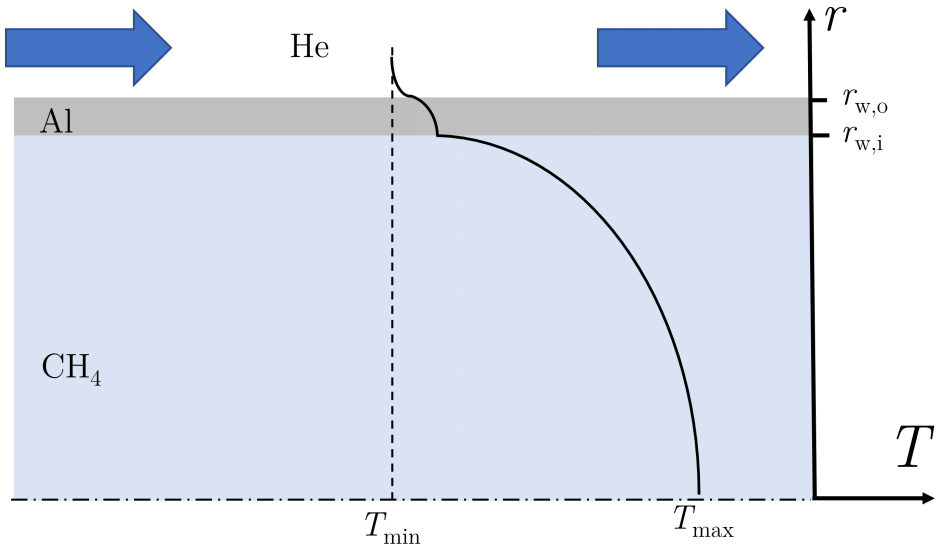

Figure 4.15: Schematic longitudinal cut view of a cylindrical cold moderator vessel to assess the problem of heat transfer in cryogenic solids.

The heat flow $\dot{Q}$ from the moderator to the coolant can be described by [77]:

$$\dot{Q} = h_T \cdot A_s \cdot (T_{w,o} - T_{He}) \tag{4.8}$$

with the heat transfer coefficient h_T, the surface for heat exchange A_s and the temperatures $T_{w,o}$ at the outer wall and T_∞ in the center of the helium flow.
The internal heat generation inside the solid methane and aluminum is defined as [77]:

$$\dot{Q} = \dot{q}_{gen} \cdot V \tag{4.9}$$

with the volumetric heat generation $\dot{q}_{gen}$ in [W · m^{-3}] and the volume V in which the heat is deposited. The volumetric heat generations for a methane volume of $V_{CH_4} = 12.6$ cm^3 and an aluminum volume of $V_{Al} = 15.4$ cm^3 are $\dot{q}_{gen,CH_4} = 0.125$ [W/cm^3] and $\dot{q}_{gen,Al} = 0.065$ [W/cm^3], respectively (taken from subsection 4.3.2). The length for these calculations is $L = 40$ mm and the radii are $r_{w,i} = 10$ mm and $r_{w,o} = 12$ mm for the smaller moderator and $r_{w,i} = 20$ mm and $r_{w,o} = 22$ mm for the larger moderator.
Using equations 4.9 and 4.10 with the heat transfer surface $A_s = 2 \cdot \pi \cdot r_{w,o} \cdot L$ and the

volumes $V_{CH_4} = \pi \cdot r_{w,i}^2 \cdot L$ and $V_{Al} = \pi \cdot (r_{w,o}^2 - r_{w,i}^2) \cdot L$, the temperature at the outer side of the moderator vessel wall can be written as:

$$T_{w,o} = T_{He} + \frac{\dot{q}_{gen,CH_4} \cdot r_{w,i}^2 + \dot{q}_{gen,Al} \cdot (r_{w,o}^2 - r_{w,i}^2)}{2 \cdot h_{T,He} \cdot r_{w,o}} \tag{4.10}$$

Therefore, the temperature at the outer surface of the moderator vessel wall depends largely on the volume and related nuclear heating, and the characteristics of the helium cooling. The latter is determined by the flow rate of helium and the flow channel dimensions. For the assumption of a turbulent flow of liquid or gaseous helium – which is accurate for most applications – one can assume the following correlation (Dittos-Boelter expression) [67]:

$$\overline{\mathrm{Nu}} = 0.023 \cdot \mathrm{Re}_D^{4/5} \cdot \mathrm{Pr}^{2/5} \tag{4.11}$$

with the Nusselt number $\overline{Nu}$ averaged over the channel length, the Reynolds number Re_D and the Prandtl number Pr, the ratio of the fluid's kinematic viscosity to its thermal diffusivity. By knowing the Nusselt number, it is possible to obtain the heat transfer coefficient h_T in unit $[\mathrm{W} \cdot \mathrm{m}^{-2} \cdot \mathrm{K}^{-1}]$ by following formula [68]:

$$\mathrm{Nu} = \frac{h_T \cdot d_h}{\lambda_{th}}, \tag{4.12}$$

where d_h is the hydraulic diameter of the flow channel. It is defined as follows [77]:

$$d_h = \frac{4 \cdot A_c}{P_e} \tag{4.13}$$

with the cross sectional area A_c and the perimeter P_e of the flow channel. In the present case, the flow channel is a rectangular one with a width of 3 mm and a height of 5.4 mm, which results in a hydraulic diameter of $d_h = 3.9$ mm.
For an exemplary mass flow of $\dot{m} = 0.2$ g/s of gaseous helium at $T_{He} = 5$ K (after warm-up from $T_{He-in} = 4.2$ K between inlet and cold moderator vessel) and the aforementioned hydraulic diameter, one obtains a heat transfer coefficient of around $h_T = 323.6 \ \frac{\mathrm{W}}{\mathrm{m}^2 \cdot \mathrm{K}}$. Using this heat transfer coefficient and Equation 4.10 for a choice of two different outer diameters of 2.4 cm and 4.4 cm, the resulting temperatures at the outside of the moderator vessel wall are $T_{w,o} = 7.0$ K and $T_{w,o} = 8.9$ K, respectively.
For the case of thermal conduction with internal heat generation, as is the case for the solid methane and the aluminum wall, one can use the following formula to describe the temperature along the radius [77]:

$$T(r) = T_{w,o} + \frac{\dot{q}_{gen}}{4 \cdot \lambda_{th}} \cdot (r_{w,o}^2 - r^2) \tag{4.14}$$

with the temperature $T_{w,o}$ at the outer surface with radius $r_{w,o}$ and the thermal conductivity λ_{th} of the respective solid.
Using Equation 4.10 and Equation 4.14, the temperature T_{max} at the center axis of a solid cylinder of methane with radius $r_{w,i}$ surrounded by a cylindrical wall of aluminum with outer radius $r_{w,o}$ and a constant coolant temperature $T_{He} = 5$ K can be calculated as follows:

$$T_{max} = T_{He} + \frac{q_{gen,CH_4} \cdot r_{w,i}^2 + q_{g_Al} \cdot (r_{w,o}^2 - r_{w,i}^2)}{2 \cdot h_{He} \cdot r_{w,o}} + \frac{q_{gen,Al}}{4 \cdot \lambda_{th,Al}} \cdot (r_{w,o}^2 - r_{w,i}^2) + \frac{q_{gen,CH_4}}{4 \cdot \lambda_{th,CH_4}} \cdot (r_{w,i}^2 - r^2) \tag{4.15}$$

The mean thermal conductivities for methane and aluminum are calculated iteratively from the tabulated data in Figure 4.14, left. The mean thermal conductivities are $\lambda_{th,CH_4} = 0.669 \ \frac{\mathrm{W}}{\mathrm{m} \cdot \mathrm{K}}$ and $\lambda_{th,Al} = 5.828 \ \frac{\mathrm{W}}{\mathrm{m} \cdot \mathrm{K}}$ for the $d_{mod} = 2$ cm solid cylinder and $\lambda_{th,CH_4} =$

0.287 $\frac{\mathrm{W}}{\mathrm{m \cdot K}}$ and $\lambda_{th,Al} = 7.552$ $\frac{\mathrm{W}}{\mathrm{m \cdot K}}$ for the $d_{mod} = 4$ cm solid cylinder. The thermal conductivities are averaged over 1 K-steps between the minimum and maximum temperature of the respective material. For the solid methane data above $T = 30$ K, the values are interpolated between $T = 30$ K and $T = 90.7$ K (freezing temperature). A peak in thermal conductivity between these temperatures is neglected, since the interpolation is a conservative assumption and such temperature are far out of the acceptable range.
Temperature curves along the radii of the two solid cylinders are presented in Figure 4.16. The values of maximum temperature for both diameters and the temperature differences between the helium and maximum temperature are shown in Table 4.7 both for the calculation procedure described above and for numerical simulations.

Table 4.7: Maximum temperatures at the center of a solid cylinder methane moderator in dependence of cooling temperature, thermal conductivity, diameter and internal heat generation.

d_{mod} [cm]	T_{max} [K]	$\Delta T_{5\mathrm{K} \rightarrow T_{max}}$ [K]	$T_{max,sim}$ [K]
2	11.8	6.5	12.6
4	52.8	44.9	52.3

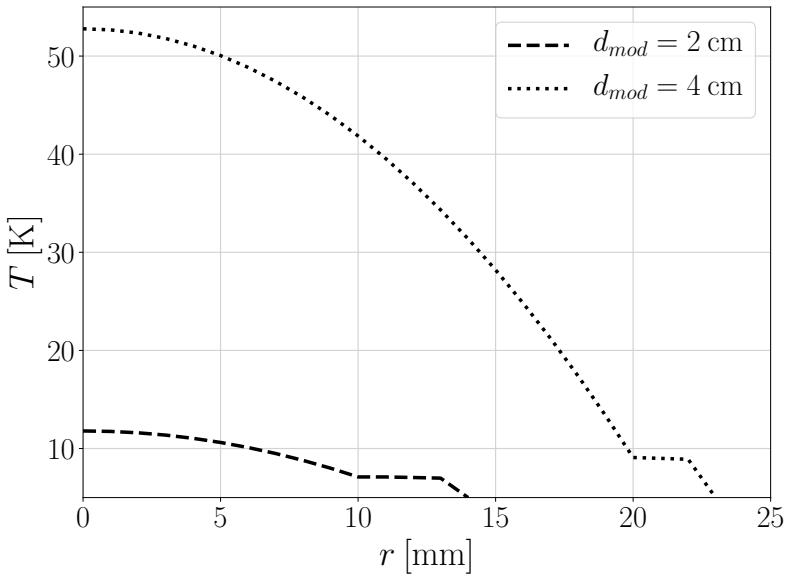

Figure 4.16: Temperature curves vs. radius for two different diameters of solid methane.

It is apparent from these results that it is not possible to maintain the solid methane at a constant low temperature during beam operation for beam powers like that of a full power HBS, especially for the larger diameter. The maximum core temperature of $T_{max} = 52.3$ K for an infinitely long cylinder or one without the impact of a base and top plate is reduced for a short cylinder ($L_{mod} = 3$ cm) to 39.4 K when including the aluminum plates at the top and bottom of the vessel, which are not directly cooled by a helium flow, but cause additional cooling by solid conduction. However, the temperature still rises by more than 30 K and approaches the larger value with increasing length of the cylinder. Furthermore, the calculations represent a best-case scenario due to assumptions of a constant helium temperature and a perfect thermal contact between the methane and the wall of the moderator vessel. Since this is not the case for the real application, the temperatures reported in Table 4.7 are even higher in reality. Additionally, the energy deposition from the MCNP6.1 calculations is time- and spatially averaged. In reality, most of the energy is deposited during single pulses and is not homogeneously distributed along the volume of

the methane. It has to be ensured that the pulsed beam operation does not result in a stepwise increase of the core temperature of the cold moderator and to an eventual melting or evaporation of the moderator. Figure 4.17 shows the distribution of the deposited energy in the cylindrical moderator. Although the energy deposition in the part of the moderator facing the target is higher by a factor of approximately 20%, the shorter distance to the coolant results in a more efficient cooling. Due to the moderators small size, the impact is negligible. However, with increasing moderator size, a more thorough investigation of the effects is necessary.

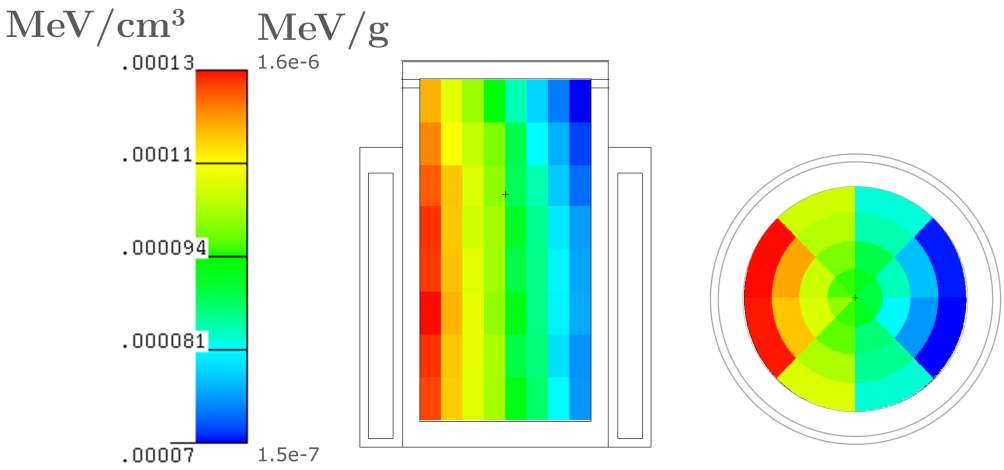

Figure 4.17: Spatial distribution of the energy deposition by neutrons inside the methane moderator. Side view (left) and top view (right).

Pulsed proton beam operation:
The effect of the pulsed beam operation with regards to energy deposition or heat load into the cold moderator can be assessed with the ANSYS module "Transient thermal". It allows the time-dependent application of internal heat generation in different parts of the cold moderator vessel. Despite still being a simplified representation of the actual problem, it can be used as a first step to estimate the temperature development inside the solid methane for a certain number of pulse periods. Nevertheless, more detailed calculations or experimental investigations are necessary to better estimate the final temperature in the actual moderator vessel used for the full power HBS (or other Hi-CANS facilities).
For the simulations, a CAD model of a solid cylinder surrounded by a cylindrical shell is generated. The solid cylinder is defined as methane and the shell as aluminium alloy Al-5083. To simulate the cooling by liquid helium, the outermost surface is set to 5 K, which is also the starting temperature of the problem. The unit of internal heat generation in ANSYS is W/mm^3, therefore the values from the MCNP6.1 simulation are converted and applied.
The heat load is simulated for complete pulse periods (single pulses with the subsequent time until the next pulse starts) to include the higher energy deposition during the pulse and the time of cooling after the pulse has ended. The simulations are performed for a pulse frequency of 24 Hz and a duty cycle of 1.6%, therefore the pulse width is 666.67 µs and the heat load has to be multiplied with a factor of 62.5 to obtain the actual heat load during the pulse, as mentioned in subsection 4.3.2. The pulse is set from 0 s to 666.67 µs, which assumes an energy deposition during a rectangular pulse. In reality, the energy deposition happens according to a time distribution, with an exponential increase and decrease during and after the proton pulse length. These time constants have not been simulated, but should be taken into account in a future, more realistic calculation of the

energy deposition during beam operation.
Figure 4.18 shows the minimum, maximum and average temperatures in the cylindrical cold moderator vessel during three consecutive pulse periods for moderator diameters of 2 cm and 4 cm. For the smaller diameter, the temperature increases to approximately 18.5 K in the center of the moderator before falling back to almost the initial temperature at the end of the pulse period. There is a small increase to $T = 5.6$ K at the beginning of the second pulse, but this increase does not continue for the third pulse. In the case of the 4 cm diameter, the maximum temperature in the core of the moderator rises to around 19 K and also rapidly falls to a stable temperature of 15.6 K. However, this temperature does not decrease further until the end of the pulse period and the average temperature rises to almost 11.5 K at the end of the third pulse. From the development during the first three pulses, the temperature is expected to rise during one second (= 24 pulses) to the maximum temperature obtained from the steady-state calculations.

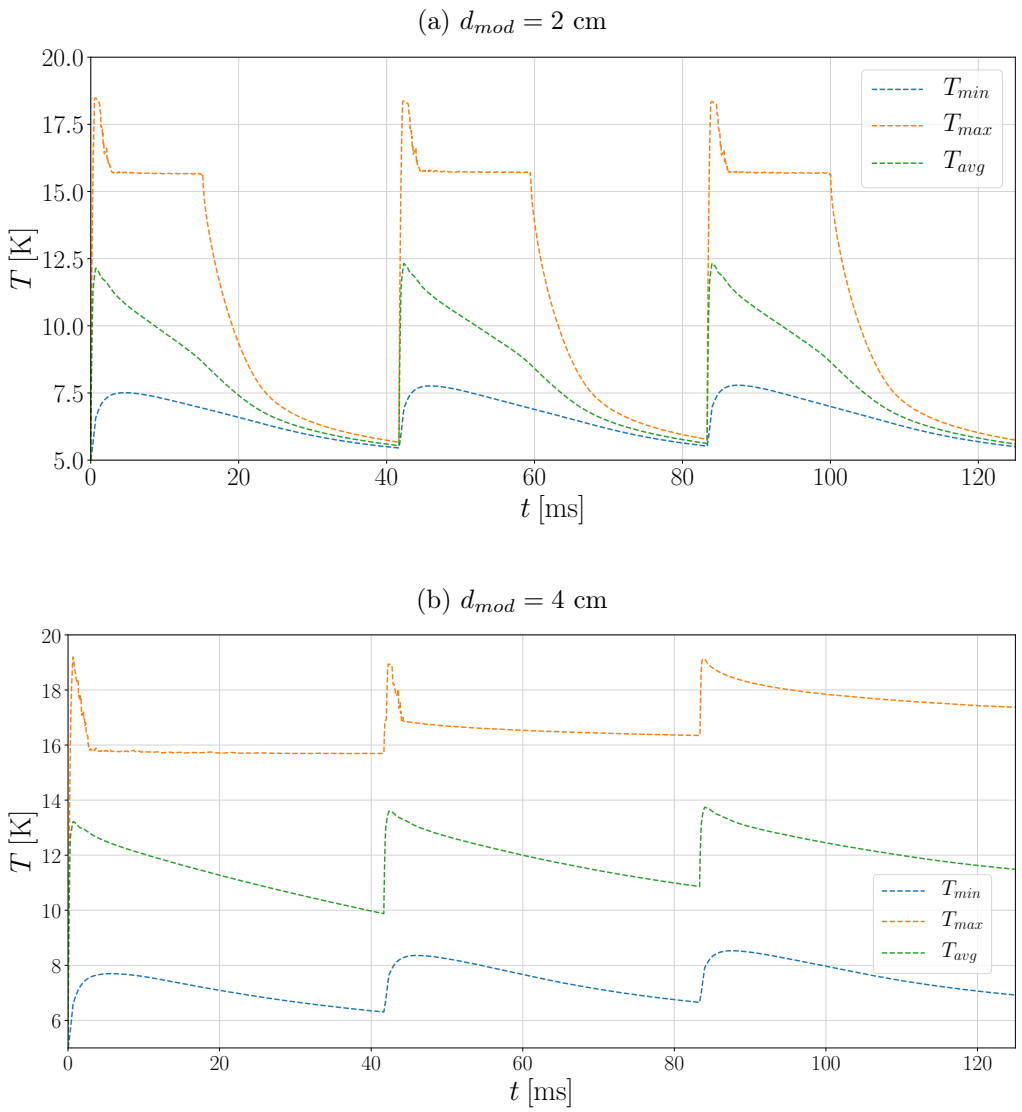

Figure 4.18: Minimum, maximum and average temperature vs. time for three consecutive pulses of width $t_{pulse} = 666.67$ µs in a cold moderator of solid methane with a diameter of $d_{mod} = 2$ cm (top) and $d_{mod} = 4$ cm (bottom).

The results indicate that in order to use a solid hydrogenous moderator with the full beam power and at a low temperature ($T_{mod} \leq 10$ K) at the HBS facility, measures have to be taken to increase its effective thermal conductivity $\lambda_{th,eff}$. One option is the use of using

highly porous structures of a material with high thermal conductivity (e. g. aluminium) inside which the methane can condense. This option is investigated in the following subsection.

4.4 Porous aluminum structures

As shown in subsection 4.3.3, the thermal conductivity λ_{th} of molecular solids is generally poor (especially at cryogenic temperatures), with peak values of 1.1 $\frac{\mathrm{W}}{\mathrm{m \cdot K}}$ at 4 K for solid methane [73] or 2 $\frac{\mathrm{W}}{\mathrm{m \cdot K}}$ at 7 K for solid oxygen [78]. Although solid ortho-deuterium shows a rather large peak thermal conductivity of around 16 $\frac{\mathrm{W}}{\mathrm{m \cdot K}}$ at approximately 5 K, it rapidly falls off towards lower and higher temperatures (e. g. 1.7 $\frac{\mathrm{W}}{\mathrm{m \cdot K}}$ at 10 K [79]).
When irradiated with neutrons and high-energy photons (gamma rays), the energy deposited in a molecular crystal can cause an unintended increase in temperature. The steepness of the increase depends on the crystal's thermal conductivity, the beam power of the source and on the spatial distance to the heat sink and its cooling power. As explained in section 3.1, this process can diminish the effectiveness of a cold moderator due to a shift in the resulting energy spectrum emitted from it. This will lead to extended times needed to perform scattering experiments to obtain the same resolution.
A potential measure to overcome this problem is by using a highly porous open-cell structure made of a material with high thermal conductivity, e. g. pure copper (1100 $\frac{\mathrm{W}}{\mathrm{m \cdot K}}$ at 4 K [80] for Cu 99.999%) or aluminum (1700 $\frac{\mathrm{W}}{\mathrm{m \cdot K}}$ at 4 K for Al 99.994% [80]), interlaced with the cold moderator. This method is applied at the Target Station II (TS-II) of the ISIS neutron and muon source at Rutherford Appleton Laboratory (RAL). Here, a high-purity aluminium foam is inserted into the cold moderator vessel, offering pathways for good thermal transport between the solid CH_4 condensed in the foam's pores and the helium cooling channels running through the vessel [81].
The most commonly applied option is aluminium foam, which can be manufactured from different alloys and with different porosities. It is commercially available (e. g. at ERG Aerospace) and is used for several applications where light-weight structures or good thermal conductors are needed. However, there are other options of porous metal structures, for example sintered fibre structures (Fraunhofer IFAM [Institute for Manufacturing Technology and Advanced Materials]) or additively manufactured (AM) grids.

4.4.1 Production

Metallic foams can be manufactured in different ways, e. g. by foaming (injecting gas into a liquid metal or adding a blowing agent, which evaporates during heating and forms cavities inside the metal) or by casting the metal into a prefabricated form made of heat-resistant resin and removing the resin afterwards [82]. Important adjustable characteristics of the foam, apart from its base material, are the pore size, which determines the ratio of surface area to volume. This is especially crucial for its heat exchanging ability and the relative density or porosity of the foam, since it defines the amount of solid material.
Metallic fibre structures are produced by extracting fibres from a melt bath by using an actively-cooled extraction wheel (*crucible melt extraction* or CME, see Figure 4.19 [83]). Adjustable parameters in fibre manufacturing include material, diameter and length. The single fibres are subsequently sintered to the desired shape and can be further processed, with porosities adjustable between 50% and 90% [83].
Porous metallic structures made by additive manufacturing (also commonly called *3D printing*) are manufactured in layers by sintering metallic powders using a laser (*laser powder bed fusion* or LPBF). The process follows a computer-aided design (CAD) model, which allows even complex shapes to be manufactured easily [84].

Figure 4.20 shows photographs of examples of the various aforementioned porous structures. The aluminium foam (left) is a sample from Fraunhofer IWU (Institute for Machine Tools and Forming Technology) made of pure aluminium with a pore density of 10 ppi (pores per inch) and a porosity of $\phi = 95.7\%$. The sintered fibre structure (center) is a product from Fraunhofer IFAM with a porosity of $\phi \approx 80\%$ and made of AlMg12. The

AM sample (right) was manufactured at the institute ZEA-1 of Forschungszentrum Jülich based on a grid designed with a CAD software (CATIA v5).

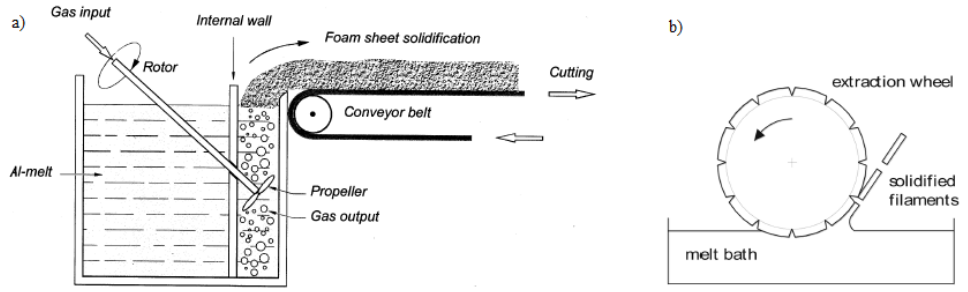

Figure 4.19: Basic principles of (a) direct foaming (taken from [82]) and (b) fibre production used for sintered structures (taken from [83])

Figure 4.20: Different samples of porous structures made of aluminium. Aluminium foam (Fraunhofer IWU, left), sintered fibres (Fraunhofer IFAM, center) and an additively manufactured grid (Forschungszentrum Jülich, ZEA-1, right)

4.4.2 Heat transfer in porous media

The main requirements for the task of cooling solid moderators demanded from all of these structures are a high porosity, a good thermal conductivity and a low thermal contact resistance. If the porosity would be low, the additional material could potentially lead to an increase in deposited energy inside the moderator, as well as reduce the moderating medium and therefore diminish the moderating efficiency (intensity or brightness at the sample position). The thermal conductivity and the low thermal contact resistance between porous structure and the walls of the moderator vessel ensure an effective transport of the deposited energy towards the cooling medium, leading to a more uniform temperature profile. The latter depends largely on the joinability of the porous material with the walls of the moderator vessel. The thermal efficiency varies largely between that of a porous structure press-fitted into the moderator vessel and one that is brazed to a region of lower temperature.
The former depends on the elastic compressibility of the porous structure. When compressed with too much force, the material could break and accumulate, producing a heterogeneous distribution of solid in the volume. The latter depends on the material and the design of the vessel. Furthermore, if the porous structure is directly connected to the

vessel's walls, only point-contacts would be established. One option for cylindrical cold moderators is the combined casting or sintering of the porous structure with a thin cylindrical shell around it. This shell can then be inserted into the moderator vessel and joined via a thin layer of brazing solder.
Another possibility is the manufacturing of the complete moderator vessel with incorporated porous structure, e. g. by casting metal foam or additive manufacturing. However, sintered materials are known to be difficult to use in high-vacuum applications due to their porous structure and corresponding permeability.
Since foams are usually isotropic, the heat transfer is independent of the direction. The conduction through the solid ligaments of a metal foam can be described by following formula [85]:

$$\lambda_{struts} = (1 - \phi) \cdot \frac{\lambda_{solid}}{3} \tag{4.16}$$

The factor $\frac{1}{3}$ describes the effect of the geometry of the perpendicular solid ligaments in a foam and is also called the tortuosity factor. This is a simplified assumption but valid for randomly distributed porous structures. ϕ describes the porosity of the foam structure and can be calculated from the fraction of the volume of the cavities inside the foam and the total volume. λ_{solid} is the thermal conductivity of the foam's base material, e. g. an aluminium alloy.
In contrast, heat transfer in fibre structures is anisotropic and dependent on the orientation of the fibres in the structure, with higher thermal conductivity in direction of the fibres than perpendicular to it. According to [83], the thermal conductivity in fibre direction is at least two times higher than in normal direction.
The heat transfer in porous cellular structures made by additive manufacturing is dependent on the design of the structure and can be adjusted to the needs of the application. Whether or not the structure shows isotropic or anisotropic behavior depends on the uniformity and periodicity of the grid design. The options offered by the use of AM are mainly limited by technical feasibility, e. g. minimum thickness of the struts.
To describe the effective thermal conductivity of a compound of a metal foam and a molecular solid like methane, one approach is using Bhattacharya's law [86]:

$$\lambda_{eff} = f_A \cdot (\phi \cdot \lambda_{CH_4} + (1 - \phi) \cdot \lambda_{struts}) + \frac{1 - f_A}{\frac{\phi}{\lambda_{CH_4}} + \frac{1-\phi}{\lambda_{struts}}} \tag{4.17}$$

with a correlation factor f_A, which changes with the selection of materials and the type of solid structure (e. g. smaller values for higher porosities). Although the values for f_A in the mentioned publication are only listed for compounds of aluminum and air, water and paraffin wax, they are used here as a first estimation. Exact values for the combination *aluminum – solid methane* have to be examined experimentally. Furthermore, the correlation factor for combinations with aluminum seems to be dependent on porosity rather than fluid density.
It is apparent from equation 4.9 that the foam material has to have a large thermal conductivity to increase the overall thermal conductivity of the compound, especially if the porosity is high (e. g. $\phi > 90\%$). Even a relatively pure aluminium alloy like Al-1100 with at least 99.0% of Al results in a maximum thermal conductivity of around 5 $\frac{\mathrm{W}}{\mathrm{m \cdot K}}$ between 5 K and 20 K. Still, this value is higher by a factor of 4.5 compared to solid methane alone and would therefore largely increase the homogeneity of the temperature profile inside the frozen methane.

4.4.3 Preliminary calculations

To assess the influence of a porous aluminium structure inserted into the cold moderator, preliminary thermal and nuclear simulations are performed using ANSYS Workbench and MCNP6.1, respectively. The input and results of these simulations are presented in the following paragraphs.

Thermal transport simulations:
The porous aluminum structure with different porosity inside the cold moderator is modeled by defining new materials in the ANSYS Workbench engineering database. The density ρ, specific heat capacity c_p and thermal conductivity λ_{th} are calculated for different porosities from the values for the respective aluminum alloy and solid methane. The first two factors are determined by adding the partial quantities of the two materials. The thermal conductivity is calculated according to Equation 4.17. Figure 4.21 shows the thermal conductivity of solid methane, aluminum alloy 1100 and the resulting conductivities for the different porosities 95%, 90% and 80%, with correlation factors of $f_A = 0.23$, $f_A = 0.31$ and $f_A = 0.71$, respectively. The correlation factors are interpolated from the values for aluminum and wax given in [86].

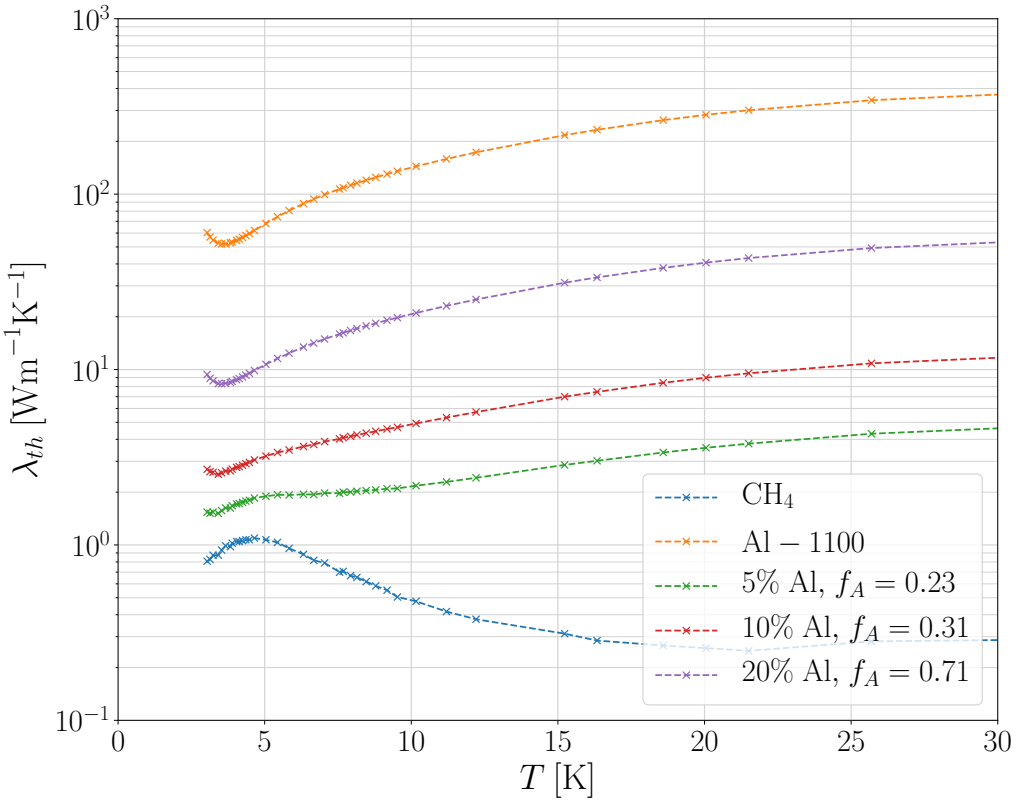

Figure 4.21: Thermal conductivity for CH_4, aluminum alloy 1100 and corresponding effective thermal conductivities for compounds with porosities of 95%, 90% and 80% and correlation factors of 0.23, 0.31 and 0.71, respectively (values extrapolated from [86]).

To study the impact of various porosities on the resulting temperature profile inside the cold moderator, the material-dependent heat load per unit mass (W/g) or volume (W/mm^3) for solid methane and aluminum determined with MCNP6.1 (see subsection 4.3.2) are used. Table 4.8 shows the maximum core temperatures obtained in such simulations for different Al alloys and cold moderator diameters for a constant heat sink temperature of 5 K.

Table 4.8: Maximum temperature increase $\Delta T = T_{max} - T_{He}$ in [K] in a cylindrical cold moderator ($d_{mod} = 2$ cm and $d_{mod} = 4$ cm) filled with different amounts of aluminum (alloys) ranging from 0% to 20%, homogeneously dispersed, for a proton beam energy of 70 MeV and a current of 89.3 mA.

		Ratio of aluminum in cold moderator $1 - \phi$			
Material	d_{mod} [cm]	0%	5%	10%	20%
Al-1100	2	7.6	3.7	2.8	2.2
	4	47.3	9.1	6.3	4.4
Al-6063	2	7.6	4.2	3.2	2.3
	4	47.3	11.3	7.4	4.8
Al-5083	2	7.6	6.5	5.6	3.8
	4	47.3	27.6	20.2	9.9

The FEA results indicate that for $d_{mod} = 2$ cm, an aluminum structure with a high porosity and a thermal conductivity like that of Al-6063 ($\lambda_{th,6063} \approx 200$ W $\cdot$ m^{-1} $\cdot$ K^{-1} at room temperature) can already sufficiently reduce the core temperature. For the $d_{mod} = 4$ cm cold moderator, a porosity of at least 80% should be chosen with alloy 6063 to avoid an increase at the core of more than $\Delta T = 5$ K. However, the results are only valid for an extremely simplified case: only heating by nuclear energy deposition is considered and the contact conditions between the different components and the cooling efficiency are assumed ideal. Therefore, the actual temperatures will be even higher and with increasing moderator volume purer aluminum alloys or lower porosities should be chosen.

Nuclear transport simulations:
To assess the influence of different amounts of aluminum in the moderator on the cold neutron intensity at the exit of the extraction channel, Monte Carlo simulations were performed for the four different porosities mentioned in Table 4.8. The input geometry is shown in Figure 4.22 and consists of a reflector and thermal moderator block with a square cross section. The cold moderator is once again positioned at the center of an extraction channel that runs along the diagonal of the reflector and thermal moderator. It has a length of 3 cm and a diameter of $d_{mod} = 2$ cm as chosen from subsection 3.3.3. The target is located above the reflector and has a square cross section as well.
Tallies are generated on both sides at the front surface of the cold moderator (3 and 4), at the interface of thermal moderator and reflector (2 and 5) and at the reflector exits (1 and 6). For each of the surfaces, tallies with $d = 1$ cm, $d = 2$ cm and $d = 3$ cm are specified. They are designated by the third digit (example: a tally with $d = 2$ cm at position 4 is designated as surface 4020). This allows a more realistic assessment of the cold moderator's performance, since most neutron guides have entrances smaller than the size of the extraction channel.
To realize a mixture of solid methane and aluminum, a new material is defined in the MCNP6.1 input. It is a compound of solid methane at $T = 22$ K and pure aluminum (Al-27) at $T = 20$ K, homogeneously distributed throughout the cold moderator volume. The difference in temperature for the materials is a product of the availability of thermal scattering cross sections. Since no significant difference between the lower temperature kernels and the 22 K kernel for solid methane was found in subsection 3.3.3, the 22 K kernel was chosen.
The peak brightness of the four different porosities is compared at the viewed cold modera-

tor surface ($A_{CM} = 4020$) and at the exit of the reflector ($A_{Ex,ref} = 6020$) (see Figure 4.23). Intensities are presented for an angle range of 0° to ±4.9°. The reduction in peak brightness at the cold moderator surface (4020.2) from $\phi = 100\%$ to $\phi = 80\%$ is only around 10% at the position of the maximum (≈ 3 meV), but rises to approximately 40% at the exit of the reflector (6020.2). However, these large differences are only present for single energy bins and the reduction in integrated neutron brightness between 1 meV and 100 meV for decreasing CH_4 content is negligible. Below neutron energies of $E_n = 1$ meV, the results indicate a larger impact of the aluminum content on the resulting peak brightness.

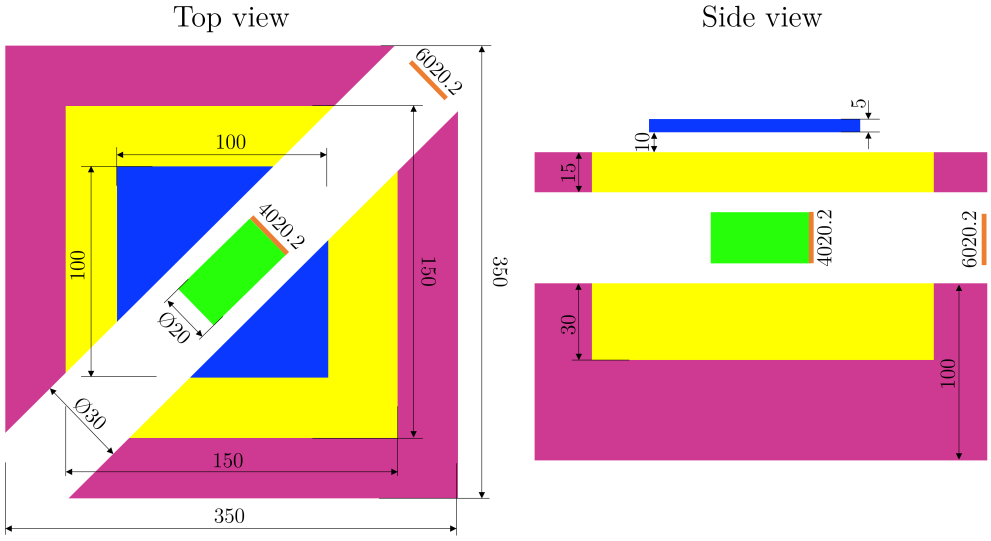

Figure 4.22: Geometry of the rectangular setup for MCNP6.1 simulations ("sandwich" structure). The setup again consists of a tantalum target (dark blue), a lead reflector (purple), a thermal moderator (yellow) and a cold moderator (green).

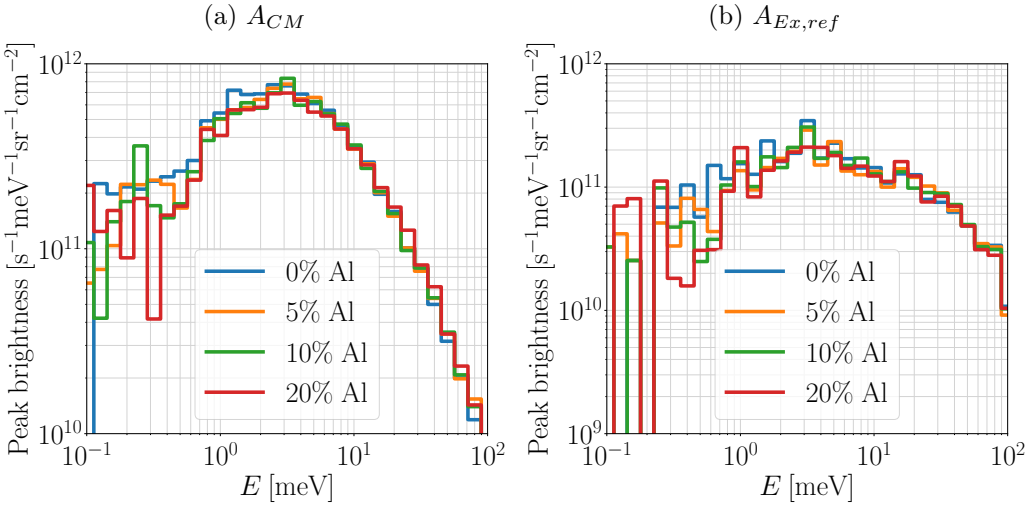

Figure 4.23: Peak brightness of a solid methane moderator at $T = 22$ K, with different amounts of aluminum homogeneously dispersed along its volume. CH_4 ratios range from 100% to 80%. Left: cold moderator front surface (4020). Right: exit of extraction channel at reflector edge (6020).

4.5 Structural analysis & design

To ensure a reliable and safe operation of the cryogenic system and its control infrastructure, the components under pressure have to be designed according to common practice standards. Furthermore, stresses and deformations introduced by cryogenic temperatures have to be considered and measures taken to ensure that the moderator vessel is in an acceptable position during operation.
As a reference for the structural analysis, the nuclear design code RCC-MRx [87] is applied, which has also been used in the design of mechanical components of the European Spallation Source. Apart from giving general design rules for pressure vessels and other components in a nuclear reactor, it allows the consideration of nuclear radiation on the performance and lifetime of the structural materials. Such a consideration is especially important for the components positioned close to the neutron target in a Hi-CANS. A similar technical code issued by the German KTA (Kerntechnischer Ausschuss, engl.: nuclear committee) will expire by 2027.
The prototype cold moderator cryostat, as a key component of the TMR unit, is classified according to safety class N2Rx, which is the second highest safety standard given in the RCC-MRx. Class N1Rx does not apply to Hi-CANS, since no critical event can occur due to the absence of fissionable material and low amounts of decay heat. However, the moderator cryostat is regarded as a radioactive component, which should be confined. Additionally, safety level A is chosen, which aims to protect the component against excessive and progressive deformation, plastic and elastic instability, fracture and fatigue. The categories of operation are SF1 (normal operation), SF2 (normal operating incidents, e. g. cool down or warm-up) and SF3 (emergency conditions). Related criteria are presented in subsection 4.5.1.
For a concise assessment of the structural stability of the different components under internal or external pressure, the module "Static Structural" in ANSYS Workbench 19 was used. It allows the calculation of stresses and deformations inside the materials based on previously defined loads (pressure, pretension) and constraints (e. g. fixed connections). Regions of interest in the cryostat are

- the vacuum recipient under external pressure due to the difference between atmospheric and vacuum pressure
- the moderator vessel with its fluid-carrying sections either under internal or external pressure
- deformations of the tubing due to thermal contraction and resulting stresses and
- stability of the custom bolted flange connections to enable the exchange of crucial components (e. g. the moderator vessel)

The effect of internal pressure on the tubes is not part of the analysis, since their wall thicknesses are oversized for the present pressure levels due to the application of commercially available products.
To make sure that the above components of the cryostat assembly can withstand the applied loading conditions, the critical regions (e. g. sharp edges and welding seams) are examined and compared to maximum allowable values defined by the RCC-MRx.

4.5.1 Geometry, structural materials and design criteria

The geometries under investigation include the vacuum recipient (see Figure 4.24, top) surrounding the inner tubing and cold moderator vessel and the cold moderator vessel itself (see Figure 4.24, bottom).

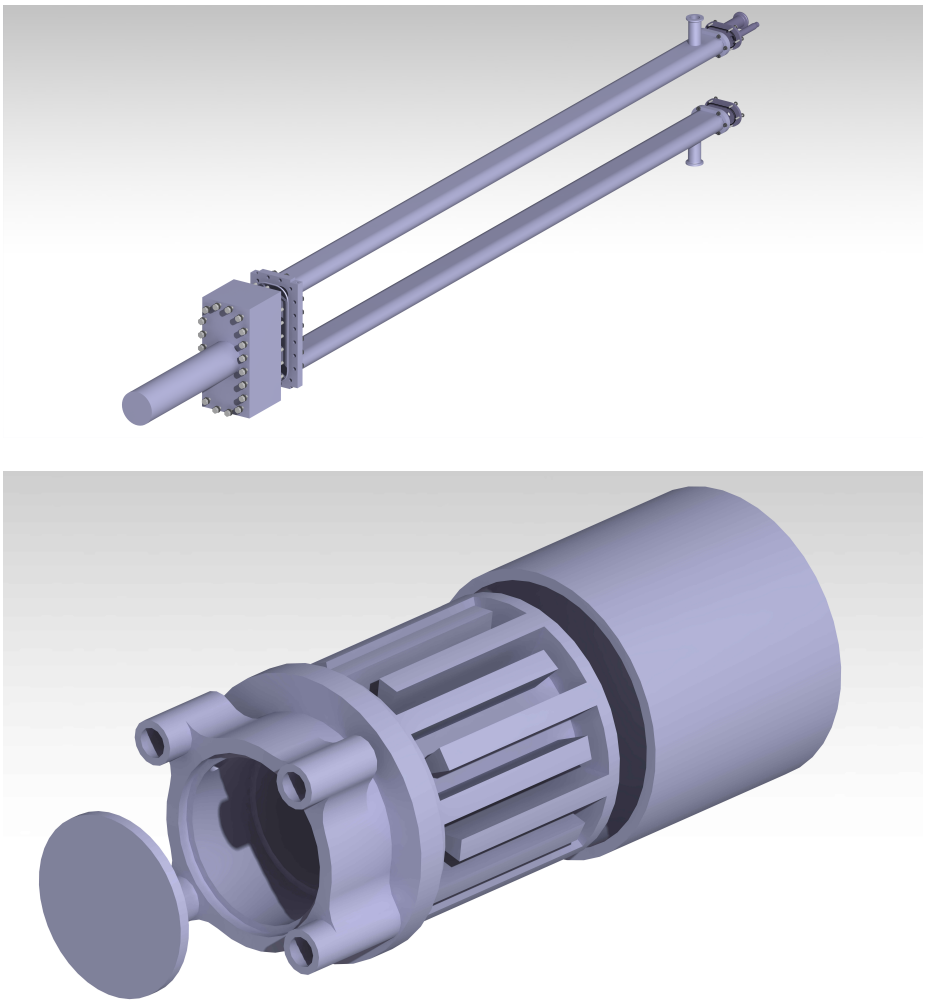

Figure 4.24: Exploded view of the vacuum recipient (top) and cold moderator vessel with lid and shell (bottom).

The cooling structure is milled into the base body and is enclosed by a cylindrical shell. The cylindrical void for condensing the cold moderator is sealed by a 1.5 mm thick circular plate. Both the shell and the lid are connected to the cold moderator's base body via electron beam welding. These connections can be regarded as critical areas with regards to mechanical stability. To obtain a conservative result for the locations of the EB welding seams, the overlapping surfaces of the components that are not merged are designed as small gaps (see Figure 4.25). This way, the full load is applied to the EB weld. Furthermore, the design process and verification of custom bolted and sealed flange connections for opening and closing the vacuum recipient are presented.
The base materials for most of the components under investigation are various aluminum alloys. Its low neutron scattering and absorption cross sections ($\sigma_s = 1.503$ b, $\sigma_a = 0.231$ b [42]) compared to other commonly used structural materials, its relatively high yield strength (up to around $R_{p0.2} = 230$ MPa, depending on the type of alloy) and its good characteristics for the use at cryogenic temperatures make aluminum alloys the material of choice for structural components used in research reactors and accelerator-driven neutron sources [88]. Especially in the region close to the neutron target, where the cold moderator vessel is positioned, only aluminum-based metals should be used to avoid the production of long-lived radioactive isotopes, for example ^{60}Co and ^{55}Fe, typically generated in stainless steel [89]. At further distances and if not directly in the trajectory of neutrons of interest, other non-ferrous or ferrous metals can be an alternative. This is valid for the conditions,

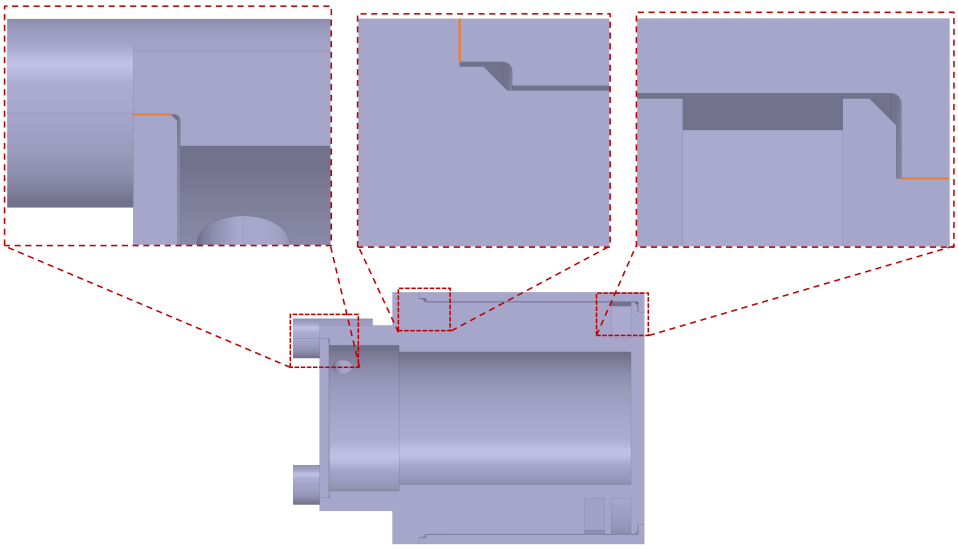

Figure 4.25: Construction of the EB welding seams (marked as orange lines).

under which the prototype cryostat is operated, but has to be investigated in more detail for a cryostat used at the full power HBS.
The RCC-MRx code gives mechanical properties for alloys 5754-O and 6061-T6. They represent lower and upper limits, respectively, with Al 5754-O as a relatively weak and Al 6061-T6 as a strong alloy of the 5000 and 6000 groups. Therefore, the choice of the former's properties is a conservative assumption. The moderator vessel, however, is manufactured solely from alloy 5083-O (AlMg4.5Mn). It can be ranked in between the two mentioned alloys with regards to mechanical properties. Values of the yield strength $R_{p0.2\%}$, ultimate tensile strength R_m and allowable stress S_m in the base material are given in Table 4.9 for the two mentioned alloys from RCC-MRx and some additional alloys used in the manufacturing process in the context of this thesis. To obtain the allowable stresses, values from [90] are divided by a factor of 1.3 to get comparable minimum values. Subsequently, S_m is determined by taking the minimum value of $R_{p0.2} \cdot (2/3)$ and $R_m \cdot (1/3)$.

Table 4.9: Yield strength, ultimate tensile strength and allowable stress in the base material according for aluminum alloys 5754-O and 6061-T6 (values taken from [87]) and derived values for 5083-O, 6060-T66 and 6063-T6.

Strength value	5754-O	6061-T6	5083-O	6063-T6
$(R_{p0.2})_{min}$ [MPa]	80	230	118	214
$(R_m)_{min}$ [MPa]	180	260	223	241
S_m [MPa]	53	87	74	62

When assessing welding seams, the allowable stress is further reduced, depending on the possibility of inspection. For alloy 6061-T6, the effects of thermal curing are destroyed by heating the material during the welding process. Therefore, the strength of the material at a welding location is further reduced to 55.0 MPa (according to Table A9.J2A.43 of the RCC-MRx). For alloy 5754-O, such a value is missing, since it is a non-heat-treatable alloy and its strength is not reduced by the welding process. Since the surfaces of the welding seams were mainly inspected from one side after the welding process, a joint coefficient of $n = 0.5$ has to be included according to Table RB 3291.1. This further reduces $S_{M,weld}$ to 26.5 MPa. However, if higher allowable stresses are required, the moderator vessel could potentially be examined using a CT machine. This would increase the allowable stress to

53.0 MPa and 55.0 MPa for alloy 5083 and 6061, respectively, since the welding seam can be examined more precisely, which reduces the required safety factor.
In the case of non-negligible irradiation, the allowable elastic membrane and total stresses S_{em} and S_{et}, respectively, are applied. The magnitude of these values depends on the temperature, the thermal neutron flux and the corresponding criteria level. Table 4.10 gives the values for alloy 5754-O and 6061-T6 for levels A and C.

Table 4.10: Allowable stress in the welding seams as well as the allowable elastic membrane and total stress for irradiation of aluminum alloy 5754-O and 6061-T6 (values taken and derived from [87]) for levels A and C.

Stress value	Level A		Level C	
Alloy	5754-O	6061-T6	5754-O	6061-T6
$S_{m,weld}$ [MPa]	26.5	27.5	39.8	41.3
S_{em} [MPa]	614	328	767	410
S_{et} [MPa]	1046	701	1307	876

According to the RCC-MRx, there are several categories associated with different operating conditions. Normal operation, start-up and shutdown fall under the 1st and 2nd category, while emergencies and highly improbable events are covered by categories 3 and 4, respectively. For each of those categories, different criteria levels are defined, which cover different types of damages. Criteria level A (necessary for the 1st and 2nd category) includes type P and type S damages. Type P damages are those which "can result from the application to a structure of a steadily and regularly increasing loading or a constant loading", while type S damages "can result from repeated application of loadings" [87].
The definition of the criteria depends on whether creep or radiation are present. Since creep (as well as thermal aging) is negligible for temperatures below $T = 50$ °C (aluminum alloy 5754-O) and $T = 75$ °C (aluminum alloy 6061-T6) according to sections A3.1A.311 and A3.2A.311 of the RCC-MRx, respectively, and the maximum temperature of the moderator vessel is approximately $T_{max} = 300$ K, it is not considered in the present work. Therefore, this value also acts as a maximum allowable temperature for the cylindrical vacuum jacket around the cold moderator vessel.
When examining the effects of nuclear irradiation on aluminum and its alloys, the thermal neutron flux plays a significant role due to transmutation events from ^{27}Al to ^{28}Si and the formation of Mg_2Si precipitates. These mutations in the material are the main reason for mechanical property changes [87].
Annexes A3.1A (for alloy EN AW-5754-O) and A3.2A (for alloy EN AW-6061-T6) of the RCC-MRx can also be used to determine the effects of the thermal neutron flux. Although mainly other alloys of the 5000 and 6000 series are used in the present setup, the values presented in RCC-MRx serve as a first estimate. However, for the full power HBS facility, the materials should either be used according to the nuclear code or investigated individually. Figure 4.26 shows the negligible and maximum allowable irradiation curves for the two alloys in dependence of time-integrated thermal neutron flux. Here, the curves are only plotted above temperatures of approximately 20 °C (Al 6061-T6) and 50 °C (Al 5754-O). Therefore, they exclusively serve as reference values and no information on the development towards cryogenic temperatures is known. The difference in the maximum allowable irradiation for the two alloys results from the higher magnitude of embrittlement due to the formation of Mg_2Si precipitates caused by thermal neutrons in the 5000 series alloys [91].
The thermal neutron flux in a PE moderator for a full power HBS target station is approximately 3.4×10^{14} $n_{th}/(cm^2 \cdot s)$. Integrated over a whole year, this value yields approximately 10.7×10^{21} n_{th}/cm^2, which lies below the limit for non-negligible irradiation for both alloys at the lowest available temperature. If Al 5754-O is taken as a conservative estimation,

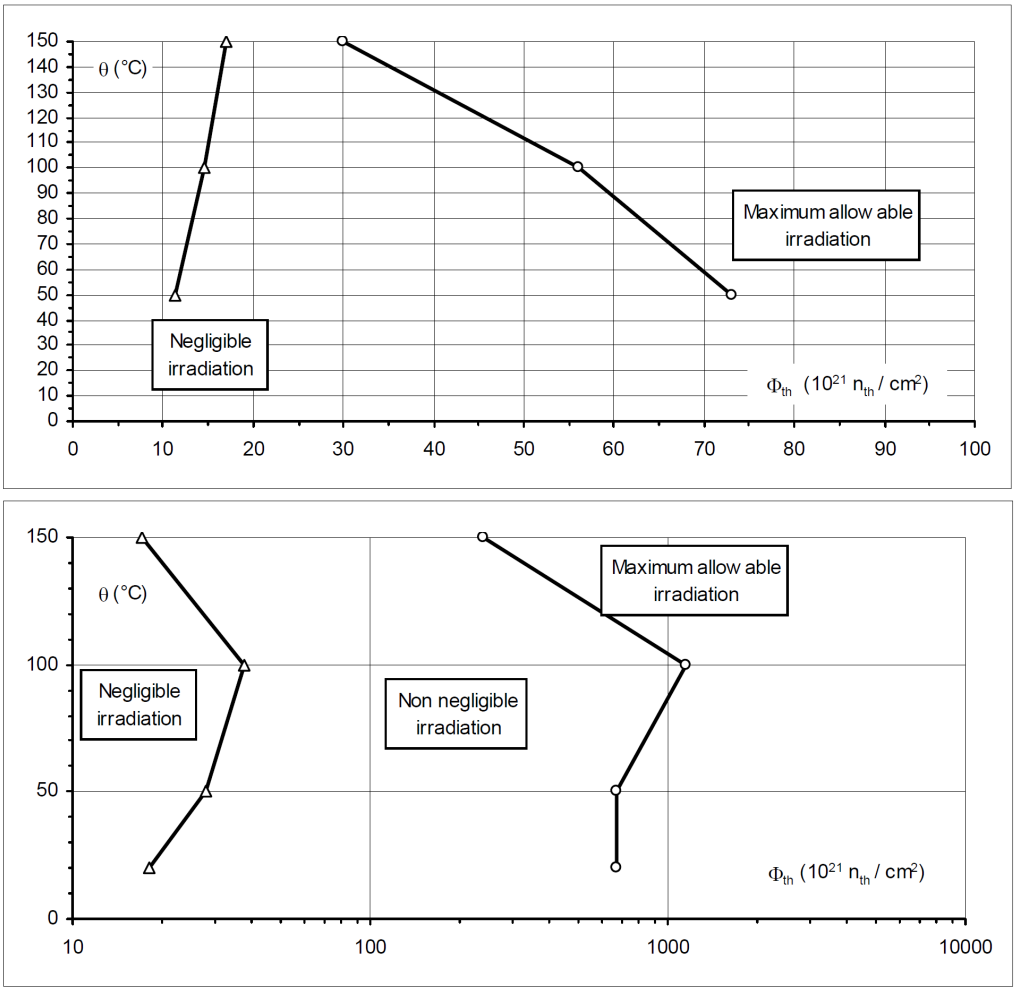

Figure 4.26: Negligible and maximum allowable irradiation fluence with thermal neutrons (E_{th} = 25.4 meV) Φ_{th} in [10^{21} n_{th}/cm^2] for the aluminum alloys EN AW-5754-O (top) and EN AW-6061-T6 (bottom) in dependence of temperature Θ in [°C] (figures taken from [87]).

the components of the cryogenic system can be used for approximately seven years before the maximum allowable irradiation is reached.
However, these values are only rough estimates and are by no means suitable for a reliable assessment of the lifetime of the cryogenic components in the present system. Since the curve for negligible irradiation for Al 5754-O progresses towards lower values with decreasing temperature, the criteria for non-negligible irradiation are considered here as well.

Criteria:
Pressure vessels: For negligible irradiation, type P damages can be avoided by satisfying the following criteria when designing a pressure vessel:

$$1.\ \overline{P_m} \leq S_m$$

$$2.\ \overline{P_L} \leq 1.5 \cdot S_m$$

$$3.\ \overline{P_L + P_b} \leq 1.5 \cdot S_m$$

with the primary membrane stress $\overline{P_m}$, the local primary membrane stress $\overline{P_L}$ and the primary bending stress $\overline{P_b}$.
If irradiation can not be neglected, the criteria for elastic analysis are following:

1. $\overline{P_m + Q_m} \leq S^A_{em}(T, \phi_{th})$

2. $\overline{P_L + P_b + Q + F} \leq S^A_{et}(T, \phi_{th})$

with the secondary equivalent stress $\overline{Q_m}$ and the peak stress $\overline{F}$.

Type S damages can be prevented by complying with following criteria for

1. Progressive deformation: $\max(\overline{P_L + P_b}) + \overline{\Delta Q} \leq 3 \cdot S_m$

2. Fatigue damage: $V_A(\overline{\Delta\epsilon}) < 1$

with the secondary stress range $\overline{\Delta Q}$ and the fatigue usage fraction V_A depending on the strain ranges $\overline{\Delta\epsilon}$.
Due to the complexity of the moderator vessel, a distinction between the general membrane stress $\overline{P_m}$ and the local membrane stress $\overline{P_L}$ is not possible. Therefore, the general membrane stress is replaced by the local membrane stress as a conservative assumption.

Bolted assemblies: There are several rules given in the RCC-MRx for the use of bolted connections. The rules for the screw core are the following:

1. $\overline{(\sigma_m)}_{fictitious} \leq S_{mB}$

2. Limitation of the mean stress: $\overline{\sigma_m} \leq 2 \cdot S_{mB}$

3. Limitation of the maximum stress: $\overline{\sigma_m + \sigma_b} \leq 3 \cdot S_{mB}$

S_{mB} is the allowable stress of the bolt, with a value of 213.3 MPa ($1/3 \cdot 640$ MPa for a strength class 8.8 steel bolt. The fictitious stress intensity $\overline{(\sigma_m)}_{fictitious}$ is defined as the maximum of either the stress resulting from the load required to crush the joint or the stress resulting from the sum of the pressure acting on the junction and the load required to maintain contact pressure on the joint. $\overline{\sigma_m}$ is the mean stress intensity in the screw core, while $\overline{\sigma_m + \sigma_b}$ is the maximum stress in the periphery of the screw core.

4.5.2 Design parameters and loading conditions

The pressures inside the moderator and coolant sections for the different phases are listed in Table 4.11. The operating pressure of the moderator is set to $p_{op} = 1$ bar(g) to ensure the pressure to stay above ambient pressure during liquefaction to avoid the inflow and condensation of ambient air. The operating pressure for the helium coolant is chosen well below the design pressure (relief pressure of the safety valve of the helium dewar), which is at $p_d = 1.5$ bar(g). The test pressures are determined by multiplying the design pressure with a safety factor of 1.43. This factor stems from the demand of a safety factor of 1.05 during testing compared to a safety factor of 1.5 during operation (safety factor for normal operation/safety factor during testing = 1.5/1.05 = 1.43). To assess the maximum loads

Table 4.11: Operating pressures, test pressures and relief pressures of the safety valves for the moderator and coolant sections.

Section	Moderator	Coolant
Operating pressure p_{op} in bar(g)	1.0	0.5
Design pressure p_d in bar(g)	1.5	1.0
Test pressure p_{test} in bar(g)	2.1	1.4

on the different components under investigation, the loading conditions of the system are presented below. Figure 4.27 shows the temperature and pressure curves for the different

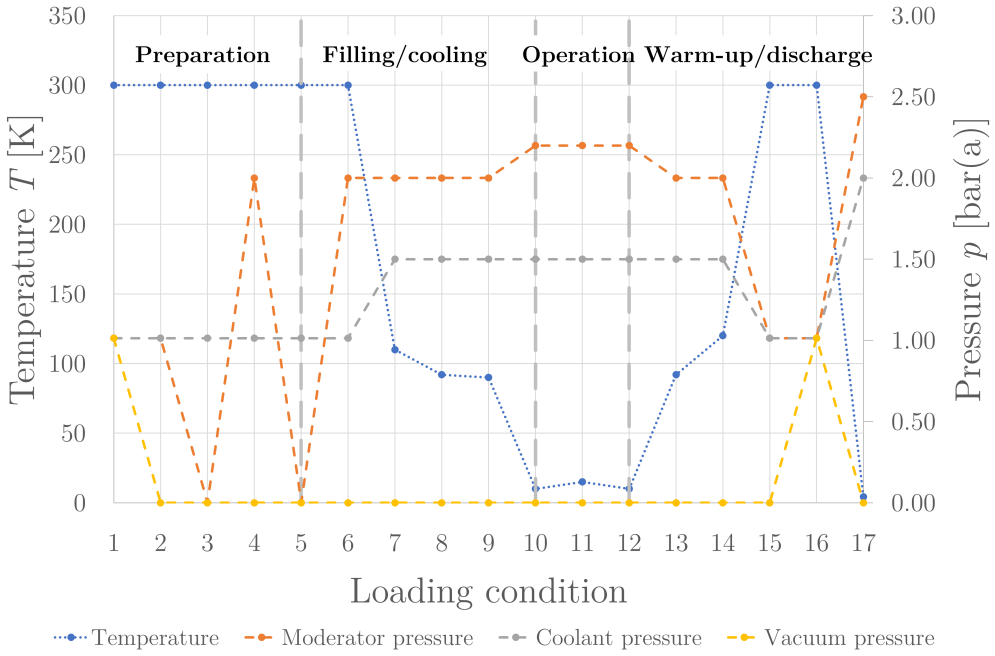

Figure 4.27: Loading conditions during operation for the cold moderator cryostat including cool-down, beam operation and warm-up. At step 17, the design conditions with highest pressures and lowest temperature are considered.

steps of operation, which are also described briefly in the following paragraphs.

1. **Preparation:** The temperature is at room temperature for all steps.
   - **#1:** All pressures are at ambient pressure. There is no load.
   - **#2:** The vacuum recipient is evacuated to a high vacuum pressure of approximately $p_{vac} = 1 \cdot 10^{-4}$ mbar.
   - **#3:** The moderator tubes and cavity are evacuated to a rough pressure of some mbar. The pressure in the coolant tubes and section of the moderator vessel is still at ambient pressure.
   - **#4:** The moderator tubes and cavity are purged with N_2 at $p = 2.0$ bar(a).
   - **#5:** The moderator tubes and cavity are evacuated again to a few mbar to get rid of residual gases.
2. **Filling/cooling:**
   - **#6:** The moderator tubes and vessel cavity are filled with methane (CH_4) gas to a pressure of $p = 2.0$ bar(a).
   - **#7:** The pressure in the helium tubes and vessel section rises to $p = 1.5$ bar(a) due to the onset of liquid helium flow. The temperature inside the moderator vessel drops to $T = 120$ K (liquefaction temperature of methane at $p = 2.0$ bar(a)).
   - **#8:** The temperature drops to 92 K and the liquid methane is sub-cooled. The pressures do not change (except for short deviations due to the cooling).
   - **#9:** The temperature is lowered to 90 K to freeze the methane in the vessel cavity.

- **#10:** The solid methane is cooled down to a minimum temperature of approximately 10 K. The pressure in the methane tubes and vessel rises to $p = 2.2$ bar(a), the setpoint of the proportional valve, due to the evaporation of small amounts of methane in the tubes.

3. **Operation:** The pressures stay almost constant during operation.

   - **#11:** The temperature of the methane rises by a few K due to energy deposition during pulsed beam operation.
   - **#12:** After each pulse, the temperature drops again to its intended minimum temperature due to the LHe cooling.

4. **Warm-up/discharge:**

   - **#13:** The temperature is increased to $T = 92$ K to melt the frozen CH_4. The pressure in the methane tubes and vessel cavity drops to $p = 2.0$ bar(a) as soon as the methane at the inlet and outlet of the vessel is liquid.
   - **#14:** The temperature increases to $T = 120$ K while the CH_4 evaporates.
   - **#15:** The helium cooling is stopped and the gas inside the tubes and moderator vessel is discharged to the vent or helium re-liquefaction line. The pressures drop to ambient pressure and the temperature increases to room temperature.
   - **#16:** The vacuum recipient is vented and the pressure inside rises to ambient pressure. The system is again at its initial state.

5. **Design conditions:**

   - **#17:** The relief pressures of the safety valves are $p_{Sa,mod} = 2.5$ bar(a) inside the moderator cavity and $p_{Sa,cool} = 2.0$ bar(a) in the cooling channels. The moderator temperature is the lowest achievable temperature of $T_{mod,min} = 5$ K.

The largest load onto the vacuum recipient is the external pressure of $p_{vac,ext} = 1.0$ bar(a) due to its evacuation, which is present for all steps except #1 and #16.
The maximum internal pressures are $p_{i,mod} = 2.5$ bar(a) in the moderator cavity (step #17) and $p_{i,cool} = 2.0$ bar(a) in the helium channels of the cold moderator vessel. These values cause the largest pressure differences to the surrounding vacuum. The maximum pressures onto the moderator cavity of the cold moderator vessel is an external pressure difference of $\Delta p_e = 1.0$ bar caused by an internal pressure $p_i = 1.0$ bar(a) in the cooling channels, which occurs during step #3 and #5. The highest internal pressure difference is $\Delta p_i = 1.0$ bar, caused by the difference between the internal pressure of $p_{i,mod} = 2.0$ bar(a) in the moderator cavity and $p_{i,cool} = 1.0$ bar(a) in the cooling channels (steps #4, #6 – #9, #13, #14). The highest external pressure onto the cooling channels comes from the cold moderator cavity and is $p_e = 1.0$ bar(a) during steps #4 and #6.

4.5.3 Results

Internal and external pressure
Following, the equivalent (von-Mises) stress is presented for the different steps of interest, where conditions of loading occur (all steps except #1 and #16). The vacuum recipient is only regarded once for step #2 (generation of the insulation vacuum). For all other steps during operation the loading condition of the vacuum recipient is assumed to stay the same as for step #2 and only the moderator vessel is considered.

Vacuum recipient: Apart from loading step #1 and #16, the vacuum recipient is in an evacuated state with an internal high vacuum of $p_{vac} \leq 10^{-4}$ mbar. The pressure difference to the ambient surrounding generates an external pressure of approximately $p_e = 1$ bar

onto the outer surfaces of the vacuum recipient during operation.
Due to the large size of the assembly and its symmetric structure, only one fourth of the recipient is regarded as a CAD model for the simulations. This way, the mesh can be refined locally without drastically increasing the required computing power. The whole structure is mounted at the corners of the rectangular plate used to seal the vacuum box enclosing the cold moderator vessel. In the FEA simulation, these points are designed as fixed supports. The metal and elastomer seals are included in the model in their compressed state, but are not considered in the results. They are subject to a more detailed investigation in a following section. The nuts and bolts are omitted, since they have no considerable effect on the problem under consideration and the demountable parts are regarded as one component with joint surfaces.
The global mesh size is set to 1 mm and refined to 0.05 mm at the location of welds and fillets. Figure 4.28 shows the equivalent stress at the fillet of the cylindrical lid near the cold moderator with decreasing element size. It is apparent that the stress converges at around 22.9 MPa. The change from a local mesh size of 0.050 mm to 0.025 mm is only about 0.2%, which is why the former is used for regions of interest.

Figure 4.29 shows the equivalent stress in the cold moderator section and one of the

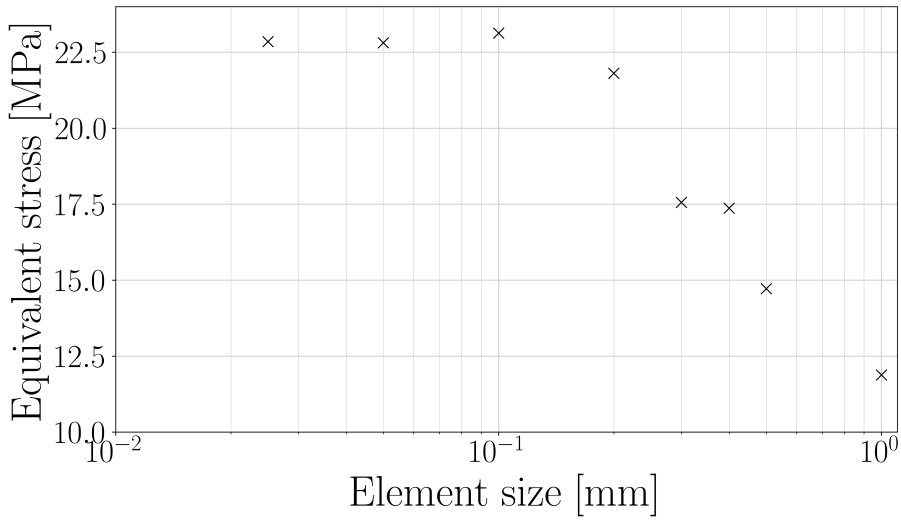

Figure 4.28: Equivalent stress at a fillet of the cylindrical lid vs. element size.

transfer line sections of the vacuum recipient. The highest stress occurs at the interface of the oval pipe and the DN16 flange connector. This stress is partly caused by a larger deformation in the flat section of the oval pipes. However, the magnitude of the stress is additionally increased by the 90° corner between the two components. This discontinuity leads to an increase in stress with decreasing element size, causing the result to not converge to a finite value. To still obtain meaningful results at this location, a stress linearization is performed. For this, a path is generated that runs along the shortest way through the thickness of the oval pipe at that location (see Figure 4.30). The displayed peak stress is higher than in Figure 4.29 because the linearized stress along a path is not averaged in ANSYS Workbench if it is located between two bodies. Therefore, the averaging is performed manually by taking into account the stresses for the different bodies. Along the path, the stress is divided into a constant membrane stress, a linearly varying bending stress and a peak stress. Figure 4.31 shows the membrane stress as well as the sum of membrane and bending stress for the path shown in Figure 4.30. Additionally, the limits defined in subsection 4.5.1 are plotted for comparison.

It is apparent that both the membrane stress as well as the sum of membrane stress and bending stress satisfy the criteria presented in subsection 4.5.1.

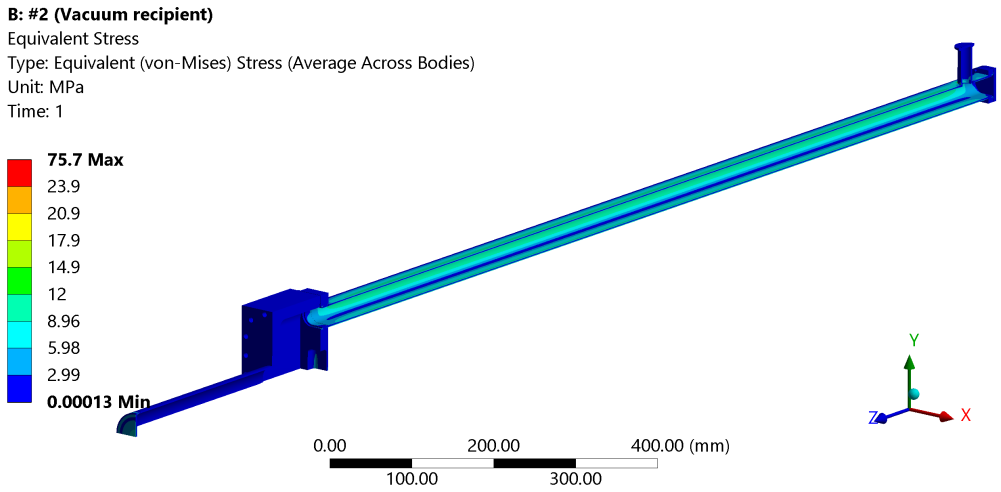

Figure 4.29: Equivalent stresses inside the vacuum recipient's material during loading steps #2 to #15. Model only shows one quarter due to symmetric conditions.

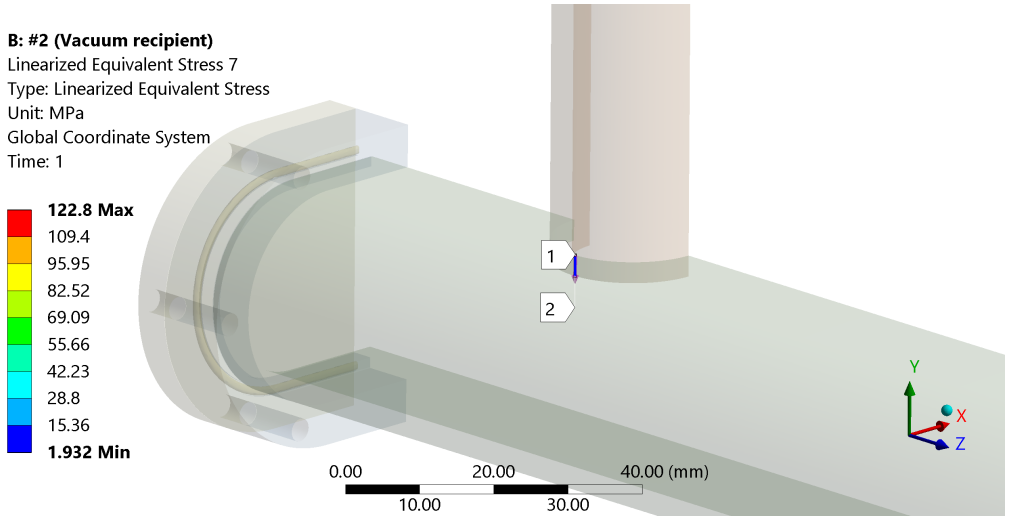

Figure 4.30: Path for stress linearization at the location of highest equivalent stress.

Figure 4.32 shows the stress values compared to the allowable limits for the case of non-negligible irradiation. Here, all values along the linearization path are also well below the allowable limits.
The lower limit of the maximum stress value in Figure 4.29 is set to 26.5 MPa to highlight regions of higher stresses (apart from singularities produced at locations of discontinuities). It is apparent that the equivalent stress at the surfaces of the oval pipe (max. 11.6 MPa) and at the lid of the cylindrical pipe containing the cold moderator vessel (max. 22.9 MPa) are highest. However, the mentioned regions contain no welding connection and are therefore well below the allowable limits ($S_m = 53...87$ MPa).
The secondary stress $\overline{Q}$ inside the vacuum recipient caused by temperature changes during beam operation is negligible, since the recipient is only mounted at the four threads at the corners of the rectangular plate. Apart from that, the recipient has some mm of space to move freely. Therefore, the criterion for the prevention of progressive deformation ($\text{Max}(\overline{P_L + P_b} + \overline{\Delta Q} \leq 3 \cdot S_m)$ is satisfied.
To rule out damage by fatigue, the fatigue usage fraction has to be determined for the

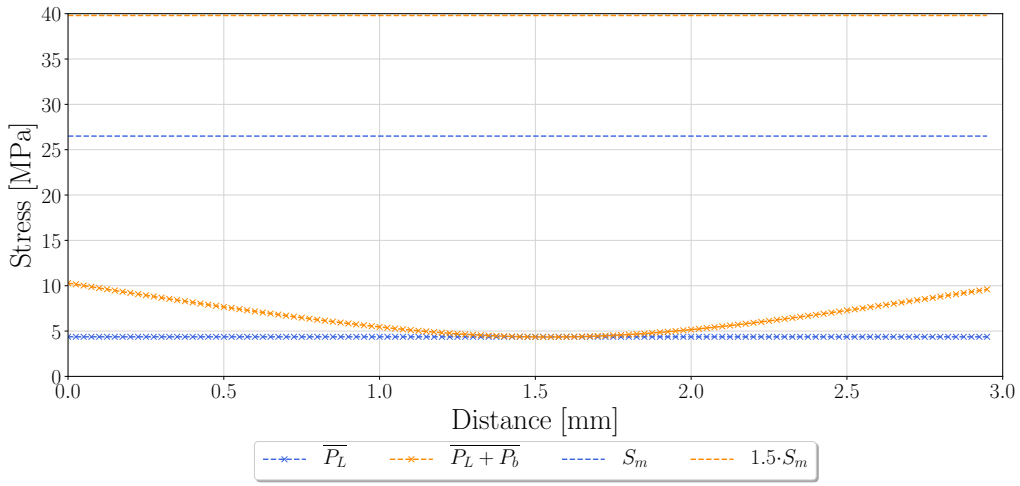

Figure 4.31: Local membrane stress $\overline{P_L}$ and the sum of local membrane and bending stress $\overline{P_L + P_b}$ along the path at the location of highest stress. Allowable stress limits are plotted for comparison.

evacuation step of the vacuum recipient. According to section RB 3261.113 of the RCC-MRx, a fatigue analysis "in zones containing geometrical discontinuities" is only necessary at a distance $d = 0.05$ mm of the discontinuity. For the area of highest stress mentioned above, this means that a total stress of $\overline{\sigma_{tot}} = 44.9$ MPa has to be regarded. Since the stress occurs in a welding zone, it has to be multiplied with an additional fatigue strength reduction factor $f = 4$ for a fillet T-weld, according to Table RB 3292.112 of the RCC-MRx. Therefore, the total stress yields $\overline{\Delta\sigma_{tot}} = 176.6$ MPa.
As a conservative assumption, the allowable strain range $\overline{\Delta\epsilon_t}$ can be determined by using following formula

$$\overline{\Delta\epsilon_t}(\%) = 100 \cdot \frac{2 \cdot (1+\nu)}{3E} \cdot (\overline{\Delta\sigma_{eq,tot}}) + \frac{\overline{\Delta\sigma_{eq,tot}}}{K}^{1/m} \tag{4.18}$$

with Young's modulus $E = 75.1$ GPa and coefficients $K = 613.1$ MPa and $m = 0.0941$ taken from Table A3.2A.46. In zones of discontinuities, the strain range additionally has to be divided by a factor $T = 1.5$. This yields an allowable strain range of $\overline{\epsilon_t} = 0.076\%$. Figure 4.33 shows the fatigue curves, taken from Figure A3.2A.47 in the RCC-MRx, and the above total strain range for a number of cycles $n = 5000$. According to the fatigue curves, a number of $n_{max} = 10^5$ cycles should not be exceeded to still make sure that the fatigue usage fraction $V(\epsilon)$ is not exhausted ($V(\epsilon) = \sum_j \frac{n_j}{N_j} < 1$).

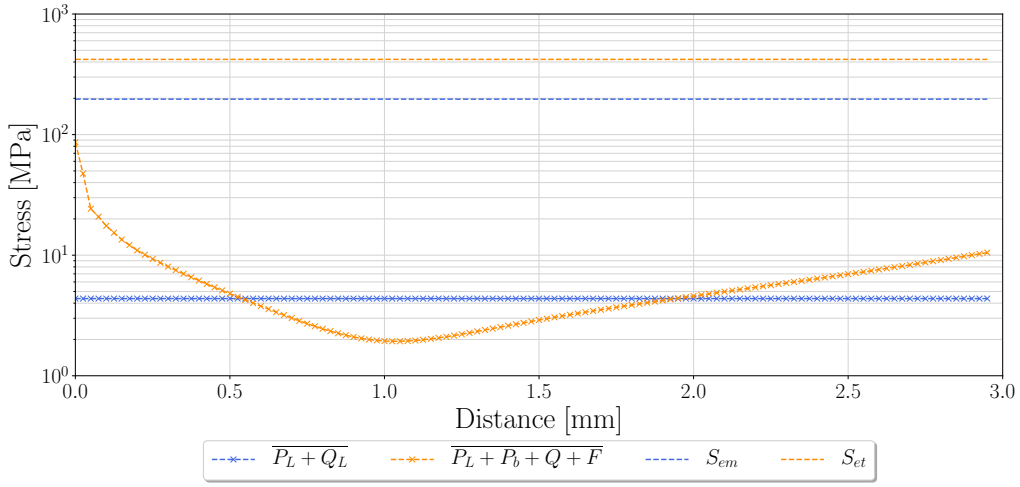

Figure 4.32: Local primary and secondary membrane stress $\overline{P_L + Q_L}$ and the sum of local membrane and bending stress, secondary stress and peak stress $\overline{P_L + P_b + Q + F}$ along the path at the location of highest stress. Allowable stress limits for non-negligible irradiation are plotted for comparison.

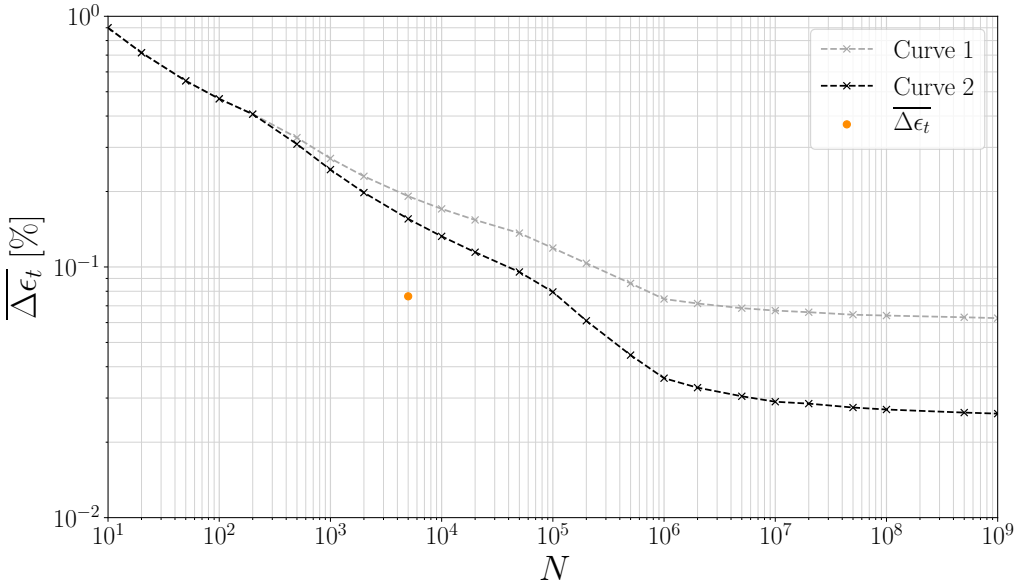

Figure 4.33: Fatigue curves for Al 6061-T6 and the total strain range for a number of 5000 cycles (evacuation/venting).

Moderator vessel: The two separate chambers of the moderator vessel – one for the moderator and one for the coolant medium – result in different pressure differences and therefore loading conditions inside the vessel during operation. There are five different states:

1. During steps #2 and #15, the pressure inside the moderator and coolant cavity is at ambient pressure. Therefore, an internal pressure of $p_i = 1$ bar(a) acts on the walls of the moderator vessel. There is no pressure difference between the moderator cavity and cooling channels.

2. During steps #3 and #5, the moderator volume is evacuated to a pressure of several mbar. Therefore, an external pressure of $p_e = 1$ bar(a) acts on the dividing wall between the moderator cavity and the cooling channels. There is no pressure difference at the front part and back side of the cylindrical moderator volume. An internal pressure of $p_i = 1$ bar(a) is still acting on the shell around the coolant volume.

3. During steps #4 and #6, the pressure inside the cavity for the moderator volume is at $p_{i,mod} = 2$ bar(a), while the coolant pressure is still at ambient. The internal pressure of $p_i = 2$ bar(a) acts on the front part and back of the moderator volume, whereas the pressure difference between the moderator and coolant volume is $\Delta p = 1$ bar. An internal pressure of $p_i = 1$ bar is still acting on the shell around the coolant volume.

4. During steps #7 to #9 and #13 to #14, the moderator pressure is at $p_{mod} = 2$ bar(a) and the coolant pressure is at a maximum of $p_{cool} = 1.5$ bar(a).

5. During steps #10 to #12, the moderator pressure rises to a maximum pressure during normal operation of $p_{i,mod} = 2.2$ bar(a). The pressure inside the helium cooling channels is still at $p_{i,cool} = 1.5$ bar(a).

6. During step #17, which corresponds to the relief pressures of the safety valves, the pressures inside the moderator and coolant volume are $p_{mod} = 2.5$ bar and $p_{cool} = 2.0$ bar, respectively.

Figure 4.34 and Figure 4.35 show the equivalent stresses inside the moderator vessel that are caused by the different loading steps. The results are once again obtained by using a tetrahedral mesh of quadratic order with a global element size of 1.0 mm and a local refinement to 0.050 mm at the locations of fillets and welds.

It is apparent that the highest stress occurs at the welding seam between the cylindrical lid and the base body of the cold moderator vessel. The effect of a further reduction in element size at the location of the fillets is negligible. However, if the mesh is further refined at the locations of the EB welds, the corresponding stresses do not converge but rise with decreasing element size, again due to the presence of geometric discontinuities and the corresponding stress concentrations.

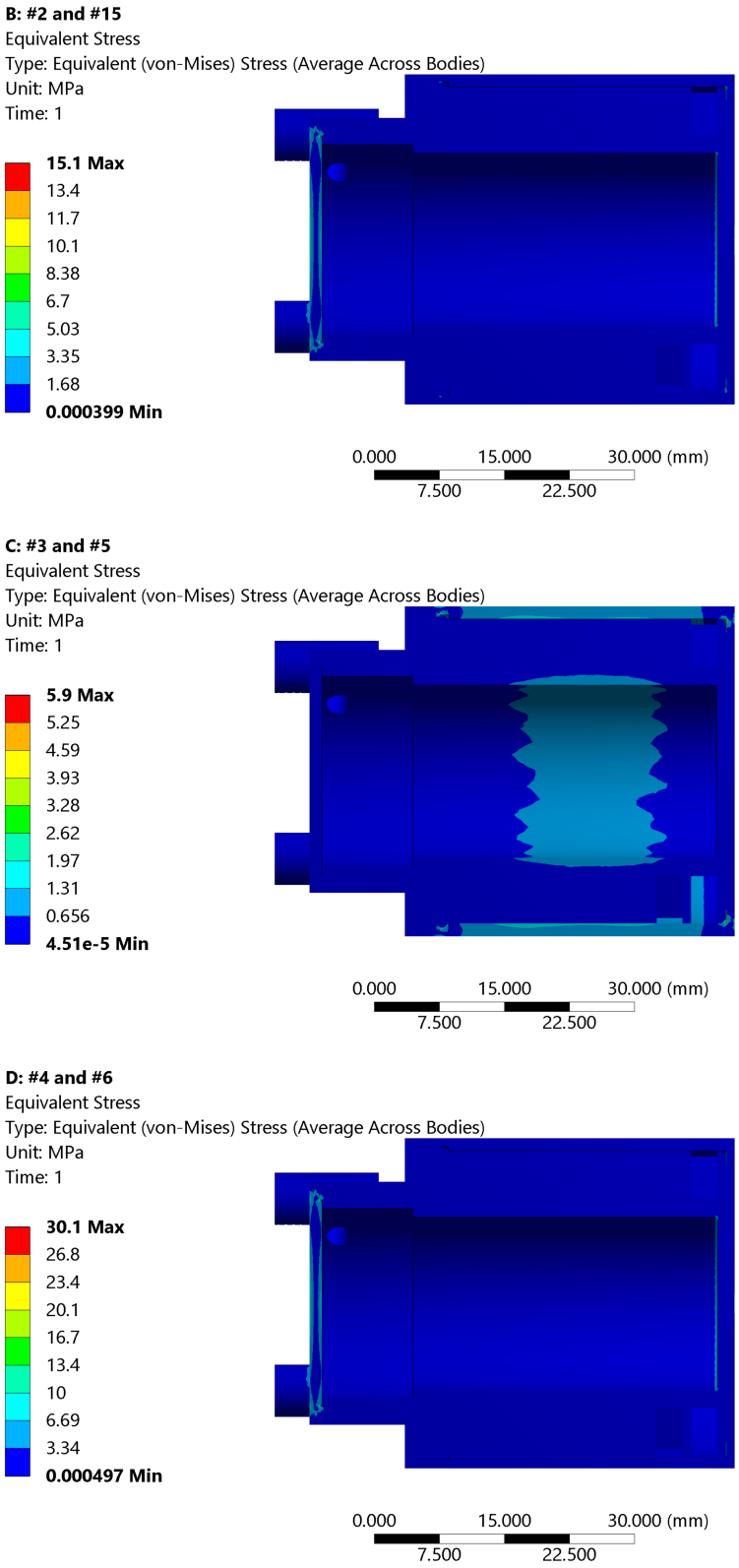

Figure 4.34: Equivalent stress in the cold moderator vessel for the loading steps #2 to #6 and #15.

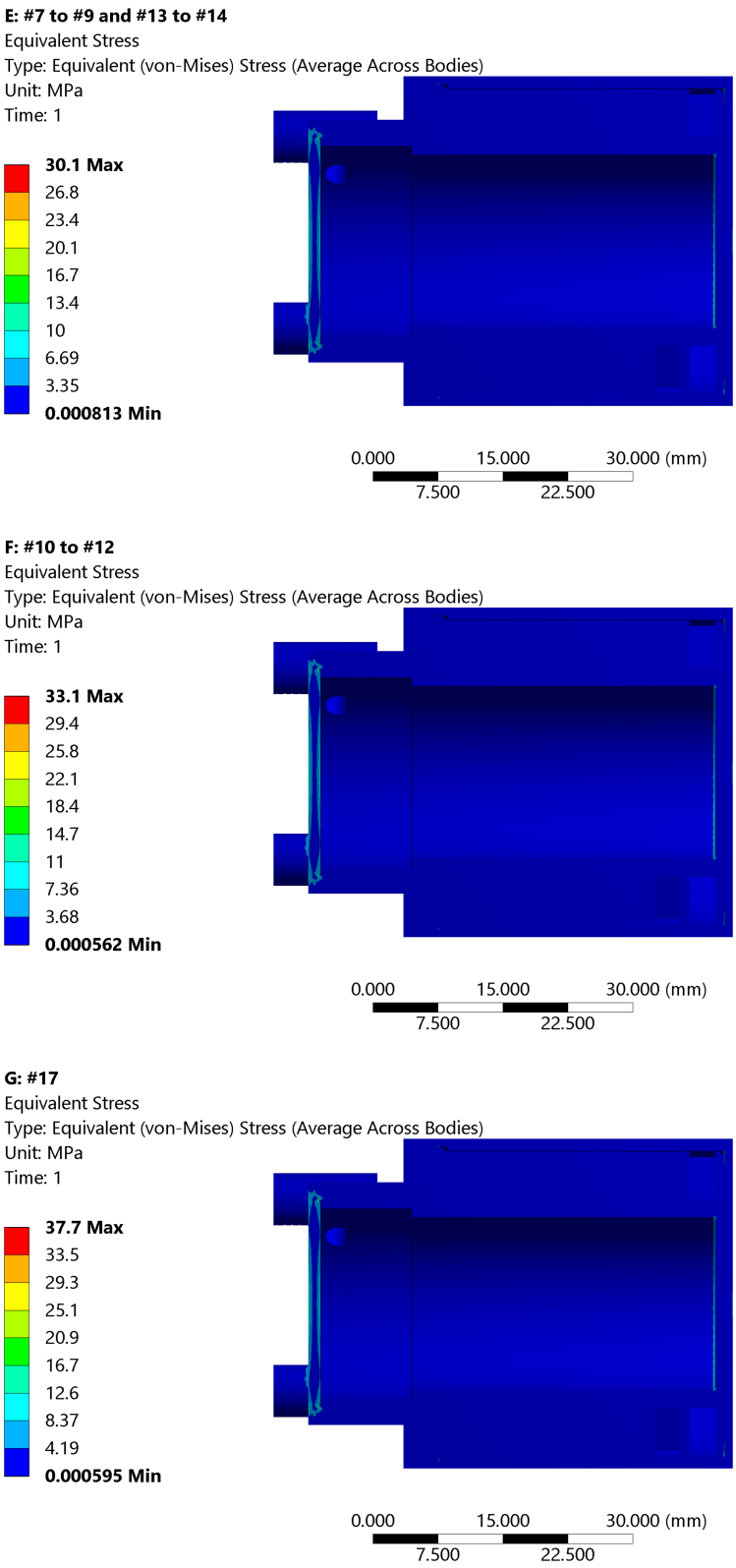

Figure 4.35: Equivalent stress in the cold moderator vessel for the loading steps #7 to #14 and #17.

As for the vacuum recipient, a stress linearization is performed for the different EB welds. Since the pressure differences are highest for step #17, the investigation is presented for this case and it is assumed to be a conservative estimate for the other steps with lower pressure differences. Since the front part of the moderator vessel is not symmetric, the stress linearization is performed at a total of eight points along the circular EB weld (see Figure 4.36).

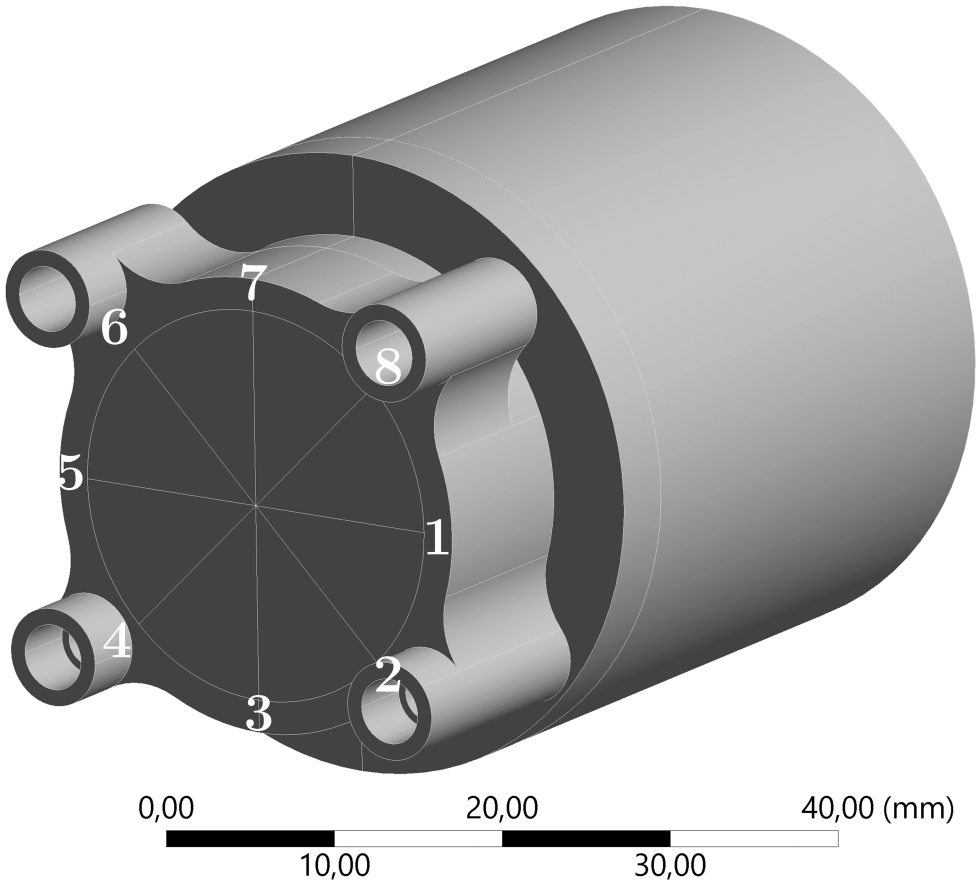

Figure 4.36: Path locations for the stress linearization at the EB weld between the cylindrical lid and the base body of the cold moderator vessel.

The results for the different paths differ only slightly, with the highest values for the membrane stress and the sum of membrane and bending stress at paths 2 and 4. At this location, the base body is reinforced by additional material for the connection of the helium tubes, which increases the stiffness and therefore the occurring stresses. The stresses at path 2 are used for the calculation of P and S damages. Figure 4.37 shows the local membrane stress $\overline{P_L}$ and the sum of local membrane and bending stress $\overline{P_L + P_b}$ compared to the allowable maximum values. It can be seen that the criteria defined in subsection 4.5.1 for the prevention of type P damages for negligible irradiation are satisfied. If irradiation is considered, the membrane and total allowable elastic stresses for a temperature of 20 °C and a thermal neutron fluence of $\phi_n = 10^{21}$ n_{th}/cm^2 are $S_{em} = 614$ MPa and $S_{et} = 1046$ MPa, respectively. Figure 4.38 shows the sum of local primary and secondary membrane stress $\overline{P_L + Q_L}$ and the sum of local membrane and bending stress, secondary stress and peak stress $\overline{P_L + P_b + Q + F}$ compared to the allowable values. Again, the occurring stresses are well below the allowable limits defined in subsection 4.5.1.

The criterion for the prevention of a progressive deformation of the cold moderator vessel ($\overline{P_L + P_b} + \overline{\Delta Q} \leq 3 \cdot S_m = 71.7$ MPa) is satisfied, since secondary stresses can again

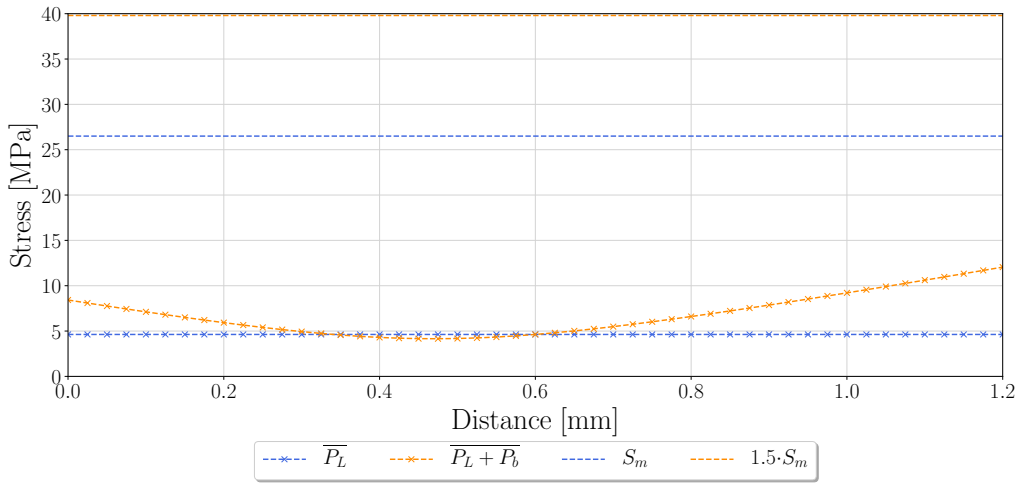

Figure 4.37: Local membrane stress and sum of local membrane and bending stress of path 2 compared to the maximum allowable stress values S_m and $1.5 \cdot S_m$.

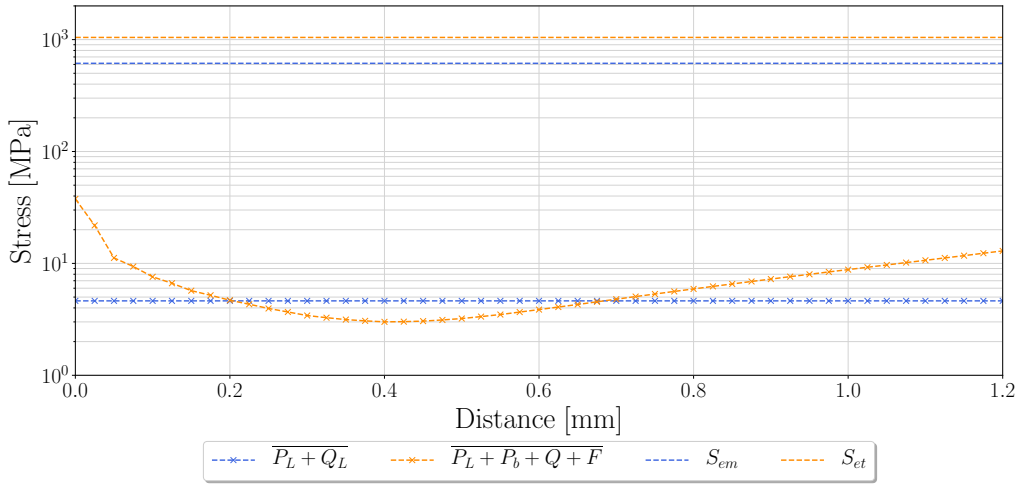

Figure 4.38: Sum of local primary and secondary membrane stress and sum of local membrane and bending stress, secondary stress and peak stress of path 2 compared to the maximum allowable stress values S_{em} and S_{et}.

be neglected. Due to the missing fixation of the vessel itself as well as the gap between the vessel and surrounding vacuum pipe, the resulting high degree of freedom allows it to expand or contract during cool down or warm-up.
To ensure the prevention of type S damages due to fatigue of the material, the highest stresses $\overline{\Delta\sigma_{eq,tot}}$ have to be determined for the different steps during operation to calculate the maximum strain range $\overline{\Delta\epsilon}$. Since the highest stress at the welding seam between the cylindrical lid and the vessel's base body is caused by a geometrical discontinuity, the equivalent stress at a distance of 0.050 mm is used. Table 4.12 shows the different loading steps and the corresponding total stresses. The total stress has to be multiplied with a fatigue strength reduction factor of $f = 4$, since the welding seam can be classified by type II.2 in table RB 3334.4a in the RCC-MRx. It is apparent that the criterion for the prevention of type S damage due to fatigue is satisfied. Furthermore, the material data for Al-5754-O has to be regarded as a lower limit. Therefore, the actual usage fraction is even smaller.

Summary: The above simulation results show that the vacuum recipient as well as the cold moderator vessel are well below the allowable stress limits, both for negligible and

Table 4.12: Total stress, strain range and usage fraction for the different loading steps defined in subsection 4.5.1.

Process	$f \cdot \overline{\Delta\sigma_{eq,tot}}$ [MPa]	$\overline{\Delta\epsilon_t}$ [%]	n_j	N_j	V_A
Evacuation of VR #1 - #2/ #15 - #16	16.7	0.013	10000	$> 10^9$	≈ 0
Pressurization moderator volume #3 - #4/ #5 - #6/ #14 - #15	33.5	0.027	40000	10^8	0.0006
Pressurization helium volume #6 - #7/ #14 - #15	33.5	0.027	20000	10^8	0.0002
Operation with solid moderator #9 - #10/ #12 - #13	36.8	0.029	20000	10^7	0.002

non-negligible irradiation. The investigation of possible type S damages shows that these damages will not affect the components for a reasonable number of load cycles.

Thermal contraction

The different temperature profiles and various materials along the helium and moderator inlet and outlet transfer lines during operation induce different deformations in the tubing system due to thermal contractions. This leads to stresses in the materials and a potential shift in the position of the cold moderator vessel. To make sure that the moderator vessel stays within its predefined position (no considerable translational motion of its center axis or angular movement of more than 1°), the effect of the different temperatures is investigated.

In steady-state operation, the helium inlet tube is at a temperature of $T_{He,in} = 4.2...10$ K, while the temperature in the helium outlet tube varies between approximately 10 K $< T_{He,out} < 20$ K. The equilibrium temperatures in the moderator tubes are largely governed by the thermal conduction between the cold moderator vessel and the connections to spacers and the vacuum recipient. Therefore, along the majority of their length, their temperature is high compared to that of the coolant tubes (see Figure 4.9).

There are different materials applied for tubing in the present design, including aluminum alloy 6060 and stainless steel, with integrated thermal contractions between $T = 300$ K and $T = 4$ K of $\frac{\Delta L}{L} = 452 \times 10^{-5}$ m/m and $\frac{\Delta L}{L} = 331 \times 10^{-5}$ m/m, respectively [66]. If the chosen material for all tubes in the transfer line section was stainless steel, the higher thermal contraction in the coolant tubes would induce large uneven deformations and subsequent stresses in the tubing system. An option to reduce the difference in length during operation is by using Invar36, an iron-nickel alloy, for the coolant tubes. With an integrated thermal contraction of $\frac{\Delta L}{L} = 40 \times 10^{-5}$ m/m between 300 K and 4 K [66], the effect of the lower temperature is partly compensated.

To assess the total deformation of the tubing system and the position of the cold moderator vessel without constraints (i. e. spacers) along the tubes, the results of the steady-state thermal simulations from section 4.3 are applied and taken as input for a subsequent simulation using the module "Static structural". Here, the oval flanges are fixed and the spacers are omitted to obtain the resulting total shift of the moderator vessel from its intended position. Figure 4.39 shows the deformation of the front part of the tubing including the cold moderator vessel for the two cases. When using Invar36 in the tubing of the helium transfer lines, the maximum deformations are is $\Delta x = 0.6$ mm, $\Delta y = -6.5$ mm and $\Delta z = -1.6$ mm. The deformation in z-direction is within the limits defined in section 4.1, while the other deformations exceed the defined maximum allowable values. Therefore, flexible elements are necessary to allow the vessel to be kept in the positioned imposed by the spacer elements. The maximum angular deviation from the ideal position is approximately 0.5 deg and therefore also within the limits defined in section 4.1.

While the use of Invar36 clearly diminishes the movement of the moderator vessel due to a reduced contraction of the coolant supply and return tubes, the remaining deformation would still introduce large stresses in the spacers and locations of fixed supports (welding seams) if only rigid tubes were used. The shift in X-direction is caused by the intake tube for the helium transfer line, which is still assumed to be made of stainless steel. This is mainly due to the poor commercial availability of different tube diameters (and wall thicknesses) made of Invar36 and their corresponding high cost.

An additional flexibility can be realized by incorporating short segments of corrugated stainless steel tube into the vertical parts of the tubing system. These segments allow a horizontal shift of the tubes and take up the remaining movement of the tubes and vessel. The required length of corrugated metal hose is calculated according to [92] as

$$L_{req} = \sqrt{(10 \cdot r_N \cdot s)} + 2 \cdot l_{fitting} \tag{4.19}$$

with the maximum lateral deformation s, the bending radius r_N and the length of the fittings $l_{fitting}$. With the resulting deformation when using Invar36 of approximately $s =$

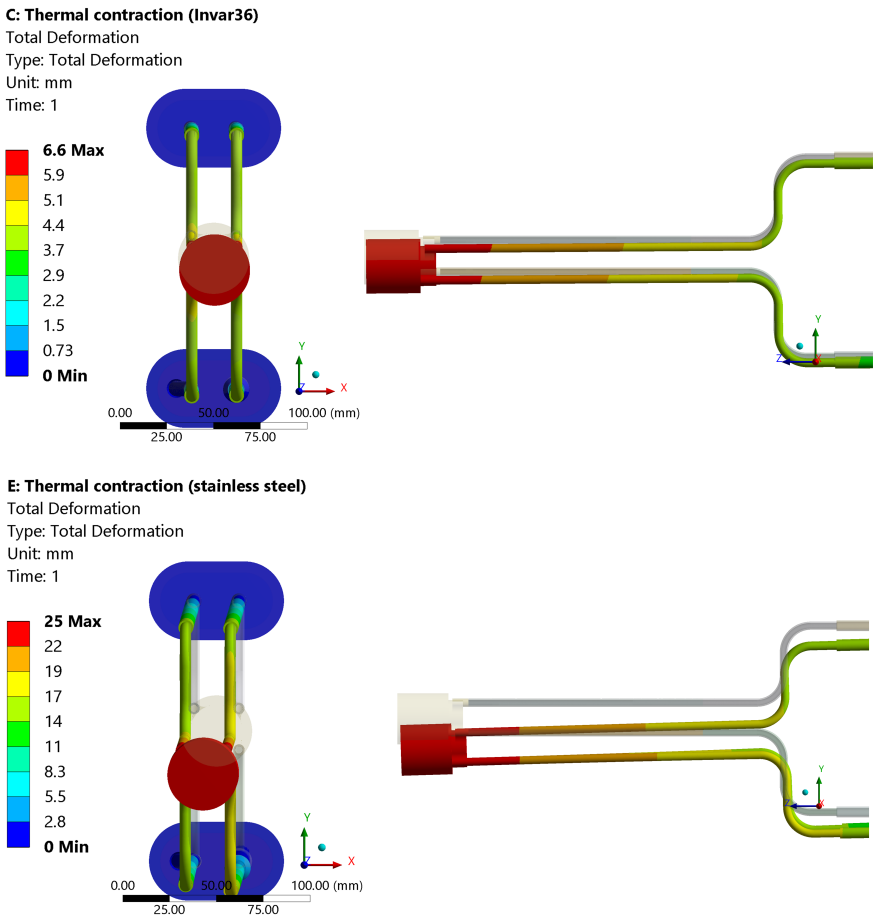

Figure 4.39: Results of the "Static Structural" simulation in ANSYS Workbench 19 using the temperature profile from subsection 4.3.2 as input. Top: Invar36 as partial replacement for stainless steel tubes in coolant lines. Bottom: only stainless steel tubes in "Transfer line" section. Left side: front view. Right side: side view.

5 mm and a bending radius of $r_N = 30$ mm, a length of $L_{req} = 36$ mm of corrugated tube is necessary. Since it is directly welded to the stainless steel elbows positioned above and below the vertical section of the tubing, no additional length due to fittings is needed and the available space in between the elbows (38.6 mm for the helium side and 36.7 mm on the moderator side) is sufficient.

Due to their low wall thickness and flexible design, the corrugated tubes pose a critical component in the tubing assembly. Therefore, their durability under the applied internal pressures has to be confirmed. However, the allowable static internal pressure for such a flexible tube is specified as 65 bar [92], which is much higher than the maximum pressure in the present system.

Although the aforementioned measures were taken to ensure the cold moderator vessel to remain in its intended position during cool down and operation, its actual position has yet to be confirmed. This can be realized by taking X-ray images of the area in which the vessel is located during cooling. Such an investigation has previously been performed for a liquid hydrogen cryostat.

Bolted flange connections

To ensure a high degree of interchangeability of the moderator system, e. g. for an exchange of the moderator vessel or modifications to the measurement equipment, multiple demountable flange connections are incorporated into the cryostat. One of them is realized at the transition from the transfer line section to the cold moderator section. The cold moderator vessel itself is attached to the moderator and coolant transfer lines via commercially available metal-sealed screw connectors (see Figure 4.40). To allow access to the joints, the vacuum recipient around them is box-shaped and allows the removal of the front part. The outer dimensions of the box amount to the maximum allowable dimensions of the duct geometry while allowing a gap of a few mm in between. The flanges are sealed by a round-wire, which is deformed by the flange surfaces made of aluminum alloy and compressed via bolt connections.

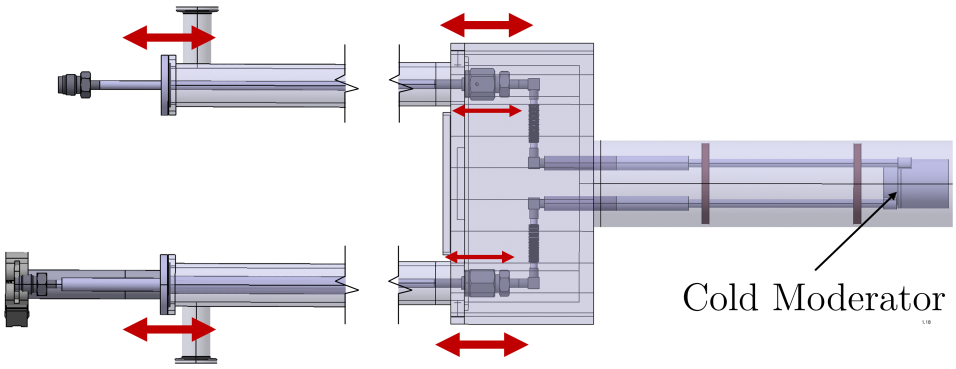

Figure 4.40: Cut CAD view of the bolted and aluminum-sealed flange connection at the interface between transfer line (TL) and cold moderator (CM) section.

Due to the high levels of radiation for the case of the full power HBS, the sealing material at this location has to be metallic to avoid a degradation of the insulation vacuum due to a radiation-induced embrittlement of the sealing material. Aluminum of high purity is a suitable material, due to its relatively low resistance against deformation and its low absorption cross section for thermal neutrons. Other options include indium, which has a much lower hardness than other metals, but tends to partly coalesce with the base material for longer operating periods. It is therefore not suited for the present case or has to be exchanged regularly.

Reported values for the force required to compress a round-wire aluminum seal are in the range of $K_{com,seal} = 30...200$ N/mm. A conservative value of $K_{com,seal} = 150$ N/mm was chosen for the present design. The wire diameter of $d_{seal} = 3$ mm could theoretically be reduced, but a larger diameter ensures more safety in avoiding small leakages by increasing the effective sealing width. The round-wire is embedded in a rectangular end-to-end groove, for which the dimensions are taken from [93]. Its length is approximately 443.1 mm (perimeter $P_{e,seal}$), which yields a total force required to deform the seal of [94]:

$$F_{assembly} = K_{com,seal} \cdot P_{e,seal} = 66.5 \text{ kN} \tag{4.20}$$

The chosen total number of bolts is $n = 20$, according to section A6.2823 of the RCC-MRx, to allow an adequate distance between the bolts. The force per bolt necessary to compress the aluminum seal during assembly is thus:

$$F_{assembly,B} = F_{assembly}/n = F_{01,min} = 3.323 \text{ kN} \tag{4.21}$$

During operation, the hydrostatic load caused by the external pressure onto the assembly

due to the vacuum inside the box can be calculated according to A6.2431.122 as follows

$$F_{op} = \pi/4 \cdot G^2 \cdot p_e/n = 10 \text{ N} \tag{4.22}$$

with the gasket mean diameter $G = 144$ mm. Since the pressure is external, it acts as a compressive force onto the flange bodies, therefore providing additional force for maintaining leak-tightness of the sealed connection. However, due to the low value of the force during operation, it is neglected for the present calculations.
According to A6.2621, using the aforementioned calculated forces during assembly, one can obtain the minimum required diameter of the bolt. For a total number of 20 bolts, the maximum required diameter for the present case is 4.5 mm. Therefore, size M6 with a core diameter of $d = 4.773$ mm is sufficient.
Subsequently, the lower and upper limits of the preloading F_0 are calculated. The maximum limit is defined by the criterion (A6.2622.1)

$$F_0 \leq (F_L - Q_i - \Lambda \cdot N_e)/\beta \tag{4.23}$$

with the force $F_L = \min(2 \cdot S_{mB} \cdot A_n; R_{p0.2} \cdot A_t)$, the axial load induced by thermal loadings Q_i, the external tensile load N_e, the rigidity coefficient Λ and the coefficient

$$\beta = \frac{K'_a \cdot K'_b}{K_a \cdot K_b} \cdot \frac{K_a + K_b}{K'_a + K'_b} \tag{4.24}$$

K_a, K_b and K'_a, K'_b are the rigidities of the assembled parts and the bolt at the assembly temperature and at the temperature during operation, respectively. Since temperature changes can be neglected and the external forces are small compared to the force required to compress the metal seal, the criterion simplifies to $F_0 \leq F_L$. For the present case $F_L = 7634$ N, which is why the maximum preloading is set to $F_{0,max} = 7$ kN.
The required tightening torque C_0 can then be determined by using the maximum limit (A6.2623.1c)

$$C_0 = \frac{F_{0,max} \cdot (0.16 \cdot p_{thread} + f_{fr,m} \cdot (0.583 \cdot d_f + 0.5 \cdot D_m)}{1 + I_{CO}} \tag{4.25}$$

with the thread pitch p_{thread} (equal to 1 mm for M6 threads), the minimum coefficient of friction $f_{fr,min}$ (0.12 for a normal thread pair), the simple pitch diameter d_f, the mean diameter of the contact surface beneath the head of the bolting element D_m and the uncertainty of the tightening means I_{CO}, which is stated as 10% for the use of a torque wrench. This formula is also in accordance with the approach given in [95].
With a maximum allowable preloading $F_{0,max} = 7.0$ kN, C_0 yields 6.4 Nm. Using this value, the minimum applied preloading $F_{02,min}$ can be calculated by following formula (A6.2623.1d)

$$F_{0,min} = \frac{(1 - I_{CO}) \cdot C_0}{(0.16 \cdot p_{thread} + f_{fr,M} \cdot (0.583 \cdot d_f + 0.5 \cdot D_m)} = 3.672 \text{ kN} \tag{4.26}$$

with the maximum coefficient of friction $f_{fr,max}$ (0.2 for a normal thread pair). The obtained value is higher than the required value for the compression of the aluminum seal, which allows the compression of the seal by the chosen tightening torque ($F_{02,min} \geq F_{01,min}$).
With the forces calculated above, the stresses mentioned in subsection 4.5.1 can be calculated. The mean fictitious stress is calculated by dividing the force required to compress the seal by the core cross section of the bolts

$$(\overline{\sigma_m})_{fictitious} = F_{01,min}/A_n = 185.7 \text{ MPa} \tag{4.27}$$

which is below the allowable bolt stress $S_{mB} = 213.3$ MPa.
The mean stress $\overline{\sigma_m}$ is calculated in the same way as the mean fictitious stress, but for the maximum preloading $F_{0,max}$. This yields a value of $\overline{\sigma_m} = 391.2$ MPa.
The maximum stress $\overline{\sigma_m + \sigma_b}$ at the bolt core periphery comprises the mean stress and an additional thread root shear stress τ_n, caused by a residual torque C_r on the engaged threads. It is calculated as follows (Appendix A6.2532):

$$(\overline{\sigma_m + \sigma_b})_n = \sqrt{\sigma_n^2 + 3 \cdot \tau_n^2} = 495.2 \text{ MPa} \tag{4.28}$$

Both the mean and maximum stress intensity satisfy the criteria defined in subsection 4.5.1 $\overline{\sigma_m} \leq 2 \cdot S_{mB}$ and $\overline{\sigma_m + \sigma_b} \leq 3 \cdot S_{mB}$.

In addition to the above analytical calculations, numerical simulations are performed, again applying the module "Static Structural" of ANSYS Workbench, to validate the feasibility of the designed bolted connection and the required deformation of the aluminum seal. The minimum and maximum values of preloading $F_{0,min}$ and $F_{0,max}$ are used and their effect on stresses in the bolt and assembled parts as well as on the deformation of the aluminum seal (using non-linear material data) are investigated. To investigate the plastic deformation of the seal, non-linear effects are enabled for the simulations and the plasticity of the aluminum seal is modeled by applying the corresponding values (see Figure 4.41, [96]).

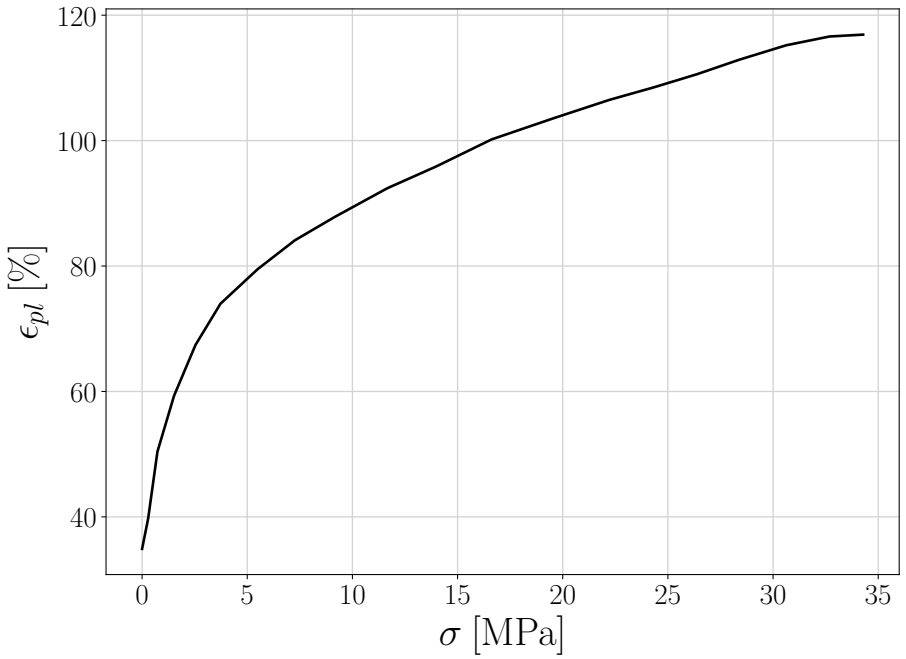

Figure 4.41: Plastic strain-stress plot for aluminum alloy 1050 (values taken from [96]).

Due to the symmetric geometry of the vacuum box, again only one fourth of it is modeled for the simulations to decrease the computation time needed (see Figure 4.42). The symmetric behaviour is incorporated by applying boundary conditions that prevent movement in normal direction of the cut surface. The bolts are simplified as cylindrical rods with a diameter equal to the root diameter of the threaded bolt ($d_n = 4.773$ mm) as a conservative assumption. All contacts between bodies are set to "frictional" with a friction coefficient of 0.2, except for the connection between bolts and nuts, which is set to bonded. The global mesh size is set to 1 mm and the cylindrical bodies (bolts, nuts and metal seal) are

meshed using hexahedral elements to improve their mesh quality.

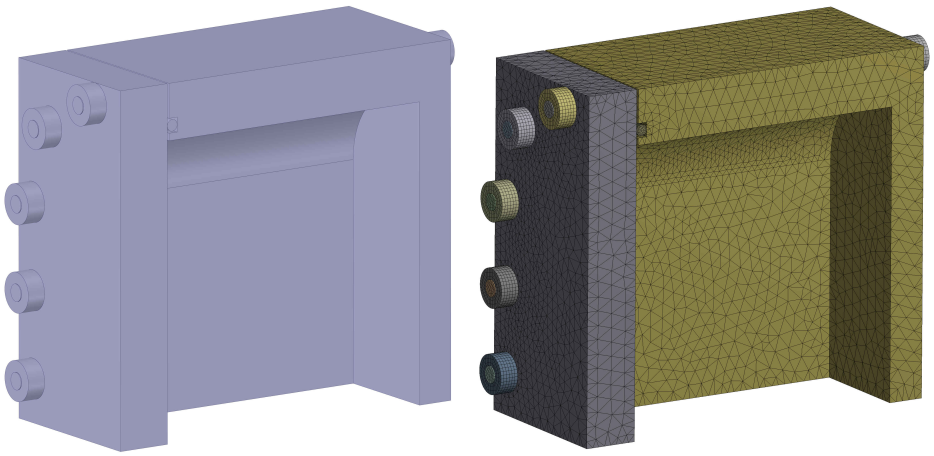

Figure 4.42: One fourth of the vacuum box model used for structural simulations in ANSYS Workbench, including the rectangular box and plate, the round-wire aluminum seal and the bolts and nuts. Bolts and nuts are simplified as cylindrical bodies without threads.

The simulation is subdivided into 5 sub-steps: the first three steps describe the state of the system during assembly, while the last two steps represent the state during operation. In the first step, the bolt connections are pre-adjusted by 5 µm to establish a surface contact between the flange bodies and the aluminum seal. In the second step, the defined preload is imposed, which allows the plastic deformation of the seal. The third step is a negative increment of 11 µm to model the effect of embedding of the bolt, nut and assembled bodies. The value is estimated using Table 5 of [95] and allows a calculation of the loss of preload due to embedding. During the fourth step, the external pressure of $p_e \approx 1$ bar due to the evacuation of the inner volume of the vacuum recipient is imposed on the system. The fifth step models the case of the assembled system without any loads.
Figure 4.43 shows a front and cross section view of the deformed aluminum seal for the cases of minimum and maximum bolt pretension. The maximum deformation in direction of the bolt axes is 0.43 mm for the minimum pretension and 0.56 mm for the maximum pretension. Both of these values should be enough to sufficiently seal the flange connection to allow the generation of a high vacuum. However, for the minimum pretension, the deformation of the seal is less uniform and only 0.33 mm at the center of the long side of the flange body. The maximum pretension, on the other hand, causes a more even deformation. Therefore, a more precise tightening means should be chosen to reduce the spread between the maximum and minimum preloading.
Figure 4.44 shows the membrane stress and the sum of the membrane and bending stress along a bolt for the maximum preloading $F_{0,max}$ at the periphery and at the center of the bolt's core diameter. The results are close to the analytically calculated values above and also satisfy the requirements of subsection 4.5.1.

The flange connections at the other end of the oval pipes are sealed with elastomeric O-rings, which is feasible due to the larger distance from the nuclear radiation source and shielding material in between. Due to the limited space available, a seal diameter of $d_{seal} = 1$ mm and a circumference of $P_{seal} = 155.8$ mm are used. A maximum force

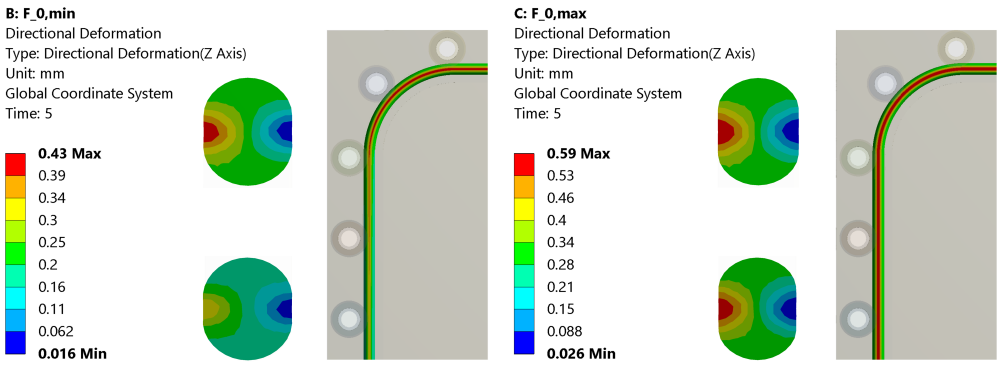

Figure 4.43: Front and cross section views of the aluminum round-wire seal in its plastically deformed state for the minimum and maximum bolt preloading calculated with ANSYS Workbench.

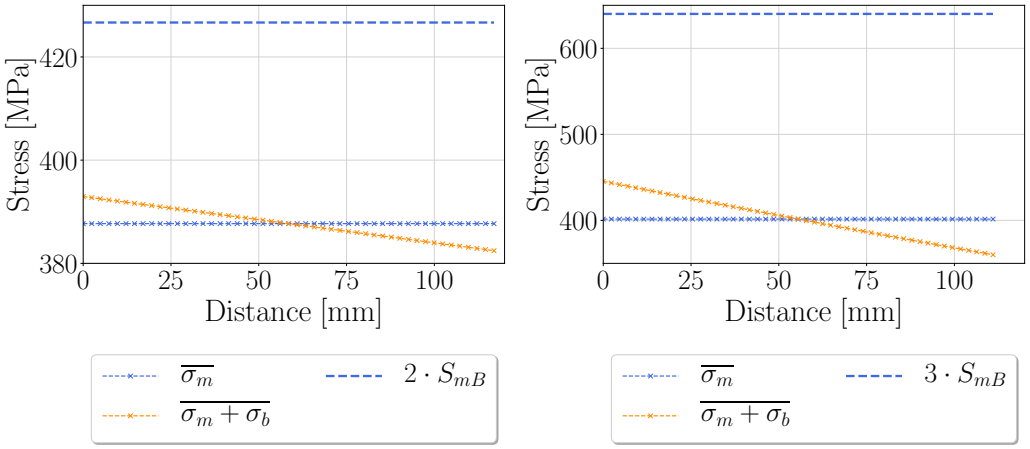

Figure 4.44: Linearized membrane and sum of membrane and bending stress for paths along the center (left) and the periphery (right) of a bolt.

required per sealing length of $K_{O-ring} = 10$ N/mm (Pfeiffer Vacuum GmbH) to compress an O-ring made of FKM yields a force of $F_j = K_{o-ring} \cdot P_{seal} = 1558$ N. Using this value, a number of $n = 6$ bolts of size M3 are sufficient to compress the seal and maintain a high vacuum during operation.

4.6 Further safety considerations

To ensure a failure- and hazard-free operation of the cryogenic system, it is necessary to assess potential risks during the design phase and implement appropriate risk reduction measures. The DGUV (Deutsche Gesetzliche Unfallversicherung e. V.) offers a guideline for such an assessment, focusing on the manufacturing and operation of equipment designed for research purposes, which also applies to the apparatus described in this thesis [97]. It is based on commonly used directives legislated by the European Union, like the Machinery Directive (2006/42/EC) or the Pressure Equipment Directive (2014/34/EU). However, due to fact that the present system is exposed to nuclear radiation, it falls outside the scope of the Machinery and Pressure Equipment Directive. Furthermore, the product of the volume and pressure for the helium and methane-carrying parts of the system is lower than the one considered by the PED (Article 4, Paragraph 3). As a result, the system is designed according to best practice and the nuclear code RCC-MRx is applied to additionally account for the impact of nuclear radiation. Due to the aforementioned reasons, the system must not receive a CE marking.
Due to the fact that the presented system is an experimental one, its intended use is not fixed and might be necessary to change. Especially the control system was not completed in the time frame of this thesis and will be optimized in the future. However, some guidelines of the Machinery Directive are followed, namely:

1. the identification of hazards
2. the estimation of risks and probability of their occurrence
3. the evaluation of the risks and possible risk reduction techniques and
4. the application of protective measures

In the next paragraphs, sources of potential hazards other than pressures are regarded and potential risk reduction measures are presented.

4.6.1 Cryogenic fluids

Most of the potential risks from the operation of the aforementioned cryostat system either stem from the use of cryogenic fluids or the use of flammable gases. Especially the former poses several risks like the pressurization of components by evaporating cryogenic fluids or solids, the displacement of air by evaporating gas and cryogenic burns.
The effects of the pressurization of different components are covered by the application of the aforementioned nuclear code RCC-MRx. It matches the pressure equipment directive in large parts, while at the same time considering irradiation. Wherever necessary, safety and proportional valves are applied to avoid the build-up of pressures exceeding the design values.
Non-destructive tests (see section 5.4 for more detail), including pressure tests above the design pressure, are performed to ensure the accurate operation of the equipment. Operating instructions are provided to avoid possible hazards due to operating errors. They additionally include instructions for assembly. The cryostat system shall only be used by trained personnel.
There are several ways to reduce or eliminate the risk of displacing the air by evaporating cryogenic fluids, also denoted as Oxygen Deficiency Hazards (ODH). On the one hand, the amount of cryogenic fluids or compressed gases shall be kept as low as possible. Furthermore, cryogens shall not be used in small rooms with a higher risk of a fast displacement of air and evaporating gas must be transported to the outside via vent lines and ducts [98]. Although specified limits regarding the maximum allowable leak rate of fluid-conducting parts minimize the amount of inert gases accumulating, failure of equipment can still lead

to an ODH. Therefore, the moderator system must not be used in rooms without ventilation and there shall always be at least two persons present during handling of cryogenic or compressed gases. Oxygen monitors warn people working in the affected areas of possible oxygen deficiencies. This is a prerequisite for using the moderator system with cryogens in smaller rooms (< 100 m^3), especially with insufficient ventilation. Although the total volume of cryogenic liquid inside the cryostat during operation is low (150 ml), the amount of cryogenic supply (e. g. LHe) should be taken into account. For a dewar of 100 l of LHe, the equivalent amount of gas at room temperature is $V_{He,gas} = 77.3$ m^3.
The only way to avoid injury from the cold is to avoid direct contact with it. This is realized by using protective equipment like goggles and insulated gloves for cryogenic application and by shielding areas of potentially low temperature from direct contact (either by insulation or barriers). During operation of the moderator system presented in this thesis, protective gear shall be worn when handling the LHe dewar or the cryostat while still in cold state. The helium exhaust line shall be covered by a layer of ArmaFlex tube made of insulating foam to avoid accidental skin contact.

4.6.2 ATEX Directives

The ATEX directives (Appareils destinés à être utilisés en ATmosphères EXplosibles, engl.: "Equipment intended for use in explosive atmospheres") are two EU directives describing the requirements for equipment and workplace in explosive atmospheres (Directive 2014/34/EU and 1999/92/EC, respectively).
According to the directive, measures are taken to prevent the formation of explosive atmospheres. These include the possibility to pump the inner tubes and vessels of the cryostat and gas management panel as well as purge the vent line with nitrogen to reduce the amount of oxygen inside it.
Electrical equipment included in the parts of the system carrying flammable gas (methane) are chosen in a design conforming to the ATEX directive. This includes the mass flow controllers for methane and a mixing gas, the pressure indicators in the moderator lines and the roughing pump for pumping the moderator and tubes. Although intrinsic explosion safety is considered in the design of the methane-carrying part of the system, those additional measures further reduce the risk of formation of an explosive mixture.
The exhaust port of the vacuum pumping system as well as a safety valve attached to the vacuum recipient are connected to the exhaust line of the gas management panel, through which flammable gas is transported to the outside. In case of a leak inside the vacuum recipient, the vacuum pump is closable via an automatically controlled angle valve, allowing the gas inside the vacuum recipient to escape via the safety valve.
Leakages can be avoided by performing a thorough leak detection of the components, especially at locations of welds and demountable connections, to make sure that leak rates are below allowable limits. In case of unforeseen leakages, e. g. by damages to components, a gas warning system will avoid hazards by automatically shutting of sources of ignition as soon as a pre-defined limit is reached. After that, a de novo operation is only possible, if the cause for the shut-off is eliminated.

4.6.3 Effects of irradiation on the moderator material

The effects of irradiation in a facility like HBS are mainly caused by the produced fast and thermal neutrons as well as gamma photons. Effects due to neutrons include *displacement damages* due to elastic collisions of high-energy neutrons with the different materials and *transmutation damages* by fast and thermal neutrons [91]. The effects of gamma radiation are mainly: energy deposition due to ionization in an interaction of a gamma photon with the electron of an atom and gamma displacement of atoms in a material. However, the mutational effects are small compared to those induced by neutron radiation.

Due to the relatively low radiation levels compared to spallation or fission-based neutron sources, the aluminum cold moderator vessel can be used for approximately seven years before the effects of neutron irradiation require a replacement of the moderator vessel (see subsection 4.5.1). However, no detailed calculations of the activation of the cold moderator vessel material have been performed in the context of this thesis. To avoid the release of short-lived radionuclides after operation, the vessel should be replaced at the same time as the target is replaced (every three to four years) with one week of waiting time in between the switch-off of the proton beam and the extraction of the moderator plug. Before the moderator vessel can be replaced, a clearance measurement shall be performed to ensure sufficiently low levels of radiation. A calculation of the necessary cooling time after the switch-off has yet to be determined.

Especially solid hydrocarbon moderators are prone to radiation damage, which can lead to the build-up of high pressures and damage to the structural materials. During long periods of high levels of irradiation, hydrocarbons are partly transformed into elementary hydrogen (H) and basic methyl (CH_3) groups. When warming up the moderator material, the hydrogen evaporates and builds up a pressure inside the matrix of the solid moderator. At the same time, unwanted temperature spikes are possible due to energy being released during the recombination of molecular structures.

There are several ways to reduce the effect of the radiation damage to avoid larger damages to the cryostat and related hazards. One is a repeated warm-up of the moderator material, as is performed at ISIS' Target Station II [81]. This procedure leads to interruptions in the performed measurements. However, due to the small volume of the HBS cold moderators, the condensation is not too time-consuming compared to bulk moderators. Other measures include designs, in which the moderator is warmed up at the exhaust first to allow a movement of the residual solid. However, the operation of a hydrocarbon moderator at the full power HBS should be preceded by extensive tests of the material with a gradual increase in beam power to assess the exact effects of the specific irradiation. Until such measurements are performed, the moderator vessel shall be heated above the freezing temperature of methane every 15 hours for proton beam powers larger than 5 kW.

4.6.4 Piping and Instrumentation Diagram (P&ID)

Apart from the critical cryogenic components and their requirements, the overall fluid flow directions and necessary control and safety devices have to be determined. Figure 4.45 shows the Piping & Instrumentation Diagram (P&ID) of the moderator system, which is used as a basis for the design of a gas management panel for the operation of the cryostat.

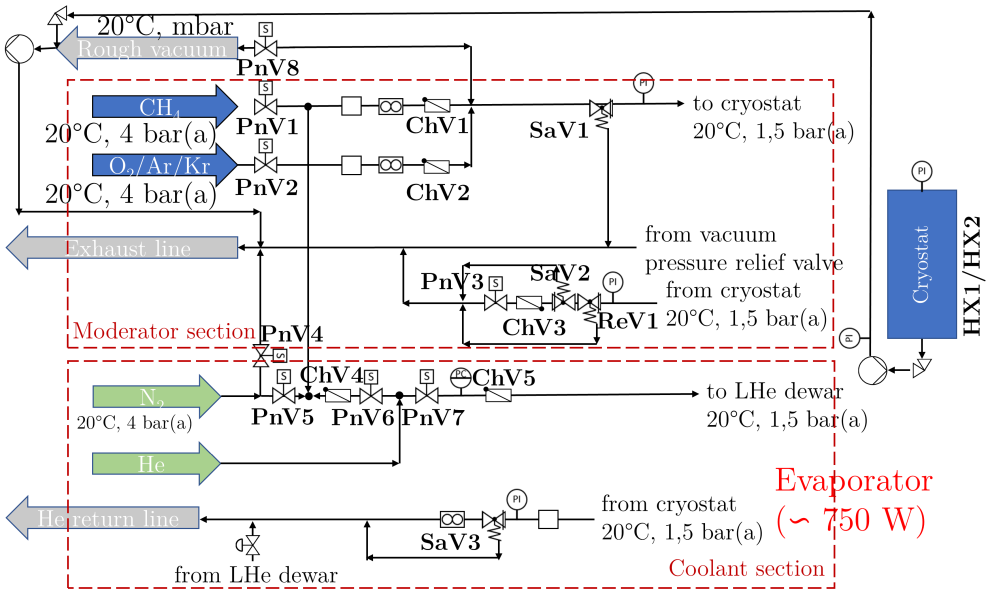

Figure 4.45: Piping and instrumentation diagram (P&ID) of the moderator system (PnV: pneumatic valve; ChV: check valve; SaV: safety valve; ReV: relief valve; HX: heat exchanger).

Since most valves as well as control and safety devices are not operable at cryogenic temperatures, they have to be located outside the cryostat system. All fluid flows have to be warmed up to room temperature before coming into contact with electronic devices to avoid damage due to the condensation of humidity from ambient air.
All gas supplies can be opened or closed via remote valves with a "normally closed" setting. Also, the roughing pump as well as the N_2 and He lines are connected to the moderator section via remotely controllable valves. This property reduces manual intervention times to a minimum, as is desired for a radiation control area. Check valves ensure that no gas flows are entering the wrong tubes to avoid other gases inside the helium return line or Dewar vessel and no flammable or explosive mixtures by reverse flows.
The main part of the P&ID can be divided into two parts: the moderator section and the coolant section. Both sections have a supply and exhaust section. The methane and nitrogen (purging) gas as well as the exhaust of the rough vacuum pump are led to an exhaust duct and to the outside. The helium exhaust gas is returned to the central helium supply facility of Forschungszentrum Jülich for re-liquefaction.
Apart from a main mass flow controller for methane, an additional MFC is incorporated into a parallel line. It allows the admixture of small amounts of other gases into the methane with a specified mixing ratio. It was suggested that adding small amounts of oxygen (O_2) or noble gases (Ar, Kr) might increase the moderating efficiency of the methane due to a prohibition of the phase transition below 20.4 K. Therefore, the present system allows the investigation of this matter. Both mass flow controllers are protected from particles by using filters upstream.
To control the pressure inside the system and avoid pressures above a defined value inside

the system, pressure indicators and safety valves have to be incorporated. The measurement range of the sensors and relief pressure of the safety valves is determined by the planned operating pressure.
The roughing pump can be switched in function by remotely controllable valves, either as a backing pump for the turbomolecular pump that is used for the generation of a high-vacuum inside the cryostat for insulation purposes or as a pump for evacuating the moderator lines prior to filling them with methane gas.

4.7 Final engineering design

Using the boundary conditions and design choices mentioned in the previous subsections, the technical design of the different components of the cryostat is finalized. In the following subsections, the final engineering design of all major components is presented.

4.7.1 Vacuum recipient

The design of the vacuum recipient is shown in Figure 4.46. It consists of two parallel oval tubes made of aluminum as a containment for the moderator and coolant transfer lines, with an outer width of 60 mm and an outer height of 30 mm. The outer radius of the circular sections is 15 mm and the wall thickness is 3 mm. The dimensions are selected according to the commercial availability of such tubes. Due to the length of 1315 mm of the oval tubes, the manufacturing tolerance is specified as ±0.2 mm to avoid a larger mismatch between the tubes and with regards to the tubing inserts.

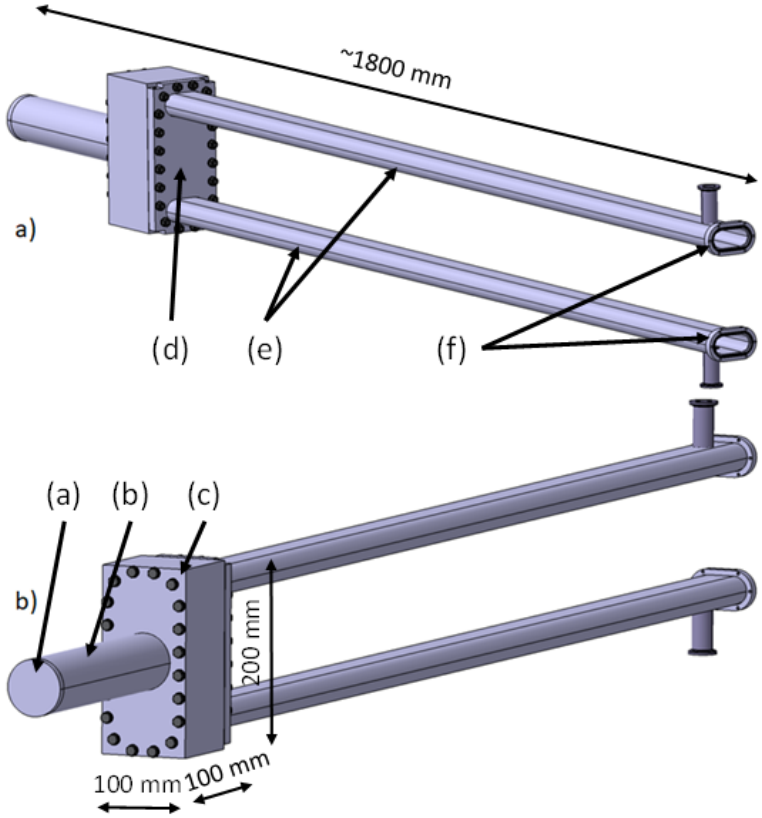

Figure 4.46: CAD model of the cryostat's vacuum recipient. Isometric back (a) and front (b) view.

At one end of the oval tubes (facing away from the moderator vessel), flanges are attached to allow a demountable vacuum-tight connection to the transfer lines via six through bores. An O-ring seal with a diameter of 1 mm and an inner diameter of 48 mm can be positioned inside a groove in the flange body and compressed via six M3x20 screws. Close to each oval flange, an ISO-KF flange (DN16) is mounted to the oval tubes to enable the connection of feed-throughs, vacuum components or safety valves.
On the opposite side, the oval tubes are connected to a rectangular plate with outer dimensions of 197 mm × 95 mm ($H \times W$). Its thickness is 15 mm. The manufacturing tolerance of the plate's height is specified as ±0.2 mm. The plate has 20 through bores with a diameter of 6.6 mm, leaving enough space for M6 screws. The plate is screw-connected

to a rectangular box-shaped aluminum block, which encloses the demountable connections between the moderator assembly and the transfer lines. It has a groove for a metallic seal and at the moderator-side a cylindrical tube with an outer diameter of 60 mm and a wall thickness of 2 mm is attached to it. This tube is closed at the end facing the target with a 3 mm-thick lid of aluminum. The working principle of the (de)mountable connections between the vacuum box and the vacuum plate and the oval flanges and the transfer lines has been demonstrated in Figure 4.40. Both the box and plate are equipped with geometric tolerances to specify their flatness to ensure an even fit when closing the sealed connection.

4.7.2 Transfer line assemblies

The transfer lines are divided into two sections (see Figure 4.47): one for the transport of the moderator medium and one for the refrigerant flow. Apart from constraints due to the available space, this also causes a thermal decoupling between the warm moderator tubes and the cold helium tubes. As for the oval tubes surrounding the transfer line assemblies, the transfer line tubes, which have a length of 1367 mm, are given a manufacturing tolerance of ±0.2 mm.

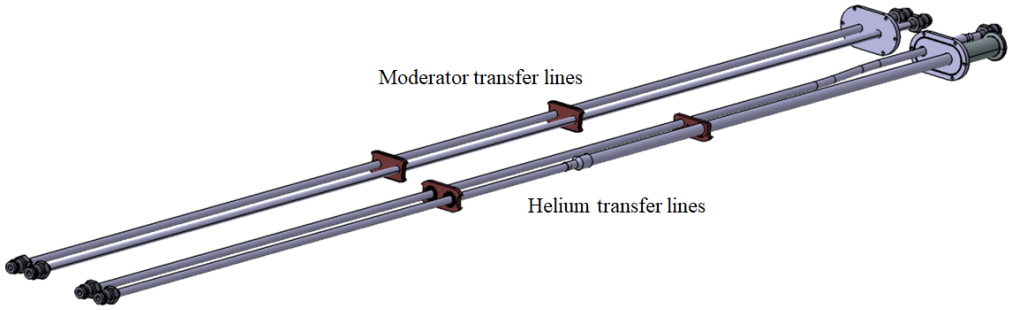

Figure 4.47: CAD view of the two transfer line sections, one for the moderator and one for the refrigerant (helium).

Moderator transfer lines: The moderator tubes are designed as two straight cylindrical tubes with a length of 1367 mm, an outer diameter of 8 mm and a wall thickness of 1 mm. The tubes are made of stainless steel. At the end facing away from the moderator, the tubes are put through bores in an oval stainless steel plate and welded to it. At both ends, the tubes are equipped with weldable metal-sealed connectors (6LV-4-VCR-3S-8MTB7, Swagelok) with threaded nuts. The distance between the axes of the two tubes is 24 mm, which allows a clearance of 1...2 mm between the two nuts at the side facing the moderator. To keep the tubes in position to avoid a thermal connection between each other or to the walls of the vacuum recipient, two spacers made of polyimide (product Vespel SP-1) are used. These have a low thermal conductivity, while at the same time being easily machinable.

Helium transfer lines: The helium transfer lines are mainly manufactured of Invar36, but have some differences in design compared to the moderator lines, mainly for thermal insulation purposes. The helium inlet line's first section is a 572 mm-long stainless-steel tube with an outer diameter of 12 mm and a wall thickness of 0.5 mm. The tube is directly connected to the inner side of the oval flange plate and allows the intake of a rigid L-shaped insulated LHe transfer line. This way, the helium enters the cryostat tubing only after about 570 mm, which largely reduces the heat load onto the liquid helium by thermal conduction from the room temperature vacuum recipient (see subsection 4.3.2). The L-shaped LHe transfer line is kept in position and sealed by a stainless-steel ISO-KF flange (DN16) press fitting. The helium exhaust line is thermally decoupled from the oval flange

plate as well by a 10 cm long section of stainless steel with a wall thickness of $t_{wall} = 0.5$ cm (see Figure 4.48)

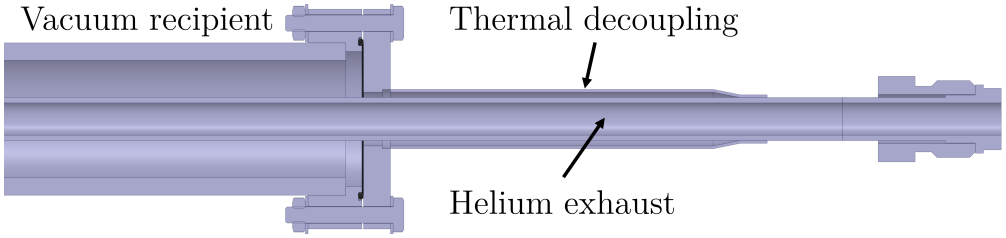

Figure 4.48: CAD view of the thermal decoupling of the helium exhaust tube to avoid a cooldown of the oval flange.

At its end, the L-shaped LHe transfer line has a press fitting, by which a semi-flexible LHe transfer line can be connected via a Johnston coupling. This semi-flexible LHe transfer line can be immersed in a LHe dewar with a capacity of 100 l or 250 l.
At the end of the 12 mm-diameter stainless-steel tube facing the moderator, the tube's diameter is lowered to 8 mm with a reducing part. The subsequent tube is 711.5 mm long and made of Invar36. Finally, a weldable metal-sealed connector for (de)mounting is attached. The helium outlet tube is made of Invar36 with an outer diameter of 8 mm and bend at the oval flange end to allow more space between the ISO-KF flange of the helium inlet and the helium exhaust outlet. On the atmospheric side, the helium outlet is connected to a 0.5 mm thick stainless-steel tube to avoid direct contact to the flange connection. This could lead to a breakdown of the elastomeric vacuum seal due to low temperatures. The tube is equipped with the aforementioned metal-sealed connectors on both sides to allow a (de)mountable connection to the gas management.
The helium tubes are again held in position by polyimide spacers, but their design is adapted to reduce the heat flow between the two tubes and between the helium inlet tube and the walls of the vacuum recipient (see subsection 4.3.2). For this, circular grooves are positioned around the tube's through bore to elongate the path for thermal conduction.

4.7.3 Cold moderator assembly

The cold moderator assembly (see Figure 4.49) consists of:

1. the tubes that connect the transfer line section to the moderator vessel and includes the transition from stainless-steel to aluminum and

2. the cold moderator vessel for condensing the moderator medium.

As for the transfer lines, the tubes are held in position inside the cylindrical tube that encases the moderator vessel (inner diameter: 56 mm). The moderator material is stored in a cylindrical bore with a diameter of 20 mm and a length of 45 mm. Along its surface shell, a curved groove runs along the whole length of the vessel and allows the refrigerant to cool the moderator along its whole shell surface area. The cooling groove is closed radially by a cylindrical shell and the moderator cavity is closed by a 1.5 mm thick cylindrical plate.
The cooling channel is realized with a rectangular cross section (see Figure 4.50), which leaves the aluminium bridges with a trapezoid cross section with the larger width further away from the moderator cavity. This shape is not optimized with regards to heat transfer,

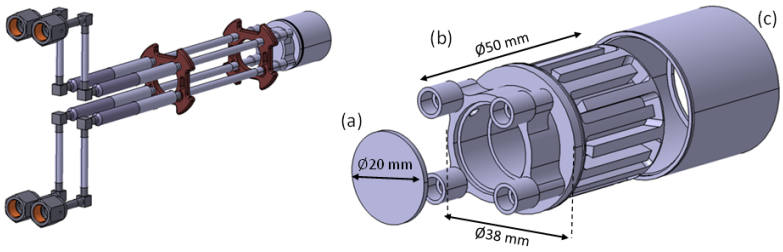

Figure 4.49: CAD model of cold moderator assembly (left) and exploded view of cold moderator vessel (2) with shell (3) and lid (1) (right).

since it adds more material for energy deposition at a position that is not beneficial for heat transfer. This is because the rectangular groove is easier to manufacture and for the intended purpose, the energy deposition is negligible. However, at a high-power source like HBS, the vessel should be optimized in this regard. The length of the cooling channels is approximately 30 mm.

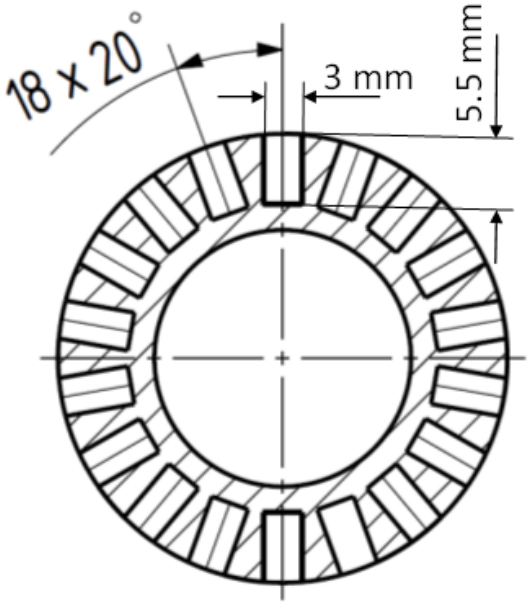

Figure 4.50: Cut view of the cooling channel cross section of the moderator vessel.

4.7.4 Control system

To control different parts of the cryostat system, e. g. temperature, pressure or mass flow, a gas management panel (GMP) is designed. It consists of different sections mentioned before – moderator feed and exhaust, helium feed and exhaust – that are separately installed on different aluminum plates. The plates are mounted to a rack of aluminum struts, which can easily be transported due to the four wheels attached to its bottom.

Flow control: The different gas feeds can be closed, opened and switched via two-way diaphragm-sealed pneumatic valves (Swagelok, part nr. *6LVV-DPS6M-C*) made of stainless steel. These valves are remotely controllable by using a valve terminal, which is used to provide the pneumatic actuators of the individual valves with pressurized air. The valves are constructed as normally closed to interrupt the gas feeds in case of failure. All pneumatic valves are equipped with normally closed indicators which can provide an

electrical signal to the programmable logic controller (PLC) about the state of the valve (open/closed). This gives an additional safety for the valve position.
The quantities of the different gas flows are controlled by using mass flow controllers by the company Bronkhorst. The specifics of the various MFCs are presented in Table 4.13.

Table 4.13: Properties of the mass flow controllers installed at the gas management panel.

Model	Gas	Mass flow range [g/s]	Accuracy	ATEX?
IN-FLOW F-201CI	CH_4	$4.0 \cdot 10^{-4}$...0.02	$\pm 0,5\%$ Rd & $\pm 0.1\%$ FS	Yes
IN-FLOW F-201CI	$Kr/Ar/O_2$	$8.0 \cdot 10^{-6}$...$4.0 \cdot 10^{-4}$	$\pm 0,5\%$ Rd & $\pm 0.1\%$ FS	Yes
EL-FLOW F-112AC	He	0.013...0.65	$\pm 0,5\%$ Rd & $\pm 0.1\%$ FS	No

The helium mass flow is controllable via a mass flow controller which is positioned at the helium exhaust line, since it is only suitable for temperatures down to -10 °C. Therefore, depending on the mass flow, the helium has to be warmed up before flowing through the MFC. This is realized by using an air heat exchanger, which is incorporated into the GMP and connected via a metal-sealed screw connector to the helium exhaust port of the cryostat.

Pressure control: The pressure of the moderator lines is measured at the inlet and at the outlet of the cryostat. By using a closable valve at the outlet, which is bypassed by a proportional valve, it is possible to adjust the maximum pressure inside the moderator line by setting the proportional valve to the desired position. For the experiments presented in section 6.2, the proportional valve was set to a pressure of $p = 1.2$ bar(g) to be able to keep an overpressure in the moderator vessel and line during the whole condensation process.
The pressure in the helium lines is measured at the helium exhaust after warming up the cold helium gas in the air heat exchanger. The pressure inside the helium dewar is measured and controlled by using a pressure controller by Bronkhorst (EL-PRESS P-602CV). This way, an overpressure can be created inside the LHe dewar to allow a transport of the liquid helium into the cryostat via the aforementioned insulated semi-flexible transfer line. The pressure of the pressurized air for controlling the pneumatic valves is adjustable by a pressure reducer at a service unit combination (MSB6, Festo).

Temperature control: The temperature is measured with four silicon diodes in total at the helium and moderator inlet and outlet of the moderator vessel. The sensors are attached to the aluminium tubes in front of the moderator vessel.
The temperature of the helium at the inlet of the moderator vessel and the two ports for the moderator medium can be heated by using a nickel-chromium heater wire. Both heater wires have a length of 75 cm and can provide heater powers of 100 W and 50 W for the helium and the moderator, respectively.
The temperature reading and control are realized through a temperature controller by the company LakeShore (TC 336). It allows a connection via Ethernet or USB to a measurement computer and has a PID loop for both heaters with adjustable elements (proportional, integral and differential).

Chapter 5

Prototype manufacturing

The aforementioned cryogenic system was manufactured at the workshops of the institutes JCNS-2/PGI-4 and ZEA-1 of Forschungszentrum Jülich. In this chapter, the different manufacturing processes as well as material and manufacturing design choices are presented, grouped by the specific types of manufacturing.

5.1 Machining

Vacuum recipient:
As mentioned in subsection 4.5.1, the cryostat's vacuum recipient is almost exclusively manufactured from aluminum alloys. The demountable box-shaped connection is manufactured from aluminum alloy EN AW-6061-T6 (AlMg1SiCu, $R_{p0.2\%} = 276$ MPa) to achieve a strength and stiffness large enough to allow the compression of a metallic round wire seal.
In a first step, the base material is cut from a larger block by using a water-jet cutting machine. After milling the plate and box (see (c) and (d) in Figure 4.46) to their nominal dimensions, the box is equipped with a groove for incorporating the sealing ring (see Figure 5.1). The sealing groove's surfaces as well as the opposing surface of the plate receive a finish to reduce its roughness to an average roughness value of $R_a \approx 0.4$ µm. This is important in vacuum applications to avoid leakage through small irregularities.
A circular pipe (see (b) in Figure 4.46), which is attached to the vacuum box as a shell enclosing the moderator vessel, is cut from a round pipe made of aluminum alloy EN AW-6060 (AlMgSi0.5, $R_{p0.2\%} = 190$ MPa). This choice is motivated by this alloy's wide range of shapes and dimensions commercially available. As a preparation for the welding of the circular pipe to the vacuum box, the pipe is turned to produce a tight fit between its outer diameter and the inner diameter of the opening in the vacuum box.
The lid to seal the cylindrical pipe (see (a) in Figure 4.46) is manufactured from a round bar of aluminum alloy EN AW-6063-T6 (AlMg0.7Si, $R_{p0.2\%} = 214$ MPa), again due to the availability of the required shape and dimensions. The bar is turned to the desired diameter of 60 mm on the outside and the inner volume is milled to obtain a wall thickness of 2 mm at the cylindrical surface and 3 mm at the flat surface. Due to the shape of the milling head, the transition from the flat to the cylindrical region shows a radius. Small grooves are attached at the joint region to the cylindrical pipe to insert a step as a beam stop for electron beam welding and a tight fit (H7/h6). A chamfer is added to the edge of the pipe to allow for enough space for the manufacturing radius of the lid. On the other side of the vacuum box, the two oval pipes (AlMgSi0.5) are cut to the appropriate length and equipped with bores to take in the ISO-KF flanges (see (e) in Figure 4.46).
The oval flange bodies (see (f) in Figure 4.46) are machined from flat bars of aluminum with initial dimensions of $80 \times 50 \times 30$ mm^3. The inner opening is carved out of the oval part to take in the oval tubes. A step is milled into the intake that acts as a field joint

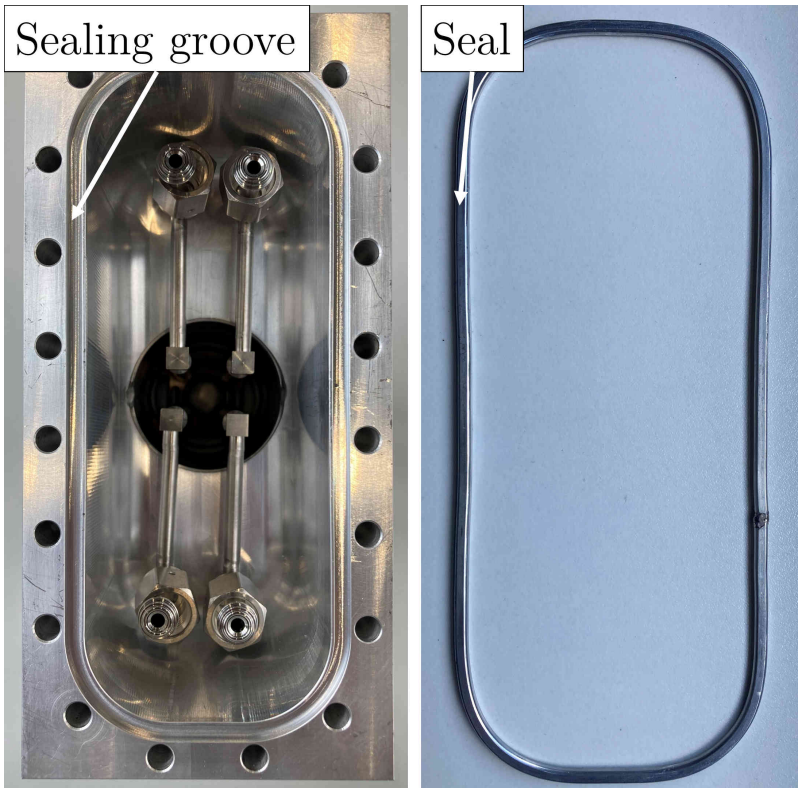

Figure 5.1: Vacuum box with sealing groove (and moderator assembly inside, left) and deformed aluminum round-wire seal (right).

for the the oval tube. Its height is chosen so that an ideal triangular welding seam can be produced. A sealing groove with a depth of 0.7 mm and a width of 1.5 mm is milled into the flange body. Around the sealing groove, six bores with a diameter of 3.2 mm each are inserted for the M3 screw connections (see Figure 5.2).

Moderator vessel:
The moderator vessel assembly is manufactured from aluminum alloy 5083 (AlMg4.5Mn0.7, $R_{p0.2\%} = 145$ MPa), which has a good suitability for welding and does not require a welding filler. As a first step, a round bar of Al-5083 is turned to the needed outer diameter of the vessel. The vessel's outer helium cooling channel is then milled into its surface area by repeatedly turning the cylindrical body around its axis (see Figure 5.3).
The outer diameter of the vessel (see (b) in Figure 4.49) and the inner diameter of the cylindrical shell (see (c) in Figure 4.49) are finished to an H7/h6 fit necessary for electron beam welding. Additionally, grooves with a width and height of 0.5 mm are added on both sides of the welding joint to allow for more flexibility and avoid high stresses in the welded components.
The radial holes connecting the cold moderator cavity with the moderator supply and return tubes are manufactured by using a sink erosion machine. Conventional drilling machines cannot be used here due to the low available space in the 2 cm diameter cavity. For the sink erosion, a cathode with the necessary diameter is manufactured from copper (see Figure 5.4). The lid (see (a) in Figure 4.49) to seal the moderator vessel's inner cavity is manufactured from a round bar of the aforementioned aluminum alloy to the desired outer diameter and thickness. As for the cylindrical shell, an H7/h6 fit between the lid and the moderator vessel is used as a preparation for electron beam welding.

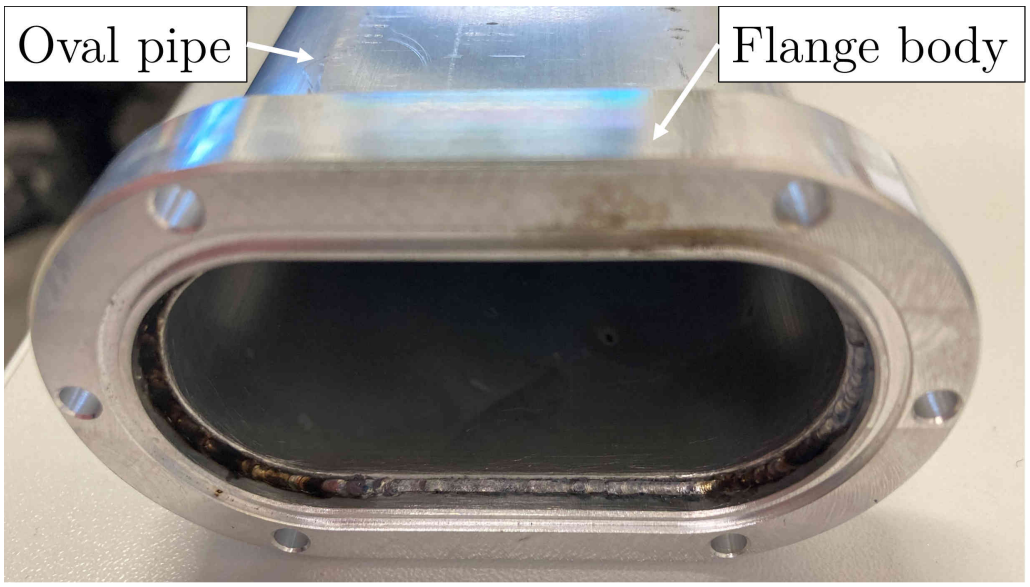

Figure 5.2: Oval flange body with sealing groove and through bores for bolts, welded to oval pipe.

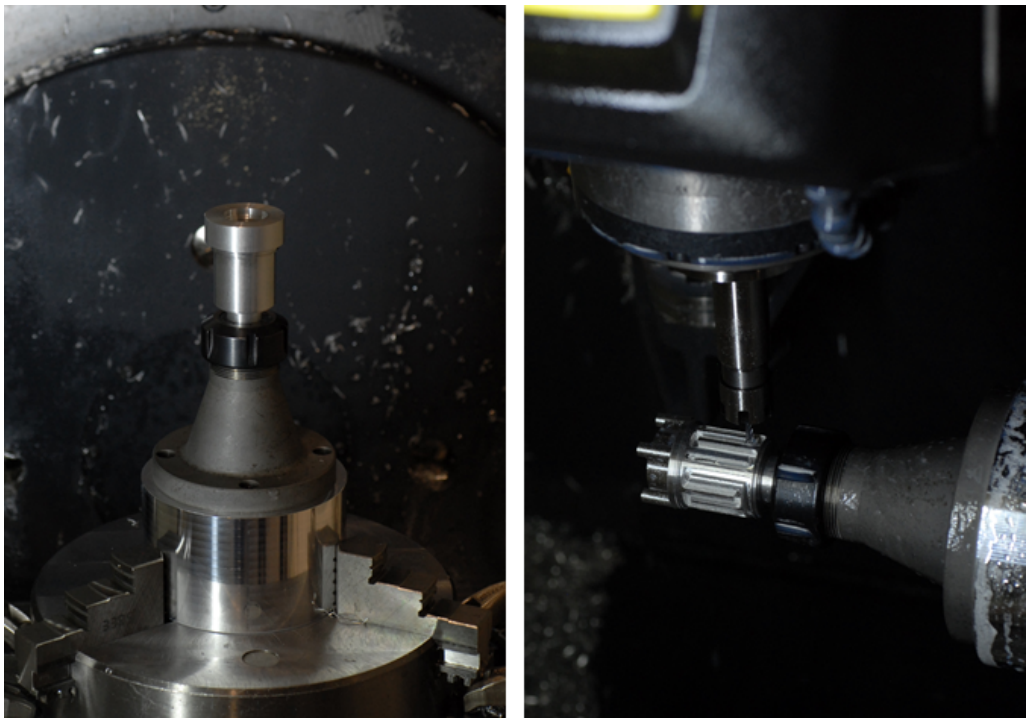

Figure 5.3: Milling of the moderator vessel's base body with helium cooling channels.

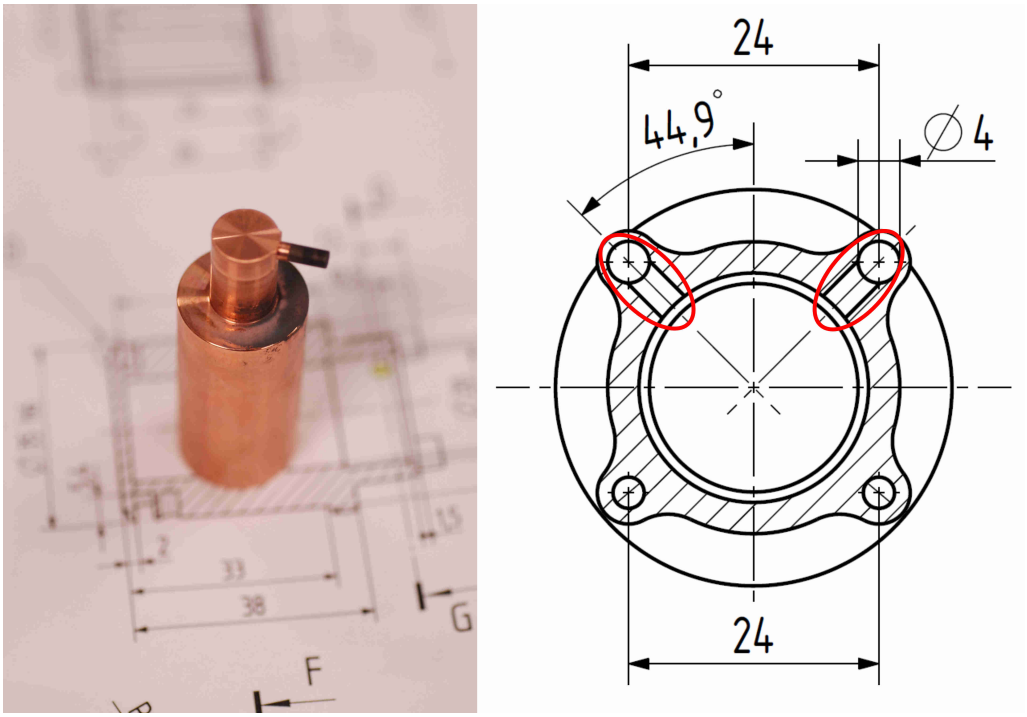

Figure 5.4: Photograph of copper cathode used for the sink erosion of radial connection holes to the moderator volume (left) and front cut view of a technical drawing of the moderator vessel with radial connection holes marked in red (right).

5.2 Welding

Vacuum recipient:
Most of the welding connections for the vacuum recipient are done by manual TIG (tungsten inert gas) welding of aluminum. A main advantage of this welding technique is its high degree of flexibility, since the welding seam geometry is not restricted by the possible movements of a welding machine and no housing for vacuum or inert gas environment are needed. On the other hand, the produced welding seams are relatively large and require enough base material. Figure 5.5 shows the TIG welding seams of the cryostat's vacuum recipient. Due to the available space, the welding joint between the cylindrical pipe and the rectangular box is realized from the outside of the vacuum recipient due to space restrictions. This is normally avoided, since internal micrometer-sized gaps between the components to be joined lead to outgassing and thus to a deterioration of the vacuum pressure ("virtual leaks"). To avoid this, the welding seams have to go all the way through the thickness of the connected parts.

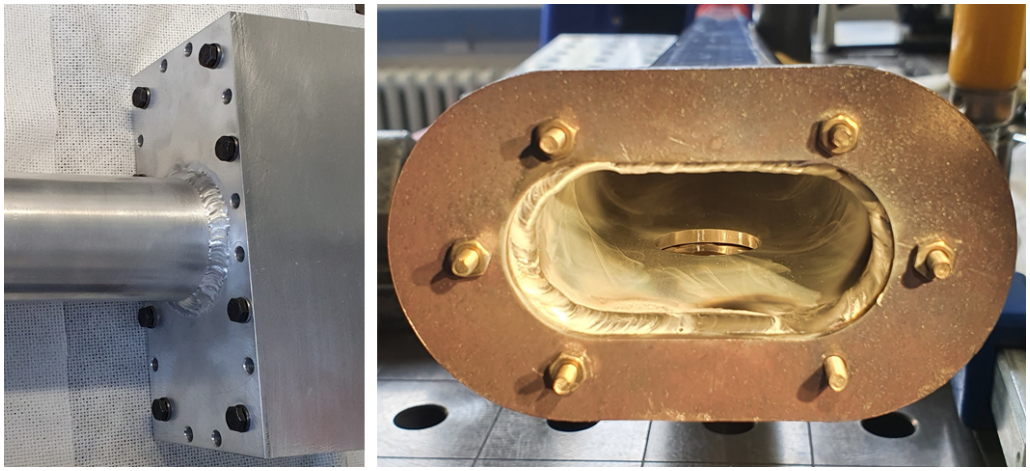

Figure 5.5: TIG welding seam between the vacuum pipe and box of the vacuum recipient (left) and copper heat bridge for the welding of flanges to the oval tubes of the vacuum recipient (right).

The cylindrical vacuum tube surrounding the moderator vessel is closed on one side with a lid-shaped plate. Since the tube should be surrounded by polyethylene during operation with only a small gap in between the parts, the connection is performed by electron beam welding. For this, tube and lid are equipped with a step, so that the inner material serves as a beam stop. Again, the fit is an H7/h6 one to allow only a small gap in between the components.

Transfer lines:
The transfer line section mainly consists of rigid and flexible tubes, either made of stainless steel, Invar36 (iron-nickel alloy) or aluminum alloy 6060 (AlMgSi0.5). The former two materials, which have similar melting temperatures and thermal conductivities, are welded together by using an orbital welding machine (see Figure 5.6, left). The tubes are clamped into a mount for the correct outer diameter. Subsequently, the circular welding path can be divided into different segments and parameters can be defined for each of the segments according to the welding requirements (rising/falling seam). If properly adjusted, a complete tube weld can be performed in approximately 20 s.
To incorporate sections of flexible stainless-steel tubes into the transfer lines, orbital welding cannot be utilized due to the relatively short straight sections of the flexible tube to connect them to a rigid tube. Therefore, laser beam welding is used for this task. It allows the connection of flexible tube by using a welding filler material and the point-wise fabri-

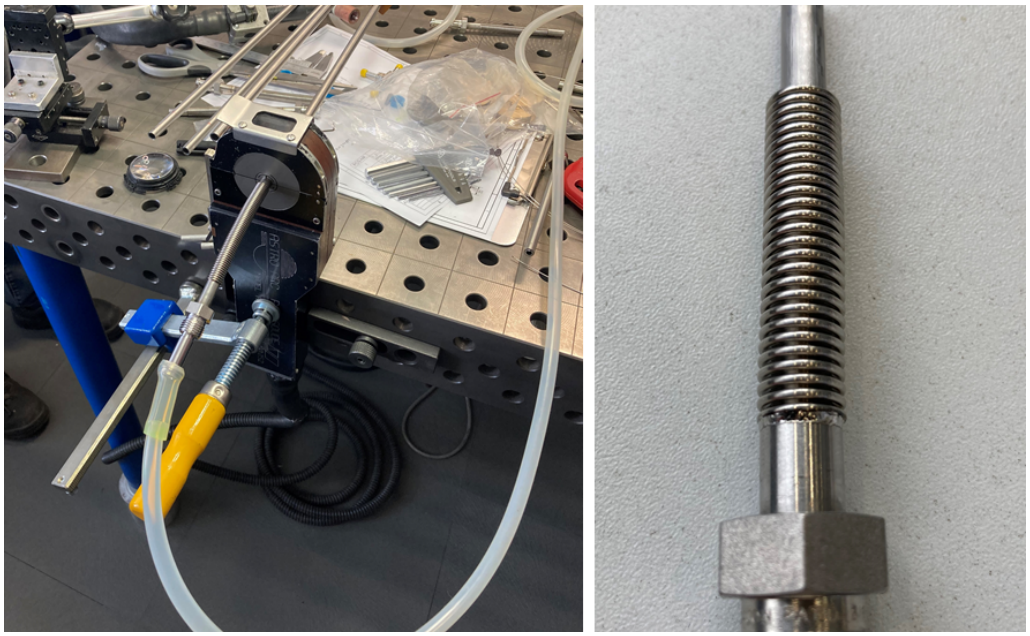

Figure 5.6: Orbital welding machine (left) and laser welding connection between a rigid and a flexible stainless-steel tube (right).

cation of the welding seam. Figure 5.6 (right) shows a laser-welded connection between a section of corrugated tube and a weld-on connector for a metal-sealed screw connection. The transition from stainless-steel to aluminium tubes is realized by using friction welding connections. The single interconnections with a maximum diameter of 10 mm are eccentrically wire-eroded from larger round bars of friction welded stainless-steel to aluminum alloy 5754 (AlMg3). The friction welds are done at the institute ZEA-1 of Forschungszentrum Jülich.

Moderator vessel:
The shell and lid are welded to the moderator vessel via electron beam (EB) welding at the workshop of ZEA-1. Figure 5.7 shows the EB machine (left) and the welding seam between vessel and shell bodies (right).

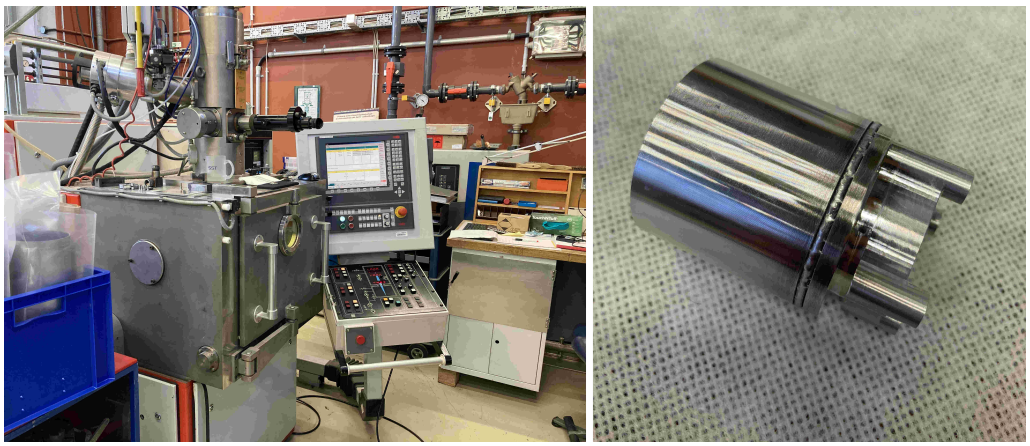

Figure 5.7: Electron beam welding of the cold moderator vessel. Left: EB welding machine. Right: welded cold moderator vessel.

As mentioned above, the material used for the cold moderator vessel is EN AW-5083. This aluminum alloy belongs to the group of non-heat-treatable aluminum alloys and is especially suited for welding. Due to its high magnesium content, no filler material is required,

as compared to curable alloys like Al-6061, which lose their strength in the welding zone and are susceptible for *hot cracks*. Such cracks lower the strength of the connection due to a reduction in joint cross section and may destroy the impermeability of the joint [99]. Due to the high energy density generated in this welding technique, magnesium and zinc evaporate from the weld pool [100].

5.3 Assembly

Cryostat assembly

For ease of handling, the cryostat is mounted on a rack made of aluminium struts to prevent damage to the welding connections between the oval tubes and the attached plate. Since additional components are attached to the flange ends of the oval pipes, high momenta would be created at the welding seams located at the transition to the rectangular plate. At a later stage, the cryostat will be inserted into a shielding plug (see Figure 2.5, bottom, in section 2.4), which was not completely manufactured at the time of commissioning and which requires additional tools for transport due to the high weight of the shielding blocks (especially lead).

Before the cryostat can be operated properly, it has to be fully assembled and equipped with the transfer lines, which have to be inserted into the vacuum recipient and connected to the moderator vessel assembly. Since the sensor and heater wires are attached to a vacuum-suitable feed-through at the opposite end of the vacuum recipient than the moderator vessel itself, they have to be pulled all the way through the oval tubes while inserting the transfer lines (see Figure 5.8). The connecting wire is divided into sections, which can be connected via electrical plugs. This avoids a complete exchange of the wire from the transfer line section when connecting a new temperature sensor or heater to the moderator assembly.

The helium supply tube is covered with a blanket of MLI. When handling and attaching the MLI there are several things to keep in mind to avoid a decline in insulating effectiveness. These are mainly due to the connection of warm to cold parts of the MLI. It shall therefore be connected layer by layer at the intersections. Also, some overlap shall be integrated at the connection points to avoid gaps between the cold and warm surfaces due to thermal contraction of the MLI. Furthermore, it shall be handled with gloves to prevent a degradation of the emissivity by touching it.

Figure 5.8: Assembly of the transfer lines into the vacuum recipient with attached sensors and heater cable.

The temperature sensors and heater wire are attached to the moderator vessel by using an epoxy resin suitable at cryogenic temperatures (Loctite StyCast 2850FT). For the sensors, copper blocks are machined to form and glued to the aluminium tubes. They have threaded holes for mounting the silicon diodes and applying pressure for a sufficient thermal transfer. The heater wire is coiled around the tubes prior to the temperature sensors and coated with the epoxy resin (see Figure 5.9).

As soon as the transfer lines and moderator vessel are connected and helium leak tested and the sensors are mounted and tested by connecting them to a temperature controller, the vacuum recipient can be closed and helium leak tested (see section 5.4).

At the top DN16 ISO-KF connector, a DN40 ISO-KF crossing is mounted (see Figure 5.12), to which in turn the electrical feed-through, a safety valve and a cold cathode vacuum pres-

sure sensor are attached. The location of the vacuum pressure sensor at the opposite end of the other oval tube allows a conservative pressure reading.

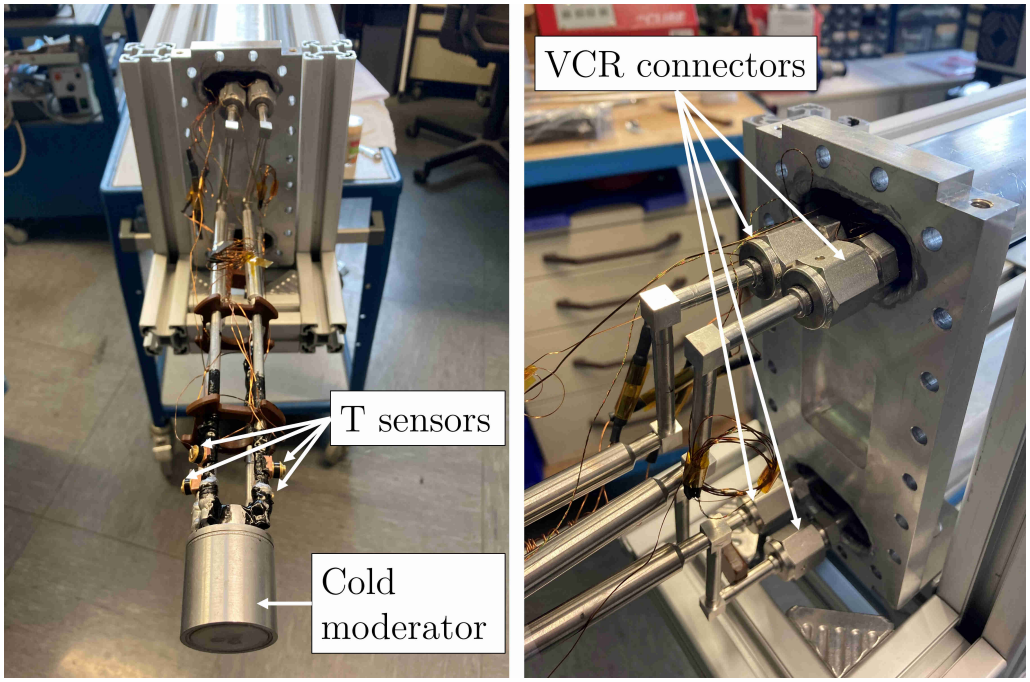

Figure 5.9: Assembled moderator vessel and mounted sensors and heater (left) and close-up on the screw connections for the four tubes (right).

Gas management panel assembly:
For the gas management panel, a base frame is mounted from aluminum struts of different length, which are equipped with wheels for easy transportation. For the installation of the components for fluid flow control, two aluminum plates with a thickness of 3 mm are water-jet cut to the desired outer dimensions. The required holes for electrical feed-throughs and mounting threads are also cut out by using the water-jet machine.
After assembly of the main components (mass flow controller, 2-way valves), the remaining parts (filters, T-pieces, crossings, etc.) are joined via cutting ring connections. The intermediate tubes are made of stainless steel with diameters of 6 mm, 10 mm, and 12 mm, and are cut to the required lengths. Where metal-sealed connectors are used, they are welded to the appropriate tube using an orbital welding machine.
Figure 5.10 shows the front and back of the completely assembled and commissioned gas management panel.
At the back side of the GMP, another water-jet-cut aluminum plate is installed, which is equipped with a rail for mounting a programmable logic control (PLC)from Siemens and the valve terminal from Festo. In a first setup, the valve terminal was replaced with a preliminary 2-way electromagnetic valve assembly due to a delay in delivery. An electric control box for central power supply and control is planned for a future upgrade of the GMP.

Infrastructure assembly:
After the cryostat is assembled and in position, the gas management panel can be connected to it mechanically and electronically. The moderator transfer lines as well as the helium exhaust line are connected to the correct inlet and outlet ports at the GMP via flexible metal tubes with metal-sealed connectors at their ends.
The vacuum pressure sensor is connected via a Profinet connection to the programmable logic controller of the GMP. The electrical feed-through is connected to the temperature controller TC336 (LakeShore). The turbomolecular pump (TMP, HiPace 80, Pfeiffer) is

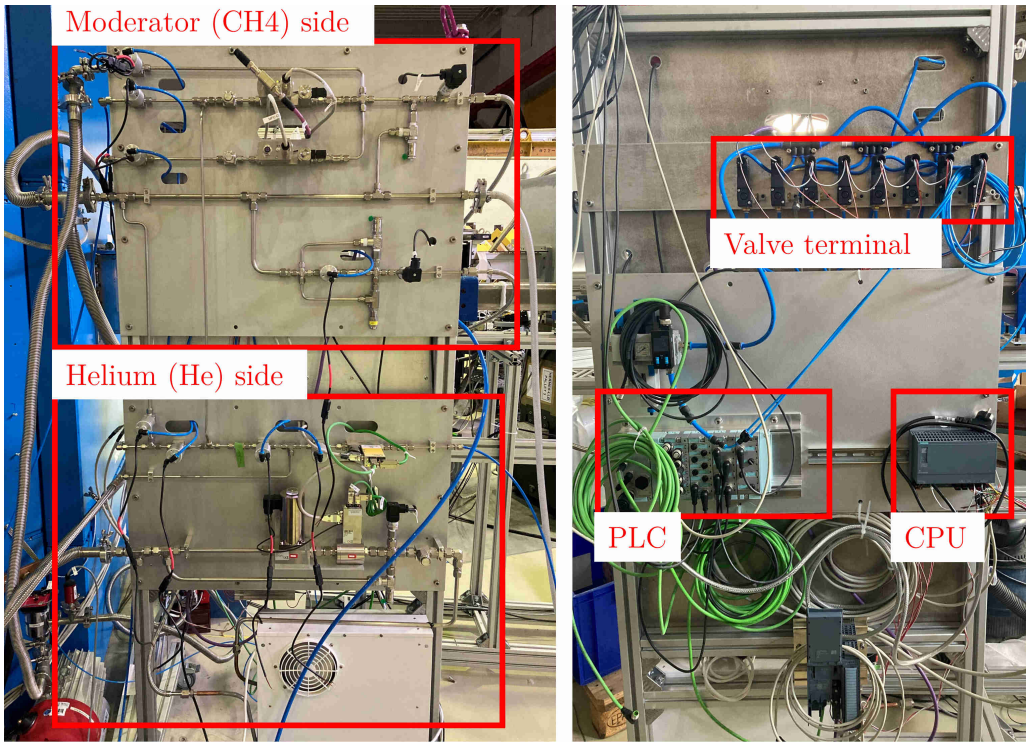

Figure 5.10: Front (left) and back (right) of the gas-management panel for the control of the moderator cryostat.

attached to the bottom DN16 ISO-KF of the cryostat's vacuum recipient. In between the TMP and the vacuum recipient, a remotely-controllable angle valve is positioned to allow a detachment of the vacuum recipient from the TMP in case of failure. Furthermore, it can be used to prevent damage to the TMP by prohibiting an opening in case the pressure inside the vacuum recipient is too high while the TMP is still in operation. The exhaust of the TMP is connected to a scroll pump (HiScroll 6, Pfeiffer), again with a remotely-controllable angle valve in between. This valve allows the aforementioned decoupling of the scroll pump from the TMP to be used as a purging pump for the gas tubes. Since the scroll pump is designed conforming to the ATEX directive, it can be used to safely pump the methane lines. To avoid the leakage of flammable gas into the room in which the system is set up, the safety valve of the vacuum recipient and the exhaust port of the scroll pump are connected to the vent line port of the GMP, which is in turn connected to a ventilation duct to the outdoors.
The mass flow controllers (MFC), helium pressure controller (PC), pressure sensors (PT) and pneumatic valves (PnV) are all connected to the PLC attached to the GMP. The PLC can be controlled by connecting it to a computer via Ethernet and using a software like LabVIEW to send commands to the PLC and receive data.
Gas supplies (N_2, He, CH_4) have to be connected to the correct ports of the GMP and a compressed gas connection has to be established to correctly control the pneumatic valves. A pneumatic valve terminal at the back of the GMP allows a centralized distribution of the pressurized air to the individual pneumatic valves. The liquid helium (LHe) supply is provided by a 100L or 250L LHe dewar. This dewar is connected to the cryostat via an insulated semiflexible transfer line. It is attached to the cryostat by using a Johnston coupling, largely reducing the heat load onto the LHe compared to a standard connection. The LHe dewar is additionaly connected to the GMP, to allow a pressure regulation inside the dewar by feeding helium gas of a high purity to it. The high purity of the helium reduces the probability for other gases to freeze at the needle valve of the insulated transfer line or by contaminating the return gas to the central helium liquefaction facility.

5.4 Non-destructive testing

After manufacturing and assembly, it is necessary to examine the weld and screw connections to make sure the system is fully functional at the chosen operating conditions. This includes testing the vacuum components for pressure resistance (either internal or external), checking components for leak-tightness and testing the various components by applying a test pressure of 1.43 times the design pressure.

Weld examination:
A way of examining welding seams for surface cracks and pores, which can lead to damages of the weld, is by applying a liquid dye with a low surface tension. It penetrates the irregularities inside the material under investigation through capillary effects. The liquid can either be fluorescent (see Figure 5.11, which shows the dye penetration inspection after welding of an oval pipe to the rectangular plate of the vacuum box connection) or non-fluorescent. Before the dye is applied, the component or weld has to be thoroughly cleaned. The technique allows a detection of leaks, but offers no precise information on the size of the leakage. In addition, the surfaces have to be mechanically prepared and cleaned to avoid a large number of dye penetrations. In case of re-welding after the application of a dye penetrant, it has to be removed thoroughly by removing the affected material to avoid an impact on the weld.

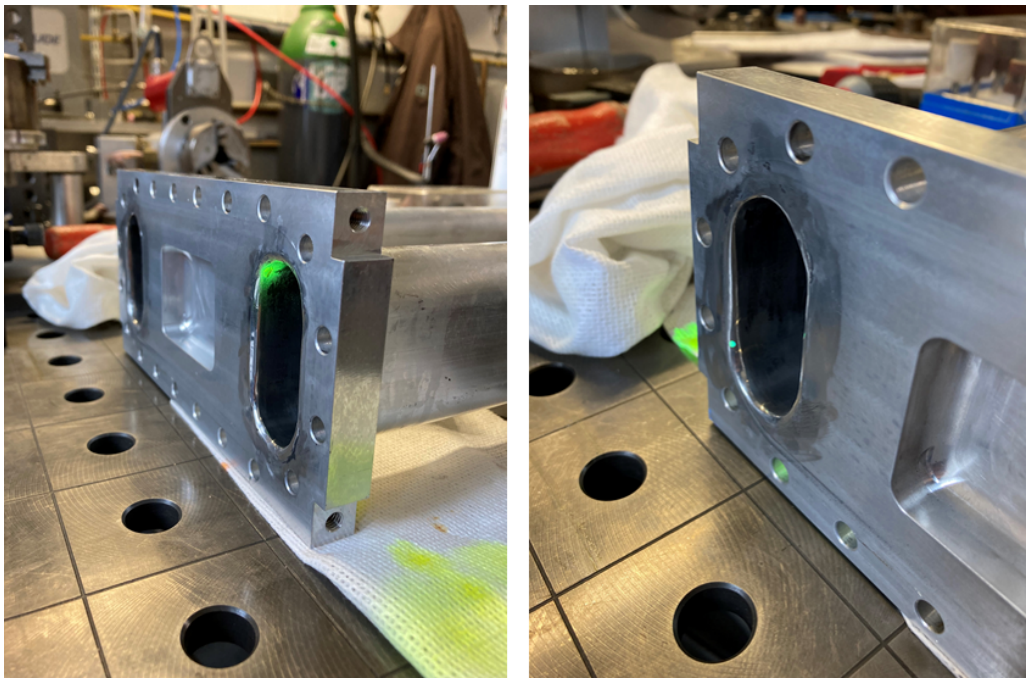

Figure 5.11: Dye penetration inspection of the welding seam between the oval tube and the attached aluminum plate.

Leak detection:
One method for the detection of larger leakages is the use of a bubble test, for which the component is pressurized and put into a water bath, in which potential leaks lead to a formation of gas bubbles. The velocity of the bubble formation gives rough information on the size of the leak. However, the method is generally not suitable for detecting small leaks ($Q_L < 10^{-3}$ mbar $\cdot$ l/s), since the formation of single bubbles takes a long time.
A more precise leak detection method is by using a commercially available spectrometer for detecting helium (see Figure 5.12) or light gas mixtures like argon-hydrogen. This method usually allows a good determination of the leak size in a short time and down to

leak rates of $Q_L < 1 \cdot 10^{-12}$ mbar$\cdot$ l/s. Instruments based on this technique usually allow two different testing methods. One is the evacuation of the component under investigation and an application of helium on its surface or connections. The other is a pressurization of the component with helium gas and the detection via a so-called sniffer probe, which constantly absorbs the environment around the probe. Although reliable, the machines are expensive and need maintenance due to their more complex internal assembly. In addition, the technique is sensitive to higher amounts of the detection gas in the surrounding atmosphere, leading to high background readings. This might make the detection of small leaks harder and tedious, depending on the location at which the tests are conducted.
All welding connections for the components in this thesis are precision leak-tested by using a mass spectrometer. The allowable leak rates were set to:

- $Q_L \leq 1 \cdot 10^{-8}$ mbar $\cdot$ l/s for the methane-carrying section
- $Q_L \leq 1 \cdot 10^{-9}$ mbar $\cdot$ l/s for the helium section and the vacuum recipient

The former is motivated by the relatively large size of the methane molecules, the latter by the size of the helium atoms and the vacuum requirements. The maximum measured leak rate was $Q_L \approx 10^{-8}$ mbar$\cdot$l/s. After testing every welding connection, the cryostat is assembled. The metal-sealed screw connectors and the O-ring sealed screw connections of the vacuum recipient are helium leak tested as well to ensure that no gas can leak from the tubes into the vacuum recipient or the ambient surrounding. Furthermore, all pressurized components withstood the applied maximum pressures.

Figure 5.12: Helium leak test of the vacuum recipient using a mass spectrometer.

5.5 Destructive testing

Apart from the non-destructive techniques for examining the cryostat system, the corrugated stainless steel tubes used for flexibility in the tubing system are investigated, which pose two problem zones: the welding seam between rigid and corrugated tube and the corrugated tube itself. The experimental tests were performed using an apparatus for pressure testing (see Figure 5.13). In this apparatus, a piston can be moved via a handwheel to compress the volume inside a test specimen. The specimen is connected to the apparatus by a thread sealed with Teflon tape. The compression space is filled with oil to avoid excessive pressures.

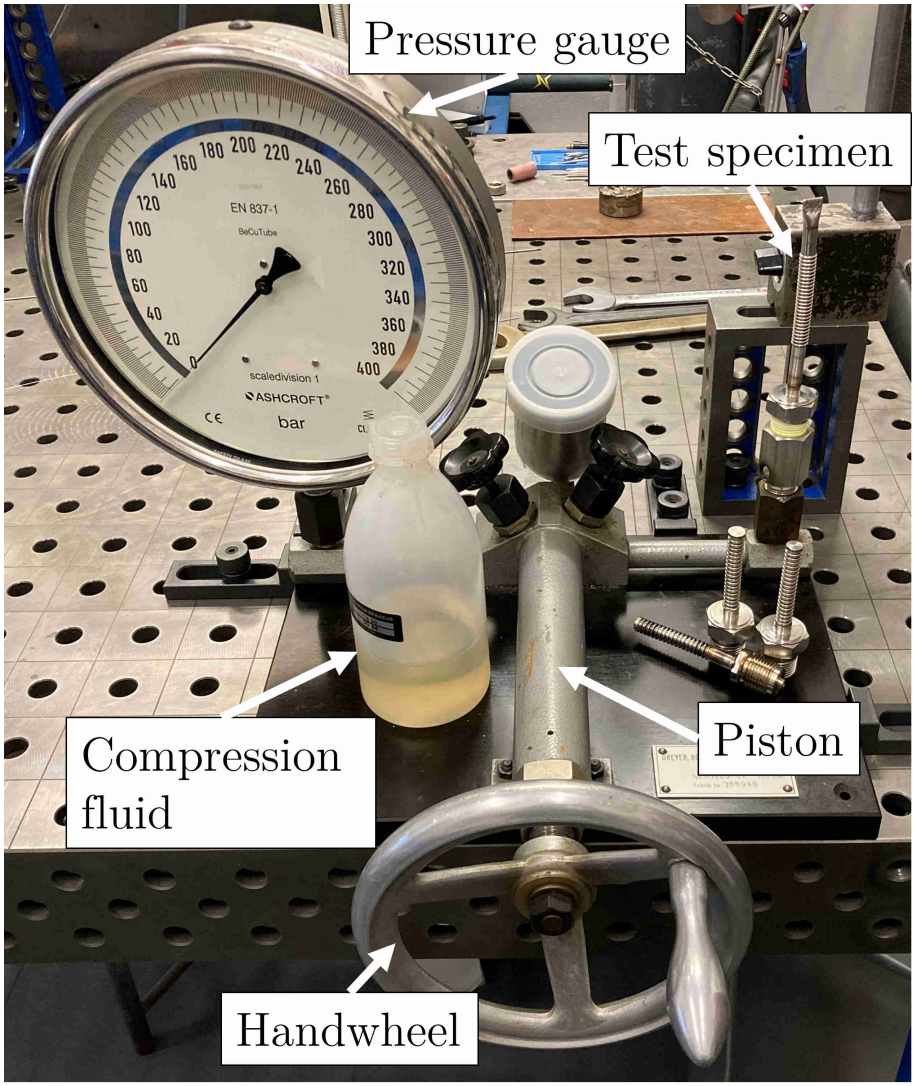

Figure 5.13: Test apparatus filled with incompressible fluid for the pressurization of test specimen. A section of a laser-welded corrugated tube is attached via a Teflon-sealed thread connection.

Figure 5.14 shows the elongation and the remaining plastic deformation of the corrugated tube at various pressures and for laser-welded and brazed connections. It is apparent from the results that the corrugated tubes can withstand pressures higher than the test pressure of the fluid transfer lines by at least a factor of 18.6 and 28 for the moderator and helium line, respectively. However, after reaching pressures of approximately 30 bar(g), a plastic deformation of $\Delta L = 0.05$ mm and $\Delta L = 0.13$ mm remains for the welded and brazed joint, respectively.

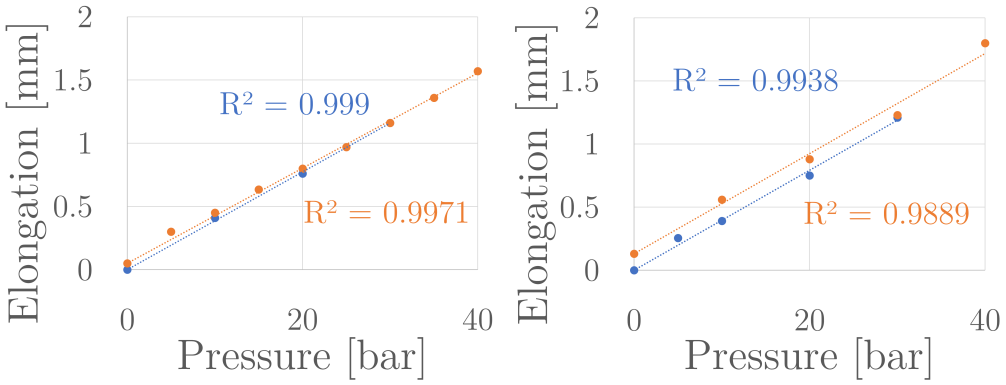

Figure 5.14: Elongation vs. applied pressure for a laser-welded (left) and brazed (right) joint with coefficients of determination (R^2). The blue curve depicts the first pressurization, while the orange curve shows the repeated pressurization after plastic deformation.

Chapter 6

Experimental validation

In this chapter, the commissioning of the manufactured cryogenic system and its operational procedure, including cool down, basic operation and warm-up, are presented. Furthermore, the system's efficiency as a cold moderator is tested at a facility providing free neutrons to perform time of flight experiments. The obtained data is subsequently corrected and analysed to allow a comparison to previously conducted experiments using a liquid parahydrogen cold moderator. This way, the feasibility of a solid methane moderator with regards to cold neutron production for the High Brilliance Neutron Source can be evaluated. The system provides a basis for further experiments with different moderator geometries and materials.

6.1 Commissioning and basic operation

Before operation with neutrons, the cryostat is cooled down to find suitable parameters for the process of condensing the methane in the moderator vessel. This way, a suitable operating procedure can be mapped out, which builds the basis for future plans of automation. The cryostat is operated mainly (with the exception of the vacuum system for insulation) via a LabVIEW-VI (Virtual Instrument) (see Figure 6.1), that was generated in the context of this thesis. It consists of multiple tabs for establishing the connection to the PLC and temperature controller, reading data from the devices and writing commands to them, as well as plotting the data. Furthermore, it allows data logging with any desired logging interval and has a comment option.
Following, the necessary steps for cooling down, liquefying and freezing as well as warming up the methane are listed:

1. Turning on the air heat exchanger to warm up the cold helium return gas.
2. Pumping the vacuum recipient until a vacuum pressure of $p_{vac} \leq 5.0 \cdot 10^{-4}$ mbar is reached at the cold cathode pressure indicator attached to the oval tube opposite to the one connected to the vacuum pumps.
3. Pumping the helium tubes of the GMP with the scroll pump down to $p \leq 5$ mbar at the helium exhaust pressure sensor.
4. Pumping the moderator tubes with the scroll pump down to $p \leq 5$ mbar and purging it repeatedly with methane gas.
5. Purging the vent line with nitrogen to avoid the accumulation of flammable mixtures.
6. Pressurizing the moderator tubes and vessel with approximately 1 bar(g) of methane gas.
7. Setting heater 1 (He) to 98 K and heater 2 (CH_4) to 110 K, ranges to "Medium".

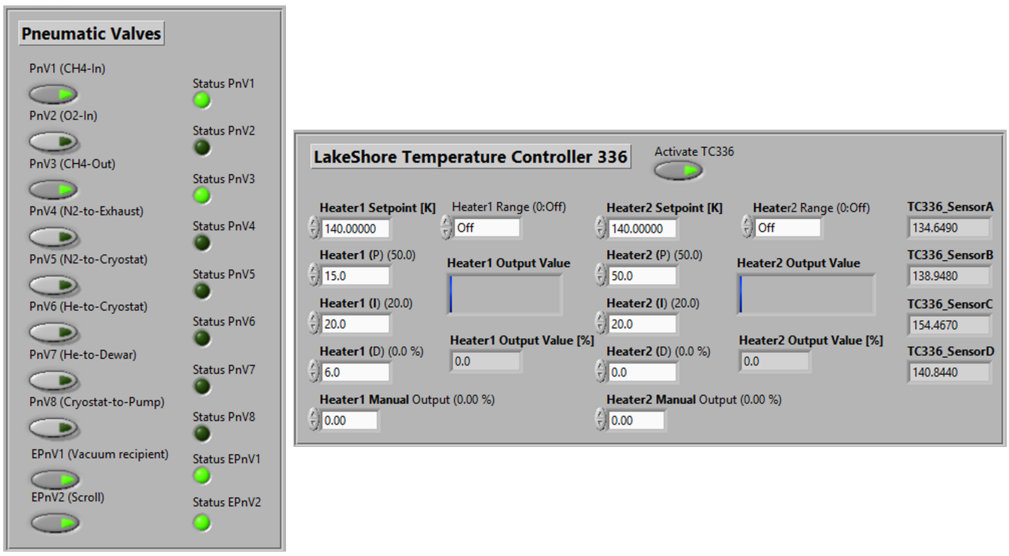

Figure 6.1: Valve and temperature controls of the user interface of a LabVIEW-VI for controlling the cold moderator cryostat.

8. Opening the helium MFC to allow a flow of coolant through the helium tubes and cooling channels of the moderator vessel.

9. The temperatures should fall until sensor B (helium-out) stabilizes at approximately 120 K, the liquefaction/evaporation temperature of CH_4 at a pressure of 1 bar(g).

10. As soon as the moderator vessel is filled with liquid CH_4, temperature sensors C (CH_4-in) and D (CH_4-out) drop to 120 K and the reading of sensor B starts decreasing again (see Figure 6.2, top).

11. The liquid CH_4 can be frozen by decreasing the set point of heater 1 to values below 90 K (freezing temperature of methane, see Figure 6.2, bottom). Heater 2 shall remain at a value above the freezing temperature to avoid a blocking of the tubes. By turning off heater 2, lower temperatures are achievable. However, during the performed measurements, the heater stayed in operation during the freezing process as a precautionary measure.

12. For warm-up, the helium mass flow shall be interrupted by closing the MFC at the exhaust. Due to insufficient cooling, the temperatures will rise. By leaving heater 2 in operation, the exhaust tube stays unblocked and the evaporating gas can escape from the moderator vessel.

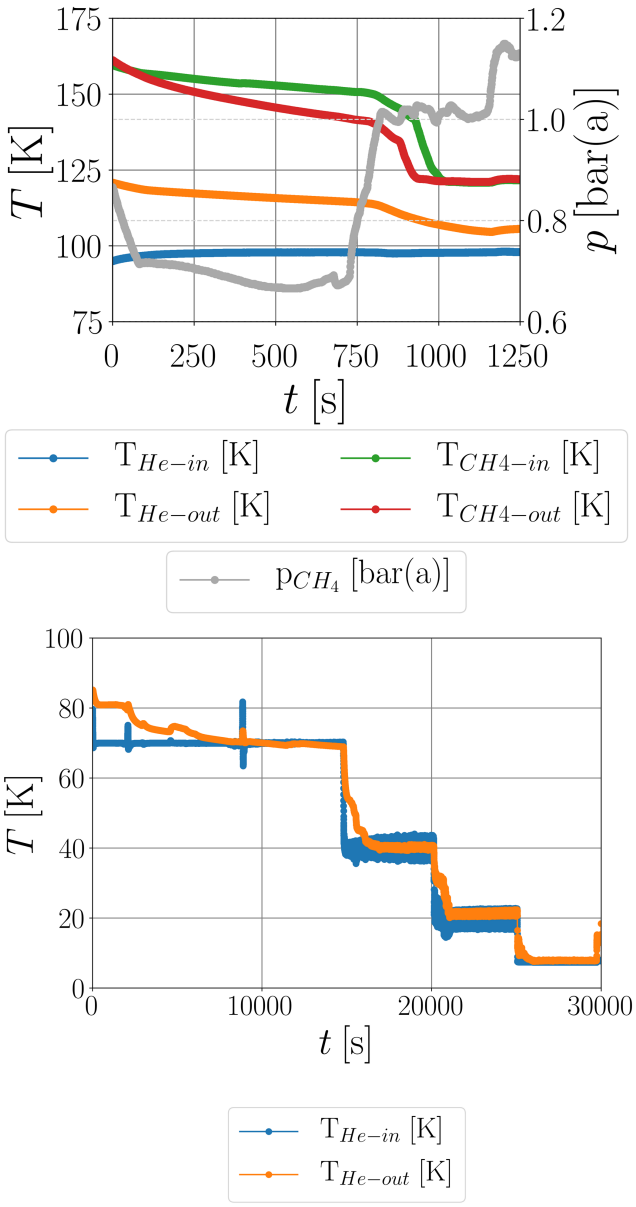

Figure 6.2: Pressure and temperature curves for the filling of the moderator vessel with liquid CH_4 (top) and helium temperatures ($\approx T_{mod}$) during operation with solid CH_4 (bottom) vs. time.

6.2 Experiments with neutrons

6.2.1 Experimental procedure

To assess the moderating efficiency of the cold moderator, the neutron time of flight (ToF) technique is applied. This technique requires a pulsed beam of neutrons, either generated by using a pulsed proton beam to produce the free neutrons or by using a chopper system in the neutron beam line. Figure 6.3 schematically shows a very basic principle of the time of flight technique.

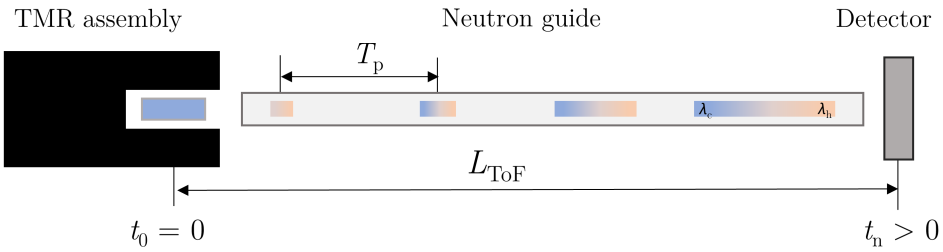

Figure 6.3: Schematic principle of the time of flight technique. T_p is the period between pulses, t is the time of flight, L_{ToF} the flight path and λ_n the wavelength of the neutrons.

Neutrons are produced in the time between $t_0 = 0$ and Δt_{pulse} (= proton pulse length). This value – plus the die-away time in the TMR assembly – also gives the intrinsic uncertainty. By knowing the exact distance L_{ToF} traveled by the neutrons and measuring the time Δt between production and detection of the neutrons, the neutron velocity $v = \frac{L_{ToF}}{\Delta t}$ in [m/s] is estimated. This information can subsequently be converted to the neutron energy, wavelength or temperature by applying the respective conversion factors. Since the neutron can be considered as both a wave and a particle, it has a wavelength λ_n and a kinetic energy E_n. The velocity can be transformed to energy or wavelength by following formulae [8]:

$$v_n = \sqrt{\frac{2 \cdot E_n}{m_n}} = \frac{h}{m_n \cdot \lambda_n} \tag{6.1}$$

with the Planck constant h, the neutron mass m_n and the neutron wavelength λ_n.
The raw data obtained by a detector at a certain distance L_{ToF} from the cold moderator surface can be corrected and normalized and subsequently serves as a figure of merit to compare the performance of cold moderators.
By using a neutron transport software like VITESS (Virtual Instrumentation Tool for ESS) or McStas (Monte carlo Simulation of triple axis spectrometer), the source characteristics can be reconstructed and used to retroactively calculate the obtainable brightness for a certain application and proton source power. In the following subsections, the necessary measures to correct the data are presented and the procedure to calculate the moderator efficiency is demonstrated.

6.2.2 Experimental setup

The ToF measurement setup is shown in Figure 6.4. The free neutrons for conducting the measurements are produced and slowed down in a target-moderator assembly, which is bombarded with protons from the isochronous cyclotron *JULIC* (JUelich Light Ion Cyclotron). This cyclotron provides pulsed proton or deuteron beams with maximum energies of 45 MeV and 76 MeV, respectively.

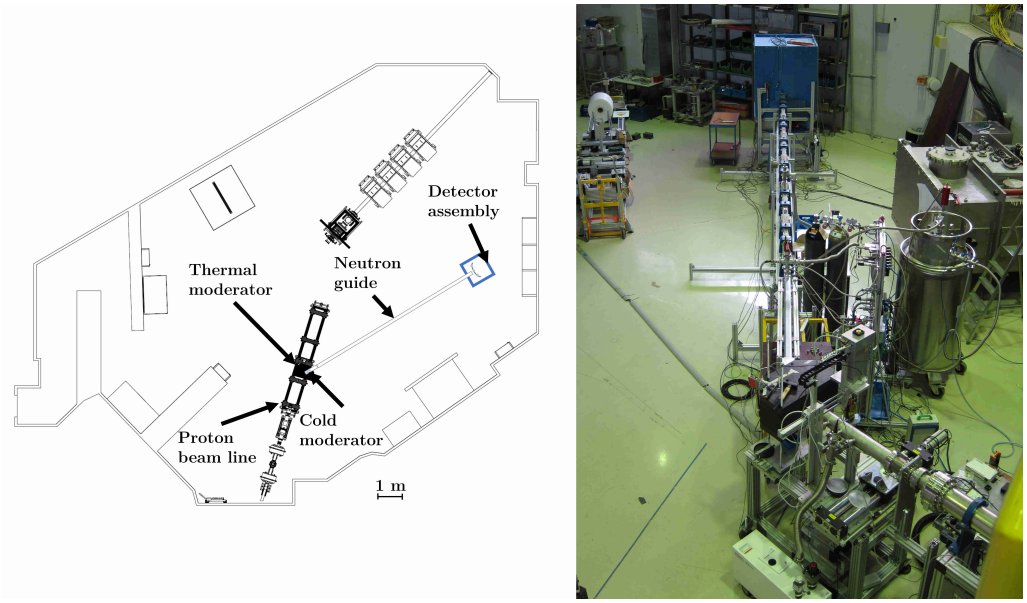

Figure 6.4: Floor plan (left) and photograph (right) of the Big Karl area at the COSY facility with the ToF measurement setup.

The H^- or D^- pulses are accelerated inside the cyclotron and extracted via a septum magnet. They are subsequently focused and directed by several quadrupole and dipole magnets, respectively. The beamline NESP (NiederEnergiebeStrahlungsPlatz) is aimed at a block of high-density polyethylene (HD-PE), which acts as a thermal moderator and embeds the neutron target and cold moderator.
The target consists of tantalum (Ta) and is a circular disc with a diameter of 80 mm and a thickness of 5 mm. This choice results from an investigation of the neutron yield of different target materials at various energies, performed at the HBS project [34]. The target is tilted by 45° with respect to the axis of the proton beam line (see Figure 6.4) to allow a positioning perpendicular to the center axis of the cold moderator vessel. The angle is a result of the available space at the Big Karl area to allow the installation of a neutron flight path of seven to eight meters with an attached detector assembly. A longer flight path enables a better resolution of longer wavelengths.
When connecting the tantalum target to ground, the protons hitting the target create a current that can be measured by amplifying and converting it into a voltage signal with a picoamperemeter. The conversion factor can be adjusted from 1 pA/V to 1 mA/V. Since the minimum resolution frequency of the data logging system EPICS (Experimental Physics and Industrial Control System) used for data storage is only 10 Hz, the voltage signal is integrated both for the pulse and for the background in between pulses by using a RedPitaya FPGA (Field-Programmable Gate Array) (see Figure 6.5). The proton count measured this way then allows a normalization of the detected neutron count, which is important when comparing different measurements performed at the Big Karl area.
The cold moderator is inserted into the HD-PE block by using an extraction channel with a diameter of 98 mm. Since the outer vacuum tube surrounding the cold moderator vessel only has a diameter of 60 mm, an additionally manufactured polyethylene "cup" is put over

the vacuum tube (see right picture of Figure 6.6) to increase the amount of polyethylene directly around the cold moderator and to avoid a large air-filled gap in between.

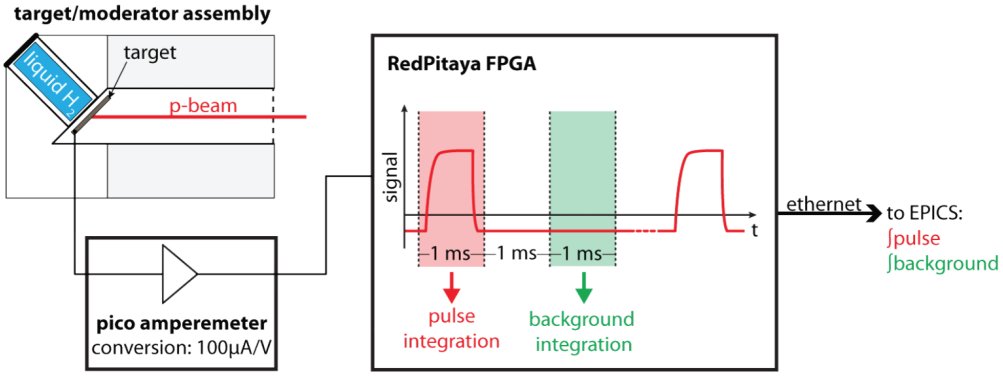

Figure 6.5: Schematic working principle of the proton current measurement performed at the Big Karl area (image taken from [101]).

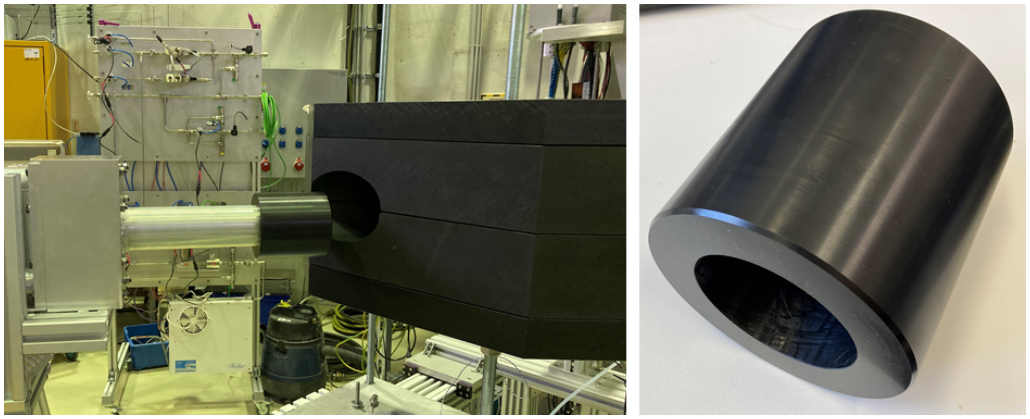

Figure 6.6: Thermal moderator blocks made of high-density polyethylene (HD-PE, left) and "cup" for compensating for the difference in diameter between extraction channel and vacuum recipient.

A neutron guide with a total length of 8 m is positioned at the edge of the vacuum box, with its entrance window facing the emitting surface of the cold moderator. The guide has a constant rectangular cross section and is constructed of four walls made of ^{58}Ni-coated glass with a neutron refractive index of $m_n = 1.2$. Its inner width is 30 mm and its inner height is 45 mm. The whole neutron guide consists of single 1 m-long segments, of which seven are connected by silicone joints and sealed at the ends by using aluminum plates to allow the generation of a rough vacuum inside the guide. An additional segment is loosely placed between the oval tubes of the cryostat and is neither connected to the rest of the neutron guide nor evacuated, due to time constraints. The choice to use an unevacuated segment of neutron guide is based on the reflectiveness of the guide's surfaces. Although scattering and absorption in air will occur inside this first guide segment, the reflecting surfaces still lead to an improvement in neutron transmission compared to the case of no guide for the first meter.
The neutrons that are transmitted through the neutron guide enter a box with walls made of borated polyethylene (B-PE) for background shielding. The walls have a thickness of 4 cm, which is sufficient to absorb most of the neutrons. Multiple ^{3}He detectors are positioned inside the box, of which three are mounted onto a goniometer assembly to allow an adjustment of their position (Figure 6.7).

Figure 6.7: Opened detector assembly box (left side of left photograph) shielded by walls of borated polyethylene (blue) and including multiple ^{3}He detector tubes (right).

These detectors consist of a cylindrical steel shell filled with ^{3}He gas with a pressure of approximately $p_{det} = 4.3$ bar(g). The steel shell has an outer diameter of $d_{o,det} = 25.4$ mm, a wall thickness of $t_{w,det} = 0.8$ mm and a height of $H_{det} = 200$ mm. Inside the detectors, neutrons are absorbed by the ^{3}He atoms, leading to (n,p) reactions, in which a ^{1}H and a ^{3}H isotope as well as approximately 0.76 MeV of energy are produced. A wire that is connected to a high-voltage supply ($U = 1.2$ kV) and runs along the center axis of the cylindrical tube creates a radial electrical field inside the detector tube. This field causes the protons from the initial reaction to be accelerated towards the detector's steel shell while generating negatively charged particles through collisions with the He gas. These negatively charged particles are in turn accelerated towards the wire and flow through it and out of the detector tube. The signal is amplified and divided into time bins by a Multi-Channel-Analyser (MCA). To make sure that only events from the neutron reactions are detected, signals with a voltage lower than a threshold voltage are suppressed. This way, the detection of contributions from e. g. gamma radiation can be omitted.
Apart from the goniometer detectors, an additional detector is attached to the outer wall of the detector box next to the neutron guide and another one is positioned at an outer surface of the thermal PE moderator. These detectors serve as additional quantities for normalization as well as a method to check the validity of the current measurement.
The distance between the cold moderator's surface viewed by the neutron guide and the detector is determined by adding up both by measurements and by taking values from CAD models. For the measurements, a laser sensor is used. Figure 6.8 shows the schematic side view with the corresponding distances. The total distance adds up to $L_{ToF} = 8588$ mm $\pm$ 10 mm.

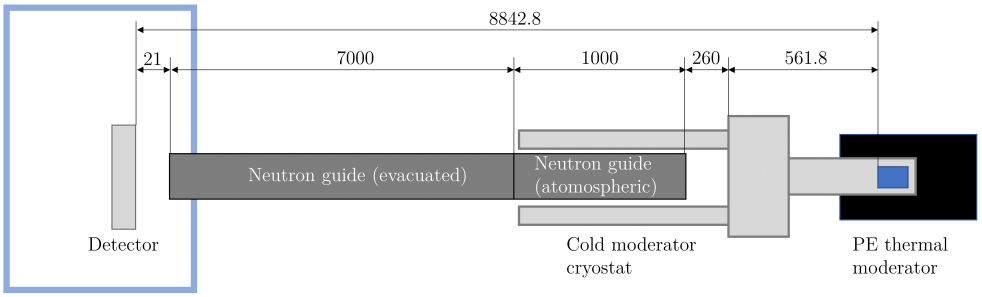

Figure 6.8: Schematic view of the ToF setup with dimensions and distances between elements in [mm] (sketch not true to scale).

6.2.3 Experimental results

Measurements were performed over two days for different temperatures of liquid and solid methane. The measurement duration was one hour for every temperature to obtain sufficient statistics. Table 6.1 lists the different temperature measurements divided by date. To enable a comparison between the different measurements, they are corrected and normalized to compensate for variations in the proton current and therefore the total amount of neutrons produced during the different runs.

Table 6.1: Measurement runs performed on two different days with moderator temperature and physical state.

Date	Run number	T_{mod} in [K]	State	Proton count
02/04/2022	#30	290	Vacuum	$1.37e+14$
	#44	100	liquid	$1.13e+14$
	#59	7.5	solid	$1.20e+14$
06/04/2022	#63	70	solid	$4.25e+13$
	#67	40	solid	$4.30e+13$
	#72	20	solid	$4.29e+13$
	#75	7.4	solid	$4.28e+13$

Raw data:
The neutrons are counted by dividing the time frame of the measurement of each pulse into a finite number of bins with a fixed size. For all of the present measurements, the time frame was set to 100 ms with a bin size of 0.2 ms, which yields a total number of 500 bins. For each pulse during one measurement, the neutrons detected in between the edges of a specific bin are summed up, creating a histogram of the time-dependent neutron intensity (see Figure 6.9). Therefore, the accuracy of the measurements improves with longer runtime, since the obtained statistics increase.

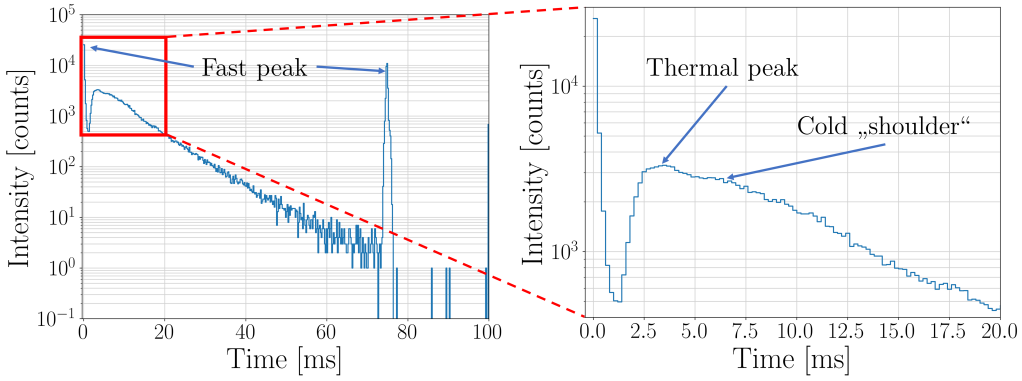

Figure 6.9: Histogram of the time-dependent intensity distribution for one measurement (#59) with solid methane at 7.5 K over the whole time frame (left) and in a detailed view (right).

The pulse frequency during all measurements was $f_p = 13.33$ Hz, which corresponds to a pulse period of $T_p = 75$ ms, which can be seen in the distance between the peak at $t = 0$ ms and the one at $t = 75$ ms in Figure 6.9. When converted to wavelength, this period yields a maximum value of $\lambda_{max} = 34.5$ Å.
The high neutron count at $t = 0$ ms can be attributed to the fast neutrons that are almost instantaneously created when the proton pulse hits the tantalum target. The following (thermal) peak at around $t = 3.5$ ms ($\lambda_n = 1.6$ Å) is caused by neutrons moderated

mainly in the polyethylene thermal moderator. The peak at around $t = 75$ ms is part of the fast pulse and can be ascribed to a delay between the trigger signal of the cyclotron and the start of the neutron detection measurement. Since the latter is delayed, the first part of the fast neutron pulse is cut away and the beginning of a new pulse is shown at the end of a pulse period.
The counts displayed directly after $t = 75$ ms are a result of slight deviations in the pulse duration of up to 2 ms. The counts at 100 ms are the sum of all neutrons detected after the termination of a time frame. Those counts are detected during a periodic discharge of the septum magnet used to extract the proton pulses from the cyclotron. This discharge happens every 2 s for 20 ms. In this case, the pulse period is expanded until a new trigger signal from the cyclotron is received.
The uncertainty of the time (or wavelength) resolution of the obtained spectra is introduced by the width of the proton pulses, which is $t_p = 300$ µs, since there is no information on which proton is responsible for the release of a certain neutron. For the wavelength, there is an additional uncertainty introduced by the uncertainty of the length travelled by the neutrons, although this value is negligible compared to the pulse length and the die-away time of the neutrons inside the cold and thermal moderator. The split-up and shift of the fast neutron peak introduces an uncertainty to the time scale of the neutron spectrum. The beginning of the neutron pulse can be defined as the center of a Gaussian curve fitted to the fast neutron peak with an uncertainty corresponding to the FWHM of the curve [102].
To obtain the flux of cold neutrons that is emitted by the cold moderator and to be able to compare it to other measurements, several corrections have to be included:

Neutron background:
Although a neutron guide is applied to mainly reflect neutrons of larger wavelengths and the detectors are shielded with borated polyethylene to absorb slow neutrons, there remains a background signal of (mainly fast) neutrons that are detected and are not directly emitted from the cold moderator. To eliminate this background from the readings of the shielded detectors, the neutron counts at detectors 1 and 3 (left and right of the center detector, see Figure 6.10) are averaged and subtracted from the spectrum. This way, the fast neutron peak vanishes from the time of flight spectrum, leaving only the thermal and cold regions. Although the thermal peaks at the background detectors exhibit different heights – which indicates that the detectors are not ideally centered – their overall intensity is low compared to the center detector (1...2%) and their mean is subtracted from the spectrum measured at the center detector. Thus, there is no visible change in the center detector's thermal peak (see Figure 6.10), right).

^{3}He detector efficiency: The thermal and cold neutrons entering the ^{3}He detector tube are partly absorbed by the surrounding metal shell before interacting with the ^{3}He gas. This absorption correction has to be taken into account when estimating the brightness of the cold source. This can be done by including the wavelength-dependent absorption cross section of iron (main contribution in stainless steel) into the overall absorption cross section of the detector tube. The wavelength-dependent absorption of the neutrons in the ^{3}He $\alpha_{abs,He}$ can be calculated as follows [101]:

$$\alpha_{abs,He} = \frac{1}{N}\sum_{i=0}^{N} 1 - e^{-\mu_{He}\cdot p_{He}/p_0 \cdot 2\cdot\sqrt{r^2-x_i^2}} \tag{6.2}$$

with the absorption attenuation factor $\mu_{He} = \rho_{He} \cdot \sigma_{a,He}$, the pressure p_{He} of the helium gas inside the detector tube and the reference pressure p_0, and the length $l = 2 \cdot \sqrt{r^2 - x_i^2}$, divided over N steps along the radius. To include the influence of the steel shell, the

absorption factor has to be multiplied additionally with the neutron absorption in the iron of the steel shell

$$\alpha_{abs,det} = \alpha_{abs,He} \cdot e^{-\mu_{Fe} \cdot t_{wall}} \tag{6.3}$$

with the attenuation factor of neutrons in iron μ_{Fe} and the wall thickness of the steel shell t_{wall}. Figure 6.11, left, shows the wavelength-dependent absorption of neutrons inside a ^{3}He detector tube with and without a shell of stainless steel for a wall thickness of 0.8 mm. The comparison between the uncorrected and corrected spectra are shown in Figure 6.11, right.

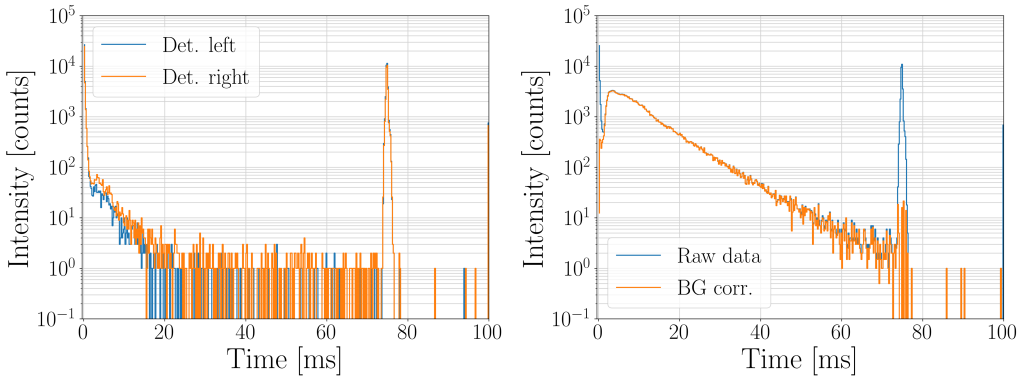

Figure 6.10: Histograms of the time-dependent neutron counts of the lateral ^{3}He detectors for measurement #59 with solid methane at 7.5 K (left) and a comparison of the raw spectrum at detector 2 and the background-corrected spectrum (right).

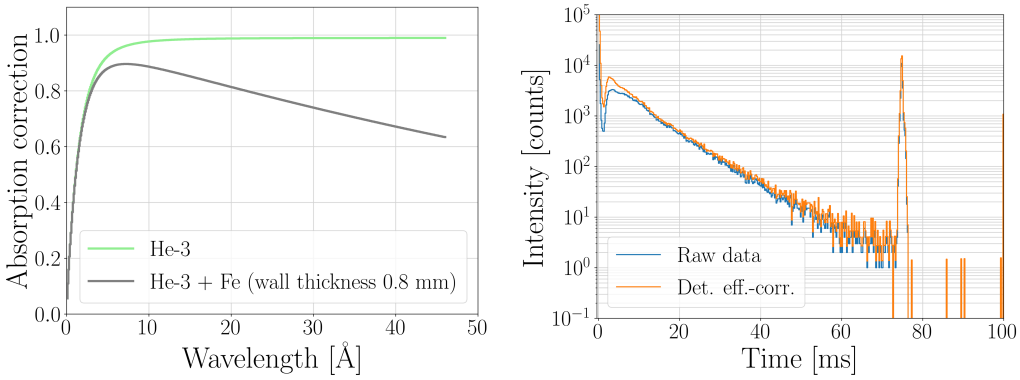

Figure 6.11: Comparison of the wavelength-dependent absorption for a ^{3}He detector tube with and without a stainless steel wall ($t_{w,det}$ = 0.8 mm) (left) and its effect on the resulting neutron spectrum for run #59 (right).

Current analysis:
To allow a comparison of the measured spectra for different temperatures performed on different days, the results have to be normalized to an appropriate reference. One approach is to use the proton counts measured at the target during the different runs. Since the neutron count at detector 10 (positioned outside the shielding of the detector assembly, close to the neutron guide) is mostly unaffected by the characteristics of the cold source, it can be used to assess the correctness of the proton current measurement. If both the detector and the current measurement were correct, the ratio of detected neutrons to protons should give a constant value (within the limits of measurement errors).

The proton count on the first day of measurements ranges from 1.13×10^{14} to 1.37×10^{14}, while that of the second day ranges from 4.25×10^{13} to 4.30×10^{13}. Therefore, the measured proton current is only around one third compared to that of the first day. If the proton measurement was consistent, this difference should also be present in the neutron count of detector 10. However, the neutron count on the second day is around 50% of that detected on the first day. Assuming a correct neutron detector reading, the proton current measurement is wrong on at least one of the two days. However, there are several factors which indicate that the proton count of the first day is more reliable:

1. the proton beam was aligned by a multi-wire proportional chamber (MWPC) before the first day's measurements

2. no such alignment procedure was performed before the second day's measurements and an increased level of radiation was detected along the proton beam line after the measurements.

To further corroborate the above assumption, a comparison to a previous beam time is performed. Since the measurement setup is similar to the one used for experiments with LH_2 as a cold moderator, one way to determine the correct proton current measurement during the experiments with CH_4 is by comparing the aforementioned ratio (detector 10/proton count) to that of the LH_2 beam time. Figure 6.12 shows these values for a number of measurement runs using LH_2 (black crosses) and CH_4 (red crosses) as a cold moderator. The LH_2 runs are arranged by parahydrogen content ranging from 25% to almost 100%. LH_2 runs with numbers below #96 are off due to differences in the current measurement technique and also have to be corrected to compare the different measurements with each other. However, most of the data points are located close to a constant value of approximately 2.19×10^{-8}.

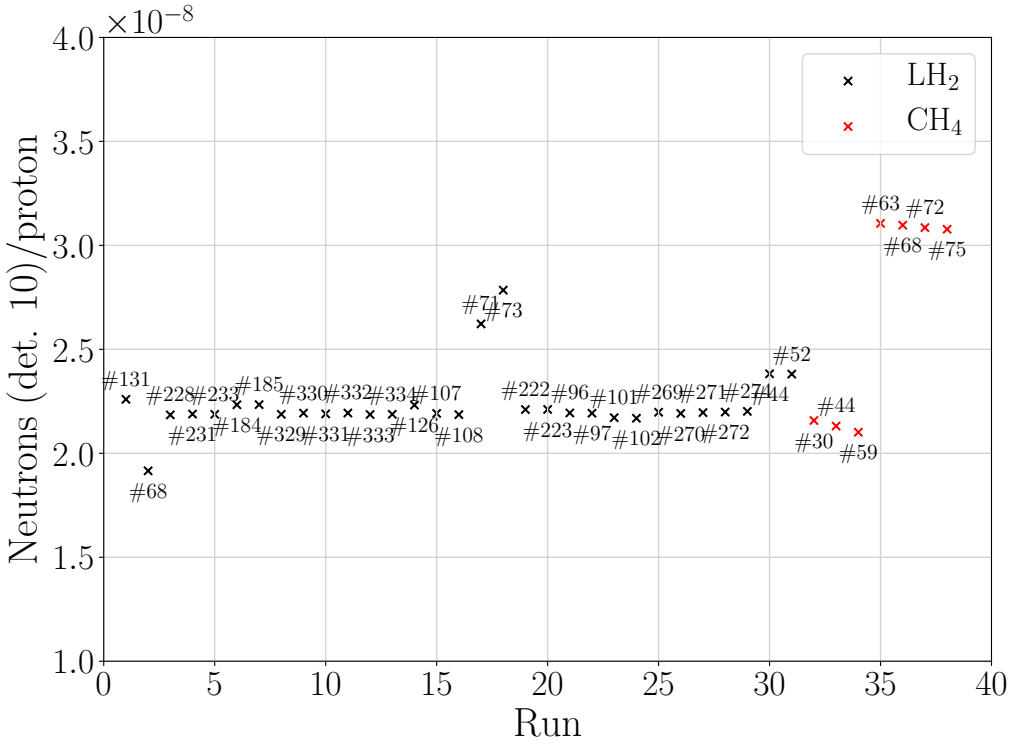

Figure 6.12: Ratios of the neutron count at detector 10 (outside the shielding of the detector assembly) and the measured proton count.

It is apparent that the ratios on the first day of measurement with CH_4 are closer to this mean value, while those of the second day are farther off, which supports the assumption

of an incorrect proton count on the second day. By applying the mean value of the ratios to the diverging proton counts, one can obtain corrected values that allow a more accurate comparison between the experimental runs of the two measurement days. However, even if applied, there is still a misalignment between the measurements of the first and second day. Therefore, detector 10 is used as a reference monitor and the spectra are adjusted to obtain a good fit of the thermal peak and curve progression for cold neutron energies. For this, the corrected currents of the second day are multiplied with an additional factor of 0.9, to omit the impact of the neutron release from the beam tube. The resulting corrected proton counts are listed in Table 6.2. Figure 6.13 shows the time of flight spectra at detector 10 normalized to the corrected proton counts with the additional correction factor.

Table 6.2: Proton counts corrected with the mean value of the LH_2 beam time and an additional correction factor.

Date	Run number	Proton count	Proton current [nA]
02/04/2022	#30	$1.35e+14$	6.0
	#44	$1.10e+14$	4.9
	#59	$1.15e+14$	5.2
06/04/2022	#63	$6.03e+13$	2.4
	#67	$6.07e+13$	2.4
	#72	$6.04e+13$	2.4
	#75	$6.01e+13$	2.4

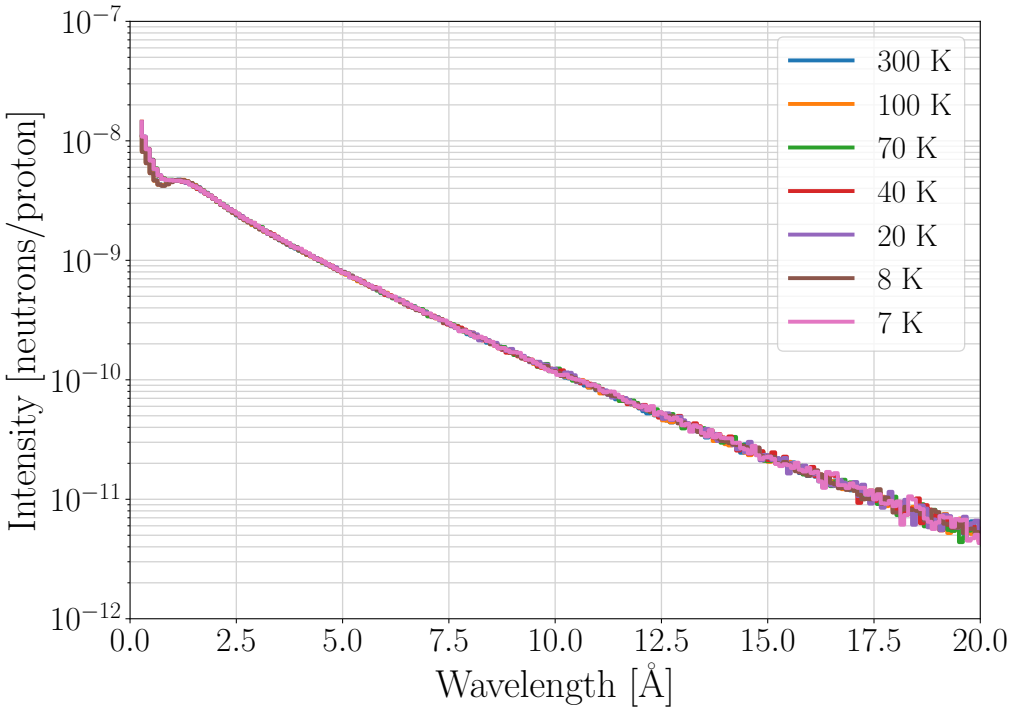

Figure 6.13: Time of flight spectra obtained at detector 10 for the different measurements normalized to the corrected proton counts.

Although the thermal peak and curve progression in the cold energy region ($t_{ToF} > 3$ ms) show a good agreement, the intensity at fast and epithermal energies ($t_{ToF} < 2$ ms) is higher for the second day's measurements. This feature additionally supports the assump-

tion that the proton beam is not optimally aligned and that (mainly epithermal) neutrons are produced in other components (e. g. the proton beam tube) without contributing to the proton count measurement.

Figure 6.14 shows the wavelength spectra of the measurement runs mentioned in Table 6.1 with applied corrections. It is apparent from the curves that there is a shift towards higher intensities at longer wavelengths with decreasing temperature. At the same time, the intensity of the thermal neutron peak decreases and a "shoulder" develops towards longer wavelengths. Differences in the thermal energy region between the measurements of the first and second day are possibly caused by differences in the procedure of condensing methane in the moderator vessel. On the first day of measurements, the applied methane gas pressure was lower ($p = 0.2$ bar(g), which generated a pressure below atmosphere inside the methane tubes and cold moderator vessel during liquefaction. For the second day, the pressure was increased to $p = 1$ bar(g), which ensured a pressure above atmosphere during the whole process. The spectra represent the results at the detector position. They include not only the characteristics of the moderator assembly but also of the flight path between the moderators and the detector with possible neutron guide elements and distances in vacuum and air in between. Therefore, to be able to compare the results with measurements of a different setup and to gain information on the achievable peak brightness, a consideration of the flight path is necessary.

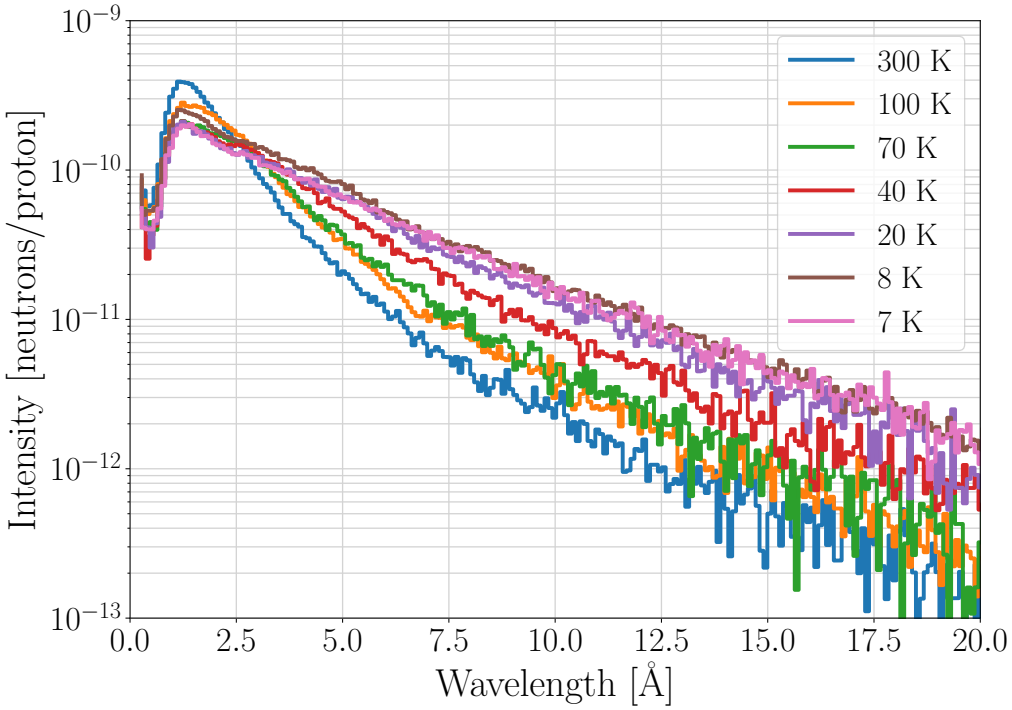

Figure 6.14: Background- and detector efficiency-corrected spectra for the methane measurements at various temperatures normalized to the measured and corrected proton count vs. neutron wavelength λ_n.

6.2.4 Comparison of selected simulations with VITESS3.4

One way to determine the brightness of the cold moderator at the different temperatures is by using the neutron transport simulation software VITESS3.4. It allows the simulation of the time of flight measurements by recreating the experimental setup through various modules, e. g. a source, neutron guide and detector. Figure 6.15 schematically shows the modules used for the simulation of the CH_4 experiments.

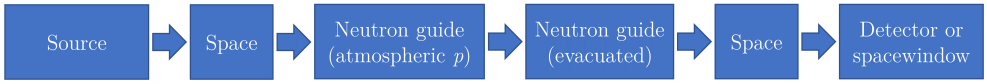

Figure 6.15: Schematic sequence of modules used in VITESS3.4 to reproduce the experimental results.

Source:
The source module is defined as a two-dimensional moderator surface, either rectangular or circular, from which the neutron rays emanate. It is the only module in which neutrons are generated, while all other modules cause a reduction of neutrons along the beam path, e. g. by absorption.
The moderator spectrum of the source module can be composed of up to three Maxwellian distributions by defining their respective temperature, the initial flux and the shape and dimensions of the moderator(s). Due to contributions from fast, epithermal, thermal and cold neutrons in the experimental spectrum and a probably insufficient moderation by the compact cold moderator, one Maxwellian distribution is typically not sufficient. In reality, the spectrum is a compilation of a multitude of Maxwellian distributions at different temperatures. However, for the present case, an adequate description of the resulting spectra can be performed by the three Maxwellian distributions offered by VITESS3.4. The diameter of the moderators is set to $d_c = 2$ cm, which is equivalent to that of the cold moderator.
The source module offers the possibility to limit the amount of neutrons reaching the subsequent module, either by defining a certain region at a specific distance ("window") or by specifying the divergence of the neutron trajectories. This way, computational power can be saved by neglecting the trajectories not important for the problem.
For the right values, this procedure allows an adequate reproduction of the original spectra of the experiments. The obtained source files can subsequently be used for the simulation of other applications. Furthermore, it is possible to monitor the brightness at a certain position, allowing the comparison of different beam time results.

Neutron guide:
The neutron guide assembly that is used to transport the cold neutrons towards the detector has a specific transmission efficiency, which largely depends on its shape (e. g. straight, elliptical, ballistic) and coating (e. g. ^{58}Ni or supermirrors). The neutrons are either transmitted directly through the guide, reflected by the inside walls of the guide depending on their angle, or absorbed. Total reflection at the inner surfaces occurs if the incident angle is below a critical value θ_{crit}. Above this critical angle, the neutrons are absorbed by the wall material of the guide.
To properly include the impact of the first meter of neutron guide that is not evacuated and – as a result – filled with ambient air, the neutron guide is split into two modules. Apart from the reflectivity of the guide's inner walls, that depend on their surface roughness, the first module includes attenuation coefficients for absorption and scattering. They are calculated from values given in [42] for room temperature. The guide has a length of $L = 1$ m.

Figure 6.16 shows the effect of the presence of air in the neutron guide compared to an evacuated one. It is apparent that its impact increases for increasing wavelength due to the $1/v$ dependency of the absorption cross section.

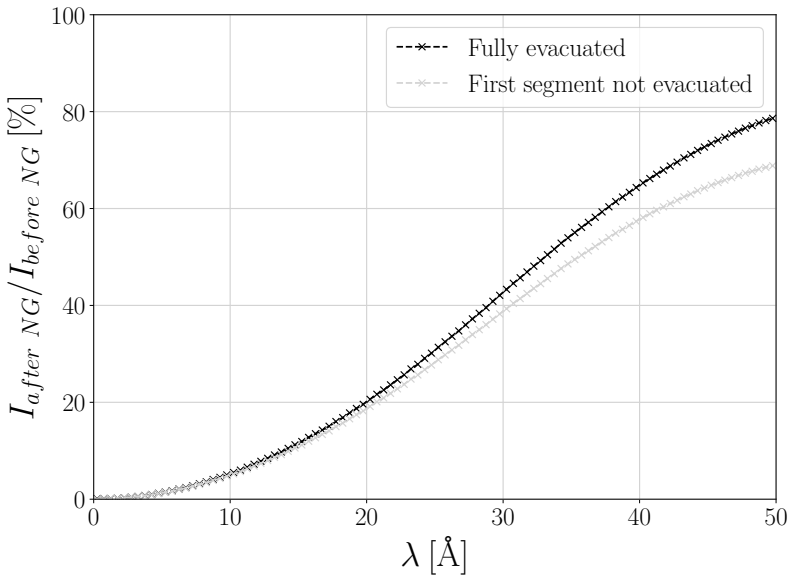

Figure 6.16: Wavelength-dependent transmission factor for a rectangular neutron guide (entrance and exit window: 3.0 cm width, 4.5 cm height) with a total length of 8 m, for the cases of a fully evacuated length and for the first meter filled with ambient air.

The second neutron guide module has a total length of $L_{evac} = 7$ m and no absorption and scattering effects are regarded, only those caused by the surface roughness of the mirrors. Figure 6.16 also shows the overall guide transmission factor for the whole neutron guide assembly.

Detector: The ^{3}He detector efficiency has already been included in the previous subsection and can therefore be neglected if the detector efficiency-corrected values are used for the comparison with VITESS3.4. It is sufficient to include a spacewindow with the dimensions of the viewed detector surface (width: 2.38 cm, height: 10 cm). However, the detector could in principal also be simulated by a corresponding VITESS module, which allows the definition of the shape and dimensions and the attenuation coefficient.

Figure 6.17 shows the different Maxwellian components and the resulting spectrum at the detector position compared to the measured and corrected neutron intensity vs. wavelength for the 7.5 K run of the first measurement day. The experimental data exhibits a thermal peak at around 1.8 Å that can be represented by a Maxwellian at approximately 350 K. The "shoulder" peak at around 5 Å complies with a Maxwellian of approximately 65 K, while the curve at longer wavelengths has an additional contribution from a 10 K Maxwellian (which corresponds roughly to the minimum attained temperature during the measurements). This composition is partly caused by an insufficient thermalization inside the cold moderator and partly by the different sizes of the cold moderator surface ($d = 2$ cm) and the entrance window of the neutron guide ($H = 4.5$ cm, $W = 3.0$ cm), which leads to a detection of thermal and epithermal neutrons directly emitted from the thermal moderator. For these reasons, the moderator assembly emits a bi-spectral output (thermal spectrum with cold extension).
Figure 6.18 shows a comparison in peak brightness and time-averaged brightness to a measurement performed with 99% parahydrogen in liquid form in a cylindrical vessel with

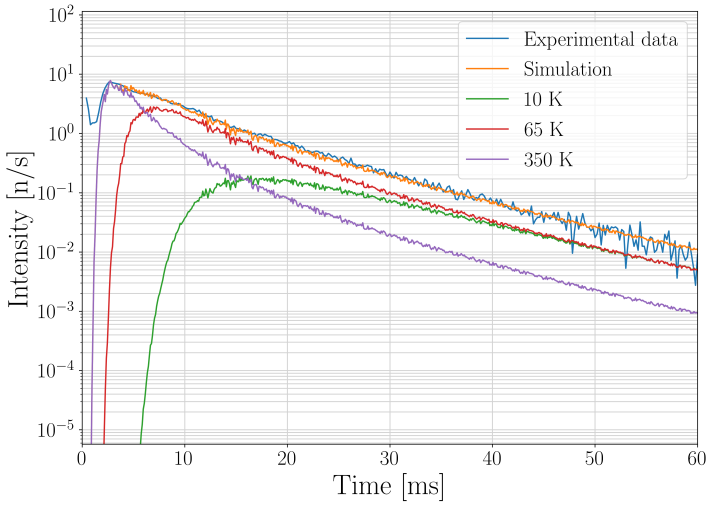

Figure 6.17: Reconstruction of the measured time of flight data using VITESS3.4 with three source definitions at 350 K, 65 K and 10 K.

a diameter of $d_{mod} = 5$ cm and a length of $L_{mod} = 10$ cm. It is apparent that the parahydrogen performs better over the cold wavelength region, but has a lower brightness for thermal neutrons. These results are qualitatively in accordance with the MCNP6.1 results from section 3.3. However, the difference in brightness for the two moderator materials increases for longer wavelength, when compared to the MCNP simulation. This is probably caused by a lower performance of the solid methane than expected and the larger diameter of the cold moderator vessel during the liquid hydrogen measurements ($d = 2$ cm compared to $d = 5$ cm). When comparing the time-averaged brightness, the solid methane moderator again performs slightly better in the thermal region, whereas it also underperforms for larger wavelengths compared to the liquid hydrogen. A larger solid cylinder ($d_{mod} = 3...4$ cm) or a re-entrant geometry would potentially perform better than the smaller diameter solid cylinder, but is most likely not going to perform better than a liquid parahydrogen moderator. Especially, since the dimensions of the parahydrogen moderator are not the optimum.

6.2.5 Summary of the experimental investigations with neutrons

By performing several measurements with solid and liquid methane at various temperatures, it is demonstrated that the wavelength spectrum is shifted towards higher intensities with increasing wavelength. However, the difference between the measurements at 20 K and 7.5 K is small. Furthermore, the chosen diameter of $d_{mod} = 2$ cm produces a largely under-moderated spectrum with a distinct thermal peak and a cold tail around an order of magnitude higher than that of the thermal measurement for the coldest temperature (bi-spectral cold moderator). When compared to a liquid hydrogen cold moderator with a diameter of $d_{mod} = 5$ cm and a parahydrogen content of 99%, the solid methane underperforms significantly in peak and time-averaged brightness for almost the whole wavelength range.

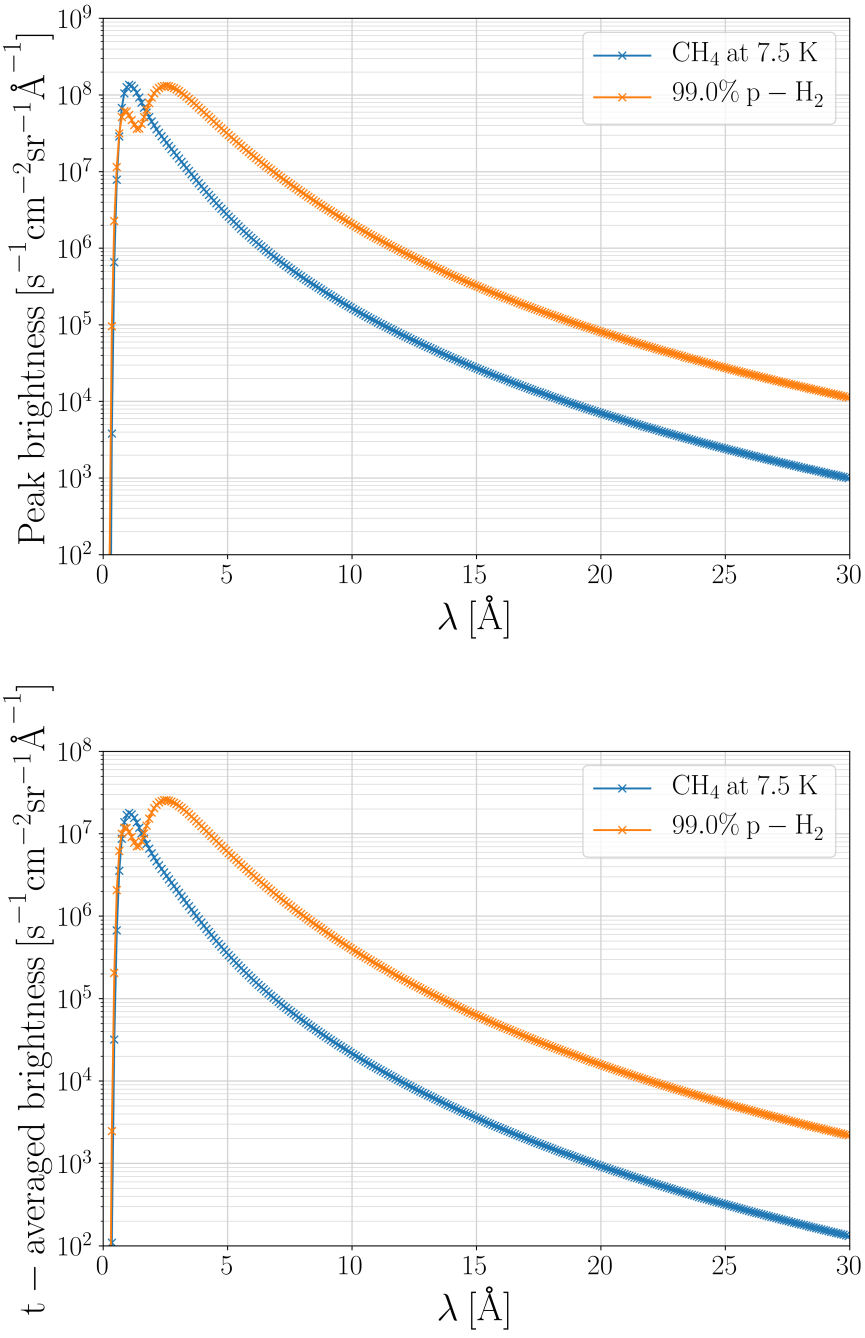

Figure 6.18: Peak and time-averaged brightness simulated with VITESS3.4 for two measurements performed at the Big Karl experimental hall using CH_4 at 7.5 K and liquid H_2 with a parahydrogen content of 99% as cold moderators.

Chapter 7

Summary & outlook

7.1 Summary

Solid methane (s-CH_4) was selected as a material for a low-dimensional cold moderator to show an increase in emitted cold neutrons by decreasing the moderator's temperature to 10 K and below. It was chosen based on the results of a literature survey and its geometry was optimized by conducting several parametric Monte Carlo simulations using the software MCNP6.1.
Based on the choice of the moderator material, a prototype cryostat system for the operation of solid and liquid cryogenic moderators was designed, manufactured and tested (with and without neutrons) at Forschungszentrum Jülich. During the design and manufacturing, requirements emerging from its intended use at a prototype target-moderator-reflector unit as well as those from a full power HBS facility were taken into account. Here, the thermal design as well as the structural integrity of the system under irradiation were paramount. It could be shown that the use of solid molecular moderators at a full power HBS is theoretically possible if the effective thermal conductivity of the cold moderator is improved, e. g. by using a porous aluminum structure interlaced with the moderator material.
Known problems with using solid or liquid methane at high-power neutron sources like "burping" or hydrogen and hydrocarbon accumulation by radiolysis are to be expected at the full-power HBS as well. However, experiences from other facilities using solid methane show that – given the appropriate measures, e. g. regular warm-ups and the release of stored energy – a safe operation could also be feasible at a Hi-CANS. Nevertheless, a more detailed investigation is necessary before CH_4 can be used as a cold moderator with full beam power.
The structural analysis of the present design showed that the prototype cryostat can be safely operated under the defined conditions. Higher pressures, especially during warm-up, are to be expected when using methane with increasing beam power. The irradiation of the methane causes a transformation of parts of the methane into hydrogen, which evaporates with increasing temperature. The hydrogen then exerts a pressure on the solid methane, which in turn presses on the vessel walls. For this case, the system shall be tested first and, where necessary, adapted to the new requirements.
The demand for a flexible system with modular parts to allow the interchanging of different components like the moderator vessel or measurement equipment proved to be difficult due to the high forces necessary to properly seal the demountable tubing joints. However, the cryostat system could be successfully assembled and tested. The lowest achievable temperature of 7.4 K met the initial requirements of a temperature $T \leq 10$ K. The specific design of the cryostat allows a further operation at a prototype TMR unit and the choice of material is not limited to the use of methane.
The experimental results from time of flight measurements showed an increase in cold neu-

trons emitted from a solid methane moderator when cooled, even below $T = 20$ K. When compared to liquid parahydrogen, however, the methane performed worse than predicted.

7.2 Outlook

As is apparent from the experimental results obtained in this thesis, cooling the solid methane to operating temperatures of $T_{op} < 20$ K increases the intensity at longer wavelengths. Nevertheless, when compared to liquid parahydrogen, the peak and time-averaged brightness obtained from experiments are lower by a factor of up to 20. Combined with the expectable problems arising from radiolysis at the full power HBS, solid methane cannot reach the performance of p-H_2 as a low-dimensional cold moderator. Nevertheless, the bispectral output of the compact methane moderator could be usable for certain instruments that require a larger amount of thermal neutrons paired with cold neutrons.
Other options that were not investigated in full detail in this thesis could potentially further increase the cold neutron brightness, e. g. the re-entrant hole geometry or a larger diameter solid cylinder. The cryostat system offers the opportunity to test the performance of such a geometry by exchanging the cold moderator vessel. However, the possibility of a sufficient cooling of the whole moderator has to be ensured. The re-entrant hole geometry offers the advantage of increasing the brightness even for low thicknesses of methane. To ensure a sufficient cooling and stable cryogenic temperatures for beam powers up to those generated at the full power HBS, further investigations are necessary.
Apart from changing the cold moderator material or geometry, adjustments to the surrounding structure could potentially increase the neutron brightness. A further focusing of the cold neutron beam could be realized by coating the beam path with nanodiamonds or MgH_2, which allow a reflection of cold neutrons even before entering the neutron guide.
In the context of this thesis, a test apparatus for the determination of the cooling efficiency of different porous aluminum structures was designed and partly manufactured. By measuring the effective thermal conductivity $\lambda_{th,eff}$ for different porous structures and different thermal contacts (press fit, brazed), the effect on the maximum temperature in the moderator can be assessed more reliable.
Furthermore, there are other promising concepts for the use of solid methane at temperatures below 20 K, mostly as a compact very cold neutron (VCN) "converter". Such a converter can consist of only a small amount of solid methane and is fed by a cold premoderator.
Apart from the results obtained with neutrons, the design of the cryostat builds a basis for further experiments at the presented prototype TMR. During the finalization of this thesis, the cryostat has repeatedly been used at this TMR unit (see Figure 7.1), also using ethane as a cold moderator. Furthermore, an adjusted design was used for the operation of a liquid parahydrogen moderator.

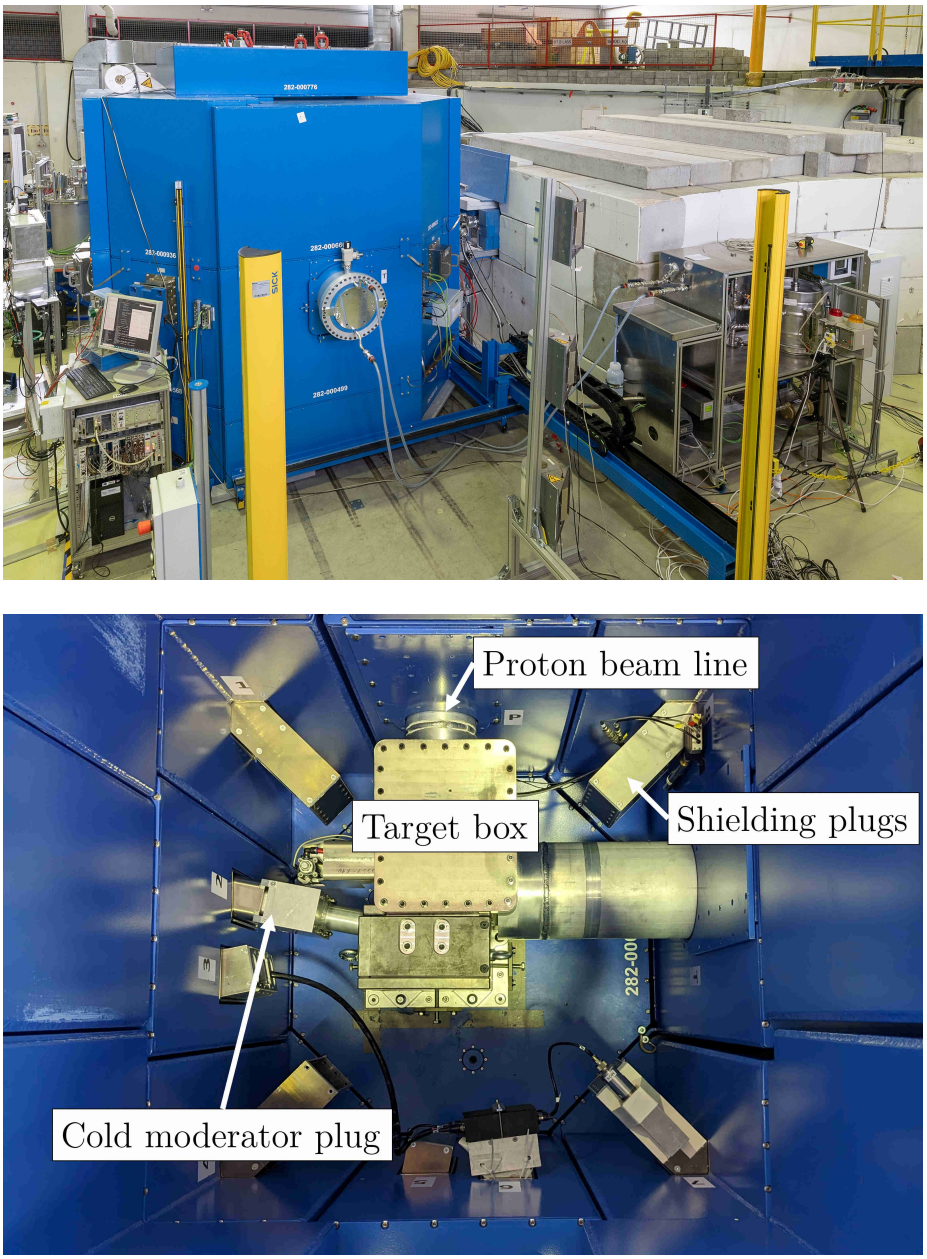

Figure 7.1: Prototype TMR unit at the Big Karl experimental hall of the COSY facility at Forschungszentrum Jülich. Top: Assembled TMR unit. Bottom: Inner setup of the TMR unit with target and cold moderator plug.

Bibliography

[1] J. Walker, "Uses of neutrons in engineering and technology," *Physics in Technology*, vol. 13, no. 6, p. 239, 1982. DOI: 10.1088/0305-4624/13/6/I01.

[2] A. Michels and J. Weissmüller, "Magnetic-field-dependent small-angle neutron scattering on random anisotropy ferromagnets," *Reports on Progress in Physics*, vol. 71, no. 6, p. 066 501, 2008. DOI: 10.1088/0034-4885/71/6/066501.

[3] S. Chapman, R. McGreevy, and L. Consortium, "The LENS Initiative: Strengthening European Neutron Science and Technology," *Neutron News*, vol. 32, no. 3, pp. 24–27, 2021. DOI: 10.1080/10448632.2021.1946343.

[4] T. Brückel and T. Gutberlet, *Conceptual Design Report-Jülich High Brilliance Neutron Source (HBS)*. Forschungszentrum Jülich GmbH, Zentralbibliothek, Verlag, 2020, ISBN: 978-3-95806-501-7. [Online]. Available: https://juser.fz-juelich.de/record/884799.

[5] J. M. Carpenter and W. B. Yelon, "2. Neutron Sources," in *Methods in Experimental Physics*, vol. 23, Elsevier, 1986, pp. 99–196. DOI: https://doi.org/10.1016/S0076-695X(08)60555-4.

[6] ELENA, *Neutron facilities*, „https://elena-neutron.iff.kfa-juelich.de/neutron-facilities", Accessed: 19th September 2023.

[7] T. Brückel, "A Neutron Primer," in *Laboratory Course Neutron Scattering: Lectures* (Schriftenreihe Schlüsseltechnologien), Schriftenreihe Schlüsseltechnologien. Forschungs-zentrum Jülich, 2015, vol. 106, pp. 2.1–2.34. [Online]. Available: https://juser.fz-juelich.de/record/202768.

[8] G. L. Squires, *Introduction to the Theory of Thermal Neutron Scattering*. Cambridge: Cambridge University Press, 2012. DOI: 10.1017/CBO9781139107808.

[9] F. J. Bermejo and F. Sordo, "Chapter 2 - Neutron Sources," in *Neutron Scattering – Fundamentals*, ser. Experimental Methods in the Physical Sciences, F. Fernandez-Alonso and D. L. Price, Eds., vol. 44, Academic Press, 2013, pp. 137–243. DOI: https://doi.org/10.1016/B978-0-12-398374-9.00002-4.

[10] OECD, "Thermal Scattering Law S(α,β): Measurement, Evaluation and Application," in *International Evaluation Co-operation*, vol. 42, 2020. [Online]. Available: https://www.oecd-nea.org/jcms/pl_23901/international-evaluation-co-operation-volume-42.

[11] R. Pynn, "Neutron Scattering: A Primer," *Los Alamos Science*, vol. 19, 1990. [Online]. Available: https://www.ncnr.nist.gov/summerschool/ss16/pdf/NeutronScatteringPrimer.pdf.

[12] M. B. Chadwick, M. Herman, P. Obložinskỳ, *et al.*, "ENDF/B-VII. 1 Nuclear data for science and technology: Cross sections, covariances, fission product yields and decay data," *Nuclear data sheets*, vol. 112, no. 12, pp. 2887–2996, 2011. DOI: https://doi.org/10.1016/j.nds.2011.11.002.

[13] J. M. Carpenter and C.-K. Loong, *Elements of Slow-Neutron Scattering*. Cambridge University Press, 2015. DOI: 10.1017/CBO9781139029315.

[14] G. S. Bauer, "Pulsed Neutron Source Cold Moderators — Concepts, Design and Engineering," *Proceedings of the International Workshop on Cold Moderators for Pulsed Neutron Sources, Argonne National Laboratory*, 1997. [Online]. Available: https://www.osti.gov/biblio/1163129.

[15] K.-H. Beckurts and K. Wirtz, *Neutron Physics*. Springer Science & Business Media, 2013, ISBN: 978-3-642-87614-1. DOI: https://doi.org/10.1007/978-3-642-87614-1.

[16] F. Mezei *et al.*, "Low dimensional neutron moderators for enhanced source brightness," *Journal of Neutron Research*, vol. 17, no. 2, pp. 101–105, 2014. DOI: 10.3233/JNR-140013.

[17] R. E. MacFarlane, "Cold Moderator Scattering Kernels," in *International Workshop on Cold Neutron Sources*, 1990, p. 193. [Online]. Available: https://www.osti.gov/biblio/5496338.

[18] Y. Shin, W. M. Snow, C.-Y. Liu, C. M. Lavelle, and D. V. Baxter, "A Neutron Scattering Kernel of Solid Methane in phase II," in *APS April Meeting Abstracts*, 2008, W14–009. [Online]. Available: https://ui.adsabs.harvard.edu/abs/2008APS..APRW14009S.

[19] M. Prager and A. Heidemann, "Rotational Tunneling and Neutron Spectroscopy: A Compilation," *Chemical reviews*, vol. 97, no. 8, pp. 2933–2966, 1997. DOI: https://doi.org/10.1021/cr9500848.

[20] J. M. Carpenter, "Cold Moderators for Pulsed Neutron Sources," in *Workshop on Cold Neutron Sources*, Argonne National Lab., IL (USA), 1990. [Online]. Available: https://www.osti.gov/biblio/6080299.

[21] S. A. Kulikov *et al.*, "Measurement of Cold Neutron Spectra Using a Model Cryogenic Moderator of the IBR-2M Reactor," *Physics of Particles and Nuclei Letters*, vol. 7, pp. 57–60, 2010. DOI: https://doi.org/10.1134/S1547477110010127.

[22] K. Nünighoff *et al.*, "Neutron experiments with cryogenic methane hydrate and mesitylene moderators," *The European Physical Journal A*, vol. 38, pp. 115–123, 2008. DOI: https://doi.org/10.1140/epja/i2008-10661-y.

[23] K. Inoue, N. Otomo, H. Iwasa, and Y. Kiyanagi, "Slow Neutron Spectra in Cold Moderators," *Journal of Nuclear Science and Technology*, vol. 11, no. 5, pp. 228–229, 1974. DOI: 10.1080/18811248.1974.9730652.

[24] K. Nünighoff *et al.*, "Ice moderator experiments at very low temperatures: Comparison of experimental data with Monte Carlo simulations using new scattering law data S(α,β,T)," *The European Physical Journal A*, vol. 22, pp. 519–528, 2004. DOI: https://doi.org/10.1140/epja/i2004-10060-6.

[25] D. Picton, S. Bennington, S. Ansell, J. Fernandez-Garcia, and T. Broome, "Composite Hydrogen-Solid Methane Moderators," in *ACoM-6, 6th Meeting of the Collaboration on Advanced Cold Moderators*, 2004, ISBN: 3-89336-363-7. [Online]. Available: https://juser.fz-juelich.de/record/39463.

[26] Z. Kókai *et al.*, *Monte Carlo study of a Very Cold Neutron source using nanodiamond reflectors*, „https://www.youtube.com/watch?v=oCzDfJKV3DM", Conference talk, International Conference on Neutron Scattering 2022, Buenos Aires, 2022.

[27] C. Lavelle *et al.*, "Neutronic design and measured performance of the Low Energy Neutron Source (LENS) target moderator reflector assembly," *Nuclear Instruments and Methods in Physics Research Section A: Accelerators, Spectrometers, Detectors and Associated Equipment*, vol. 587, no. 2-3, pp. 324–341, 2008. DOI: https://doi.org/10.1016/j.nima.2007.12.044.

[28] Y. Kiyanagi, "Neutron imaging at compact accelerator-driven neutron sources in japan," *Journal of Imaging*, vol. 4, no. 4, 2018, ISSN: 2313-433X. DOI: 10.3390/jimaging4040055.

[29] T. Brückel *et al.*, "The High Brilliance neutron Source (HBS): A project for a next generation neutron research facility," in *EPJ Web of Conferences*, EDP Sciences, vol. 286, 2023, p. 02 003. DOI: https://doi.org/10.1051/epjconf/202328602003.

[30] Ott, Frédéric *et al.*, "ICONE – Towards a French HiCANS Neutron Source for materials science and industry," *EPJ Web Conf.*, vol. 286, p. 02 001, 2023. DOI: 10.1051/epjconf/202328602001.

[31] M. Pérez, F. Sordo, I. Bustinduy, J. L. Muñoz, and F. J. Villacorta, "ARGITU compact accelerator neutron source: A unique infrastructure fostering RD ecosystem in Euskadi," *Neutron News*, vol. 31, no. 2-4, pp. 19–25, 2020. DOI: 10.1080/10448632.2020.1819140.

[32] J. Baggemann *et al.*, *Technical Design Report HBS*. Forschungszentrum Jülich GmbH, Zentralbibliothek, Verlag, 2023, vol. 2. DOI: 10.34734/FZJ-2023-03723.

[33] M. Rimmler, *Development of a Multiplexer System and Measurement of the Neutron Yield for a Low-Energy Accelerator-Driven Neutron Source*. High Brilliance Source, 2021, FZJ-2021-05472, ISBN: 978-3-95806-600-7. [Online]. Available: https://juser.fz-juelich.de/record/903839.

[34] M. Rimmler *et al.*, "Determination of the neutron yield of Be, V and Ta targets irradiated with protons (22-42 MeV) by means of prompt gamma neutron activation analysis," *Nuclear Instruments and Methods in Physics Research Section A: Accelerators, Spectrometers, Detectors and Associated Equipment*, vol. 990, p. 164 989, 2021. DOI: https://doi.org/10.1016/j.nima.2020.164989.

[35] K. H. Andersen *et al.*, "Optimization of moderators and beam extraction at the ESS," *Journal of Applied Crystallography*, vol. 51, no. 2, pp. 264–281, 2018. DOI: 10.1107/S1600576718002406.

[36] J. R. Granada, J. I. M. Damián, and C. Helman, "Studies on Reflector Materials for Cold Neutrons," in *EPJ Web of Conferences*, EDP Sciences, vol. 231, 2020, p. 04 002. DOI: https://doi.org/10.1051/epjconf/202023104002.

[37] D. L. Price and F. Fernandez-Alonso, "Chapter 1 - An Introduction to Neutron Scattering," in *Neutron Scattering – Fundamentals*, ser. Experimental Methods in the Physical Sciences, F. Fernandez-Alonso and D. L. Price, Eds., vol. 44, Academic Press, 2013, pp. 1–136. DOI: https://doi.org/10.1016/B978-0-12-398374-9.00001-2.

[38] K. Inoue, "Slowing Down of Neutrons to Very Low Temperature by Cold Solid Hydrogenous Moderators," *Journal of Nuclear Science and Technology*, vol. 7, no. 11, pp. 580–587, 1970. DOI: 10.1080/18811248.1970.9734745.

[39] F. Cantargi and J. R. Granada, "Thermal neutron cross-section libraries for aromatic hydrocarbons," *Nuclear Instruments and Methods in Physics Research - Section B*, vol. 268, no. 16, pp. 2487–2491, 2010. DOI: https://doi.org/10.1016/j.nimb.2010.04.030.

[40] K. Inoue, N. Otomo, M. Utsuro, and Y. Fujita, "Slow Neutron Spectra in the Liquid and Solid Methane," *Journal of Nuclear Science and Technology*, vol. 9, no. 6, pp. 374–375, 1972. DOI: 10.1080/18811248.1972.9734861.

[41] M. Utsuro and M. Sugimoto, "Pulsed Cold Neutron Source of Solid Methylbenzene," *Journal of Nuclear Science and Technology*, vol. 14, no. 5, pp. 390–392, 1977. DOI: 10.1080/18811248.1977.9730775.

[42] V. F. Sears, "Neutron scattering lengths and cross sections," *Neutron News*, vol. 3, no. 3, pp. 26–37, 1992. DOI: 10.1080/10448639208218770.

[43] E. W. Lemmon, M. L. Huber, and M. O. McLinden, *NIST Standard Reference Database 23: Reference Fluid Thermodynamic and Transport Properties - REFPROP, Version 8.0*, Gaithersburg: National Institute of Standards and Technology, 2007. [Online]. Available: https://tsapps.nist.gov/publication/get_pdf.cfm?pub_id=912382.

[44] T. Mitsuyasu, N. Morishima, and Y. Nagaya, "Cold neutron production in solid and liquid CH4 moderators. II: On the reentrant-hole configuration," *Nuclear Instruments and Methods in Physics Research Section A*, vol. 537, no. 3, pp. 610–613, 2005. DOI: https://doi.org/10.1016/j.nima.2004.08.097.

[45] E. B. Iverson *et al.*, "Enhancing neutron beam production with a convoluted moderator," *Nuclear Instruments and Methods in Physics Research Section A*, vol. 762, pp. 31–41, 2014. DOI: https://doi.org/10.1016/j.nima.2014.04.047.

[46] F. X. Gallmeier, E. B. Iverson, W. Lu, D. V. Baxter, G. Muhrer, and S. Ansell, "Introducing single-crystal scattering and optical potentials into MCNPX: Predicting neutron emission from a convoluted moderator," *Nuclear Instruments and Methods in Physics Research Section A*, vol. 814, pp. 39–49, 2016. DOI: https://doi.org/10.1016/j.nima.2015.12.053.

[47] I. Lux and L. Koblinger, *Monte Carlo Particle Transport Methods: Neutron and Photon Calculations*. CRC Press, Inc., 1991. DOI: https://doi.org/10.1201/9781351074834.

[48] J. F. Briesmeister *et al.*, "MCNP^{TM} — A General Monte Carlo N-Particle Transport Code. Version 4C.," *LA-13709-M, Los Alamos National Laboratory*, vol. 2, 2000. [Online]. Available: https://mcnp.lanl.gov/pdf_files/TechReport_2000_LANL_LA-13709-M_Briesmeisterothers.pdf.

[49] R. A. Forster and T. N. K. Godfrey, "MCNP — A General Monte Carlo Code for Neutron and Photon Transport," in *Monte-Carlo Methods and Applications in Neutronics, Photonics and Statistical Physics: Proceedings of the Joint Los Alamos National Laboratory-Commissariat à l'Energie Atomique Meeting Held at Cadarache Castle, Provence, France April 22–26, 1985*, Springer, 1985, pp. 33–55, ISBN: 978-3-540-39750-2. DOI: https://doi.org/10.1007/BFb0049033.

[50] J. S. Hendricks, M. T. Swinhoe, and A. Favalli, *Monte Carlo N-Particle Simulations for Nuclear Detection and Safeguards: An Examples-Based Guide for Students and Practitioners*. Springer Nature, 2022, ISBN: 978-3-031-04131-0. DOI: https://doi.org/10.1007/978-3-031-04129-7.

[51] J. R. Granada, F. Cantargi, and J. M. Damian, "Neutron Cross Sections Libraries for Methane in Phase II and Solid Deuterium," *J. Korean Phys. Soc*, vol. 59, p. 1076, 2011. DOI: https://doi.org/10.3938/jkps.59.1076.

[52] V. McLane, "ENDF-201, ENDF/B-VI summary documentation supplement 1, ENDF/HE-VI summary documentation," Tech. Rep., Dec. 1996. DOI: 10.2172/481571.

[53] J. K. Shultis and R. E. Faw, "An MCNP Primer," Kansas State University, Tech. Rep., 2011. [Online]. Available: http://hdl.handle.net/2097/15754.

[54] J. R. Granada, "Synthetic scattering kernel to describe the interaction of slow neutrons with solid methane in phase II," *Nuclear Instruments and Methods in Physics Research Section B*, vol. 266, no. 1, pp. 164–172, 2008. DOI: https://doi.org/10.1016/j.nimb.2007.10.038.

[55] Y. Shin *et al.*, "Measurements of the neutron brightness from a phase II solid methane moderator at the LENS neutron source," *Nuclear Instruments and Methods in Physics Research Section A*, vol. 620, no. 2-3, pp. 375–381, 2010. DOI: https://doi.org/10.1016/j.nima.2010.03.108.

[56] F. X. Gallmeier, T. Hügle, E. B. Iverson, W. Lu, and I. Remec, "Options for a very cold neutron source for the second target station at SNS," in *Journal of Physics: Conference Series*, IOP Publishing, vol. 1021, 2018, p. 012 083. DOI: 10.1088/1742-6596/1021/1/012083.

[57] Y. Nakasone, S. Yoshimoto, and T. Stolarski, *Engineering Analysis with ANSYS Software*, 2006. DOI: https://doi.org/10.1016/B978-0-7506-6875-0.X5030-3.

[58] D. V. Hutton, *Fundamentals of finite element analysis*. The McGraw Hill Companies, 2003, ISBN: 978-0072922363.

[59] J. N. Reddy, *An Introduction to the Finite Element Method*. McGraw-Hill, Inc., 1993, ISBN: 978-0070513556.

[60] D. Mann, "LNG materials and fluids: A user's manual of property data in graphic format," Jan. 1977. [Online]. Available: https://www.osti.gov/biblio/6271374.

[61] Z. Zhang, S. R. Lorentz, J. P. Rice, and R. Datla, "Measurement of thermophysical properties of polyimide and a black paint for future development of cryogenic radiometers," *Metrologia*, vol. 35, no. 4, p. 511, 1998.

[62] H. Lee, *Finite Element Simulations with ANSYS Workbench 19*. SDC Publications, 2018, ISBN: 9781630572112. [Online]. Available: https://www.sdcpublications.com/Textbooks/Finite-Element-Simulations-ANSYS-Workbench/ISBN/978-1-63057-211-2/.

[63] C. A. Foster, D. E. Schechter, and J. M. Carpenter, "Methane Pellet Moderator Development," in *ACoM-6, 6th Meeting of the Collaboration on Advanced Cold Moderators*, 2004, ISBN: 3-89336-363-7. [Online]. Available: https://juser.fz-juelich.de/record/39463.

[64] S. Lang, M. Gerschitzka, D. Bauer, and H. Drück, "Thermal Conductivity of Vacuum Insulation Materials for Thermal Energy Stores in Solar Thermal Systems," *Energy Procedia*, vol. 91, pp. 172–181, 2016. DOI: https://doi.org/10.1016/j.egypro.2016.06.196.

[65] J. W. Ekin, *Experimental Techniques for Low-Temperature Measurements: Cryostat Design, Material Properties and Superconductor Critical-Current Testing*. Oxford University Press, 2006, ISBN: 9780198570547. DOI: https://doi.org/10.1093/acprof:oso/9780198570547.001.0001.

[66] J. G. Weisend II, *Cryostat Design*. Springer, 2016, ISBN: 978-3-319-80976-2. DOI: https://doi.org/10.1007/978-3-319-31150-0.

[67] S. W. Van Sciver, K. D. Timmerhaus, and A. F. Clark, *Helium Cryogenics*. Springer, 2012, ISBN: 978-1-4939-0159-3. DOI: https://doi.org/10.1007/978-1-4419-9979-5.

[68] M. Kind and H. Martin, *VDI-Wärmeatlas*. Springer, 2013, ISBN: 978-3-642-19981-3. DOI: https://doi.org/10.1007/978-3-642-19981-3.

[69] A. L. Woodcraft and A. Gray, "A low temperature thermal conductivity database," in *AIP Conference Proceedings*, American Institute of Physics, vol. 1185, 2009, pp. 681–684. DOI: https://doi.org/10.1063/1.3292433.

[70] J. R. Maddocks, P. Maddocks, M. Fay, B. P. M. Helvensteijn, and A. Kashani, "Performance Test of Pulse Tube Cooler with Integrated Circulator," in *International Cryocooler Conference*, Georgia Institute of Technology, 2008, ISBN: 978-1-934021-02-6. [Online]. Available: http://hdl.handle.net/1853/39679.

[71] C. Wang, E. Brown, and A. Friebel, "A Compact Cold Helium Circulation System with GM Cryocooler," in *18th International Cryocooler Conference ICC*, 2014, ISBN: 978-1-934021-04-0. [Online]. Available: https://cryocooler.org/Cryocoolers-18.

[72] T. Cronert *et al.*, "High brilliant thermal and cold moderator for the HBS neutron source project Jülich," in *Journal of Physics: Conference Series*, IOP Publishing, vol. 746, 2016. DOI: 10.1088/1742-6596/746/1/012036.

[73] P. Stachowiak, E. Pisarska, A. Jeżowski, and A. I. Krivchikov, "Glass-like behaviour of thermal conductivity of CH4–CD4 solid solutions," *Europhysics Letters*, vol. 74, no. 1, pp. 96–102, 2006. DOI: 10.1209/epl/i2005-10508-1.

[74] D. E. Daney, "Thermal conductivity of solid argon, deuterium, and methane from one-dimensional freezing rates," *Cryogenics*, vol. 11, no. 4, pp. 290–297, 1971. DOI: https://doi.org/10.1016/0011-2275(71)90185-8.

[75] A. N. Gerritsen and P. Van Der Star, "The Heat Conductivity of Solid Methane," *Physica*, vol. 9, no. 5, pp. 503–512, 1942. DOI: https://doi.org/10.1016/S0031-8914(42)90086-7.

[76] J. H. Colwell, E. K. Gill, and J. A. Morrison, "Thermodynamic Properties of CH_4 and CD_4. Interpretation of the Properties of the Solids," *The Journal of Chemical Physics*, vol. 39, no. 3, pp. 635–653, 1963. DOI: 10.1063/1.1734303.

[77] Y. A. Cengel, *Heat Transfer: A Practical Approach*. McGraw-Hill Professional, 2002, ISBN: 978-0072458930.

[78] A. Jeżowski, P. Stachowiak, V. V. Sumarokov, J. Mucha, and Y. A. Freiman, "Thermal Conductivity of Solid Oxygen," *Physical Review Letters*, vol. 71, no. 1, p. 97, 1993. DOI: 10.1103/PhysRevLett.71.97.

[79] O. A. Korolyuk, B. Y. Gorodilov, A. I. Krivchikov, and V. V. Dudkin, "The role of normal processes in the thermal conductivity of solid deuterium," *Low Temperature Physics*, vol. 26, no. 4, pp. 235–239, 2000. DOI: 10.1063/1.593891.

[80] G. Ventura and M. Perfetti, *Thermal Properties of Solids at Room and Cryogenic Temperatures*. Springer, 2014, ISBN: 978-94-017-8968-4. DOI: https://doi.org/10.1007/978-94-017-8969-1.

[81] O. Kirichek, C. R. Lawson, D. M. Jenkins, C. J. T. Ridley, and D. J. Haynes, "Solid methane in neutron radiation: Cryogenic moderators and cometary cryo volcanism," *Cryogenics*, vol. 88, pp. 101–105, 2017. DOI: https://doi.org/10.1016/j.cryogenics.2017.10.017.

[82] J. Banhart, "Manufacture, characterisation and application of cellular metals and metal foams," *Progress in Materials Science*, vol. 46, no. 6, pp. 559–632, 2001. DOI: https://doi.org/10.1016/S0079-6425(00)00002-5.

[83] O. Andersen, J. Meinert, T. Studnitzky, G. Stephani, and B. Kieback, "Highly heat conductive open-porous aluminium fibre based parts for advanced heat transfer applications," *Materialwissenschaft und Werkstofftechnik*, vol. 43, no. 4, pp. 328–333, 2012. DOI: https://doi.org/10.1002/mawe.201200949.

[84] S. Chowdhury *et al.*, "Laser powder bed fusion: a state-of-the-art review of the technology, materials, properties & defects, and numerical modelling," *Journal of Materials Research and Technology*, vol. 20, pp. 2109–2172, 2022. DOI: https://doi.org/10.1016/j.jmrt.2022.07.121.

[85] L. R. Glicksman, "Heat transfer in foams," in *Low density cellular plastics: Physical basis of behaviour*, N. C. Hilyard and A. Cunningham, Eds., Dordrecht: Springer Netherlands, 1994, pp. 104–152, ISBN: 978-94-011-1256-7. DOI: 10.1007/978-94-011-1256-7_5.

[86] A. August, A. Reiter, A. Kneer, M. Selzer, and B. Nestler, "Effective Thermal Conductivity of Composite Materials Based on Open Cell Foams," *Heat and Mass Transfer Research Journal*, vol. 2, no. 1, 2018. DOI: 10.5445/IR/1000084246.

[87] AFCEN, *RCC-MRx Design and Construction Rules for Mechanical Components of Nuclear Installations*. AFCEN, 2012, ISBN: 2-913638-40-6.

[88] K. Farrell, "Performance of Aluminum in Research Reactors," in *Comprehensive Nuclear Materials*, vol. 5, Oxford: Elsevier, 2012, ch. 7, pp. 143–175. DOI: https://doi.org/10.1016/B978-0-08-056033-5.00113-0.

[89] J. C. Evans *et al.*, "Long-Lived Activation Products in Reactor Materials," Pacific Northwest Lab., Richland, WA (USA), Tech. Rep. NUREG/CR-3474, 1984. DOI: 10.2172/6776358.

[90] "Materials Properties Data Book. Volume I. Introduction and Light Metals," Aerojet Nuclear Systems Co., Sacramento, CA (United States), Tech. Rep. AGC-2275 (Vol.1), 1970. DOI: 10.2172/4240042.

[91] M. Kolluri, "Neutron Irradiation Effects in 5xxx and 6xxx Series Aluminum Alloys: A Literature Review," in *Radiation Effects in Materials*, W. A. Monteiro, Ed., Rijeka: IntechOpen, 2016, ch. 15. DOI: 10.5772/63294.

[92] Witzenmann GmbH, *Metal Hose Manual*, „https://www.witzenmann.com/mediapool/documents/brochures/metal-hose-manual.pdf", Pforzheim, Germany, 2015.

[93] Parker Hannifin Corporation, *Metal Seal Design Guide*, „https://www.parker.com/content/dam/Parker-com/Literature/Composite-Sealing-Systems-Division/CSS5129-Metal-Seal-Design-Guide.pdf", North Haven, CT, 2013.

[94] Arbeitsgemeinschaft Druckbehälter, "AD 2000-Merkblatt B7 – Schrauben," in *AD 2000 Regelwerk*, TÜV-Verband e. V., 2022, ISBN: 978-3410309505.

[95] VDI-Gesellschaft Produkt- und Prozessgestaltung, *VDI 2230 Blatt 1: Systematische Berechnung hochbeanspruchter Schraubenverbindungen: Zylindrische Einschraubenverbindungen* (VDI-Richtlinien). VDI Verein Deutscher Ingenieure e.V, 2015. [Online]. Available: https://www.beuth.de/de/technische-regel/vdi-2230-blatt-1/242566299.

[96] G. Deng *et al.*, "A Study on the Aluminum Alloy AA1050 Severely Deformed by Non-Equal Channel Angular Pressing," in *Engineering Materials and Application*, ser. Advanced Materials Research, vol. 651, Trans Tech Publications Ltd, Mar. 2013, pp. 442–447. DOI: 10.4028/www.scientific.net/AMR.651.442.

[97] Deutsche Gesetzliche Unfallversicherung e.V. (DGUV), *Manufacturing and operation of equipment designed for research purposes*, 2019. [Online]. Available: https://publikationen.dguv.de/widgets/pdf/download/article/3498.

[98] T. G. Peterson and J. G. Weisend, *Cryogenic Safety - A Guide to Best Practice in the Lab and Workplace* (International Cryogenics Monograph Series). Springer, 2019, ISBN: 978-3-030-16508-6. DOI: https://doi.org/10.1007/978-3-030-16508-6.

[99] A. Komlodi, "Detection and Prevention of Hot Cracks during Laser Welding of Aluminium Alloys Using Advanced Simulation Methods," Ph.D. dissertation, Friedrich-Alexander-Universität Erlangen-Nürnberg (FAU), 2006, 155 pages, 89 figures, 14 tables. DOI: 10.25593/978-3-87525-248-4.

[100] H. J. Fahrenwaldt and V. Schuler, *Praxiswissen Schweißtechnik: Werkstoffe, Prozesse, Fertigung*. Vieweg+Teubner Verlag Wiesbaden, 2011, ISBN: 978-3-8348-8199-1. DOI: https://doi.org/10.1007/978-3-8348-8199-1.

[101] M. Strothmann, *Efficiency of a mesitylene based cold moderator system for a compact accelerator driven neutron source*, Master's thesis, 2020. [Online]. Available: https://juser.fz-juelich.de/record/884844.

[102] C. Coceva, M. Frisoni, M. Magnani, and A. Mengoni, "On the figure of merit in neutron time-of-flight measurements," *Nuclear Instruments and Methods in Physics Research Section A*, vol. 489, no. 1-3, pp. 346–356, 2002. DOI: https://doi.org/10.1016/S0168-9002(02)00903-8.

Appendix A

Appendix

A.1 Neutron cross sections of cold moderators

Table A.1: Melting temperature T_{melt}, density ρ (at specific temperature), number density N in molecules per cm^3 and mean free paths for inelastic scattering $\Lambda_{s,inel}$ at thermal energy (subscript "th") and at 10 meV and the mean free path for absorption Λ_a at thermal energy for some commonly used cold moderator materials. If not specified otherwise, thermodynamical data is taken from [43] and cross sections are taken from [12].

Material	T_{melt} [K]	ρ [g/cm^3]	N [10^{24}/cm^3]	$\Lambda_{s,inel,th}$ [cm]	$\Lambda_{s,inel,10meV}$ [cm]	$\Lambda_{a,th}$ [cm]
p-H_2	13.8	0.071 (20 K)	0.021	1.0	19.4	71.6
o-D_2	18.7	0.164 (23 K)	0.024	5.5	3.4	40618.3
H_2O	273.2	0.934 (93 K)	0.031	1.8 [24]	3.0 [24]	48.1
CH_4	90.7	0.51 (22 K)	0.019	1.2	1.1	39.2
C_9H_{12}	228.4	1.07 (228 K)	0.005	0.8 [39]	1.8 [39]	46.3

A.2 Simulation results

A.2.1 Time-averaged brightness

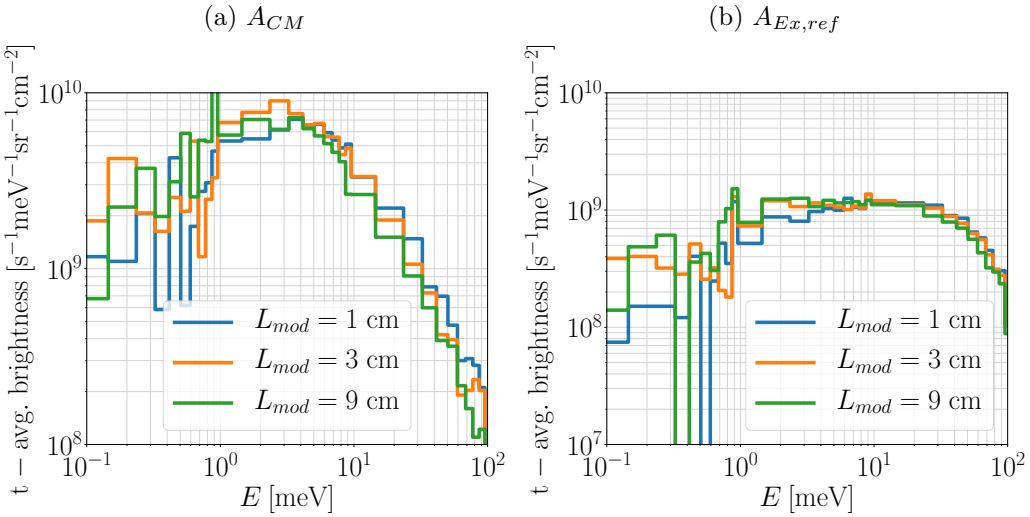

Figure A.1: Time-averaged brightness for a solid cylinder of solid methane at $T = 5$ K with a diameter of $d_{mod} = 2$ cm and different lengths L_{mod}.

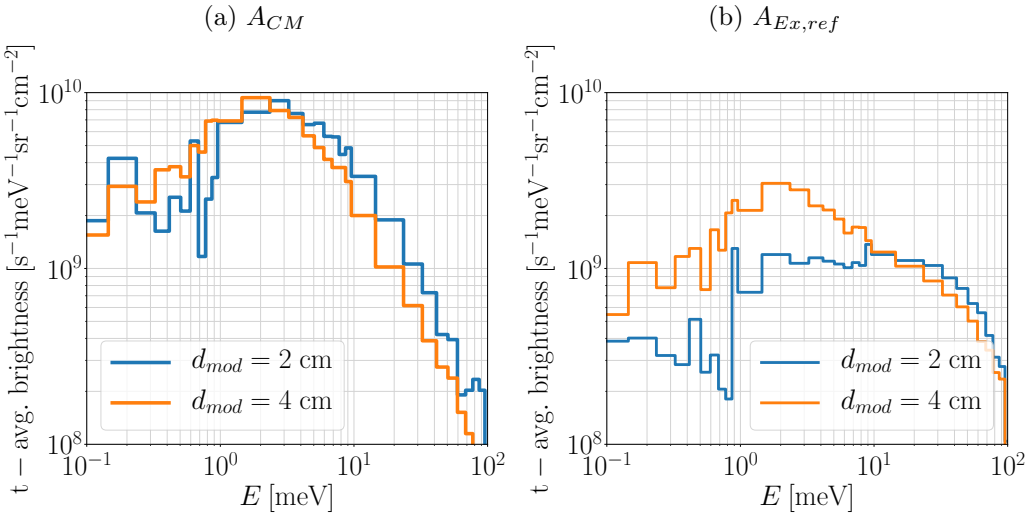

Figure A.2: Time-averaged brightness for a solid cylinder of solid methane at $T = 5$ K with a length of $L_{mod} = 3$ cm and different diameters d_{mod}.

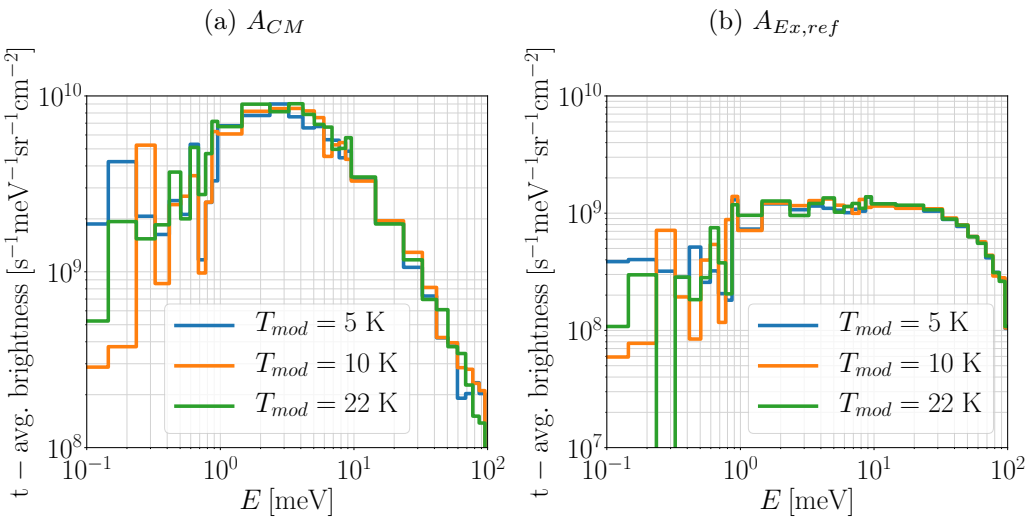

Figure A.3: Time-averaged brightness for a solid cylinder ($d_{mod} = 2$ cm, $L_{mod} = 3$ cm) of solid methane at different temperatures T_{mod}.

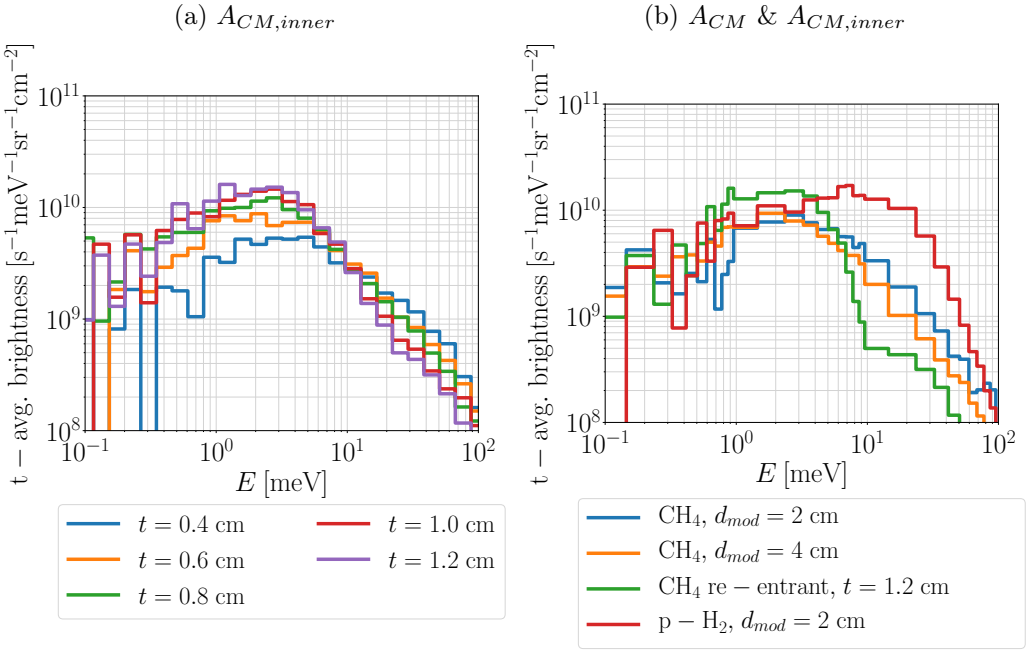

Figure A.4: (a) Time-averaged brightness at $A_{CM,inner}$ for re-entrant moderators with different ring and bottom thicknesses t; (b) Comparison of solid cylinders ($L_{mod} = 3$ cm) with different diameters d_{mod} and re-entrant hole CH_4 cold moderators compared to a solid cylinder liquid parahydrogen (p-H_2) moderator with a length of $L_{mod} = 10$ cm at $T = 20$ K (right graph).

A.2.2 Re-entrant hole

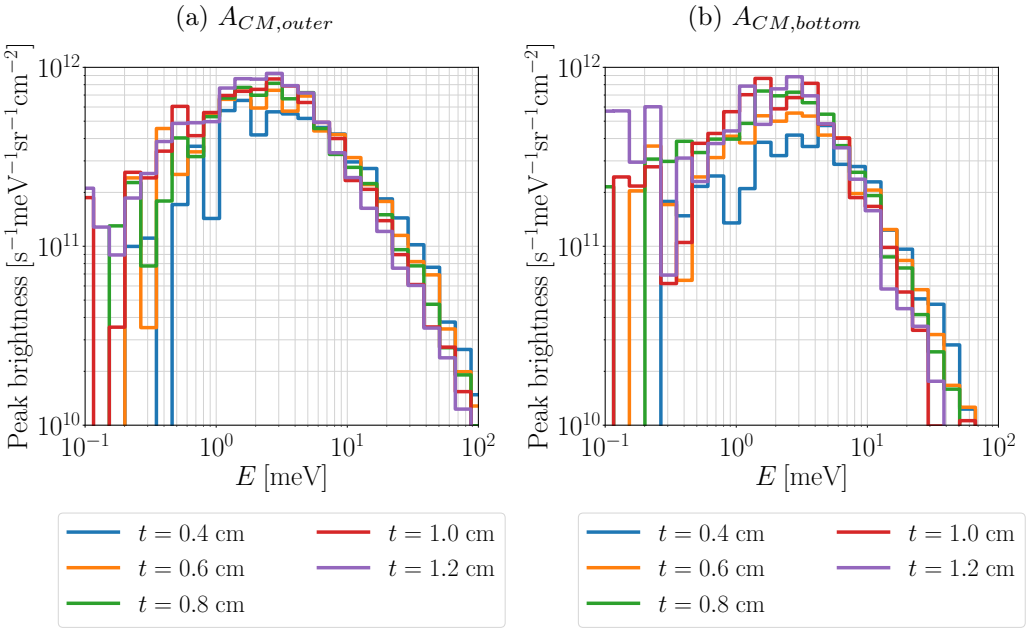

Figure A.5: Peak brightness at different surfaces for solid CH_4 cold moderators at $T_{mod} = 22$ K with different ring and bottom thicknesses t.

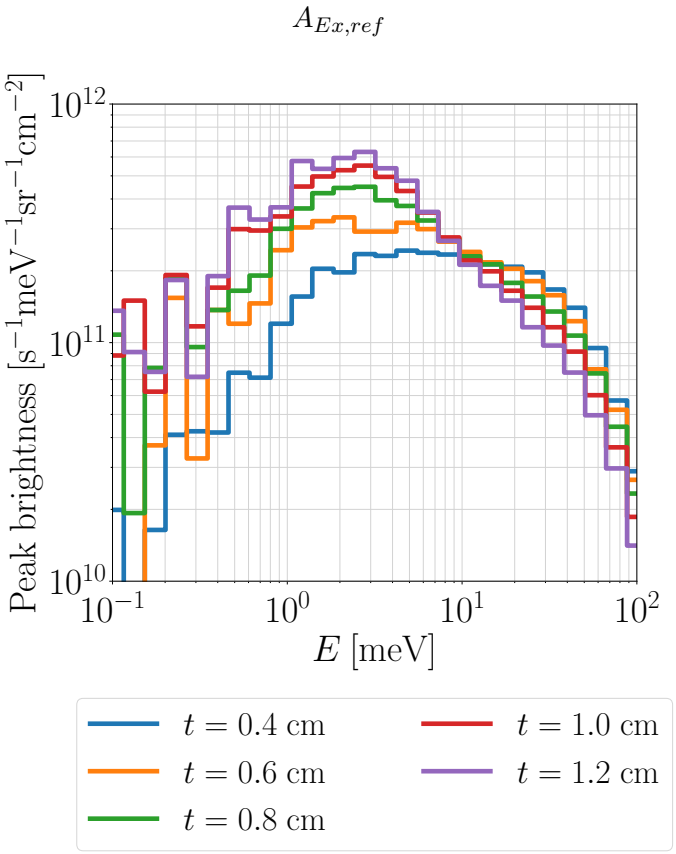

Figure A.6: Peak brightness at the exit surface of the reflector $A_{Ex,ref}$ for solid CH_4 cold moderators at $T_{mod} = 22$ K with different ring and bottom thicknesses t.

Acknowledgements

This PhD thesis would not have been possible without the support of many people. Therefore, I would like to express my profound gratitude to

- Prof. Ghaleb Natour and Prof. Thomas Brückel for supervising my PhD thesis and enabling the project of the cold methane moderator.
- Prof. Lorenz Singheiser for supporting me during the last part of the thesis and being one of the reviewers.
- Dr.-Ing. Yannick Beßler for supporting the thesis on a daily basis and for giving me professional advice on cryostat design and manufacturing as well as for all the help with the organizational hurdles of a PhD thesis.
- my colleagues at the HBS project that were actively involved in the realization of the thesis' project, especially Dr. Paul Zakalek, Dr. Ulrich Rücker, Dr. Jingjing Li, Dr. Johannes Baggemann, Dr. Thomas Gutberlet, Norberto Schmidt.
- my colleagues at ZEA-1 and JCNS-2, especially Dr. Eberhard Rosenthal, Max Hannot, Mathias Strothmann, Dr. Klaus Lieutenant, Dr. Jörg Voigt, Dr. Eric Mauerhofer, Frank Suxdorf, Harald Kleines, Andreas Möller, Frank Gossen, Peter Kämmerling and Berthold Schmitz.
- my office colleagues over the years: Dr. Nileena Nandakumaran, Dr.-Ing. Qi Ding, Dr. Niklas Ophoven and Norberto Schmidt for creating a nice working atmosphere and for giving me a reason to take on the commute to Jülich time and again.
- the colleagues from the workshops of PGI-TA/JCNS-TA and ZEA-1 for realizing the cryostat. I would especially like to thank Norbert Bernard for all his welding work and helpful advice.
- Sebastian Eisenhut for all the work on the parahydrogen cryostat and discussions on cryostat design.
- my family, friends and my girlfriend Nora for always supporting me and giving me the motivation to finish this thesis.